Behrmann, J.H., Lewis, S.D., Musgrave, R.J., et al., 1992
Proceedings of the Ocean Drilling Program, Initial Reports, Vol. 141

7. SITE 860[1]

Shipboard Scientific Party[2]

HOLE 860A

Date occupied: 8 December 1991

Date departed: 9 December 1991

Time on hole: 8 hr, 20 min

Position: 45°51.972′S, 75°45.101′W

Bottom felt (rig floor; m, drill-pipe measurement): 2159

Distance between rig floor and sea level (m): 11.22

Water depth (drill-pipe measurement from sea level (m): (No mudline)

Total depth (rig floor; m): 2165.5

Penetration (m): No mudline

Number of cores (including cores with no recovery): 1

Total length of cored section (m): 9.5

Total core recovered (m): 9.5

Core recovery (%): 100.0

Oldest sediment cored:

Depth (mbsf): 9.5
Nature: Silty claystone
Youngest age: Quaternary
Oldest age: Quaternary

HOLE 860B

Date occupied: 9 December 1991

Date departed: 17 December 1991

Time on hole: 8 days, 0 hr, 10 min

Position: 45°51.972′S, 75°45.101′ W

Bottom felt (rig floor; m, drill-pipe measurement): 2157.1

Distance between rig floor and sea level (m): 11.22

Water depth (drill-pipe measurement from sea level (m): 2145.9

Total depth (rig floor; m): 2774.9

Penetration (m): 617.8 m

Number of cores (including cores with no recovery): 70

Total length of cored section (m): 617.8

Total core recovered (m): 225.8

Core recovery (%): 36.6

Oldest sediment cored:

Depth (mbsf): 617.8
Nature: Silty claystone
Youngest age: Quaternary
Oldest age: early Pliocene
Measured velocity (km/s): 2.075

Principal Results: Drilling at Site 860 penetrated and sampled the seaward flank of a forearc basin and the underlying accretionary wedge. The ages of both the forearc basin strata and the fault wedges drilled in the underlying accretionary wedge range from upper Pliocene to lower Pliocene, with 70 m of Quaternary slope hemipelagic material overlying the older units.

Three lithologic units are identified at Site 860.

Unit I: 0–87.7 mbsf. Quaternary to upper Pliocene, clayey silt to silty clay with nannofossils and with graded silt and sand interbeds, and one 10-m-thick massive sand unit at base.

Unit II: 87.7–242.5 mbsf. Upper Pliocene to lower Pliocene, claystone to silty claystone plus sandstones and thin conglomerate beds.

Subunit IIIA: 242.5–309.8 mbsf: upper Pliocene to lower Pliocene, clayey siltstone, silty claystone with or without nannofossils plus sandy silty claystone with thin conglomerate beds.

Subunit IIIB: 309.8–617.8 mbsf: upper Pliocene to lower Pliocene, gravel, clayey siltstone, silty claystone with or without nannofossils plus sandy silty claystone with thin conglomerate beds in three intervals.

The upper section of Unit I is interpreted to be the result of hemipelagic sedimentary processes, with high- and low-density distal (fine-grained) turbidites dominating the lower section. The massive sand unit that defines the base of Unit I is the result of a single grain-flow depositional event.

Unit II is characterized in its upper section by hemipelagic sedimentation mixed with mud turbidite deposition, but it also exhibits evidence of traction transport and reworking by bottom current flow.

The upper section of Subunit IIIA contains hemipelagic and fine-grained turbidite depositional units, with the lower section of this subunit composed of high-density fine-grained turbidites with signs of reworking. Subunit IIIB exhibits a grain-flow event accompanied by background hemipelagic deposition in its upper section, with successions of high-density, fine-grained turbidites in its lower section. Subunit IIIB also shows signs of bottom current reworking.

Unit III contains at least five repetitions of sedimentary sequences. This is likely the result of imbrication by thrust faults. Microfossil abundance and preservation are improved relative to Site 859. Diatoms are moderately well preserved at the top of Hole 860, but are sparse between 10 and 150 mbsf. Below 150 mbsf no diatoms are present in the cores. Radiolarian abundance is similar to that of diatoms, with many barren cored intervals.

The Pliocene/Pleistocene boundary occurs at about 70 mbsf, with lower Pleistocene sediment between 20 and 70 mbsf. The depth interval 70–617.8 mbsf is of Pliocene age. Two biostratigraphically documented age reversals are observed: at about 240 mbsf and at 310 mbsf. Both age reversals are characterized by upper Pliocene strata appearing beneath a section of lower Pliocene. Probable lower Pliocene foraminifers were recovered from below Core 141-860B-63X, at 560 mbsf.

Paleowater depth determinations based on benthic foraminifers indicate that Site 860 has experienced uplift during the upper Pliocene and lower Pleistocene. Down to approximately 370 mbsf, paleo water depths were middle bathyal. Below about 370 mbsf paleowater depths were lower bathyal to abyssal.

There is a large excursion of magnetic susceptibility at 42–49 mbsf that exceeds by six to seven times the susceptibility elsewhere in the cores. There is a similar but lower amplitude susceptibility anomaly at approximately 8 mbsf.

Three structural domains are defined at Site 860:

1. 0–100 m: near-surface slump deformation,
2. 100–420 m: thrust stack, and
3. 420 m to total depth (TD): broken formation and stratal disruption.

On the basis of structural observations, faults are inferred at depths of 240 mbsf(?), 310 mbsf, 420 mbsf(?), 520 mbsf, and 580 mbsf. All bedding laminations below 420 mbsf are deformed or sheared. Bedding above 420

[1]Behrmann, J.H., Lewis, S.D., Musgrave, R.J., et al., 1992. *Proc. ODP, Init. Repts.*, 141: College Station, TX (Ocean Drilling Program).
[2]Shipboard Scientific Party is as given in list of participants preceding the contents.

mbsf is shallowly dipping 10° SE in oriented APC cores. The thrust faults must be flats or shallow ramps at this location and have large (hundreds of meters) offsets to produce the observed stratal repetitions and simultaneously maintain the observed shallow bedding dips.

Some short sections of coherent core yield a sequence of deformation events. The earliest deformation is characterized by flat-lying deformation bands. The intermediate-aged deformation is manifested by shear surfaces with moderate dips and normal offsets. The last observed deformation event is expressed by high-angle deformation bands showing reverse offsets. This sequence of deformation applies to at least 90 m of core.

The upper 200 m of Site 860 contains biogenic hydrocarbon gas, while below 200 mbsf the gas has a clear thermogenic component. There was no methane in the top core, and below this the methane level found in headspace gas samples was relatively constant at approximately 10,000 ppm to TD. The first appearance of ethane occurred at 60 mbsf, and propane first appeared at 250 mbsf. No gas hydrates were recovered.

Inorganic geochemical trends do not display typical equilibrium profiles at Site 860. Sulfate quickly drops from typical seawater values to near 0 above 60 mbsf, but then maintains a level of about 5–10 mM to TD. Chloride decreases below 100 mbsf, and has local minima at 140 mbsf, 200 mbsf, and 360 mbsf. The chloride profile might reflect relict hydrate dissociation, which would decrease the salinity of pore waters. Other explanations include freshwater transport from land along subsurface aquifers, or release of interlayer water from clay dehydration reactions at depth with fluid migration along thrust faults.

Bulk density measurements on discrete samples show a local minimum at 100 mbsf. Thrust faults identified by other criteria have no apparent signature in bulk density, perhaps suggesting that there is no recent movement on the faults. Grain density shows a local increase at 40–50 mbsf, the same interval that contains a peak in magnetic susceptibility, suggesting that high-density and strongly magnetic minerals may be concentrated at this depth interval. Site 860 displays a compaction profile more typical of marine sediments than did Site 859.

A combination of ADARA piston core shoe and WSTP/Uyeda temperature measurements establishes a geothermal gradient of about 140°C/km in the upper 70 m of Hole 860B, but one apparently reliable measurement at about 130 mbsf suggests that the gradient is about 30°C/km at depth.

Downhole sonic data show a relative high-velocity interval at 120 mbsf. The bottom-hole temperature was 26°C, establishing an overall geothermal gradient of about 38°C/km for the drilled interval.

BACKGROUND AND OBJECTIVES

Site 860 is the central of three sites positioned along seismic Line 745 that together comprise a downdip transect across the trench slope in the region of the Chile margin triple junction. Site 860 is located near the seaward side of a small forearc basin (Fig. 1) underlain by deformed and accreted forearc material and/or by autochthonous South America basement. The primary drilling objectives at Site 860 were to determine the lithologies and depositional environment(s) of the sediment sequences of the forearc basin, to determine the vertical motion history at this position in the forearc, and to determine the lithology and age of the basement of the forearc basin.

A prominent seismic reflector, seen at approximately 0.7 s sub-bottom at the landward end of Line 745 (Fig. 1), can be traced seaward to within about 6 km of the base of the trench slope. This reflector, offset by a series of normal faults near CDP 1800, is interpreted to be continental basement in this region.

The recognition of large-offset normal faults in the mid-slope region strongly suggests that this portion of the margin is subsiding, presumably through the removal of forearc material as the ridge-trench collision progresses. If so, then the record of that subsidence is preserved in the sedimentary record of the forearc basin sampled at Site 860. The combination of lithofacies analysis in terms of depositional environment and paleontological age dating and paleo-water-depth determinations can provide the observations necessary to constrain the vertical motion history of this segment of the forearc during the time period up to and including ridge subduction.

Seismic reflection data and drilling in Peru during ODP Leg 112 (Suess, von Huene, et al., 1988) show that the forearc there is characterized by subsided continental basement extending to within a few tens of kilometers of the trench axis. The drilling results from Peru document the subsidence of the forearc, but the mechanisms that generate the observed subsidence remain poorly constrained. Addressing the issues of forearc mass balance and isostatic adjustments to mass transfer at Site 860 is important for developing new observational data regarding the processes that control mass transfer in subduction zones.

Nearly all of the seismic lines collected in the region of the triple junction, including Line 745, show the prominent basement reflector, typically about 0.5- to 0.9-s sub-bottom beneath the shelf and upper continental slope (Fig. 1). It represents the deepest coherent seismic event that is clearly associated with the overriding continental plate. Drilling to or near this reflection will provide information on the vertical motion history of the overriding plate as the ridge-trench collision progresses, the paleoenvironment of the likely shallow-water sediments deposited over basement, the metamorphic and hydrothermal effects on basement of the subducting spreading ridge, and the relationships between subduction accretion and subduction erosion.

The continental basement seismic reflector can be followed trenchward on seismic lines south of Site 860 to within 2–3 km of the trench, suggesting that subduction erosion has apparently nearly completely removed the accretionary prism south of Site 860 and continental basement is likely being directly eroded. Ascertaining the position of the contact between subsided continental basement and deformed and accreted sediment by drilling at Site 860 will constrain the rate of subduction erosion in the triple-junction region.

A bottom-simulating reflector is present in seismic reflection data at Site 860, presumably resulting from the presence of a zone of frozen gas hydrate in the shallow sub-bottom. Downhole samples using the pressure core sampler (PCS) and water sampling temperature probe (WSTP) were acquired for use in the analysis of the physical chemistry of gas hydrates.

OPERATIONS

Transit to Site 860

Transit over the 3.3 nm from Site 859 to Site 860 was commenced as soon as the pipe cleared the mudline at Hole 859B, at 1115 hr (local time is used throughout, local = UTC–3 hr) on 8 December 1991, and was accomplished in dynamic positioning mode at slow speed with the thrusters still down. The seismic survey and beacon drop had already been carried out during the combined survey of proposed sites SC-1 to SC-3 prior to operations at Site 859. The 14-kHz Datasonics commandable/ releasable beacon was activated at 1830 hr on 8 December 1991, commencing operations at Site 860. (Table 1).

Hole 860A

While still in slow-motion transit from Site 859 we assembled the bottom-hole assembly (BHA) for the next hole, including a large cutter PDC drag bit (10.125 × 3.80 in.) and required subs to allow motor-driven core barrel (MDCD) operations (if appropriate formation was found). Also included was a newly developed anticlog valve as part of the new extended core barrel (XCB)/flow control coring system.

Water depth over the beacon was 2113 meters below sea level (mbsl) according to the precision depth recorder (PDR). Several hours were spent feeling for bottom until it was discovered at about 2159 meters below rig floor (mbrf) according to a somewhat uncertain driller's tag. One overfilled advanced piston corer (APC) core was acquired that did not satisfactorily establish the

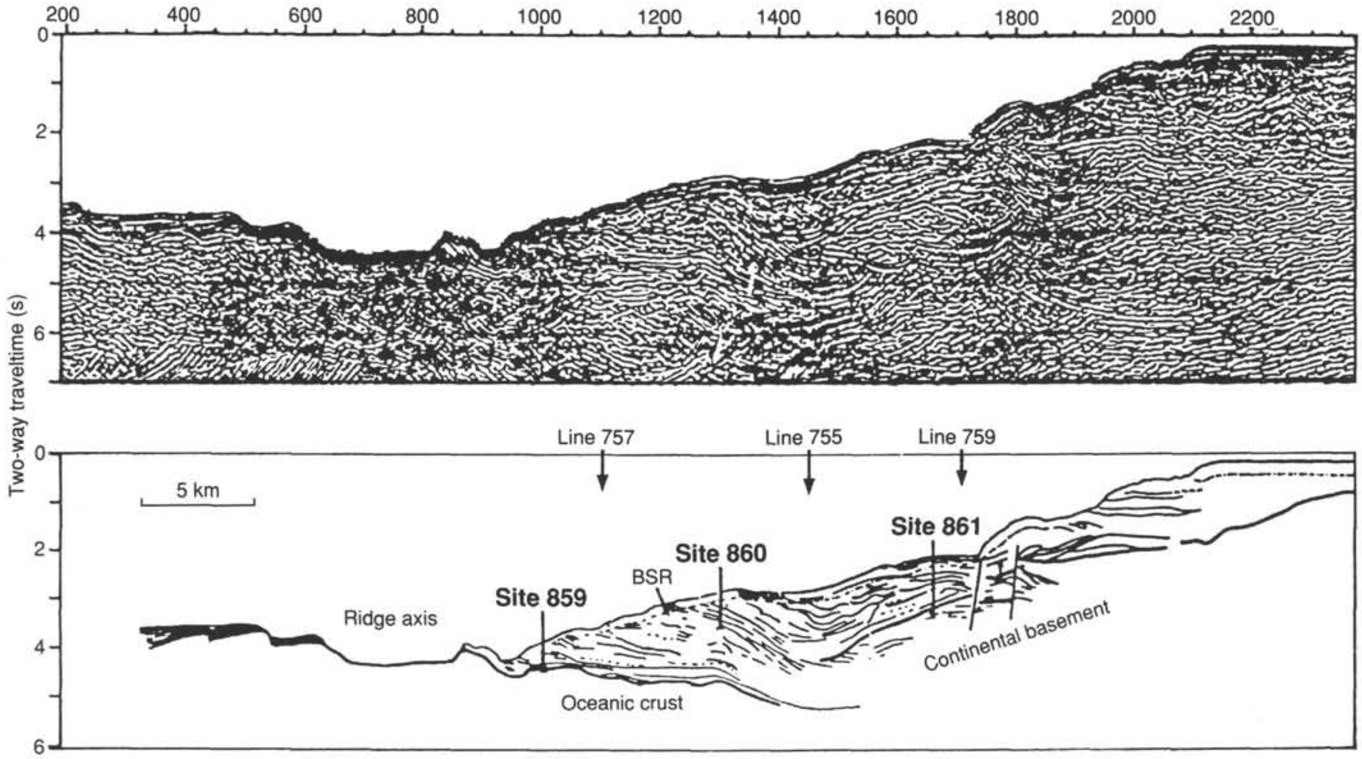

Figure 1. Seismic Line 745, showing the locations of Sites 859 (SC-3), 860 (SC-2), and 861 (SC-1).

depth to the mudline. The pipe was pulled up 7 m to try again, ending operations at Hole 860A at 0250 hr, 9 December 1991.

Hole 860B

The next APC core contained a partially full liner and enabled mudline depth to be set at 2157.1 mbrf. APC coring proceeded only for seven cores, at which point the core barrel could not be extracted with 130,000 lb overpull. The barrel was washed over for 3 m and then pulled free with the sandline. The final four APC cores failed to achieve full initial stroke but each recovered a core more than 8.5 m long. Either the core barrel continued to work its way into the formation after the initial stroke or the extra core was flow-in material sucked in when the barrel was extracted from the formation. Core 141-860B-6H contained almost 9 m of fine-grained sand loosely bound with clay.

Core 141-860B-8P was a deployment of the pressure core sampler (PCS), which was successful from a mechanical viewpoint but did not capture any core sample. The PCS did actuate correctly and came back with pressure inside at 3791 psi, about 540 psi over hydrostatic pressure at bottom hole depth. After Core 141-860B-8P, a water sampler-temperature probe (WSTP) was deployed that became stuck at the bit when retrieval was attempted. Jarring with the wireline "spang" jars managed to get it free but apparently caused a switch in the temperature circuitry to fail and all temperature data was lost. A good in-situ water sample was obtained, however. Evidence of sand stuck in critical parts of the WSTP deployment tool suggested that backflow sand had been responsible for the tool being stuck in the BHA.

The coring mode was then changed to extended core barrel (XCB) for the remainder of the hole to a sub-bottom depth of 617.8 meters below sea floor (mbsf). In general, the XCB coring efforts were moderately successful although core recovery was sometimes poor and rate of penetration was not impressive considering the weakly indurated sediments being drilled.

Cores 141-860B-13P and -18P were PCS cores deployed in an attempt to recover in-situ gas hydrates thought to be present in sufficient quantities to account for a prominent bottom-simulating reflector (BSR) seen on the seismic records. Core 141-860B-13P was successful in capturing 0.61 m of core (total core capacity for the PCS is 0.86 m) and retained pressure on deck of 3012 psi, about 300 psi less than hydrostatic. Core 141-860B-18P experienced what was to be the first of a series of frustrating mechanical failures with the PCS which prevented the recovery of either cores or in-situ pressure.

The WSTP tool was deployed routinely up to 155 mbsf after about every third core. In general, good water and temperature samples were obtained until the formation became too stiff to allow insertion of the probe tip without cracking the sediments. Some temperature records were obtained that taxed the ability of the scientific staff to interpret the results in a meaningful fashion and arrive at a reliable determination of in-situ temperature.

Ten of the XCB cores were taken using the new XCB/flow control (XCB/FC) system, which uses special, flow-regulated core barrels. The XCB/FC deployments were spaced over various sub-bottom depths in the hole. The pressure-flow characteristics of the special barrels were very close to computer model predictions and the regulator function apparently worked as designed to inhibit clogging of the cutting shoe water jets. Unfortunately, this response characteristic did not, as desired, produce more or better core recovery. Recovery for the ten XCB/FC cores ranged from zero to 8.93 m with an average of 15.9%. The standard XCB barrels were deployed 59 times, averaging 31.9% recovery for the entire hole.

All of the cores recovered contained hydrocarbon gases and most showed signs of expansion in the liners. Vacutainer samples were taken whenever possible and monitored for gas composition. The gases present were predominantly methane but significant quantities of heavier molecular-weight hydrocarbon gases were

Table 1. Site 860 coring summary.

Core	Date (December 1991)	Time UTC	Depth (mbsf)	Length cored (m)	Length recovered (m)	Recovery (%)	Age
141-860A							
-1H	9	0600	0.0–9.5	9.5	9.78	103.0	Barren
Coring totals				9.5	9.78	103.0	
141-860B							
-1H	9	0645	0.0–1.4	1.4	1.37	97.8	u. Pleistocene
-2H	9	0730	1.4–10.9	9.5	9.76	103.0	u. Pleistocene
-3H	9	0845	10.9–20.4	9.5	9.96	105.0	u. Pleistocene
-4H	9	1000	20.4–29.9	9.5	10.34	108.8	l. Pleistocene
-5H	9	1300	29.9–39.4	9.5	11.38	119.8	l. Pleistocene
-6H	9	1500	39.4–48.9	9.5	8.88	93.5	l. Pleistocene
-7H	9	1700	48.9–58.4	9.5	10.77	113.3	l. Pleistocene
-8P	9	1845	58.4–59.9	1.5	0.00	0.0	l. Pleistocene
-9X	9	2145	59.9–68.7	8.8	0.12	1.4	l. Pleistocene
-10X	9	2300	68.7–78.1	9.4	0.40	4.3	u. Pliocene
-11X	10	0010	78.1–87.7	9.6	0.00	0.0	u. Pliocene
-12X	10	0130	87.7–97.6	9.9	5.99	60.5	Barren
-13P	10	0220	97.6–99.1	1.5	0.61	40.6	Barren
-14X	10	0520	99.1–107.2	8.1	3.31	40.8	u. Pliocene
-15X	10	0630	107.2–116.8	9.6	6.68	69.6	Barren
-16X	10	0720	116.8–126.5	9.7	3.85	39.7	u. Pliocene
-17X	10	1000	126.5–136.1	9.6	7.40	77.1	u. Pliocene
-18P	10	1100	136.1–137.1	1.0	0.00	0.0	u. Pliocene
-19X	10	1215	137.1–145.8	8.7	8.26	94.9	u. Pliocene
-20X	10	1420	145.8–155.5	9.7	2.41	24.8	u. Pliocene
-21X	10	1815	155.5–165.1	9.6	1.53	15.9	u. Pliocene
-22X	10	1930	165.1–174.8	9.7	4.14	42.7	u. Pliocene
-23X	10	0030	174.8–184.4	9.6	0.14	1.5	u. Pliocene
-24X	10	2230	184.4–194.1	9.7	2.27	23.4	u. Pliocene
-25X	11	0020	194.1–203.7	9.6	2.55	26.5	?
-26X	11	0155	203.7–213.4	9.7	0.00	0.0	?
-27X	11	0320	213.4–223.1	9.7	0.03	0.3	?
-28X	11	0540	223.1–232.8	9.7	1.54	15.9	?
-29X	11	0735	232.8–242.5	9.7	2.31	23.8	Barren
-30X	11	0945	242.5–251.9	9.4	2.73	29.0	Barren
-31X	11	1200	251.9–261.6	9.7	4.38	45.1	u. and l. Pliocene
-32X	11	1330	261.6–271.2	9.6	1.91	19.9	u. Pliocene
-33X	11	1600	271.2–280.8	9.6	2.55	26.5	l. Pliocene
-34X	11	1815	280.8–290.4	9.6	4.94	51.4	l. Pliocene
-35X	11	2200	290.4–300.1	9.7	1.57	16.2	l. Pliocene
-36X	12	0015	300.1–309.8	9.7	4.90	50.5	l. Pliocene
-37X	12	0330	309.8–319.4	9.6	5.12	53.3	u. Pliocene
-38X	12	0540	319.4–328.7	9.3	3.01	32.3	u. Pliocene
-39X	12	0900	328.7–338.4	9.7	2.82	29.1	?
-40X	12	1115	338.4–348.0	9.6	0.40	4.2	?
-41X	12	1410	348.0–357.7	9.7	8.93	92.0	?
-42P	12	1945	357.7–359.2	1.5	0.30	20.0	?
-43X	12	2145	359.2–367.3	8.1	2.08	25.7	Barren
-44X	12	2320	367.3–376.9	9.6	0.17	1.8	u. Pliocene
-45X	13	0150	376.9–386.6	9.7	0.45	4.6	Barren
-46X	13	0445	386.6–396.3	9.7	2.66	27.4	Barren
-47X	13	0630	396.3–406.0	9.7	0.58	6.0	Pliocene
-48X	13	0900	406.0–415.7	9.7	5.95	61.3	Pliocene
-49X	13	1115	415.7–425.3	9.6	1.11	11.5	Piocene
-50X	13	1300	425.3–434.8	9.5	5.61	59.0	Barren
-51X	13	1530	434.8–444.4	9.6	4.31	44.9	Pliocene
-52X	13	1745	444.4–449.1	4.7	0.35	7.4	Pliocene
-53X	13	2000	449.1–453.7	4.6	3.12	67.8	Pliocene
-54X	13	2250	453.7–463.8	10.1	0.14	1.4	Pliocene
-55X	14	0040	463.8–473.4	9.6	0.42	4.4	Barren
-56X	14	0250	473.4–483.1	9.7	0.31	3.2	Pliocene
-57X	14	0550	483.1–492.8	9.7	0.47	4.8	Barren
-58X	14	0750	492.8–502.4	9.6	4.29	44.7	u. Pliocene
-59X	14	1000	502.4–512.0	9.6	0.47	4.9	Barren
-60X	14	1200	512.0–521.7	9.7	4.98	51.3	Pliocene
-61X	14	1400	521.7–530.9	9.2	9.75	106.0	Pliocene
-62X	14	1745	530.9–540.5	9.6	5.41	56.3	?
-63X	14	2010	540.5–550.2	9.7	0.15	1.5	Pliocene
-64X	14	2315	550.2–559.9	9.7	4.20	43.3	Barren
-65X	15	0210	559.9–569.5	9.6	0.24	2.5	l. Pliocene
-66X	15	0520	569.5–579.2	9.7	2.91	30.0	l. Pliocene
-67X	15	0800	579.2–588.8	9.6	5.37	55.9	?
-68X	15	1230	588.8–598.4	9.6	0.00	0.0	?
-69X	15	1600	598.4–608.2	9.8	0.45	4.6	l. Pliocene
-70X	15	1915	608.2–617.8	9.6	0.32	3.3	?
Coring totals				617.82	25.83	36.6	

found, including species above C_6. When these compounds were identified and the C_1/C_2 ratio dropped to below 500 it was presumed that the gases were from a thermally mature source and had migrated to their present location from an unknown distance. Drilling operations were stopped after Core 141-860B-41X (357.7 mbsf) in accordance with standard Pollution Prevention and Safety Panel (PPSP) policy. The PPSP authorities were contacted for further authorization to deepen the hole. The authorization was received via Marisat and the coring continued. A final PCS core (141-860B-42P) was deployed in an attempt to capture a core at in-situ pressure conditions in hopes of getting some measure of total gas content in situ. This attempt was frustrated by still another mechanical failure of the complex PCS latching system, which again did not latch shut and close the ball valve.

Heavy hydrocarbon gases detected in the cores almost immediately dropped off with further drilling and, although the Vacutainer C_1/C_2 ratio dipped to as low as 321, the evidence for a nearby reserve of petroleum or natural gas with dangerous pollution potential steadily decreased and hydrocarbons did not play a role in the determination to stop drilling in the hole.

The sonic core monitor (SCM) system was tested briefly (with Cores 141-860B-64X, -66X, and -68X) and performed well. Minor software problems on deck were corrected and three runs were completed in which the downhole electronic monitoring unit was able to accurately track and record core entry. Unfortunately, the last run was marred when the core barrel apparently landed 6 m above its normal land/latch-in location (as determined by the sandline depth recorder during recovery). No core was recovered. The next core barrel was pumped down with tell-tale paint and recovered to check for obstructions in the BHA but no problems were found.

A multishot drift survey of the hole was taken at 100-m stations during the recovery of Core 141-860B-70X. The inclination of the hole slowly increased with depth to a maximum of 4° at terminal depth (TD). The hole was terminated at 2774.9 mbrf (617.8 mbsf) when the co-chief scientists determined that the continental basement target may, in fact, not be present below this site. By that time significant hole problems were beginning to crop up including 22 m of fill following the last core.

At this site the BHA was set up to allow for MDCB coring and the intention had been to test the MDCB if possible. However, the plans to do so were abandoned because of inappropriate formation conditions for a good test (stiff siltstone rather than crystalline rock suitable for diamond coring) and the increasingly troublesome hole problems encountered at the bottom of the hole.

Logging operations (Table 2) began at 1630 hr on 15 December 1991 with a mud sweep and full-length wiper trip. To enhance the potential for successful open-hole logging the hole was displaced with high-viscosity mud containing 1% KCl. Reaching the lowermost 126 m of the hole required rotation and circulation during the downward portion of the wiper trip to clean out fill and minor bridges. An aluminum go-devil was pumped down to lock open the lockable float valve. Rig-up of the geophysical tool string began at 0130 hr on December 16. The first logging run, the Quad combo, was attempted without the side-entry sub. The tools were stopped by a bridge at 188 mbsf and logging was achieved only from that point to the logging depth of the bit (55 mbsf). When the tools were pulled into the BHA they encountered an obstruction assumed to be the float valve that either had not locked open or had become unlocked during the logging. By pumping down the pipe and working the tools we induced them to re-enter the BHA, and they were recovered undamaged.

The side-entry sub was picked up and placed in the drill string to achieve more access to the hole for the remainder of the logging program. The bit was run to 2762 mbsl (616 mbsf) while the abbreviated logging tool string (TCC-NGT-MCD-LSS-DIT) was run through the pipe. This string would not exit the pipe and while attempting to determine why the tools would not go down we apparently overran the logging cable, resulting in an abrupt separation of the line between the cable head and torpedo connection. A core barrel with a "Larson" core catcher was lowered to determine the location of the fish and, if possible, get a grip on it. The logging tools were tagged at a location suggesting that they were well up inside the BHA but no grip on the up-looking cable head could be achieved. It was not known what was holding the tools in the BHA or how secure the tools were held, so further attempts to fish out the tools were abandoned. The pipe was tripped to the deck and the tools were removed from the BHA there. The bit cleared the rotary table at 0300 hr on 17 December 1991, ending operations in Hole 860B. The logging tools were found with the aluminum bullnose at the bottom of the string (installed to lock open the lockable float valve flapper) wedged against the flapper, which was prevented from opening completely by rocks and sediment jammed behind it.

The hole was abandoned with only high-viscosity logging mud in place rather than with the added barite-weighted mud that should have been pumped into the hole for abandonment. With the logging tools held in the BHA by an unknown mechanism it was not considered prudent to pump against the jammed tools for fear of losing them completely. The trip out of the hole and very short transit to the next site was conducted at night and in poor weather. Accordingly, the beacon at Site 860 was not released. Plans were made to return to the site after completion of the next site to collect the beacon.

Table 2. Well log data from Hole 860B.

Log type	Depth (mbsf)
Resistivity	70.5–181.3
Sonic velocity	70.5–173.4
Gamma ray	70.5–162.7
Caliper	70.5–165.5
LDGO temperature	0.0–615.0

Note: Assumes seafloor at 2145.8 mbsf. Log depths may be off by 4–6 m compared to core (see Log Quality discussion in Wireline Measurements section, this chapter).

LITHOSTRATIGRAPHY

Lithostratigraphic Units

At Site 860 two holes were cored using the APC/XCB technique. Hole 860A has a total penetration of more than 9.5 mbsf; the exact depth is not known, as no mudline was established. Hole 860B provides a continuous recovery of the upper 58.8 mbsf, then variable recovery down to 617.8 mbsf. The lithostratigraphy is based on visual descriptions and smear-slide and thin-section studies. The results of structural, chemical, and physical studies are also considered.

At Site 860 the stratigraphic succession is divided into three major units according to their lithology, microfossil content, and on the basis of their mode of deposition (Table 3; Fig. 80). Unit I is characterized by clayey silt to silty clay with a distinct biogenic component of nannofossils and foraminifers, moderately inter-

Table 3. Litholstratigraphy for Site 860.

Units	Age	Interval (depth)	Lithology	Sedimentary process
Unit I	late to early Pleistocene and late Pliocene	Core 141-860A-1H and Cores 141-860B-1H through 141-860B-11X (0–87.7 mbsf)	Clayey silt to silty clay with nannofossils, + graded silt and sand interbeds, massive sand	Hemipelagic sedimentation + high to low-density fine-grained turbidites
Unit II	late Pliocene to early Pliocene	Cores 141-860B-12X through 141-860B-29X (87.7–242.5 mbsf)	Claystone to silty claystone, (lapilli bed) + sandstones, thin beds of conglomerate	Hemipelagic sedimentation, mud turbidites + traction, transport, reworking
Subunit IIA	late Pliocene to early Pliocene	Cores 141-860B-30X through 141-860B-36X (242.5–309.8 mbsf)	Clayey siltstone, silty claystone ± nannofossils + sandy-silty-claystone (diamictite), thin beds of conglomerate	Hemipelagic sedimentation, fine-grained turbidites + debris flows, high-density fine-grained turbidites, reworking
Subunit IIIB	late Pliocene to early Pliocene	Cores 141-860B-37X through 141-860B-70X (309.8–617.8 mbsf)	Gravel, clayey siltstone, silty claystone ± nannofossils + sandy-silty-claystone (diamictite) within three intervals, thin beds of conglomerates	Debris flow, hemipelagic sedimentation + debris flows, high-density fine-grained turbidites, reworking

bedded with relatively thin beds of silt and normally-graded fine sand. These small-scale cycles are upward fining. Overall, Unit I shows a slight coarsening-upward character and sand beds are more abundant in the upper portions. The contact between Unit I and Unit II is placed at the top of Core 141-860B-12X at 87.7 mbsf. Unit II is dominantly fine-grained and consists of mainly consolidated claystones and silty claystones with some organic fragments and pyrite nodules. Fine-grained sediments, mostly clayey siltstones, in the middle part of Unit II also contain small proportions of calcareous components. In the lower part of this unit, coarser sediments form laminated intervals, massive beds, and intraformational conglomerates. The contact between Unit II and Unit III is located at 242.5 mbsf at the base of Core 141-860B-29X. Unit III is characterized by a range of lithologies from matrix-supported, disorganized sandy-silty-claystones with dispersed pebble- to granule-sized lithic clasts ("diamictite"), to bedded silty claystones and nannofossil siltstones in the upper parts of the successions. The interval between Cores 141-860B-30X and 141-860B-36X (Subunit IIIA) represents a typical sequence of Unit III with upward-fining small-scale sedimentary cycles, now structurally bracketed by two major thrusts (see Structural Geology section, this chapter). The lower part of Unit III below 309.8 mbsf (Subunit IIIB) is characterized by several sequences that are distinctly similar to Subunit IIIA. Subunit IIIB also consists mostly of disorganized sediment beds associated with silty claystones having relatively low microfossil content. In total, it is composed of three superimposed, relatively similar sedimentary successions that may either represent a cyclic sedimentation history or, more likely, a tectonic imbrication. Overall, Unit III shows a slightly coarsening-upward trend in which sandy-silty-claystones with dispersed larger clasts become more abundant upsection.

Unit I (Core 141-860A-1H; Cores 141-860B-1H to -11X; age: late Pleistocene to late Pliocene; depth: 0–87.7 mbsf)

This unit consists predominantly of grayish olive green (5GY 3/2) to dark greenish gray (5GY 4/1) clayey silt to clay with nannofossils, foraminifers, and siliceous microfossils (diatoms, radiolarians, sponge spicules, silicoflagellates). Siliceous microfossil content is overall very low and concentrated in the uppermost part of the unit. Calcareous microfauna constitute a relatively minor component (0%–20%) that decreases downhole (Fig. 2). Total carbonate content within Unit I ranges from 0.4% to 5.2% (Table 4; Fig. 3). The calcareous clayey silt to silty clay succession is moderately bedded with very thin graded beds of silt (Fig. 4) and some fine sand (Fig. 5). Lower contacts are sharp, and usually there is a short gradational change to overlying sediments. These sandy intervals and their heavy mineral content may correlate with higher grain density values (see Physical Properties section, this chapter). The terrigenous fraction of these sediments consists predominantly of quartz and feldspar, with minor amounts of volcanic glass, amphibole, and opaque minerals, e.g., pyrite. Total abundance of terrigenous and clay components vs. sub-bottom depth is shown in Figure 6. In some sands the volcanic component is as high as 25%. Some local irregular concentrations of granule- to pebble-sized gravel and shell fragments are present (e.g., intervals 141-860A-1H-5, 103–111 cm, -1H-6, 0–5 cm, 141-860B-2H, 91–100 cm, -2H-6, 135–140 cm), generally with nondistinct contacts.

Core 141-860B-6H consists of massive, dark gray (N3) fine- to medium-grained sand. This sand is relatively well sorted and composed of subrounded siliciclastic, volcaniclastic (up to 30%), and opaque mineral grains. Grain densities and magnetic susceptibility increase in the lower part of this sand bed (see Paleomag-

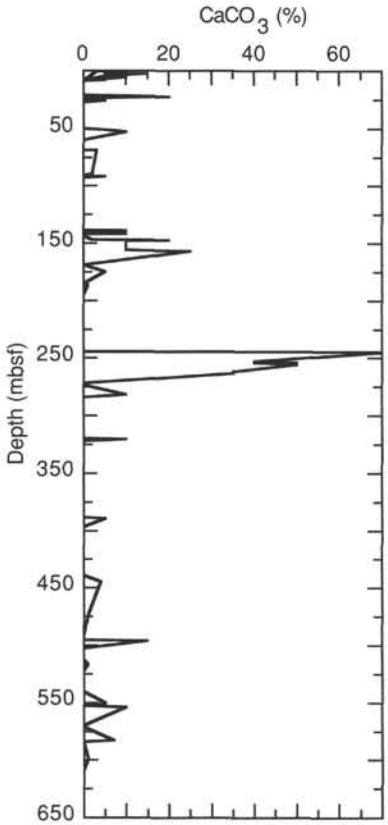

Figure 2. Abundance of calcium carbonate at Site 860 as determined by petrographic estimation of the percentage of calcareous components from smear slides.

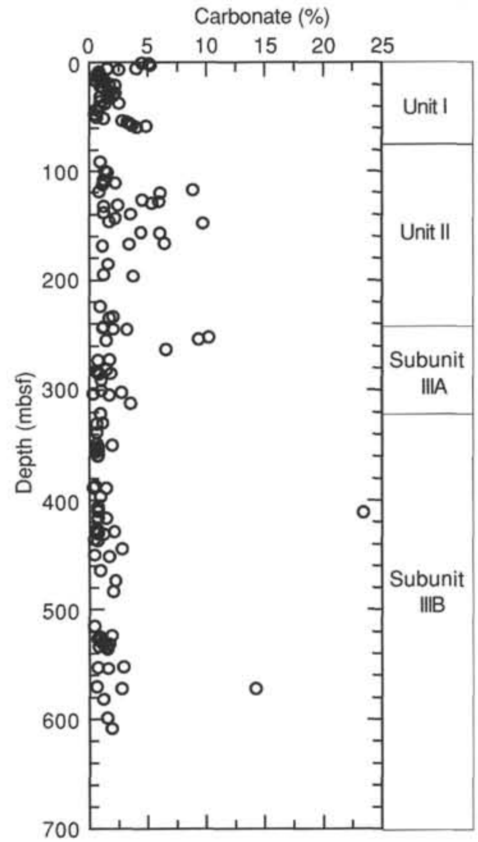

Figure 3. Total carbonate content at Site 860 as determined by geochemical analysis (see Table 4).

netism and Physical Properties sections, this chapter). The recovered thickness of this sand bed may be exaggerated by flow-in processes in the core liner.

Depositional Processes

Because Unit I recovery was high and drilling disturbance low, sedimentological interpretation is straightforward. The bulk of recovered sediment is interpreted to be the product of deposition from suspension. Unit I represents mixed deposition from hemipelagic fallout and from low-density fine-grained turbidity currents (clayey silt to silty clay with microfossils and thin beds of graded or laminated silt). Low-density flows generally carry largely clay- and silt-sized particles and they may produce fine horizontal lamination. The graded sand (e.g., in Sections 141-860A-1H-7 and -CC, and 141-860B-2H-5) has been deposited by turbidity currents of higher density. Massive sand could have been transported down steep slopes by grain flow. However, pure grain flows in nature are rare, and thicker sand beds as in Core 141-860B-6H are generally produced by high concentration turbidity currents, with transport in turbulent suspension followed by rapid settling from suspension, resulting in a structureless sand bed (Pickering, et al., 1989).

Unit II (Cores 141-860B-12X to -29X; age: late to early Pliocene; depth: 87.7–242.5 mbsf)

This unit consists predominantly of olive-gray (5Y 4/1) to grayish olive-green (5GY 3/2) claystones and silty claystones. Bulk densities are lower for the upper part of this unit where the claystones are more abundant (see Physical Properties section, this chapter). Isolated, black pyrite-bearing streaks and spots of organic matter are common in the upper part of this unit. Carbonate-containing sediments are relatively rare in this unit except for one interval of calcareous sandy-silty-claystones in Core 141-860B-20X at 145.8–155.8 mbsf (see Figs. 2 and 6), with a total carbonate content as high as 9.7% (Table 4; Fig. 3). In Unit II total carbonate content generally ranges from 0.8 to 3.5% but slightly higher values (4.5-8.8%) occur at 116.8–136.1 mbsf in Cores 141-860B-16X to -17X and at 145.8–165.1 mbsf in Cores 141-860B-20X to -21X (Table 4; Fig. 3). The silt and sand components in Unit II are mostly quartz and feldspar with lesser amounts of amphibole, volcanic glass, and opaques. Volcanic glass is mostly colorless or light brownish, with some showing microlitic texture. The uppermost cores of this unit are disturbed by drilling. Material in cores is often structureless drilling breccia that grades into biscuited zones; however, where original bedding is preserved (e.g., Cores 141-860B-15X and -16X), one sees a succession of moderately to thickly bedded claystones and clayey siltstones with color ranging from grayish olive-green (5GY 2/1) to greenish black (5G 2/1). Small shells of micro- and macrofauna occur in Sections 141-860B-17X-1 to -3 and -5, and -19X-2 and -4. A light gray (N8) lapilli bed of highly vesicular vitric clasts is present in the interval from 144.7–144.92 mbsf (intervals 141-860B-19X-6, 10–20 cm, and -CC, 0–12 cm). The lower part of Unit II also contains sand-sized sediment. Dark gray (N4), laminated sandy siltstone and some thin interbeds of silty sandstone occur in Sections 141-860B-22X-3 and -CC. Finely-laminated, wedge-shaped sets of sandy siltstone in intervals 141-860B-22X-3, 12–15 cm, and 35–39 cm, are slightly inclined compared to general bedding, and resemble cross-lamination (Fig. 7). Silty claystone

Table 4. Total carbonate content in Site 860 samples.

Core, section, interval (cm)	Depth (mbsf)	% Carbonate
141-860B-		
1H-1, 22–24	0.22	4.5
1H-1, 98–100	0.98	5.1
2H-1, 74–76	2.14	5.2
2H-3, 114–116	5.54	4.0
2H-3, 117–119	5.57	1.5
2H-4, 56–58	6.46	2.5
2H-5, 98–100	8.38	0.8
2H-6, 101–103	9.91	0.7
2H-CC, 15–17	11.01	0.9
3H-1, 100–102	11.90	0.6
3H-2, 104–106	13.44	0.8
3H-3, 114–116	15.04	1.2
3H-4, 104–106	16.44	0.6
3H-5, 100–102	17.90	1.2
3H-6, 104–106	19.44	1.7
3H-7, 50–52	20.40	2.2
4H-1, 104–106	21.44	0.9
4H-2, 97–99	22.87	1.2
4H-4, 96–98	25.86	1.7
4H-5, 05–107	27.45	2.2
4H-6, 105–107	28.95	1.7
4H-7, 50–52	29.90	2.0
4H-CC, 29–31	30.41	1.5
5H-1, 131–133	31.21	0.9
5H-2, 104–106	32.44	1.7
5H-4, 80–82	35.20	0.9
5H-5, 94–96	36.84	2.5
5H-6, 24–26	37.64	1.3
5H-7, 74–76	39.64	0.9
6H-3, 16–18	42.56	0.6
6H-3, 97–99	43.37	0.7
6H-6, 21–23	47.11	0.4
7H-1, 100–102	49.90	0.6
7H-2, 88–90	51.28	1.2
7H-3, 103–105	52.93	2.8
7H-4, 88–90	54.28	3.2
7H-5, 88–90	55.78	3.4
7H-6, 80–82	57.20	3.6
7H-7, 10–12	58.00	4.8
7H-CC, 10–12	59.34	4.0
12X-3, 48–49	91.18	0.9
14X-1, 52–54	99.62	1.3
14X-2, 35–37	100.95	1.5
15X-1, 100–102	108.20	1.2
15X-2, 100–102	109.70	1.3
15X-3, 94–96	111.14	2.2
15X-4, 90–92	112.60	1.1
16X-1, 76–78	117.56	8.8
16X-2, 76–78	119.06	0.8
16X-3, 27–30	120.07	6.0
17X-1, 29–31	126.79	4.5
17X-2, 29–31	128.29	5.9
17X-3, 29–31	129.79	5.3
17X-4, 29–31	131.29	2.4
17X-5, 29–31	132.79	1.2
19X-1, 133–135	138.43	1.2
19X-2, 127–129	139.87	3.5
19X-5, 43–45	143.53	2.2
20X-1, 55–57	146.35	1.7
20X-CC, 10–12	148.03	9.7
21X-1, 90–91	156.40	4.4
2:X-CC, 2–4	156.86	6.0
22X-1, 121–123	166.31	6.4
22X-2, 70–72	167.30	3.4
22X-3, 56–58	168.66	1.1
24X-1, 96–98	185.36	1.6
25X-1, 75–77	194.85	1.2
25X-CC, 12–14	196.41	3.7
28X-1, 114–116	224.24	0.9
29X-1, 40–42	233.20	2.0
29X-2, 19–21	234.49	1.7
30X-1, 22–25	242.72	1.2
30X-2, 60–62	243.67	1.1

Table 4 (continued).

Core, section, interval (cm)	Depth (mbsf)	% Carbonate
141-860B- (Cont.)		
30X-3, 20–22	244.77	2.0
30X-CC, 25–27	245.12	3.2
31X-1, 36–38	252.26	10.2
31X-2, 26–28	253.66	9.3
31X-3, 18–20	255.08	1.4
32X-2, 82–84	263.18	6.5
33X-1, 119–121	272.39	1.7
33X-2, 17–19	272.87	0.7
34X-1, 31–33	281.11	1.4
34X-2, 30–32	282.60	0.5
34X-3, 25–27	284.05	0.7
34X-4, 27–29	285.07	1.8
34X-CC, 15–17	285.57	0.8
35X-1, 73–75	291.13	1.0
36X-1, 18–20	300.28	1.0
36X-2, 74–76	302.34	2.7
36X-3, 34–36	303.44	0.3
36X-4, 26–28	304.36	1.7
37X-2, 92–94	312.22	3.5
38X-2, 42–44	321.23	0.9
39X-1, 108–110	329.78	1.1
39X-2, 62–64	330.82	0.6
40X-CC, 20–22	338.60	0.6
41X-1, 42–44	348.42	0.6
41X-2, 42–44	349.92	1.9
41X-3, 42–44	351.42	0.7
41X-4, 42–44	352.92	0.7
41X-5, 42–44	354.42	0.7
41X-6, 42–44	355.92	0.6
43X-1, 28–30	359.48	0.7
43X-1, 76–78	359.96	0.7
46X-1, 63–65	387.23	0.5
46X-2, 31–33	388.20	0.3
46X-CC, 21–23	389.14	1.4
47X-CC, 46–48	396.76	0.9
48X-1, 28–30	406.28	0.7
48X-2, 6–8	407.56	0.7
48X-4, 22–24	409.76	0.7
48X-5, 9–11	411.13	23.4
49X-1, 36–38	416.06	0.7
49X-CC, 20–25	416.64	1.4
50X-1, 80–83	426.10	0.6
50X-2, 40–42	427.20	0.7
50X-3, 40–42	428.70	2.1
50X-4, 60–62	429.55	0.5
50X-5, 41–44	430.36	0.7
50X-CC, 28–30	430.79	1.2
51X-1, 90–93	435.70	0.4
51X-2, 91–94	437.21	0.7
52X-CC, 25–27	444.65	2.8
53X-1, 82–84	449.92	0.4
53X-2, 80–82	451.40	1.7
55X-CC, 33–35	464.13	0.9
56X-CC, 16–18	473.56	2.2
57X-CC, 43–44	483.53	2.0
60X-3, 54–56	514.94	0.4
61X-2, 18–21	523.38	1.9
61X-3, 22–25	524.92	0.9
61X-4, 10–12	526.30	0.7
61X-5, 15–17	527.85	0.8
61X-6, 11–13	529.31	1.1
61X-CC, 12–14	531.27	1.7
62X-1, 73–76	531.63	1.2
62X-2, 99–102	533.39	0.8
62X-3, 35–38	534.25	1.5
62X-4, 38–40	535.78	1.5
64X-2, 32–34	552.02	2.9
64X-3, 65–67	552.85	0.7
64X-4, 45–47	553.65	1.6
66X-1, 69–71	570.19	0.6
66X-2, 91–93	571.91	2.7
66X-CC, 7–9	572.07	14.2
67X-2, 100–102	581.70	1.2
69X-CC, 16–18	598.56	1.5
70X-CC, 22–24	608.42	1.9

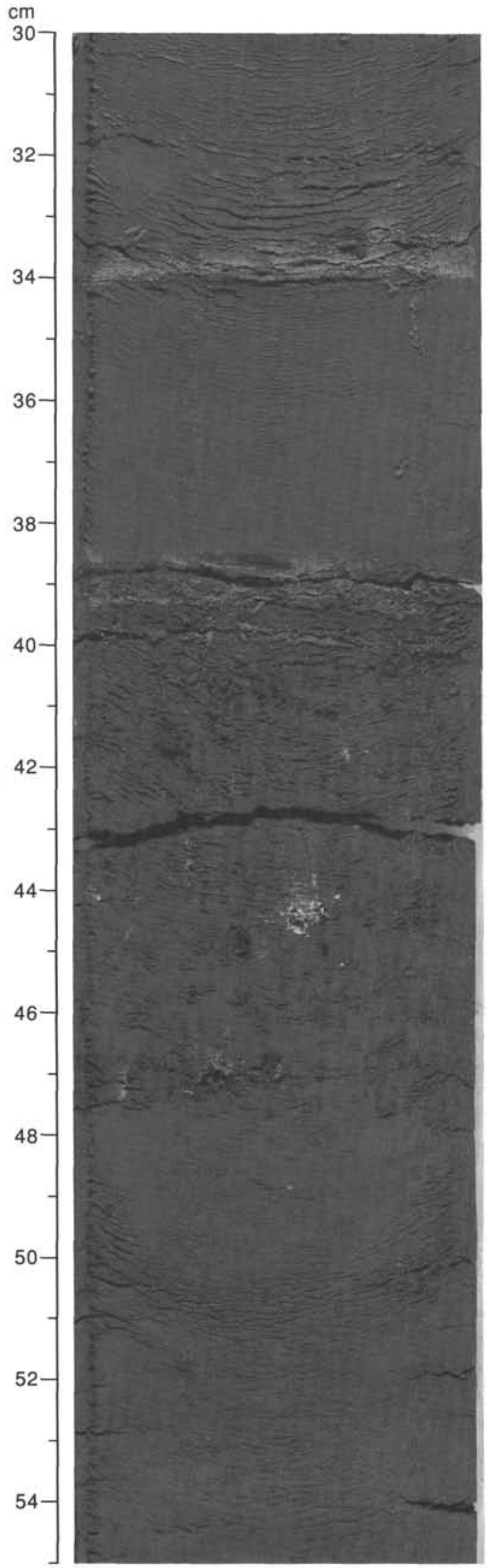

Figure 4. Core photograph, silty clay to clay with calcareous microfossils overlain by thin graded layers of silt (interval 141-860B-4H-4, 30–55 cm).

to clayey siltstone in Core 141-860B-25X is associated with thin interbeds of intraformational granule-sized conglomerate (intervals 141-860B-25X-2, 40–41 cm, and -CC, 3–6 cm and 18–20 cm), sandy siltstone and claystone (Fig. 8). This same type of conglomerate also occurs in interval 141-860B-28X-1, 98-101 cm. Clasts are mostly sedimentary siltstone and claystone but shale clasts and concretional pyrite also occur. Maximum clast size is 3 cm. The conglomerates are predominantly clast-supported but their upper parts may be matrix supported.

Depositional Processes

The sediments of Unit II are predominantly the result of hemipelagic deposition, but their relatively low microfossil content suggests that they may be fine-grained mud turbidites. Mud turbidites are generally homogeneous with only very minor proportions of sand-sized particles, and lower parts may show lamination. Preserved laminations in Unit II indicate transport by traction currents. The thin beds of intraformational conglomerates are inferred to be produced by sediment reworking.

Unit III (Cores 141-860B-30X to -70X; age: late to early Pliocene; depth: 242.5– 617.8 mbsf)

This unit is dominated by clayey siltstone to silty claystone with some interbeds of nannofossil ooze and nannofossil clayey siltstone (see Fig. 2) and matrix-supported sandy-silty-claystones with dispersed granule- to pebble-sized lithic clasts ("diamictite"). Bedded silty claystones and thin beds of intraformational, generally clast-supported conglomerates also occur. One typical sequence of all these lithologies forms Subunit IIIA (60-m interval from top of Core 141-860B-30X through the bottom of -36X). Diamictite occurs in one interval (271.7–280.8 mbsf) in Core 141-860B-33X (Fig. 9). Subunit IIIB contains this same type of lithology with varying amounts of calcareous microfossils in the fine-grained sediments (interval from top of Core 141-860B-39X through the bottom of -70X). Several units of diamictite, up to 1.5 m thick, occur in Cores 141-860B-41X through -44X, -58X, and -64X (Fig. 9).

Subunit IIIA

Clayey siltstone and silty claystone within Subunit IIIA are generally grayish green (5GY 3/2) to olive-gray (5Y 3/2) and moderately bedded to laminated. Some of these have a distinct calcareous component (see Figs. 2 and 9), and contain organic matter, plant debris, and rare shell fragments (e.g., Cores 141-860B-31X and -32X in 251.9–271.2 mbsf). Total carbonate content ranges from 1.4% to 10.2% (Table 4; Fig. 3). Terrigenous mineral components in these sediments are mostly quartz, feldspar, and minor amounts of volcanic glass, amphibole, and opaque minerals. In the diamictic sandy-silty-claystones, dispersed clasts include shell fragments, small pyritized wood stems, and granule- to some pebble-sized clasts of volcanic rocks, claystones, and siltstones. Clasts are subangular to subrounded.

In the lowermost section of Subunit IIIA intraformational conglomerates are interbedded with clayey siltstones and silty claystones (intervals 141-860B-36X-2, 50–60 cm, and -36X-4, 24–27 cm). The conglomerate beds range from clast- to matrix-supported and have diffuse contacts with underlying lithologies. Maximum clast size is 0.8 cm and some clasts are well-rounded (Fig. 9).

Subunit IIIB

The top of this subunit is marked by a 5-m-thick bed of olive-gray (5Y 4/1), poorly sorted to olive-gray (5Y 3/2), moderately sorted, granule- to pebble-sized gravel. Clasts range from rounded to very well rounded (Fig. 10). Maximum grain size is 2 cm.

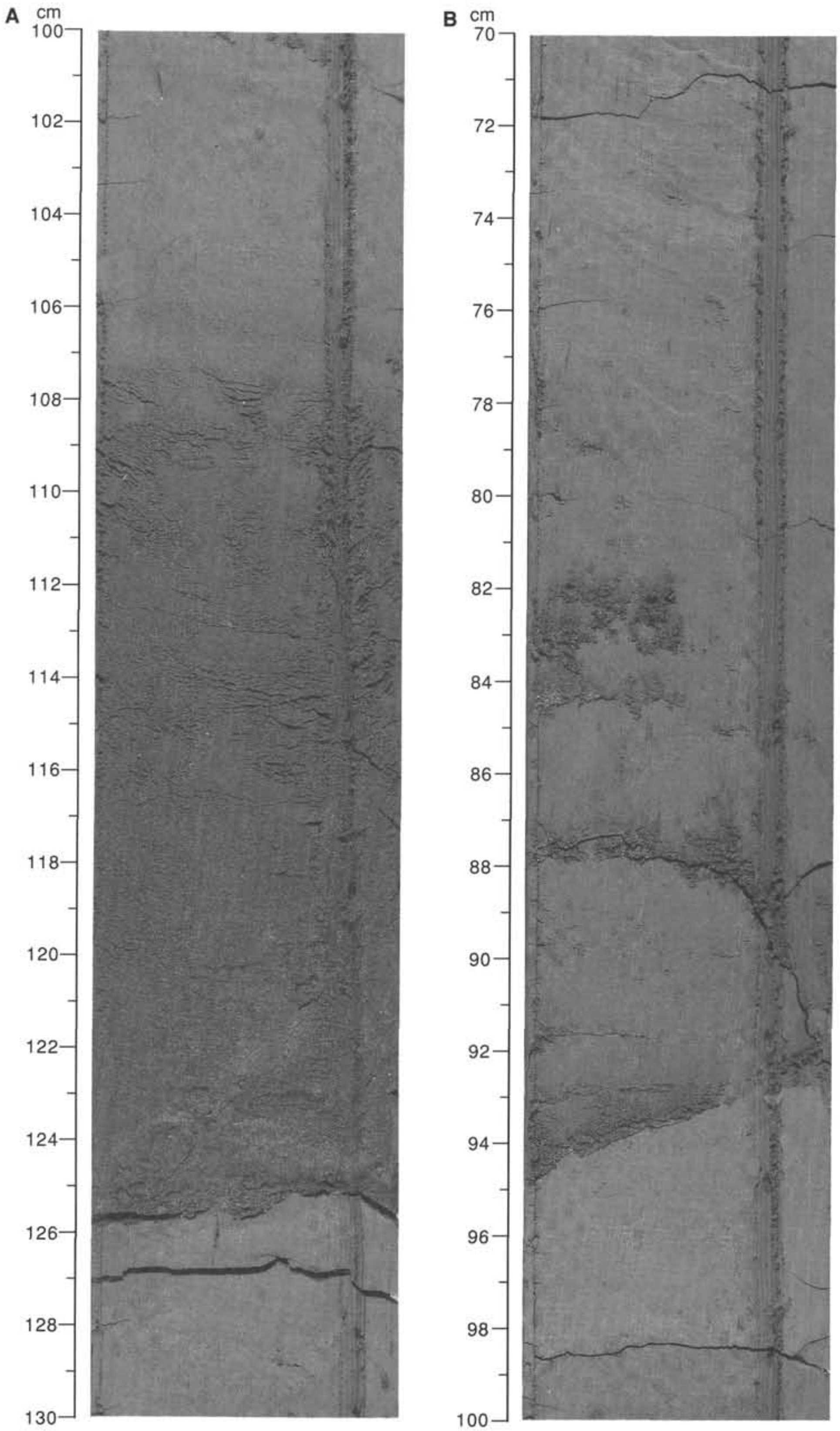

Figure 5. Core photographs. **A.** Normally-graded, medium-grained sand bed with scoured lower contact overlain by laminated finer-grained sand and clayey silt (interval 141-860B-2H-5, 100–130 cm). **B.** A scoured contact overlain by thinly bedded, graded fine sand and silty clay (interval 141-860B-2H-5, 70–100 cm).

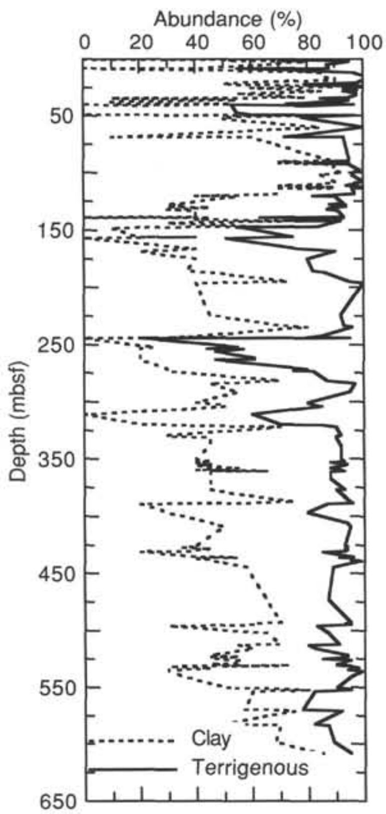

Figure 6. Abundance of clay and silt-to-sand-sized terrigenous components in Hole 860B from smear-slide observations.

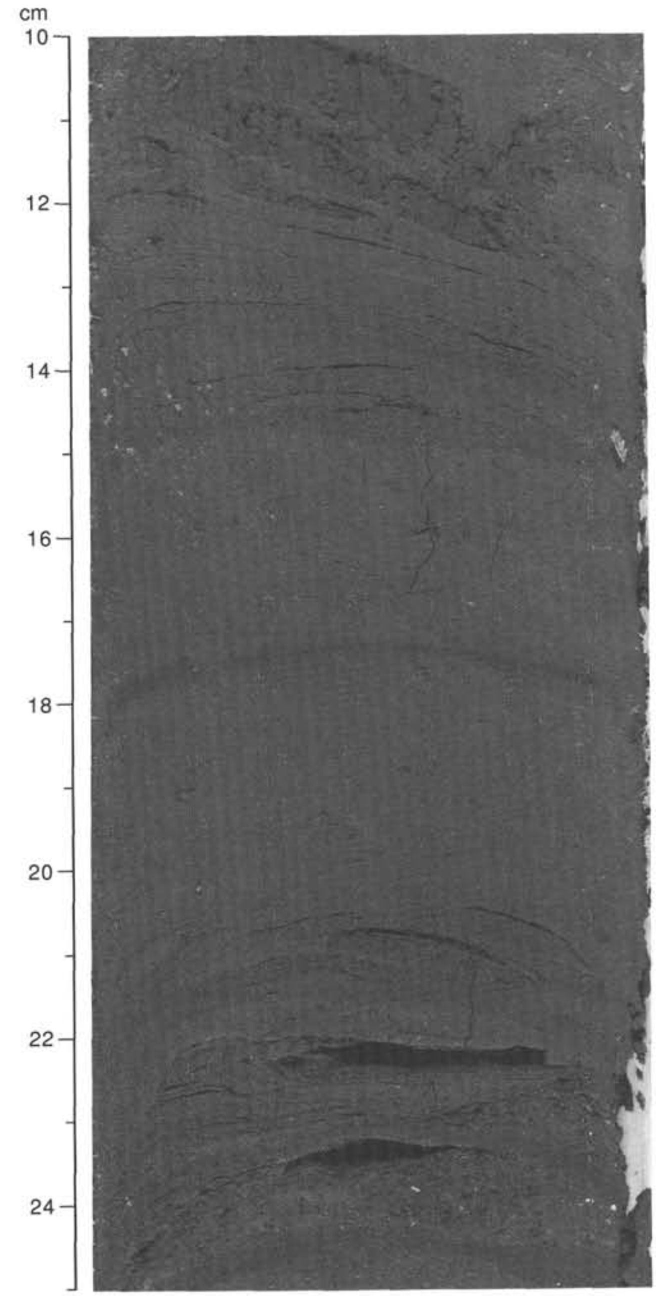

Figure 7. Core photograph, finely laminated siltstones and sandstones. Laminated sets are wedge shaped compared to general bedding (interval 141-860B-22X-3, 10–25 cm)

Clayey siltstones and silty claystones are dominantly olive-gray (5Y 3/2). Often bedding is not preserved due to drilling disturbance, however some lamination may occur within drilling biscuits (e.g., Cores 141-860B-43X, -47X, and -49X). Thin interlaminae of nannofossil ooze occur in interval 141-860B-49X-1, 70–71 cm and minor zones of nannofossil chalk in intervals 141-860B-60X-1, 134–135 cm, -60X-2, 66–73 cm, and -61X-2, 30–31 cm. Olive-black (5Y 3/2) micaceous silty claystone occurs at intervals 141-860B-67X-1, 20–35 cm, and -4, 20–50 cm. Olive-gray (5Y 3/2) micritic carbonate concretions in Core 141-860B-48X at about 409.5–415.7 mbsf are composed of up to 23.4% carbonate (Table 4; Fig. 3).

The dispersed clasts in the diamictic olive-gray (5Y 3/2 to 5Y 4/1) sandy-silty-claystones have angular to subangular shapes and maximum clast diameters are generally 1.5–2 cm. In Core 141-860B-58X, 492.8–502.4 mbsf, these diamictites show four, 80- up to 150-cm-thick, fining-upward sequences. These are as "key beds" for possible determination of repeated sections (Fig. 9). Interval 141-860B-58X-1, 65–70 cm, which constitutes the lower 5 cm of one distinct sequence is inverse graded, exhibiting a gradual change to silty claystone (Fig. 11). The clasts consist of coarse sand- to pebble-sized siltstone, calcareous sandstone and siltstone, pyrite concentrations, dark volcanic lithics, some greenish shale and shell fragments. These clasts are locally concentrated in some intervals, but the sediments have an overall matrix-supported texture (Fig. 12). The sand-to-silt-sized matrix components of these sediments are mostly quartz and feldspar, with minor amounts of volcanic glass, amphibole, and opaques. These sediments generally contain small proportions (up to 2.9%) of micritic carbonate.

Thin beds of intraformational, granule-sized conglomerate occur in Cores 141-860B-46X and -48X, much resembling those seen in Subunit IIIA. They are clast-supported above their sharp lower contacts, but their upper parts are matrix-supported and show gradational contacts with the overlying sediments. Clasts within these conglomerates are mostly sedimentary.

Overall, Subunit IIIB seems to be composed of three sedimentary successions with relatively similar lithological characters: (1) a first succession of diamictites and associated slightly calcareous fine-grained sediments is seen in the interval between 319.4 and 415.7 mbsf in Cores 141-860B-38X to -48X; (2) a second succes-

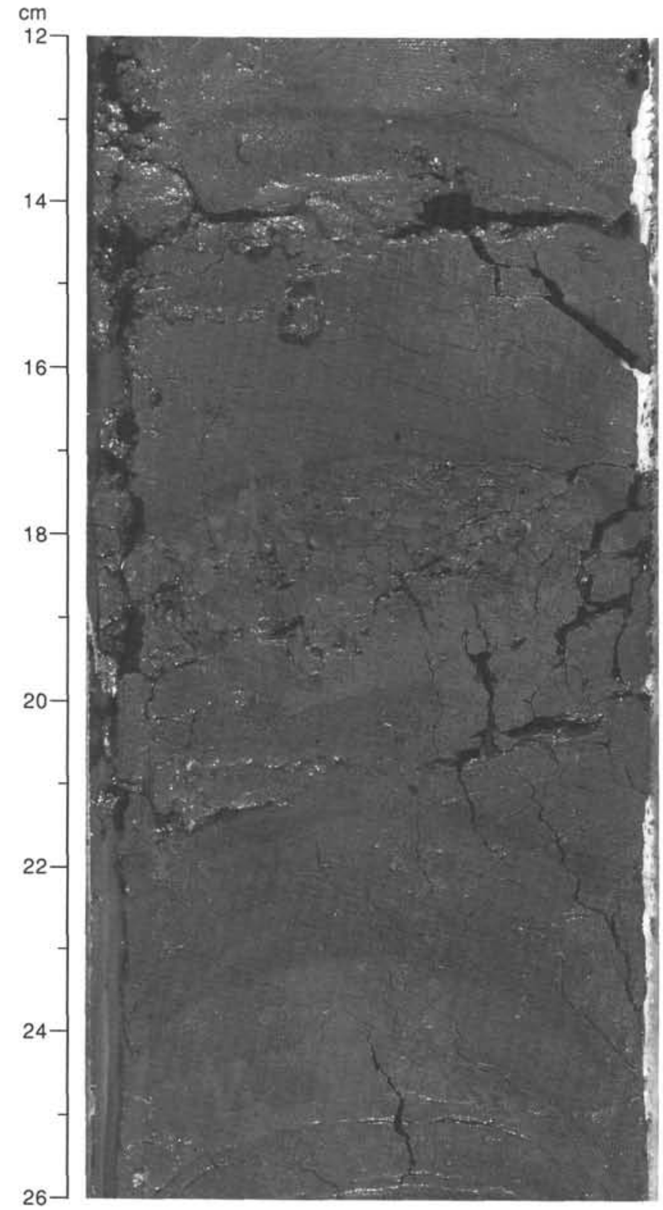

Figure 8. Core photograph, intraformational conglomerate interbedded with claystones and sandy siltstones (interval 141-860B-25X-CC, 12–26 cm).

sion, 415.7–512.0 mbsf in Cores 141-860B-49X to -59X; and (3) a third succession between 512.0–617.8 mbsf in Cores 141-860B-60X to -70X. Thrusts or thrust zones may be present between each succession (Fig. 9). Olive-black (5Y 3/2) micaceous silty claystone occuring in Intervals 141-860B-67X-1, 20–35 cm, and -67X-4, 20–50 cm, may indicate the location of faults at a sub-bottom depth of about 590 mbsf.

Depositional Processes

Unit III is characterized by clayey siltstones and silty claystones with a minor calcareous component representing more or less hemipelagic background sedimentation. Diamictic intervals are interpreted to be high-concentration sediment flows which, when they cease to flow, preserve a matrix-supported texture with dispersion of granule- to pebble-sized clasts. Fine material can be transported by high-density turbidity currents on relatively gentle slopes. However, diamictic deposits may also be

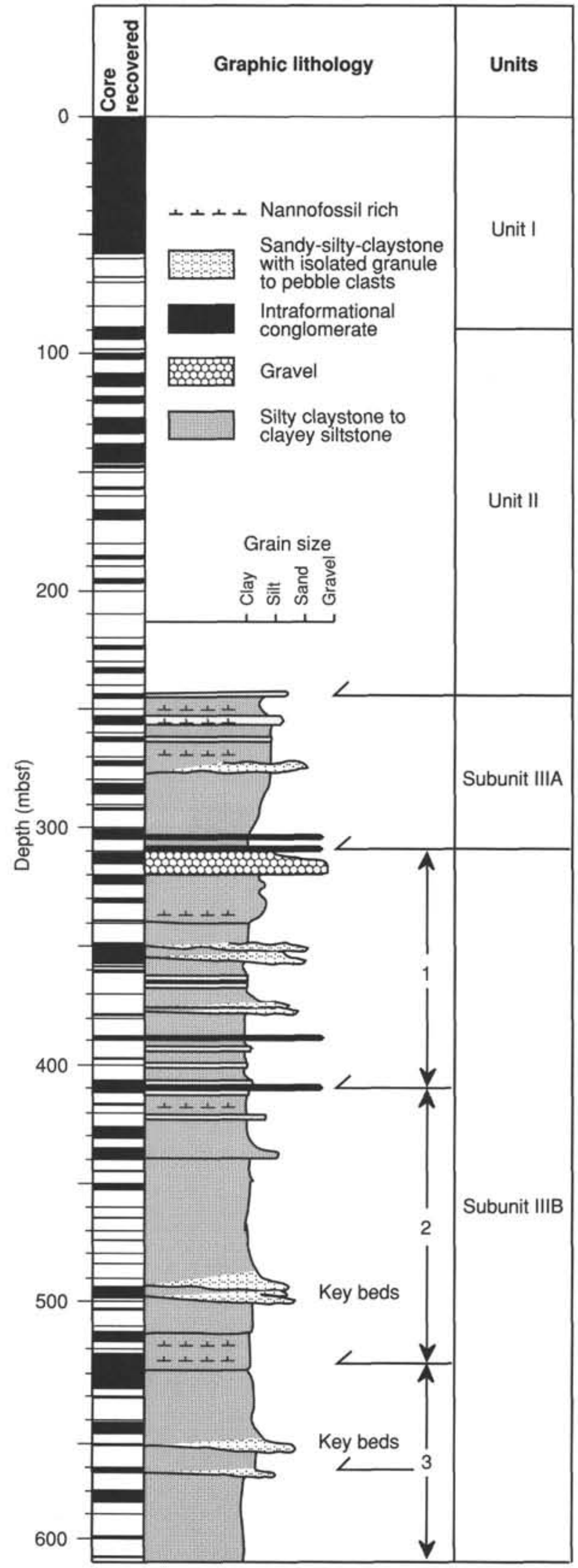

Figure 9. Graphic lithology for Unit III. Possible thrusts (horizontal arrows) bound four relatively similar sedimentary successions possibly repeated due to tectonic imbrication. See text for discussion.

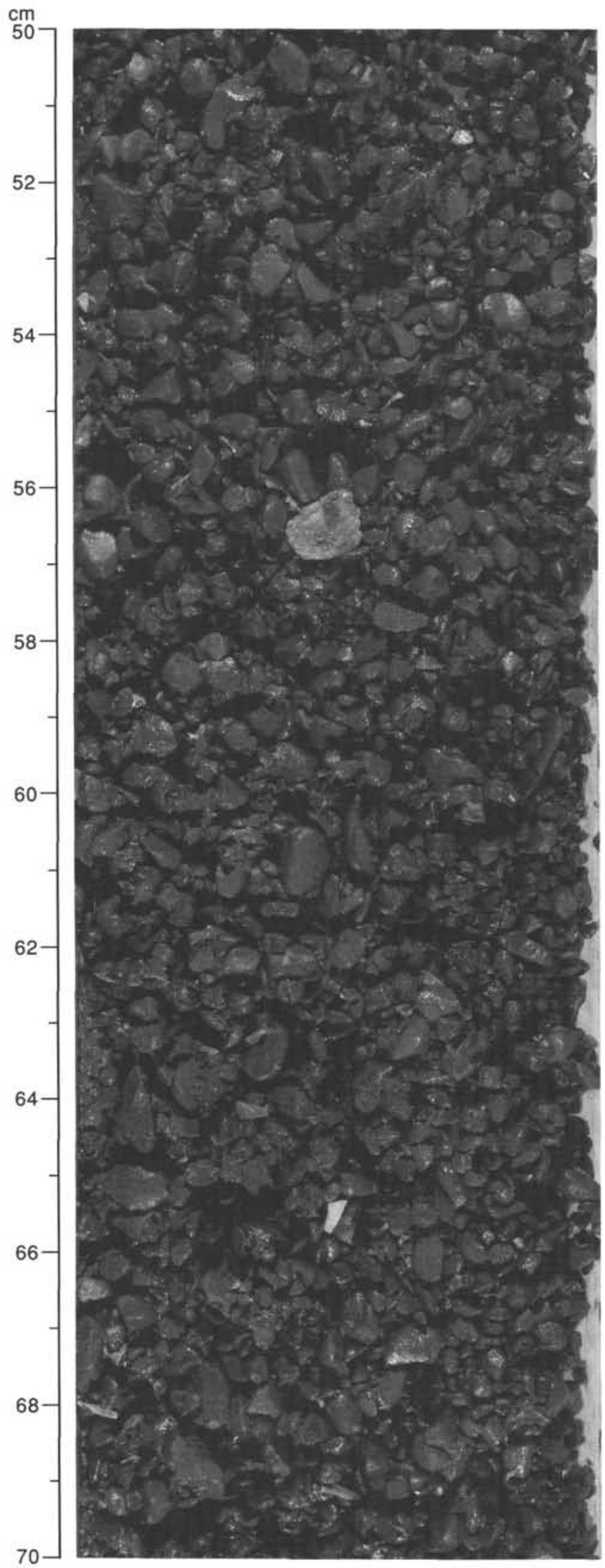

Figure 10. Core photograph, moderately sorted gravel with rounded and well-rounded granule- to pebble-sized clasts (interval 141-860B-37X-3, 50–70 cm).

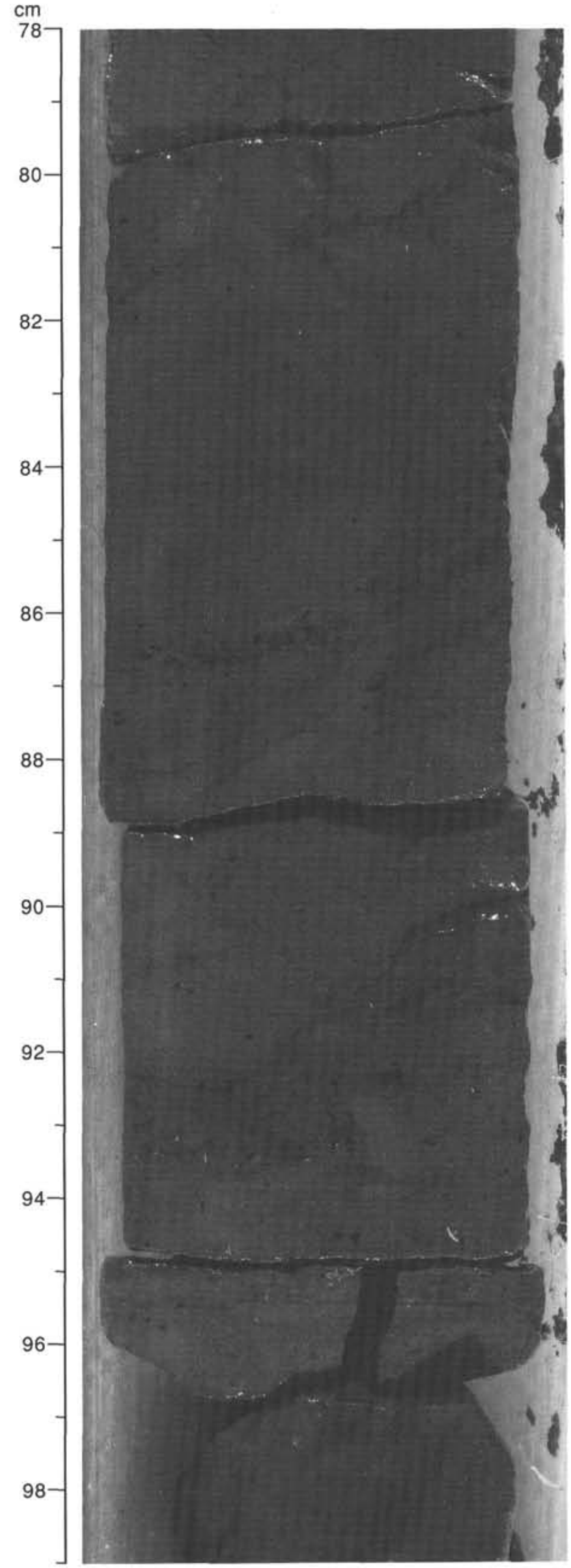

Figure 11. Core photograph, lower part of a sandy silty claystone sequence with dispersed clasts showing inverse grading from 92–97 cm (interval 141-860B-58X-1, 78–99 cm).

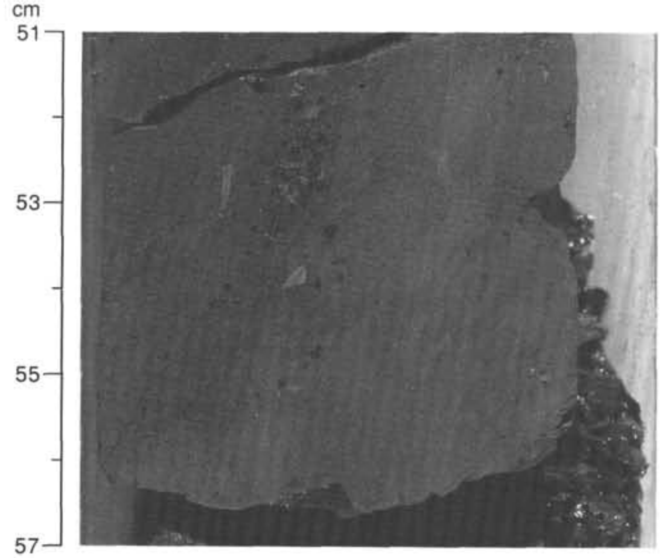

Figure 12. Core photograph, sandy silty claystones in interval 141-860B-64X-4, 51–57 cm, showing clast concentrations and an overall matrix-supported texture. The sediment is fractured (see Structural Geology section, this chapter).

transported as fluidized sand-silt-clay debris flows (cf. Pickering, et al., 1989). The uniform, poorly-sorted gravel in Core 141-860B-37X probably represents a debris flow unit.

Relatively similar sedimentary successions in Unit III may represent cyclicity in sedimentation possibly controlled by changes in tectonic activity. Alternatively, this repetition of lithologies may represent large-scale tectonic imbrication of a thinner Pliocene sequence (see Sediment Accumulation Rates, this chapter).

XRD Analysis of Sediments

Seventy-nine samples were selected from Site 860 cores for X-ray diffraction analysis. Bulk powders (51 samples), and clay-size separates (28 samples) were prepared, and analyzed using the shipboard Philips ADP 3520 X-ray diffractometer.

The dominant phases present in all of the bulk samples from Hole 860B are quartz and feldspar with only small fluctuations in their abundance (Table 5). All samples have a minor -to-trace amount of hornblende. In Samples 141-860B-14X-2, 85–87 cm, -15X-4, 80–82 cm, and -30X-2, 106–109 cm, hornblende was secondary in amount. Calcite is rare, being present only in trace to minor amounts in Samples 141-860B-1H-1, 48–50 cm, -2H-1, 115–117 cm, -19X-3, 91–93 cm, -20X-1, 96–98 cm, -21X-1, 100–103 cm, -30X-2, 106–109 cm, -31X-1, 100–102 cm, -32X-2, 28–32 cm, -37X-2, 82–84 cm, -55X-CC, 26–28 cm, and -64X-1, 70–71 cm. A strong peak at 2.30Å on the diffractogram for Sample 141-860B-1H-1, 48–50 cm, probably represents a carbonate-apatite phase. An unidentified amorphous phase is present in all samples. The samples overall are very similar in the presence and relative abundance of mineral phases. Chlorite and illite appear to be present in the bulk samples in roughly equal amounts. Smectite is not conspicuous on these diffractograms.

The analysis of clay mineral separates shows that the main part of the fine fraction consists of illite and chlorite (together forming from 78% to 97% of the fine fraction). The remaining portion (from 3% to 22%) is composed of smectite (Table 6). Trace amounts of clay-sized cristobalite, quartz, feldspar, an amorphous phase, and amphibole (hornblende) are present in all samples.

Unidentified reflection peaks of nonclay mineral(s) appear in Samples 141-860B-32X-2, 28–32 cm, -33X-1, 49–52 cm, -36X-3, 58–60 cm, -38X-1, 117–119 cm, -41X-3, 70–72 cm, and -44X-CC, 10–11 cm, at 4.17Å and 3.76Å. Additional laboratory tests will have to be performed at a later time to identify these phase(s).

The distribution of clay minerals in samples from Hole 860B (Fig. 13) shows ubiquitous and relatively constant chlorite, illite, and smectite contents throughout the hole. In general, the content of smectite in the clay fraction is low. The samples with greater amounts of smectite are more often from the upper Pliocene sediments. The maximum concentration of smectite (22%) is found in Sample 141-860B-41X-3, 70–72 cm. The unidentified mineral phase(s) (peaks 4.17Å and 3.76Å) are concentrated in sediments from the middle part of Hole 860B. The comparison of smectite concentrations in sediments from Hole 859B and Hole 860B shows that, in general, there is less smectite in Hole 860B. The concentrations of smectite in Hole 860B, overall, are similar to those levels seen in the lower part of Hole 859B.

Diagenetic processes have not apparently affected illites or chlorites with stable crystalline structures. Variations of the abundances of these minerals, and probably that of smectite as well, are believed to primarily reflect sedimentation processes and the primary composition of terrigenous clay minerals.

Sediment Accumulation Rates

Important constraints regarding sediment accumulation are illustrated in Figure 14. These include age constraints based on nannofossils from Cores 141-860B-1H, -3H, -4H, 9X, -10X, -58X, -59X, and -70X with age-diagnostic fauna from Zones NN15–NN21, and constraints based on foraminifers from Cores 141-860B-20X, -24X, -31X, -32X, -37X, -44X, -58X, -63X, and 69X. Most of the constraints come from age-restricted assemblages, but in some cases very age-specific constraints arise from either unique assemblages or cores that bracket two biostratigraphic zones. These constraints allow an apparent accumulation rate of 46.9 m/m.y. between the base of the Quaternary and the lower Pliocene in the upper 130 m of Hole 860B. However, as was the case at Site 859, the apparent rate for the lower part of the hole (shown by the dashed line) is 250 m/m.y., which is over five times higher. In this case, however, paleontologic, lithostratigraphic, and structural data show that this depth interval has two clear fault zones and possibly at least three others. Thus structural thickening on the order of that suggested by the five thrusts we propose is required to explain this phenomena. At Site 859 evidence for structural thickening on the same order was observed.

Remarks on Controls of Sedimentation

It is suggested that, for the upper part of Site 860, deposition took place in a tectonically active, restricted part of a slope basin adjacent to a trench. Tectonic uplift of the accretionary wedge may have controlled deposition by providing changes in slope instability, inducing slope slumping, and by producing structurally restricted depressions within the basin. The lower parts of the Site 860 sequence may represent a more open and deeper water phase in the evolution of a trench-slope basin. The abundance of debris flows and high-density turbidites in Unit III could be related to tectonically active periods or be associated with glacial sedimentation (see discussion in Lithostratigraphy section, Site 861 chapter). Downslope redistribution of sediments also may have occurred as a result of earthquakes and general oversteepening of the upper slope, or may have been due to fluctuations in sea level during the Pliocene-Pleistocene. During sea-level lowstands, larger quantities of terriginous sediments are supplied to the deep sea by turbidity currents and related gravity flows (Shanmugam and Moiola, 1982). The mineralogical content of the sediments suggests significant input from the volcanically active margin transported by turbidity currents. The source of these sediments was apparently also associated with glacial processes

Table 5. X-ray diffraction mineralogy of sediments in Hole 860B.

Core, section, interval (cm)	Depth (mbsf)	Nonclay mineral phases (100%)[a, b]					Phyllosilicates (100%)	
		Quartz	Feldspar	Hornbld.	Calcite	Amorph.	Chlorite	Illite
141A-860B-								
1H-1, 48–50	0.48	4	3	1	1	2	4	4
2H-1, 115–117	2.55	4	3	1	1	2	4	4
3H-4, 87–89	16.27	4	3	2	0	2	4	4
4H-1, 82–84	21.22	4	3	1	0	2	4	4
5H-2, 90–92	32.30	4	4	1	0	2	4	4
6H-6, 90–92	47.80	3	4	1	0	2	4	1
7H-1, 133–135	50.23	4	4	2	0	2	4	4
12X-2, 88–89	90.08	4	4	2	0	2	4	4
14X-2, 85–87	101.45	4	4	3	0	2	3	4
15X-4, 80–82	112.50	4	4	3	0	2	4	4
17X-5, 97–99	133.47	4	4	1	0	2	4	4
19X-3, 90–93	141.00	3	4	1	1	2	4	4
20X-1, 96–98	146.76	4	4	1	1	2	4	4
21X-1, 52–53	156.02	4	4	0	2	2	4	4
21X-1, 100–103	156.50	4	4	2	1	2	4	4
22X-2, 113–115	167.73	4	3	1	0	2	4	4
24X-1, 85–87	185.25	4	3	1	0	2	4	4
25X-1, 67–69	194.77	4	3	1	0	2	4	4
28X-1, 110–112	224.20	4	4	1	0	2	4	4
29X-1, 89–91	233.69	4	4	2	0	2	4	4
30X-2, 106–109	244.13	4	4	3	1	2	4	4
31X-1, 100–102	252.90	4	4	1	2	2	4	4
32X-2, 28–32	262.64	4	3	2	1	2	4	4
33X-1, 8–10	271.28	4	2	0	1	1	4	4
33X-1, 46–49	271.66	4	4	1	0	2	4	4
34X-1, 77–79	281.57	4	4	2	0	2	4	4
35X-1, 67–69	291.07	4	3	1	0	2	4	4
36X-1, 2–4	300.12	3	1	0	0	1	4	4
36X-3, 56–58	303.66	4	4	2	0	2	4	4
37X-2, 82–84	312.12	4	3	2	1	2	4	4
38X-2, 24–25	321.05	2	2	1	0	1	4	4
38X-2, 74–76	321.55	4	3	2	0	2	4	4
39X-1, 120–122	329.90	4	3	1	0	2	4	4
40X-CC, 2–4	338.42	4	2	1	0	2	4	4
48X-1, 91–93	406.91	4	3	2	0	2	4	4
48X-5, 6–8	411.10	4	4	2	0	2	4	4
49X-1, 39–41	416.09	4	3	2	0	2	4	4
50X-2, 97–100	427.77	4	3	2	0	2	4	4
51X-1, 114–117	435.94	4	3	1	0	2	4	4
52X-CC, 15–17	444.55	4	2	1	0	2	4	4
53X-1, 15–17	449.25	4	2	1	0	2	4	4
55X-CC, 26–28	464.06	4	3	2	1	2	4	3
56X-CC, 30–31	473.70	4	3	2	0	2	4	4
57X-CC, 30–31	483.40	2	3	2	0	2	3	4
58X-1, 43–45	493.23	3	4	2	0	2	3	4
60X-1, 100–102	513.00	4	3	2	0	2	4	4
60X-2, 68–70	514.18	4	3	1	0	2	4	4
61X-2, 114–117	524.34	4	4	2	0	2	4	4
62X-3, 27–30	534.17	4	3	1	0	2	4	3
64X-1, 57–58	550.77	4	2	1	0	2	4	4
64X-1, 70–71	550.90	4	3	2	1	2	4	4

[a] Numbers indicate: 4. dominant, 3. secondary, 2. minor, and 1. trace phases. 0 indicates no phase detected.
[b] All diffractograms have a phase with a small peak at 2.71Å; possibly from trace amounts of pyrite.

providing changes in general sediment input. For closer discussion of source areas see Lithostratigraphy section, Site 859 chapter.

BIOSTRATIGRAPHY

Introduction

At Site 860 a sequence of Pleistocene and Pliocene sediments was recovered. Only one core was recovered from Hole 860A. At Hole 860B we employed both advanced piston coring (APC) and extended core barrel (XCB) methods for recovering sediments to 618 mbsf. Diatoms, radiolarians, and planktonic and benthic foraminifers were examined onboard from 67 core-catcher samples as well as from selected additional samples within cores. Additional age determinations based on calcareous nannofossils were given by shore-based investigations (C. Müller). A summary of biostratigraphic investigations conducted at Site 860 is given in Figure 15.

Although siliceous microfossil preservation at Site 860 is better than that of Site 859, diatoms are present only in about half of the uppermost 20 core catchers of Hole 860B, and show poor preservation, thus allowing the assignment of only one sample to a diatom zone. Radiolarians are found intermittently throughout the hole, with frequent barren intervals, providing minor age control. Low-diversity assemblages of planktonic foraminifers are found in 80% of the samples examined and benthic foraminifers in 87%. Calcareous nannofossils are few to common, allowing some inferences about biostratigraphy.

The Pliocene/Pleistocene boundary is placed between Samples 141-860B-9X-CC and -10X-CC, bracketed by calcareous nanno-

Table 6. XRD mineralogy of sediment files in Hole 860B.

Core, section, interval (cm)	Depth (mbsf)	Smectite	Illite (%)	Chlorite (%)	Cristobalite (%)	Amphibole (%)	Quartz (%)	Feldspar (%)	Amorphous (%)
141-860B-									
1H-1, 34–36	0.34	4	58	38	[a]TR	TR	[b]M	M	M
3H-4, 84–86	16.24	4	49	47	TR	TR	M	M	M
5H-2, 54–56	31.94	5	52	43	TR	TR	M	M	M
7H-4, 27–29	53.67	11	44	45	TR	TR	M	M	M
12X-2, 89–90	90.09	6	52	42	TR	TR	M	M	M
16X-2, 54–55	118.84	14	46	40	TR	TR	M	M	M
17X-5, 100–102	133.50	4	60	36	TR	TR	M	M	M
19X-3, 94–96	141.04	9	44	47	TR	TR	M	M	M
22X-2, 106–108	167.66	6	42	52	TR	TR	M	M	M
24X-1, 87–90	185.27	3	62	35	TR	TR	M	M	M
25X-1, 67–69	194.77	4	53	43	TR	TR	M	M	M
28X-1, 110–112	224.20	10	44	46	TR	TR	M	M	M
32X-2, 28–32	262.64	11	48	41	TR	TR	M	M	M
33X-1, 49–52	271.69	12	43	45	TR	TR	M	M	M
36X-3, 58–60	303.68	5	54	41	TR	TR	M	M	M
38X-1, 117–119	320.57	8	48	44	TR	TR	M	M	M
41X-3, 70–72	351.70	22	44	34	TR	TR	M	M	M
44X-CC, 10–11	367.40	6	49	45	TR	TR	M	M	M
45X-CC, 37–39	377.27	5	54	41	TR	TR	M	M	M
48X-4, 121–123	410.75	6	54	40	TR	TR	M	M	M
51X-1, 111–114	435.91	5	51	44	TR	TR	M	M	M
53X-1, 60–62	449.70	4	62	34	TR	TR	M	M	M
56X-CC, 18–19	473.58	3	55	42	TR	TR	M	M	M
58X-1, 41–43	493.21	10	43	47	TR	TR	M	M	M
61X-2, 105–108	524.25	9	44	47	TR	TR	M	M	M
64X-1, 69–70	550.89	5	51	44	TR	TR	M	M	M
67X-2, 70–72	581.40	8	47	45	TR	TR	M	M	M
70X-CC, 2–4	608.22	6	50	44	TR	TR	M	M	M

[a] TR = trace amounts
[b] M = minor amounts

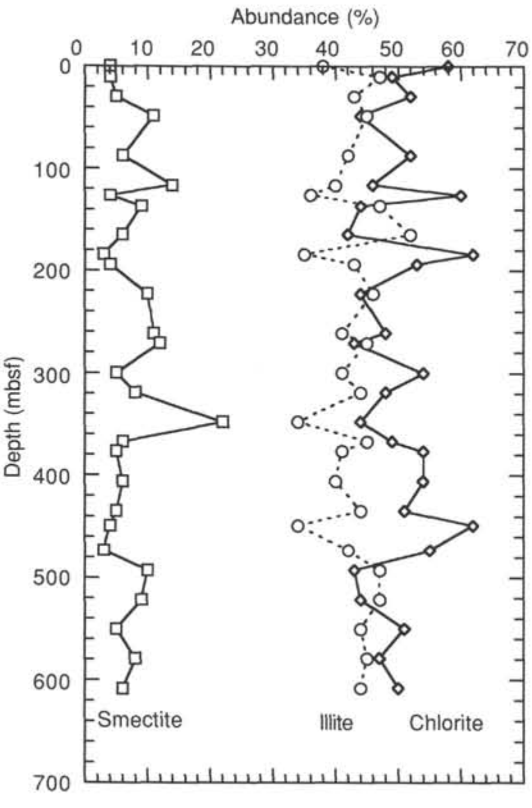

Figure 13. Downhole distribution of clay mineral types in samples from Hole 860B.

fossil ages. This falls in an interval more than 65 m deeper compared with planktonic foraminifer definitions (see below) and lies within the *G. inflata* Zone of the planktonic foraminifer biostratigraphy.

Repetition of sedimentary sequences was inferred largely from the distribution of planktonic foraminifers, indicating structural complexity at this site.

Climatic intervals indicating warm-, temperate-, and cold-water environments were recognized primarily based on planktonic foraminifers. Analogous to Site 859, preservation of siliceous microfossils, especially radiolarians, tends to be significantly better in the intervals inferred to be warm-water environments from their assemblages of planktonic foraminifers (Fig. 15 and Table 7).

Diatoms

The occurrence pattern of diatoms at Site 860 is similar to that of Site 859. Moderately preserved and common assemblages occur only in the uppermost few meters of the sequence. However, it seems that the assemblage recovered in Sample 141-860B-1H-CC is older than the assemblage recovered at Site 859 at an approximately equivalent sub-bottom depth. The assemblage from Hole 860B is assigned to Subzone B of the *Nitzschia reinholdii* Zone due to the concurrent appearance of *Pseudoeunotia doliolus* and *Nitzschia fossilis* and the absence of *Rhizosolenia praebergonii.* The absence of *Nitzschia reinholdii* makes the zonal assignment somewhat uncertain since the *N. reinholdii* Zone is defined as the interval where *N. reinholdii* and *P. doliolus* show concurrent occurrences (Burckle, 1977). The occurrence of *N. fossilis,* however, is a strong argument to assign the sample to the *N. reinholdii* Zone as this species shows its last occurrence prior to the top of this Zone (Barron, 1985). Other components of the observed assemblage include the dominant *Thalassiosira eccentrica* group, *Thalassiosira oestrupii, Thalassiosira* spp., *Paralia sulcata, Thalassionema nitzschioides* (including variety *parva*), *Nitzschia kerguelensis*, and *Chaetoceros* resting spores.

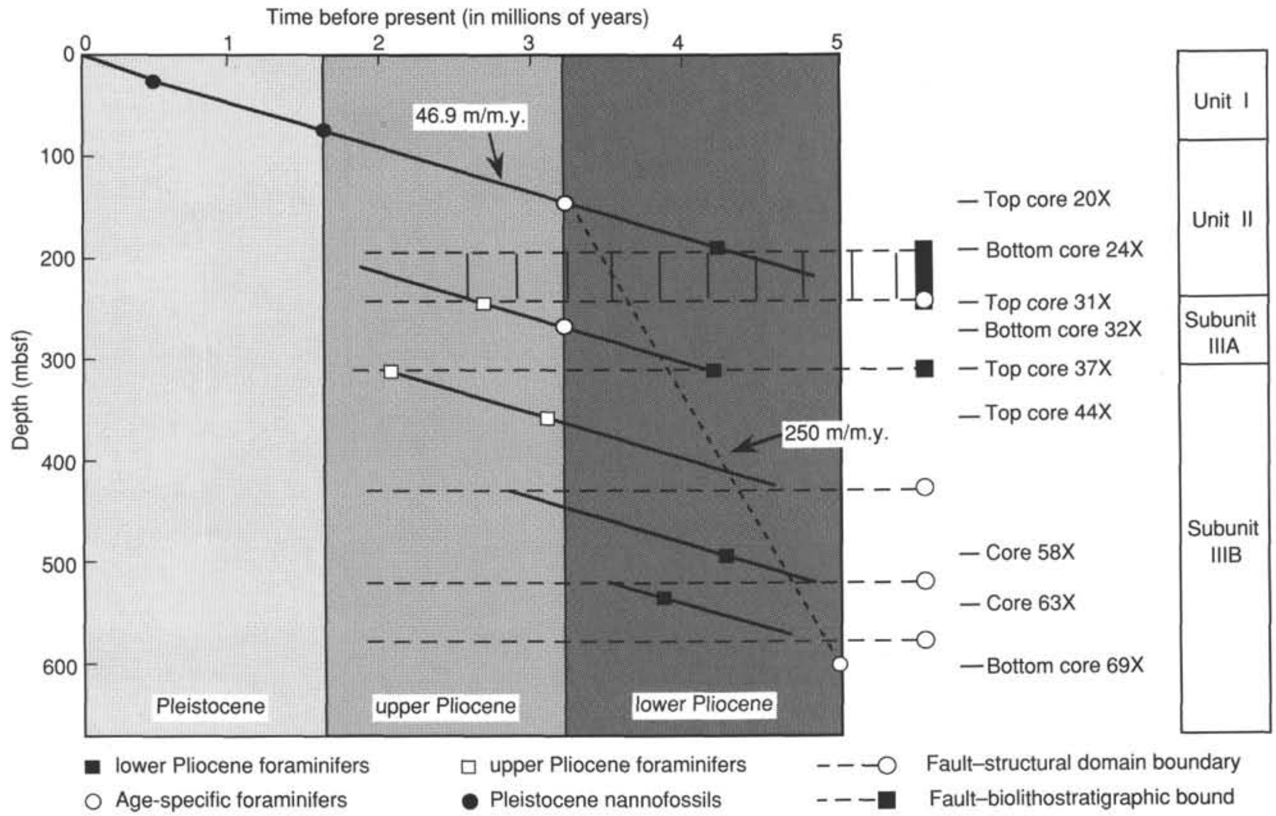

Figure 14. Estimates of the sediment accumulation rate at Site 860 incorporating a model of tectonic thrusting to explain the increased accumulation rates and thicknesses of the sequences.

With the exception of Sample 141-860B-1H-CC, examination of core-catcher samples from Site 860 did not reveal any occurrences of marker species useful for age determinations. The few cores that contained diatoms in the core catcher were scattered among the first 20 cores recovered at Hole 860B, with the exception of Cores 141-860B-30X and -36X. Diatoms are rare to few within this interval. Preservation is consistently poor in all these samples. In a few core-catcher samples rare large diatoms (e.g., *Coscinodiscus oculus iridis*) were observed in the slides prepared for radiolarian analysis in which particles greater than 63 μm were concentrated.

Sample 141-860B-20X-1, 117–119 cm, was taken from a short interval of sediment containing a high proportion of biogenic components (mainly calcareous nannofossils). This specific attempt to obtain a diatom assemblage with undissolved key taxa for age assessments only revealed a rare occurrence of *N. kerguelensis.* At least, the occurrence of this species indicates an age of 2.7 Ma or younger for sediments at 148 mbsf in Hole 860B. This conclusion is based on the reported first occurrence of *N. kerguelensis* at 2.7 Ma in the Southern Ocean (McCollum, 1975).

Radiolarians

The preservation state of radiolarians at Site 860 is clearly better than that observed at Site 859, despite the proximity to terrigenous sediment sources (i.e., dilution). Only 31 samples, however, of 68 samples examined (core catchers and selected intervals within cores) contained radiolarians (46%). Of these only 13 samples (19%) yielded useful age assignments (Fig. 15). The low-latitude radiolarian zonation of Sanfilippo et al. (1985) is applied.

Sample 141-860A-1H-CC is barren. Sample 141-860B-1H-CC (1.4 mbsf) belongs to the uppermost part of the *Anthocyrtidium angulare* (RN13) to *Buccinosphaera invaginata* Zone (RN16) of the Quaternary as it contains a few *Lamprocyrtis nigriniae* (first appearance datum (FAD): 1.02–1.07 Ma). The foraminifer age of this sample is the *Truncorotalia tosaensis* Zone and that of the diatom assemblage is the *Nitzschia reinholdii* Subzone B. Therefore, combining the radiolarian, diatom, and foraminifer ages this sample can be placed in the lower Pleistocene. In contrast, the calcareous nannofossils dated Sample 141-860B-1H-CC as upper Pleistocene. Moderately preserved abundant radiolarians in this sample indicate a warm-water environment. Although a small number of cold-water taxa are observed, the assemblage is dominated by warm-water taxa:

*Lamprocyrtis nigriniae** (F = few), *L. hannai* (F), *Lamprocyclas maritalis* (C = common), *Eucyrtidium erythromystax** (R = rare), *E. hexagonatum* (F), *E. acuminatum* (R), *Cornutella profunda*(F), *Pterocanium praetextum praetextum* (R), *P. trilobum?* (R), *Theocorythium trachelium dianae* (R), *Botryostrobus acquilonaris* (F), *Carpocanarium papillosum*(F), *Phormostichoartus corbula* (R), *Spirocytis subscalaris* (F), *Tetrapyle octacantha**, *Heliodiscus asteriscus* (R), and *Spongocore puella* (F).

Cold-water taxa:

Antarctissa denticulata (R), *Eucyrtidium calvertense* (R), *Cycladophora bicornis* (F), *C. davisiana davisiana** (F), *C. davisiana cornutoides* (F), *Pterocanium korotonevi* (R), and *P. diplotriaena* (R).

Several upwelling species (marked by asterisks) are observed at this site, similar to Site 859. Notably, ten specimens of *L. nigriniae* were found. As is discussed in the Biostratigraphy section of the Site 859 chapter, the presence of a relatively large number of this rare species together with other upwelling indicators (Fig. 16 of the Site 859 chapter) suggests an upwelling regime. *E. calvertense* is found in this sample (141-860A-1H-CC)

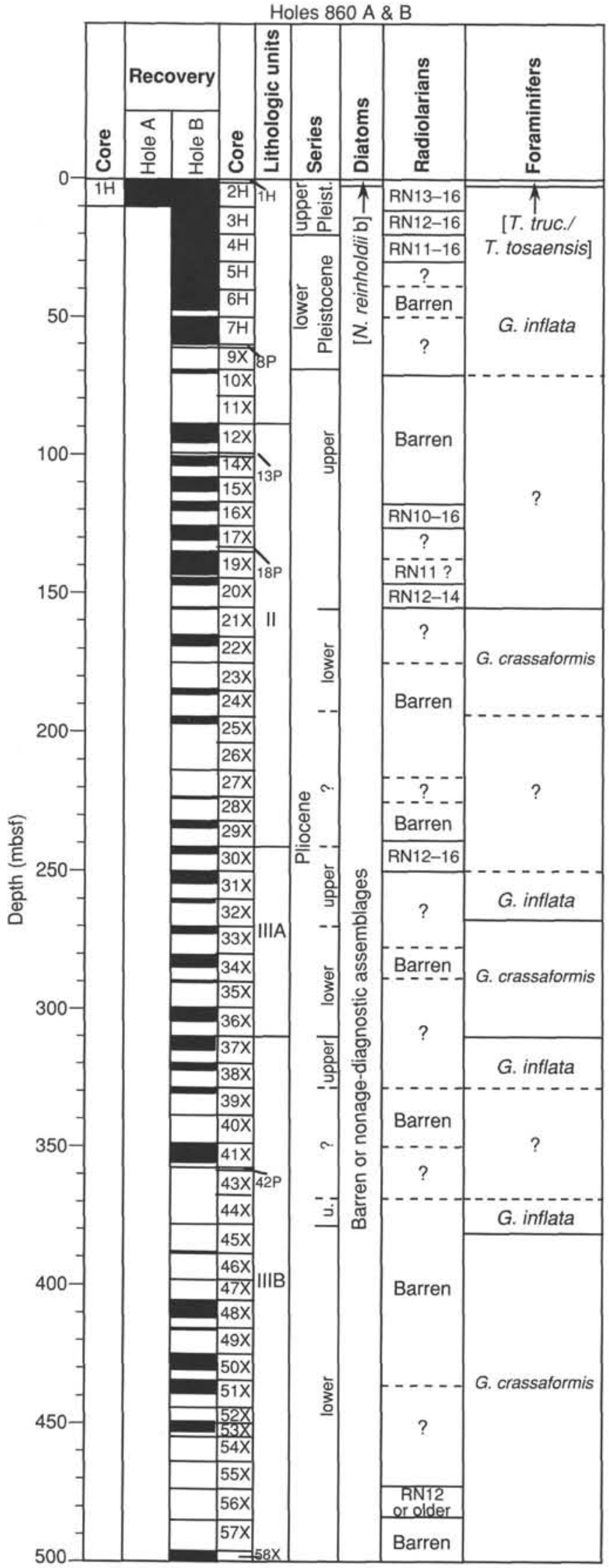

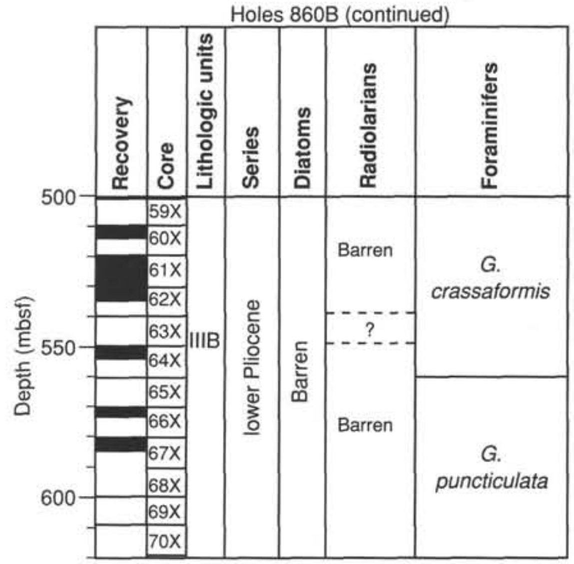

Pliocene and Quaternary radiolarian zones
(After Sanfilippo et al., 1985)

RN 16 = *Buccinosphaera invaginata*
RN 15 = *Collosphaera tuberosa*
RN 14 = *Amphirhopalum ypsilon*
RN 13 = *Anthocyrtidium angulare*
RN 12 = *Pterocanium prismatium*
RN 11 = *Spongaster pentas*
RN 10 = *Stichocorys peregrina*

Figure 15. Summary of biostratigraphic age for the sediments recovered at Site 860.

Table 7. Occurrence, preservation, and estimated relative abundance of planktonic foraminifers of samples from Hole 860B.

Hole 860B Sample	Depth (mbsf)	Abundance	Preservation	*T. tosaensis*	*N. dutertrei*	*O. universa*	*G. bulloides*	*G. inflata*	*G. crassaformis*	*G. scitula*	*G. crassula*	*N. pachyderma D*	*N. pachyderma S*	*G.* cf. *marginata*	*G. puncticulata*	*N. dutertrei*	*G. sphericomiozea*	Paleotemperatures	Zones
1H-CC	1.37	C	G	R	R	R	F	F										Warm	*T. tosaensis*
2H-CC	10.90	F	M			R	R	R	R										
3H-CC	20.40	C	G				R	C	R										
4H-CC	29.90	C	G			R	R	C	R										
5H-CC	39.40	C	G				R	C	R	R									*G. inflata*
6H-CC	48.28	R	M				R												
7H-CC	58.40	C	G			R	F	C	R	R									
9H-CC	60.02	C	G			R	C	C	R	R									
10X-CC	69.10	F	M			R		F	R	R		R	R						
12X-CC	93.69	B																	
13P-1, 46–48 cm	98.06	B																	?
14X-CC	102.41	F	M				R	R	R									Temperate	
15X-CC	113.88	B																	
16X-CC	120.65	F	G				F	F		R									*G. inflata*
17X-CC	133.90	F	M					R	F		R								
18P, bottom	137.10	F	M				R		R				R						?
19X-CC	145.36	C	M			R	C		C	R	R		R	R					
20X-2, 24–26 cm	146.04	F	M				R	F	F	R									*G. inflata*
20X-CC	148.21		M				C		C	R									
21X-CC	157.03	F	M						F										
22X-CC	169.24	R	M						R										
23X-CC	174.94	C	M				C		C				R						*G. crassaformis*
24X-CC	186.67	R	P				R		R										
25X-CC	196.65	R	P				R			R			R						
27X-CC	213.43	R	P				R		R										
28X-CC	224.64	R	P										R						
29X-CC	235.11	B																	?
30X-CC	245.23	B																	
31X-CC	256.28	R	P					R	R		R		R		R				*G. inflata*
32X-CC	263.51	F	G				R	F											
33X-CC	273.75	R	P				R		R			R	R					Cold to temperate	
34X-CC	285.74	R	P						R			R	R						*G. crassaformis*
35X-CC	291.97	R	P				R		R		R		R						
36X-CC	305.00	R	P						R										
37X-4, 39–41 cm	310.19	R	P				R	R	R										
37X-CC	314.92	R	P				R	R	R				R						*G. inflata*
38X-CC	322.41	R	P			R		R	R				R						
39X-CC	331.52	R	P				R						R						?
40X-CC	338.80	R	P										R						
41X-6 bottom	356.93	R	P										R						?
43X-CC	361.28	B																	
44X-CC	367.47	R	P					R	R										*G. inflata*
45X-CC	377.35	B																	
46X-CC	389.26	B																	
47X-CC	396.88	R	P								R		R						
48X-CC	411.95	R	P										R						
49X-CC	416.81	F	P				F		R				R						
50X-CC	430.91	B																	
51X-CC	439.11	R	P										R					Cold to temperate	
52X-CC	444.75	R	P										R						
53X-CC	452.22	R	P										R						
54X-CC	453.84	R	P						R				R						
55X-CC	464.22	B																	
56X-CC	473.71	R	P						R				R			R			*G. crassaformis*
57X-CC	483.57	B																	
58X-CC	497.09	R	P				F		R				R						
59X-CC	502.87	B																	
60X-CC	516.98	R	P						R				R						
61X-CC	531.45	R	P																
62X-CC	536.31	R	P										R						
63X-CC	540.65	R	P										R			R			
64X-CC	554.40	B																	
65X-CC	560.14	R	P						R						R		R		
66X-CC	572.41	R	P														R		
67X-CC	584.57	R	P										R						
69X-CC	598.85	F	P				R				R	R	R				R		
70X-CC	608.52	R	P										R						

without any other apparently reworked specimens; the same observation was made in the Pleistocene sediments at Site 859. Therefore, it is no longer considered here that this species is reworked; its last appearance datum (LAD) must be later in this region than the 1.9-Ma age reported by Lazarus (1990).

Sample 141-860B-2H-CC (10.9 mbsf) also belongs to the uppermost part of the *Anthocyrtidium angulare* (RN13) to *Buccinosphaera invaginata* Zone (RN16) as it contains three specimens of *L. nigriniae.* The assemblage in this sample is represented by poorly preserved, few specimens of the following taxa besides the above stratigraphic marker: *Cycladophora d. davisiana*, C. d. cornutoides, C. bicornis, Antarctissa denticulata, Tetrapyle octacantha*,* and *Pterocanium clausus.* As the preservation is poor, it is difficult to tell exactly in which environment they lived, but they were probably in a temperate climate, and influenced by upwelling (upwelling marker indicated by asterisks).

Sample 141-860B-3H-CC (20.4 mbsf) contains poorly preserved, few radiolarians of the following taxa: *Cycladophora bicornis, C. davisiana davisiana, C. davisiana cornutoides, Lamprocyrtis hannai, Spirocyrtis subscalaris, Eucyrtidium acuminatum, Botryostrobus acquilonaris, Carpocanistrum papillosum, Stylodictya valdispina, Antarctissa denticulata, A. deflandrei,* and *T. octacantha.* This sample can be placed in the *Pterocanium prismatium* (RN12) to *Buccinosphaera invaginata* Zone (RN16) of the upper Pliocene to Holocene by the presence of *C. d. davisiana,* with its FAD about 2.7 Ma in the Antarctic region (Lazarus, 1990) and about 2.42–2.44 Ma in tropical regions (Nigrini, 1991).

Below Core 141-860B-3H, radiolarian preservation becomes poorer and only a small number of specimens are found. Sample 141-860B-4H-CC (29.9 mbsf) contains only two specimens of *Spongaster tetras* (FAD: 3.83–3.85 Ma in tropical regions; Nigrini, 1991) and hence it is placed in the *Spongaster pentas* (RN11) to *Botryostrobus invaginata* Zone (RN16) of the lower Pliocene to Holocene.

Only one specimen of *Botryostrobus acquilonaris* is found in Sample 141-860B-5H-CC. It can only be bracketed from the middle Miocene to the Holocene. Sample 141-860B-6H-CC is barren. Sample 141-860B-7H-CC is placed within the middle Miocene to Holocene as it contains poorly preserved, rare *B. acquilonaris, Stylodictya valdispina, Siphcampe* sp., and *Carpocanarium* sp. Sample 141-860B-9X-CC cannot be provided with an appropriate age other than noting it is in the Neogene. It only contains poorly preserved, rare *S. valdispina* and circular spongodiscids. Samples 141-860B-12X-CC, -14X-CC, and -15X are barren. Sample 141-860B-13P-CC contains a trace amount of radiolarians of stratigraphically insignificant taxa and thus no age can be given.

Sample 141-860B-16X-CC probably belongs to the Pliocene-to-Holocene age bracket. It contains *Antarctissa denticulata, A. robusta, Heliodiscus asteriscus, S. valdispina, Carpocanistrum papillosum,* and *B. acquilonaris.* The exact FAD of *A. denticulata* is not known, but Lazarus (1990) reports this taxon from the Pliocene-to- Holocene sediments in the Weddell Sea. Sample 141-860B-17X-CC contains only several specimens each of *S. valdispina* and *B. acquilonaris.* This sample is younger than the middle Miocene. Sample 141-860B-18X-CC contains poorly preserved rare *A. denticulata, A. robusta, A. deflandrei,* and *B. acquilonaris,* and *S. valdispina.* It probably belongs to the Pliocene to Holocene. Sample 141-860B-19X-CC contains one specimen of *Spongaster* cf. *pentas* besides several specimens each of *A. denticulata, B. acquilonaris,* and *S. valdispina.* Thus, it appears to belong to the upper Pliocene.

Sample 141-860B-20X-1, 117–119 cm contains the following taxa: *A. robusta, A. deflandrei, B. acquilonaris, Spyrocytis subscalaris, Stylodictya valdispina, Siphcampe arachnea,* and *Carpocanistrum* sp. It is likely that this sample belongs to the upper Pliocene to Holocene. Sample 141-860B-20X-2, 24–26 cm, can be unambiguously placed in the *Pterocanium prismatium* (RN12) to *Amphirhopalum ypsilon* Zone (RN14) of the upper Pliocene to lower Pleistocene as it contains *Axoprunum angelinum* and *Cycladophora d. davisiana.* Other taxa found in this sample include: *S. valdispina, B. acquilonaris, Cornutella profunda, Antarctissa robusta, A. deflandrei, S. subscalaris, Eucyrtidium acuminatum, E. calvertense, Carpocanarium papillosum,* and *Spongaster tetras.* Sample 141-860B-20X-CC can only be bracketed to the middle Miocene to Holocene as it contains *B. acquilonaris* and *Stylodictya valdispina.* Sample 141-860B-21X-CC is bracketed from the middle Miocene to the *A. ypsilon* Zone (RN14) of the lower Pleistocene. The species included in the assemblage are: *Axoprunum angelinum, E. calvertense, B. acquilonaris,* and *Carpocanistrum flosculum.*

Sample 141-860B-22X-CC contains only three specimens of circular spongodiscids and thus no age can be given. Samples 141-860B-23X-CC through 141-860B-29X-CC are barren except for Sample 141-860B-27X-CC, which contains a trace amount of non-age-diagnostic taxa. Sample 141-860B-30X, 30–32 cm, contains *S. valdispina* and *Siphcampe* sp. but no age can be given. Sample 141-860B-30X-CC is represented by *Cycladophora* cf. *d. davisiana, B. acquilonaris, S. valdispina, S. subscalaris,* and *Acrosphaera* cf. *murrayana.* It can be placed in the upper Pliocene through Holocene, although the age assignment is pending confirmation of *C. d. davisiana.* Sample 141-860B-31X-CC contains *B. acquilonaris, S. valdispina,* and circular spongodiscids, providing only a middle Miocene to Holocene age bracket. Sample 141-860B-32X-CC from the next core down is represented by the same three species as the above sample, as well as a broken specimen of *Cycladophora* cf. *d. davisiana.* It may be placed in the upper Pliocene to Holocene, certainly in the middle Miocene to Holocene. Sample 141-860B-33X-CC contains only a trace amount of radiolarians. Samples 141-860B-34X-CC is barren, and below this Sample 141-860B-35X-CC has only a trace amount. Sample 141-860B-36X-CC contains *B. acquilonaris* and thus it represents the middle Miocene through Holocene. A specimen of *Antarctissa denticulata* is found in Sample 141-860B-37X-CC, placing this sample in the upper Miocene through Holocene. Sample 141-860B-38X-CC contains *Siphocampe lineata* and circular spongodiscids and hence no useful age information can be given other than to put it in the Neogene. Samples 141-860B-39X-CC and 141-860B-40X-CC are both barren. Sample 141-860B-41X-CC contains merely circular spongodiscids. Samples 141-860B-43X-CC through 141-860B-50X-CC are barren. Sample 141-860B-51X-CC contains a well- preserved non-age-diagnostic *Cenosphaera* sp. It may have been contaminated. Samples 141-860B-52X-CC through 141-860B-55X-CC are all barren.

Sample 141-860B-56X-CC contains *Lamprocyrtis heteroporos, Siphocampe* sp., *Antarctissa* sp., and *Eucyrtidium* sp. It belongs to the *Pterocanium prismatium* Zone RN12 of the upper Pliocene. Samples 141-860B-57X-CC through -62X-CC are all barren. Pebbles are found in Sample 141-860B-63X-CC, which contains *Spongotrochus glacialis, Stylodictya* sp., and *Cycladophora* sp. of Neogene age. Samples 141-860B-64X-CC through -70X-CC are barren except for Sample 141-860B-66X-CC, which contains a trace amount of non-age-diagnostic taxa.

As noted at Site 859, a positive correlation exists between foraminifer-derived paleotemperature estimates (warm, temperate, cold) and radiolarian preservation (Fig. 16). It may be that during warm intervals higher biological production occurred as evidenced by the presence of the upwelling species, than during cold intervals. The proximal location of the present site to the continental shelf and terrigenous sources may have always tended

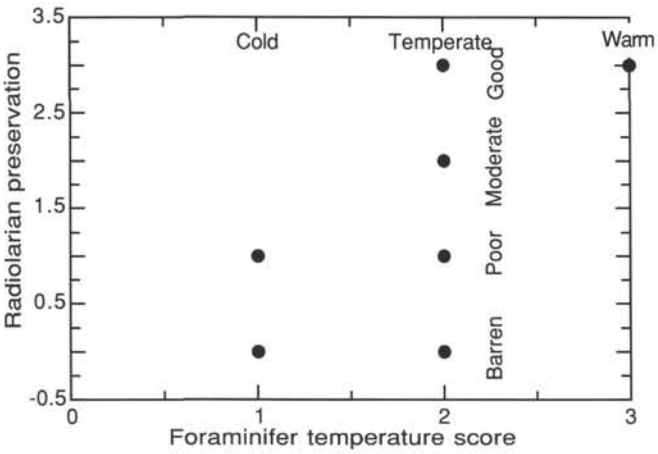

Figure 16. Plot of foraminifer-derived paleotemperature vs. state of radiolarian preservation. The following scores are employed: warm water, 3; temperate, 2; cold, 1; good preservation, 3; moderate, 2; poor, 1; barren, 0. Note that a positive correlation exists between the variables.

to dilute the siliceous microfossils with clays and silts. Consequently, such a dilution may have caused lower dissolved silicon concentrations in interstitial waters, enhancing dissolution of biogenic silica, unless siliceous shell supply rates were high enough to compensate for the high sedimentation rates.

Planktonic Foraminifers

In Hole 860B (Table 7), low-diversity planktonic foraminifer assemblages are generally common in abundance and well preserved down to Sample 141-860B-23X-CC, providing an age assignment to the Pleistocene and Pliocene. Below Sample 141-860B-23X-CC the abundances are categorized as rare and the preservation is poor. To acquire enough fossils, the entire residue was picked out.

The sequence drilled at Hole 860B can generally be described as an alternation of assemblages with *Globoconella inflata* and assemblages where *G. inflata* is missing. The sequence terminates at the top, as documented in Sample 141-860B-1H-CC, in a layer of 1.37 m thickness relating to the warm-water influenced assemblages in the *Truncorotalia tosaensis* Zone with the zone fossil and with *Neogloboquadrina dutertrei* and *Orbulina universa.*

In Hole 860B one last occurrence datum (LOD) and two first occurrence datums (FOD) were used to determine boundaries of different zones. The first appearance of *T. tosaensis* lies around the Pliocene/Pleistocene boundary (Kennett and Srinivasan, 1983: Bolli and Saunders, 1985). In Hole 860B this species is observed in Sample 141-860B-1H-CC; it is characteristic of the lower Pleistocene. In contrast the calcareous nannofossils date this sample as upper Pleistocene. The FAD of *G. inflata* usually marks the boundary between early and late Pliocene, i.e., the boundary between the *Globorotalia crassaformis* Zone and the *G. inflata* Zone, respectively (Kennett and Srinivasan, 1983; Srinivasan and Kennett, 1981). This event is observed in Hole 860B at least five times: between Samples 141-860B-17X-CC and -18X-CC, in Core 141-860B-20X, between Samples -32X-CC and -33X-CC, between Samples -38X-CC and -39X-CC, and between Samples 141-860B-44X-CC and -45X-CC. These alternating successions seen in Hole 860B core catchers needs further examination involving additional samples between the core-catcher samples and by additional observations of calcareous nannofossils. The LOD of *Globorotalia* cf. *sphericomiozea* might indicate the lower Pliocene in Sample 141-860B-65X-CC and below. For more details see Table 7.

Paleotemperatures in this region appear to be reflected in the assemblages of planktonic foraminifers. Warm-water-masses are represented in Sample 141-860B-1H-CC by the occurrence of *O. universa, T. tosaensis,* and *N. dutertrei*. From Sample 141-860B-2H-CC down to Sample -23X-CC, assemblages of planktonic foraminifers reflect the temperate water conditions of the Transitional Zone with *G. inflata* and minor occurrences of *N. pachyderma* in the sinistral coiling direction, and below Sample 141-860B-24X-CC the assemblages of planktonic foraminifers mainly consist of the cold-water species *N. pachyderma* sin.

Benthic foraminifers

Quaternary and Pliocene benthic foraminifers recovered at this site down to Sample 141-860B-44X-CC are middle bathyal assemblages. Below Sample 141-860B-47X-CC there are some signs of lower bathyal to abyssal environments in the poor assemblages of benthic foraminifers. In the whole sequence of Hole 860B downslope-displaced assemblages of different species are recognized (Table 8). In Hole 860B benthic foraminifers are common and well preserved down to Sample 141-860B-27X-CC. Below this sample the abundances are categorized as rare and the preservation is poor. Therefore, the analysis below Sample 141-860B-27X-CC is not well substantiated. *Bulimina mexicana* is rare but broadly distributed through the whole sequence of Hole 860B. In the Peru-Chile Trench area this species was found at depths of 150–2000 m, and greatest abundances occurred from 500–1500 m (Ingle et al., 1980). *Uvigerina peregrina* occurs most often in the samples from the top of the hole down to Sample 141-860B-37X-CC, and it sporadically occurs down to Sample -54X-CC in a more finely striated form. The bathymetry of this species ranges from 400 to 2000 m water depth (Resig, 1990). *Planulina wuellerstorfi* occurs in the drilled sequence from the top down to Sample 141-860B-44X-CC. This taxon ranges bathymetrically from 500-m water depth through abyssal depths (van Morkhoven et al., 1986). *Pyrgo murrhina* and *Melonis pompilioides* both occur sporadically in the sequence of Hole 860B. *P. murrhina* is one of the species representative of upper middle bathyal depths in the Gulf of California (Bandy, 1961), whereas *M. pompilioides* is an outer neritic to middle bathyal species. Voloshinova (1958) described a deep-water ecotype of *M. pompilioides,* named *M. sphaeroides,* as a reliable bathymetric indicator for abyssal depths (van Morkhoven et al., 1986). This taxon is observed as a few specimens in Samples 141-860B-65X-CC, -63X-CC, and -69X-CC. This observation and the occurrences of different *Uvigerina* taxa should be further examined using additional samples. In Table 8, samples marked by an asterisk contain taxa indicative of shelf deposition and therefore they are indicative of downslope displacement. In Holocene material off South Chile the occurrence of these taxa reaches from shelf through upper slope environments, as described by Boltovskoy and Theyer (1970).

Calcareous Nannofossils

Seventy core-catcher samples and some additional samples from Cores 141-860B-1H to -70X were investigated. This series belongs to the Pleistocene (Zones NN19–NN21) and upper Pliocene (Zones NN16–NN18). Nannofossils are missing below Sample 141-860B-62X-CC.

The Pleistocene was determined from Cores 141-860B-1H–9X. The upper part of this sequence belongs probably to the upper Pleistocene (Zones NN20–NN21) based on the absence of *Pseudoemiliania lacunosa*. Nannofossils are few to common. The following assemblages have been observed: *Cyclococcolithus leptoporus, Gephyrocapsa ericsonii, G. oceanica,* and *Coccolithus pelagicus.*

Table 8. Occurrence, preservation, and estimated relative abundance of selected benthic foraminifers of samples from Hole 680B.

Hole 860B Sample	Depth (mbsf)	Abundance	Preservation	Displaced Sediments	*Bulimina mexicana*	*Uvigerina* cf. *peregrina*	*Planulina wuellertorfi*	*Pyrgo murryhina*	*Melonis pomp. sphaeroides*	*Uvigerina hispida*	*Uvigerina cushmani*	*Uvigerina senticosa*	*Hoeglundina elegans*	*Nodogenerina bradyi*	*Mucronia* sp.	*Bulimella elegantissima*	*Nonionella chiliensis*	*Nonionella auris*	*Nonionella* cf. *turgida*	*Bolivina costata*	*Bulimina marginata*	*Rosalina peruviana*	Paleoenvironments
1H-CC	1.37	C	G		R	R	R			F			F										Middle bathyal and displaced neritic sediments
2H-CC	10.90	F	G	*		R					R							R		R			
3H-CC	20.40	F	G	*	R	F	R				F		R						R				
4H-CC	29.90	C	G	*		R	C	R			C		F						R		R	R	
5H-CC	39.40	C	G			R	F				F		R	R									
6H-CC	48.28	R	P			R																	
7H-CC	58.40	C	G	*	R	F	C	R		F	C							R	R		R		
9H-CC	60.02	C	G	*	R	F	C	R		F	C		F					R				R	
10X-CC	69.10	F	P			R	R				R		R										
12X-CC	93.69	B																					
13P-1, 46–48 cm	98.06	B																					
14X-CC	102.41	F	G	*		R	R				F								R	R	R	R	
15X-CC	113.88	B																					
16X-CC	120.65	F	G		R	F			R		R												
17X-CC	133.90	F	P	*	R	R	R	R		R										R			
18P, bottom	137.10	F	M			R					R												
19X-CC	145.36	F	G		R	F					R	R	R		R								
20X-2, 24–26 cm	146.04	F	M			F								R	R								
20X-CC	148.21	R	M		R	R						R			R								
21X-CC	157.03	R	M		R	R	R																
22X-CC	169.24	R	M		R	R	R																
23X-CC	174.94	F	M	*	R	R	R		F			R					R						
24X-CC	186.67	F	P	*	R	R	F	R	R				R		R		R		R		R	R	
25X-CC	196.65	R	P	*		R						R				R			R		R		
27X-CC	213.43	F	P	*	C	R			R					R	R		R						
28X-CC	224.64	R	P					R															
29X-CC	235.11	B																					
30X-CC	245.23	B																					
31X-CC	256.28	R	P	*		R				R				R	R						R		
32X-CC	263.51	R	P	*	R	R								R		R	R					R	
33X-CC	273.75	R	M		R	R						R		R									
34X-CC	285.74	R	P		R	R																	
35X-CC	291.97	R	P		R	R								R									
36X-CC	305.00	R	P											R									
37X-4, 39–41 cm	310.19	R	M		R	R			R		R		R			R	R				R		
37X-CC	314.92	R	P	*						R				R									
38X-CC	322.41	R	P									R											
39X-CC	331.52	R	P		R							R		R									
40X-CC	338.80	R	P											R									
41X-6 bottom	356.93	R	P	*	R									R	R							R	Middle bathyal
43X-CC	361.28	B																					
44X-CC	367.47	R	M		R	R	R	F						R	R								
45X-CC	377.35	B																					?
46X-CC	389.26	B																					
47X-CC	396.88	R	P												R								Abyssal(?) to lower bathyal and displaced neritic sediments
48X-CC	411.95	R	P										R	R									
49X-CC	416.81	R	P	*	R								R	R								R	
50X-CC	430.91	B																					
51X-CC	439.11	B	P		R									R									
52X-CC	444.75	B	P		R	R								R									
53X-CC	452.22	B	P											R									
54X-CC	453.84	B	P	*	R	R						R		R								R	
55X-CC	464.22	B	P	*										R								R	
56X-CC	473.71	B	P						R					R	R								
57X-CC	483.57	B																					
58X-CC	497.09	B	P			R		R						R	R		R						
59X-CC	502.87	B																					
60X-CC	516.98	B	P		R																		
61X-CC	531.45	B	P		R									R									
62X-CC	536.31	B	P							R				R									
63X-CC	540.65	B	P		R				R				R	R		R							
64X-CC	554.40	B																					
65X-CC	560.14	R	P	*	R									R								R	
66X-CC	572.41	F	M										R										
67X-CC	584.57	R	P																				
69X-CC	598.85	F	M		R				R			R		R	R								
70X-CC	608.52	R	P		R																		

Nannoplankton Zone NN19 of early Pleistocene age is present from Cores 141-860B-4X to -9X. Nannofossils are few, but they become more common in Cores 141-860B-7H to -9X.

The Pliocene/Pleistocene boundary (based on calcareous nannofossils) is placed below the level suggested by the assemblage of planktonic foraminifers. The nannofossil position for this boundary is determined by the last occurrence of *Cyclococcolithus macintyrei*, and the presence of only the small *Gehyrocapsa* sp. Unfortunately, *Cyclococcolithus macintyrei* is not a very good marker for the Pliocene/Pleistocene boundary in Leg 141 sediments because this species is often very rare.

It seems that the entire series from Core 141-860B-10X to -63X is of late Pliocene age (Zones NN16–NN18). However, an imbrication of the series that would explain its thickness (540 m) cannot be excluded.

Nannofossils are rare to few within the sediments of Cores 141-860B-10X to -20X with the exception of Sample 141-860B-19X, where nannofossils are common. The following assemblages were observed: *Coccolithus pelagicus, Helicosphaera carteri, H. sellii, Cyclococcolithus leptoporus, C. macintyrei, Pseudoemiliania lacunosa,* and *Gephyrocapsa* sp. Nannofossils are more common and of larger size in Cores 141-860B-21X to -23X. A small variety of *Reticulofenestra pseudoumbilica* occurs within this interval. This form has been observed in other regions within the lower part of Zone NN16 or within the uppermost part of early Pliocene nannoplankton Zone NN15. Cores 141-860B-24X to -28X are barren of nannoplankton.

Comparable assemblages to those mentioned above were observed in Cores 141-860B-29X to -37X. Within this interval nannofossils are few to abundant, they are well preserved, and their large size may indicate warm surface-water temperatures.

Nannofossils are absent or rare throughout the lower part of the sequence (Cores 141-860B-38X to -62X). Only in Sample 141-860B-58X-CC do they become common. The assemblage consists of *Coccolithus pelagicus, Gephyrocapsa* sp., *Cyclococcolithus macintyrei, C. leptoporus, Pseudoemiliania lacunosa, Helicosphaera carteri, Pontosphaera pacifica,* and *Discolithina japonica,* indicating a late Pliocene age (Zones NN16–NN18). The last two species have been observed more frequently in upper Pliocene sediments from a number of areas. This observation seems to be of stratigraphic use. This age determination is confirmed by radiolarians obtained from Core 141-860B-56X (Zone RN12, late Pliocene). As at Site 861, the small variety of *Reticolofenestra pseudoumbilica* has also been found in several samples.

Nannofossils are absent from the lowermost part of the sequence (Cores 141-860B-63X to -70X).

PALEOMAGNETISM

Introduction

Magnetic measurements using the pass-through cryogenic magnetometer were taken on APC and XCB split archive-half sections recovered from Holes 860A and 860B. Some sections were not measured because of excessive drilling disturbance. Hole 860A is represented by a single core, which failed to recover the mudline. Hole 860B penetrated to a depth of 617.8 mbsf but low recovery and extensive drilling disturbance make it impossible to establish a systematic magnetostratigraphy. Moreover, there is independent evidence of repeated sequences (see Biostratigraphy and Lithostratigraphy sections, this chapter) so that the very interrupted record of polarity is uninterpretable in magnetostratigraphic terms. Alternating field (AF) demagnetization on these cores was performed at 10-cm intervals using field intensities of 10 and 15 mT. Cores 141-860B-2H, -3H, -4H, and -7H were oriented with the tensor tool in situ with respect to the downhole ambient field. Discrete samples from the working half were also measured after stepwise demagnetization up to 60 mT. Many cores from Hole 860B were pervasively fragmented and disturbed by drilling and/or structural deformation. Magnetic susceptibility of all cores was measured on the multi-sensor track (MST).

Remanence and Susceptibility

Figure 17 records the variation with depth of natural remanent magnetization (NRM) inclination before demagnetization, and inclination and intensity after 15-mT demagnetization, measured along continuous sections in Hole 860B. Demagnetized remanent intensity rises and falls over three broad cycles. After a steep increase from values of less than 10 mAm^{-1} over the first 15 mbsf to around 200 mAm^{-1} at about 20 mbsf, the average intensity remains roughly constant down to at least 50 mbsf. Intensity then decreases over the interval from 80 to 150 mbsf, to a minimum of about 50–100 mAm^{-1}. Intensity within the poorly recovered interval from about 150 to 245 mbsf again increases, reaching more than 300 mAm^{-1} before falling to values less than 50 mAm^{-1} at about 260 mbsf. From 280 to about 540 mbsf, although the record is again patchy, there is an overall increase in the average intensity from about 100 mAm^{-1} to about 400 mAm^{-1}. Below 540 mbsf drops again to an average of about 150 mAm^{-1}.

Figure 18 records the variation in bulk magnetic susceptibility. Susceptibility roughly mimics the rises and falls in demagnetized intensity, suggesting that, unlike Site 859, no cyclic alteration in magnetic-phase grain size and/or composition operated at Site

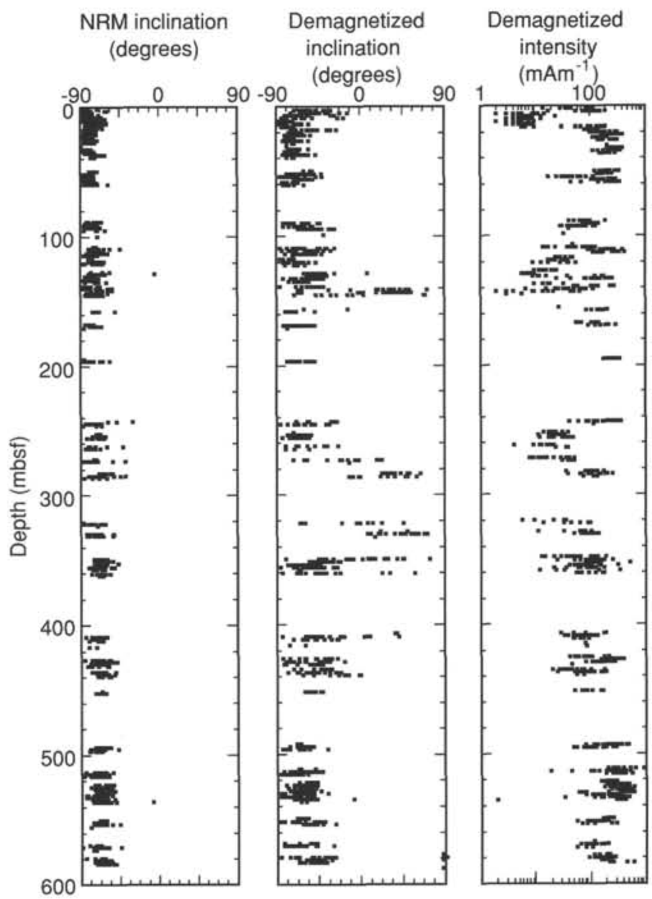

Figure 17. NRM inclination, demagnetized inclination, and demagnetized intensity in Hole 860B.

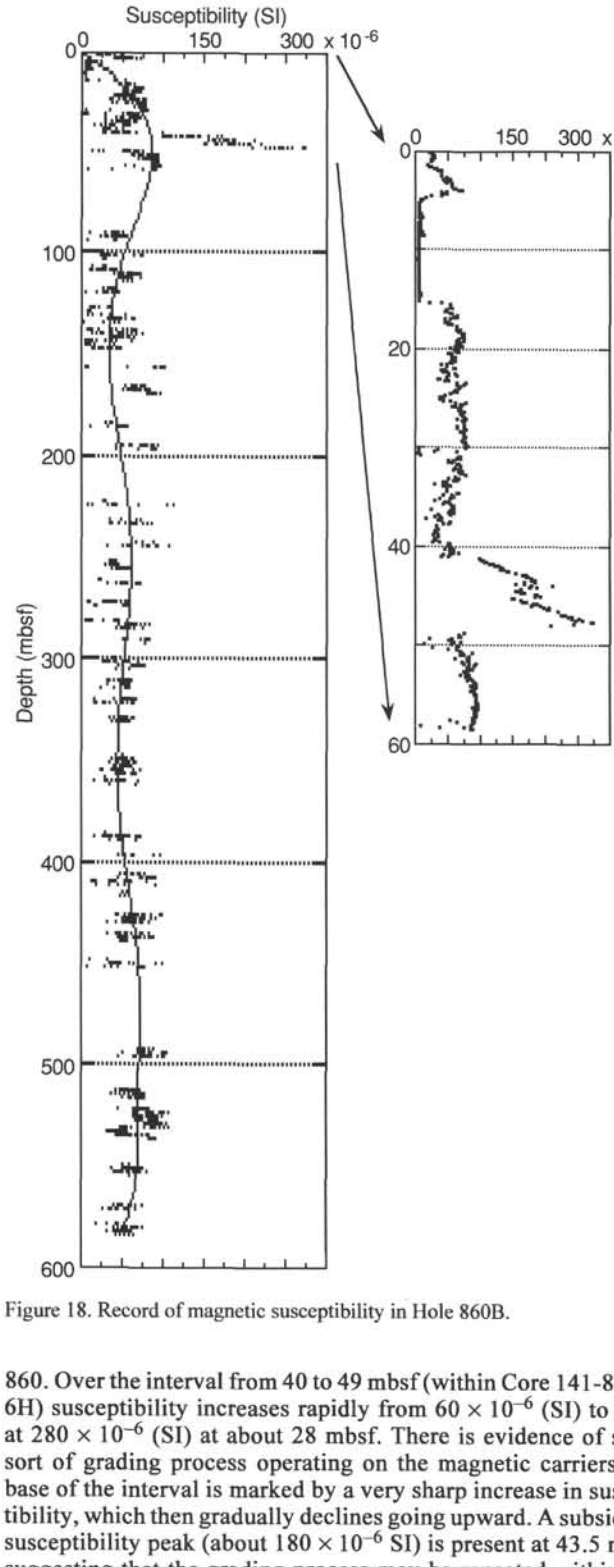

Figure 18. Record of magnetic susceptibility in Hole 860B.

860. Over the interval from 40 to 49 mbsf (within Core 141-860B-6H) susceptibility increases rapidly from 60×10^{-6} (SI) to peak at 280×10^{-6} (SI) at about 28 mbsf. There is evidence of some sort of grading process operating on the magnetic carriers; the base of the interval is marked by a very sharp increase in susceptibility, which then gradually declines going upward. A subsidiary susceptibility peak (about 180×10^{-6} SI) is present at 43.5 mbsf, suggesting that the grading process may be repeated within this interval. Grain density also peaks at about 48 mbsf (see Physical Properties section, this chapter); however, the increase is less dramatic, and grain density does not rise appreciably above background until below 43.5 mbsf. This interval spans a layer of coarse, well-sorted sand (see Lithostratigraphy section, this chapter); this sand layer is massive, however, and there is no visual evidence for grading, at least among the larger clasts. The susceptibility pattern evidently reflects a grading according to density, which may only affect the finer sand fraction. This finer fraction may be present only in small quantities, but it will dominate the susceptibility if a significant proportion of it is composed of magnetite. Whether this pattern is depositional is open to some question; it is possible that the finer sand fraction was remobilized during drilling, and the apparent grading may reflect no more than settling in the core barrel. If it is depositional, it repesents an interesting difference in response to the same flow regime between larger, lower-density grains and smaller, higher-density grains.

Demagnetization of Discrete Samples

Although the polarity sequence determined from measurements in the cryogenic magnetometer does not allow us to propose a magnetochronology, the progressive AF demagnetization of discrete samples from each core helps us to define the polarity of the characteristic remanent magnetization (ChRM), especially for sections where NRM of apparently normal polarity (defined by negative inclinations) exhibits a very shallow inclination after 15 mT demagnetization (the limit allowed on archive-halves). Figure 19 illustrates examples of two such samples that show a reverse polarity after demagnetization at 30 mT. Remanence trends toward positive inclinations, and appears to stabilize in direction above 30 mT. The highly concave intensity vs. demagnetization plots indicate that viscous remanence (VRM) constitutes a very large proportion of NRM in these two specimens; the remanence at 30 mT may represent the ChRM, although the inclination in the two specimens shown is surprisingly shallow (see below). In contrast, Figure 20 illustrates the demagnetization behavior of two normally-polarized specimens that remain normally polarized on demagnetization and that trend toward an inclination close to the expected dipole (±65°) for this latitude. An inflection in the Zijderveld plots occurs at a demagnetization level of about 15 mT, above which the linear trend of the demagnetization vectors toward the origin of the plot implies that the ChRM has been isolated; the intensity vs. demagnetization plot is less concave, also suggesting that VRM is less significant in these specimens.

Structural Orientation

As the majority of cores were not oriented by the tensor or multishot tools, we wished to test the suitability of VRM as a reference with which to orient cores from this site to their in-situ north. A set of discrete specimens from APC cores were oriented by reference both to the tensor orientation and the direction of VRM isolated from each; the results are compared in Table 9. The directions oriented with respect to VRM are better grouped than those oriented by the tensor tool, and lie closer to the dipole field direction. The significance of the difference between the tensor and VRM orientations is not clear: it may result from incorrect magnetic tool face (MTF) orientation, or it may reflect rotation of parts of the core within the core liner. Alternatively, it may indicate that VRM has not been completely removed from the primary remanence, so that the supposed ChRMs are biased toward the VRM direction.

Although the inclination of demagnetized remanence from Hole 860B is usually close to that of the dipole field, consistent with low bedding dips, there are intervals where the demagnetized inclinations are shallow. In discrete samples taken over the sub-bottom depth 415 to 440 mbsf (Cores 141-860B-49R to -51R) inclinations of what appears to be a reversely magnetized, stable end-point of demagnetization (the ChRM) are more than 30° lower than the dipole reversed inclination (see Fig. 19). If this remanence is depositional or early post-depositional in origin, it should be possible to determine bedding through the method described in the Paleomagnetism section of the Site 859 chapter.

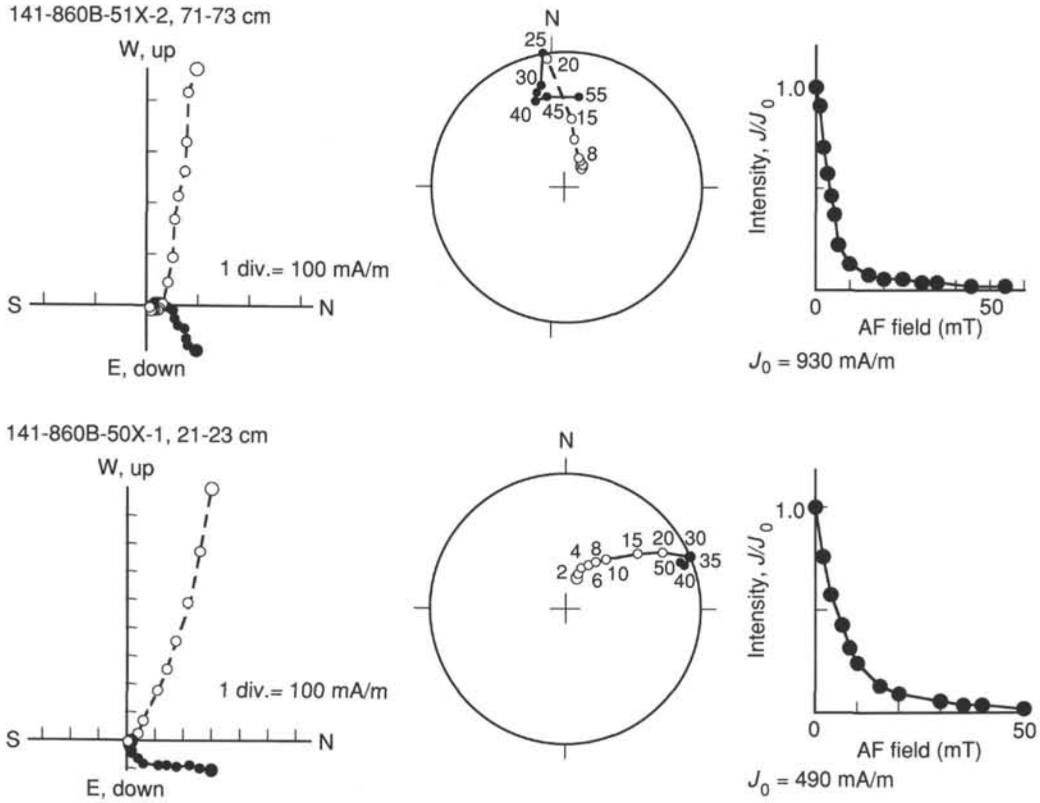

Figures 19. Zijderveld plot, stereographic projection, and plot of remanence intensity vs. AF demagnetization level, for reversely polarized discrete samples from Hole 860B. Zijderveld plot: open symbols are on the vertical/N-S plane, closed symbols on the horizontal plane. Stereographic projection: open symbols are in the upper hemisphere, closed on the lower hemisphere.

This was carried out for four discrete specimens from this interval (Table 10). Dips determined by this method are high, from 48° to 85°. Bedding surfaces were directly observed at Intervals 141-860B-50X-5, 53–54 cm and -51X-2, 66–69 cm; these show true dips of 16° and 23°, respectively. The divergence between the measured bedding and the paleomagnetic analysis suggests that the ChRM of Cores 141-860B-49R to -51R is not the depositional remanence, and in fact the ChRM may not represent a single, well-isolated component. Inclination shallowing in marine sediments due to compaction has frequently been reported (e.g., Arason and Levi, 1990; Deamer and Kodama, 1990; Tarduno, 1990). If this is the cause, then Site 860 provides an extreme example. Alternatively, the shallow inclination may result from incomplete removal of a normal overprint from a reversed primary magnetization.

STRUCTURAL GEOLOGY

Summary

Three structural domains can be defined at Site 860: an upper domain characterized by generally subhorizontal bedding with rare slump folds and intraformational breccia (0–88 mbsf); a middle thrust-stack domain with little internal deformation (88–420 mbsf); and a lower domain of broken formation (420–617.8 mbsf). Figure 21 shows these domains, together with a record of core recovery and the amount of recovered core in which structures are preserved.

Within the thrust-stack domain, biostratigraphic and lithostratigraphic data constrain major thrusts at about 240 mbsf and 310 mbsf (see Biostratigraphy and Lithostratigraphy sections, this chapter, and Fig. 80). These thrust faults were not observed in the cores and may not have not been recovered. Bedding remains nearly flat-lying throughout this domain. At about 420 mbsf a marked change in lithification and structural style corresponds to a possible lithostratigraphic repetition, suggesting that a thrust fault is present. This postulated thrust separates the upper, thrust stack domain from the lower, broken formation domain.

Below 420 mbsf the dominant lithology, silty claystone to clayey siltstone, is cut by an intense network of deformation bands. The deformation bands vary in mesoscopic and microscopic geometry, internal strain, and the mechanisms that contribute to their formation. The deformation bands that characterize broken formations first appear at 90 mbsf. At shallow depths, these small, isolated structures are insignificant and do not cause stratal disruption. Below 420 mbsf deformation bands are larger, more abundant, and more complex in geometry; primary bedding surfaces are modified, and significant stratal disruption is observed. Both structural chronology and deformation-band geometry vary systematically down the borehole. Detailed structural analysis suggests that a broad, simple shear zone between 520 and 580 mbsf separates domains dominated by more general volumetric deformation. Within the broad, simple shear zone more intense, flat-lying simple shear zones occur at 520 and 580 mbsf. These probably accommodate significant displacement with a thrust geometry.

Detailed structural data recorded on spreadsheets for Holes 860A and 860B are presented in Table 11. Wherever possible, structural measurements have been reoriented into a geographical reference frame. Sections where reorientation was possible are shown in Figure 21.

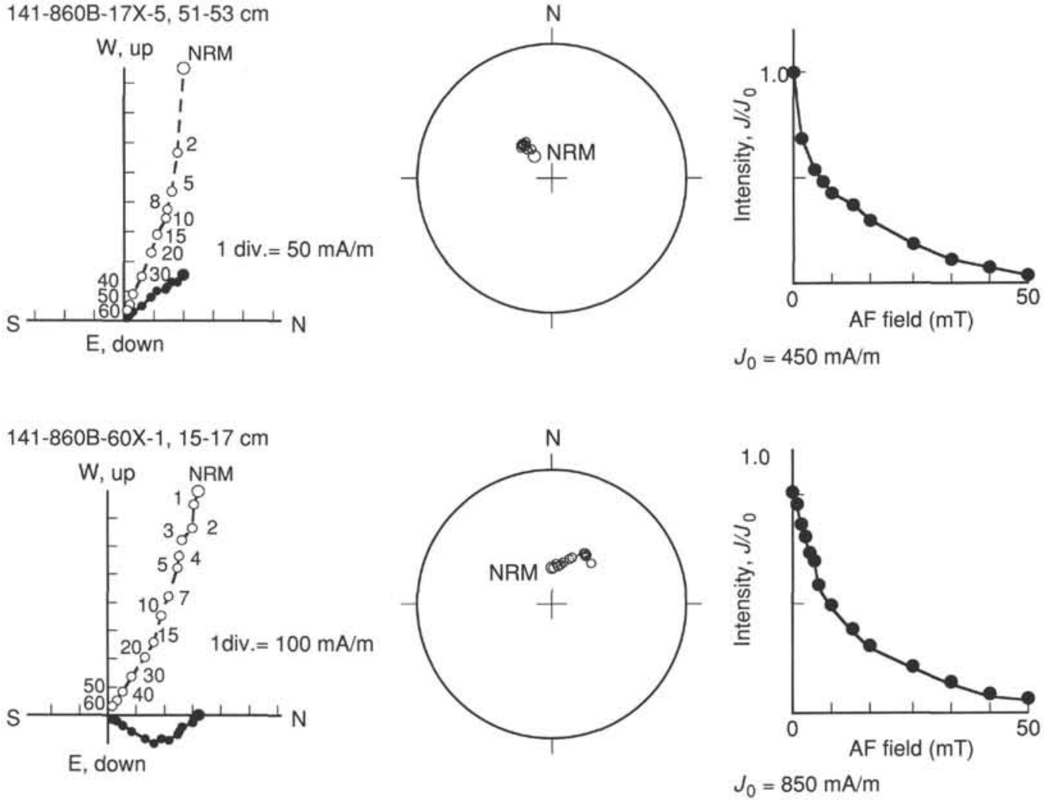

Figure 20. Zijderveld plot, stereographic projection, and plot of remanence intensity vs. AF demagnetization level for normally polarized discrete samples from Hole 860B. Zijderveld plot: open symbols are on the vertical/N-S plane, closed symbols on the horizontal plane. Stereographic projection: open symbols are in the upper hemisphere, closed on the lower hemisphere.

Table 9. Comparison of core reorientation in geographic coordinates using tensor orientations and VRM. Fisher's precision parameter (k) and 95% confidence limit (α_{95}) are presented for the mean of the directions oriented by each method.

	ChRM (Core)		ChRM (Tensor)		VRM		ChRM (wrt VRM)	
Sample	Decl.	Incl.	Decl.	Incl.	Decl.	Incl.	Decl.	Incl.
141-860B-2H-2, 06–108 cm	019	−55	338	−55	022	−60	357	−55
141-860B-3H-3, 5–17 cm	219	−27	223	−27	191	−65	028	−27
141-860B-4H-1, 26–128 cm	051	−66	323	−66	044	−73	007	−66
141-860B-7H-4, 3–45 cm	310	−76	260	−76	288	−65	022	−76
	Mean: $N = 4$		277 $k = 6.9$ $\alpha_{95} = 45°$	−67			015 $k = 17.2$ $\alpha_{95} = 27°$	−57

Table 10. Reconstruction of apparent bedding directions in Hole 860B using paleomagnetic criteria. Strike direction is to the right of dip azimuth.

	ChRM (Core)		VRM		ChRM (Geogr.)		Dip	Strike
Sample	Decl.	Incl.	Decl.	Incl.	Decl.	Incl.	(Geog. coords.)	
141-860B-49X-1, 58–60 cm	088	−17	077	−69	011	−17	748	110
141-860B-50X-1, 21–23 cm	069	7	009	−65	060	7	80	132
141-860B-51X-1, 60–62 cm	343	31	330	−60	013	31	85	275
141-860B-51X-1, 71–73 cm	333	25	338	−68	005	25	83	280

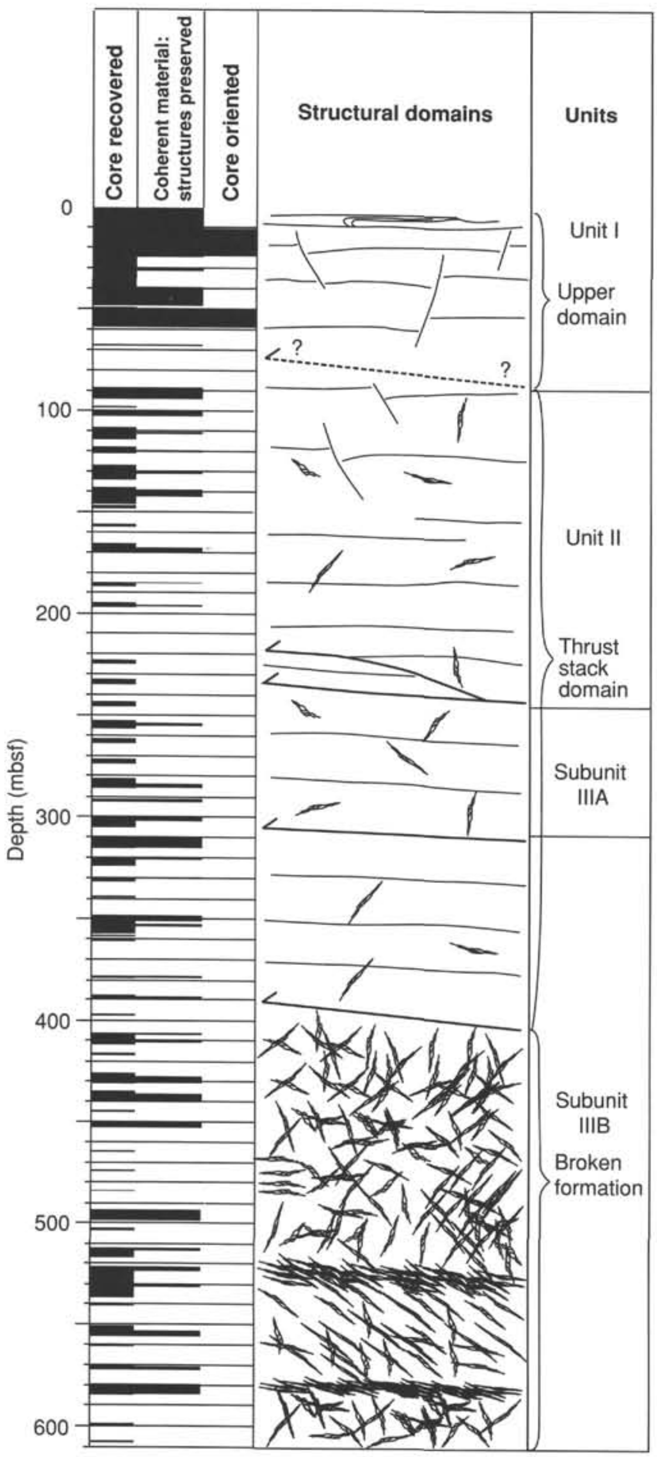

Figure 21. Schematic illustration of major structural features and changes at Site 860, plotted against depth in the borehole. The first three columns show distribution of sediment recovery, the distribution of material sufficiently coherent to make structural observations, and the distribution of material in which structural measurements could be reoriented into a geographical reference frame. Approximate boundaries of lithostratigraphic Units are shown for reference.

Upper Domain

The upper domain is characterized by poorly lithified sediments in which the majority of structures are interpreted as having formed near the sediment surface. The base of the upper domain is marked by an increase in lithification in the 69.0–87.7 mbsf layer (between Cores 141-860B-10X and -12X). The contact corresponds to a change in deformation style: the first deformation bands appear in Core 141-860B-12X. A marked perturbation in porosity and grain densities (see Physical Properties section, this chapter) occurs in the region of this boundary together with freshwater signatures in pore waters (see Inorganic Geochemistry section, this chapter) and a marked increase in maturation (see Organic Geochemistry section, this chapter). It is tempting to suggest that this is a thrust contact. Biostratigraphy (see Biostratigraphy section, this chapter) can neither define or preclude a thrust in this interval.

In Hole 860A and the upper part of Hole 860B, bedding is indicated by color, composition, and grain size changes. Some of the bedding contacts are sharp, particularly the bases of graded beds interpreted as turbidites; other contacts are diffuse and gradational, or are mottled and irregular (probably due to bioturbation). In intervals where pronounced changes in composition and texture are absent, probable bedding is indicated by dark stringers and fragments of organic material. Bedding is flat-lying (Fig. 22). Good-quality Tensor-tool orientation data were available for four piston cores, and structural data from these cores have been re-oriented in the geographical reference frame using a magnetic deviation of 14°. The rotations used in each case are shown in Table 12. The poles to bedding for oriented data form a cluster rather than falling on a great circle (Fig. 22B), suggesting that no significant fold structure is present. The mean bedding orientation strikes 028° with a dip of 12°E. These data are consistent with the very shallow reflectors observed on seismic line 745. Many beds strike sub-parallel to the seismic line; apparent dips on the seismic line may be significantly shallower than true dips.

Isolated recumbent isoclinal fold closures are interpreted as slump folds. Inclined beds (e.g., interval 141-860A-1H-7, 17–43 cm, Fig. 23) also can be interpreted as parts of slump folds. Textural grading preserved in turbidite beds indicates that the sequence is the right way up. A shear zone occurs at 38 cm in Section 141-860B-2H-2, apparently defining the base of a complex slump fold.

Isolated, thin wedge-shaped beds occur within the upper domain, e.g., intervals 141-860A-1H-2, 79–81 cm, -1H-4, 18–20 cm, and -1H-6, 27–71 cm. Some beds are bounded by inclined planes that suggest the bed thins to a wedge with its edge outside the core. These features might be interpreted as necking and thinning due to layer-parallel extension during downslope sliding and slumping. Examples are in Cores 141-860A-1H, 141-860B-2H, and 141-860B-3H.

Discrete normal faults occur throughout the upper 420 m of Hole 860B and the clearest examples are in the upper domain. Typically, these faults occupy discrete black- to dark gray-stained zones, 0.2–0.5 cm wide on the core face. Figure 24 shows a particularly large and well-preserved normal fault, with a dip separation of 10 cm, in interval 141-860B-3H-6, 122 cm, to -3H-7, 27 cm.

Thrust Stack Domain

Large-scale tectonic breaks must be inferred from stratigraphic repetitions. Assemblages of planktonic foraminifers suggest that lower Pliocene sediment in Core 141-860B-24X overlies upper Pliocene sediment in Core 141-860B-31X (see Biostratigraphy section, this chapter). This repetition occurs again between Cores

Table 11. Tabulation of detailed structural data on a section-by-section basis for Holes 860A and 860B.

Core, section, interval (cm)	Depth (mbsf)	X-ref hand sheets	Photo?	ID	Identifier	Thickness (cm)	Core face orientation App. dip	Core face orientation Direction	Corrected Core ref frame Strike	Corrected Core ref frame Dip	Corrected Core ref frame Dir	Comments
141-860A-												
1H-1		NIL										
1H-2, 79–81	2.26	1		B	Bedding		25	270	218	31	W	
1H-2, 93–95	2.43	2		B	Bedding		17	270	237	29	N	
1H-3, 20–21	3.20	3		B	Bedding		11	90	15	11	E	
1H-3, 122–123	4.22	4		B	Bedding		8	270	135	11	E	
1H-3, 124–125	4.24	4		B	Bedding		8	270	135	11	E	
1H-4, 18.5–20	4.69	5		B	Bedding		0	90	0	0		
1H-5, 135–136	7.35	6		B	Bedding		10	270	141	13	W	
1H-6, 5–5	7.55	7		B	Bedding		0	90	0	0		
1H-6, 19–22	7.69	8		B	Bedding		0	90	0	0		
1H-6, 40–42	7.90	9		B	Bedding		0	90	0	0		
1H-6, 65–71	8.15	10		B	Bedding		0	90	0	0		
1H-6, 83–84	8.33	11		B	Bedding		13	270	189	13	W	
1H-6, 133–134	8.83	12		B	Bedding		18	270	135	25	W	
1H-6, 139–142	8.89	13		B	Bedding		0	90	0	0		
1H-7, 17–22	9.17	14		B	Bedding		15	90	329	17	E	
1H-7, 20–30	9.20	15		B	Bedding		64	90	325	68	E	
1H-7, 37–42	9.37	16	Yes	F	Fold	5						
1H-7, 37–42	9.37	16	Yes	Fax	Fold Axis		35	90				22/35, fold axis
1H-7, 37–42	9.37	16	Yes	Fap	Axial Plane		28	90	315	37	N	?
1H-7, 37–42	9.37	16	Yes	B	Bedding		20	90	14	21	E	Overturned fold limb
1H-7, 37–42	9.37	16	Yes	B	Bedding		31	90	16	32	E	Lower fold limb
1H-7, 43–45	9.43	17	Yes	B	Bedding		22	90	348	22	E	
1H-7, 45–48	9.45	18	Yes	Ft	Faults		40	270	138	48	W	Normal fault, welded
1H-7, 45–48	9.45	18	Yes	B	Bedding		53	90	32	58	E	
1H-CC		NIL										
141-860B-												
1H-1	0	NIL										
1H-CC	1.15	NIL										
2H-1, 85–85	2.25	1		B	Bedding		0	90	0	0		
2H-1, 135–136	2.75	2		B	Bedding		3	270	266	39	N	
2H-1, 145–150	2.85	3		B	Bedding		12	270	158	13	W	
2H-2, 31–38	3.21	4	Yes	F	Fold	7						
2H-2, 31–38	3.21	4	Yes	B	Bedding		10	270	191	10	W	Upper fold limb
2H-2, 31–38	3.21	4	Yes	B	Bedding		42	270	178	40	W	Overturned fold limb
2H-2, 31–38	3.21	4	Yes	Ft	Fault		0	90	0	0		Basal slip plane, welded
2H-2, 135–136	4.25	5		B	Bedding		5	270	225	7	W	
2H-3	4.4	NIL										
2H-4, 97–98	6.77	6		B	Bedding		48	270	189	48	W	
2H-4, 97–98	6.77	7		B	Bedding		8	270	123	14	S	
2H-5, 40–43	7.7	8		B	Bedding		16	90	32	19	E	
2H-5, 87–88	8.17	9		B	Bedding		14	90	356	14	E	
2H-5, 92–95	8.22	10		B	Bedding		20	270	144	24	W	
2H-5, 126–126	8.56	11		B	Bedding		1	270	92	29	S	
2H-6, 51–53	9.31	12		B	Bedding		19	90	42	25	E	
2H-7, 10–10	10.4	13		B	Bedding		2	90	297	4	N	
2H-7, 13–14	10.43	14		B	Bedding		12	90	30	14	E	
2H-CC, 20–20	10.85	15		B	Bedding		0	90	0	0		
3H-1, 64–66	10.9	1		B	Bedding		29	90	29	32	E	
3H-2, 90–94	13.3	2		B?	Bedding?		45	90	19	47	E	
3H-2, 134–135	13.74	3		B	Bedding		15	90	49	22	S	
3H-3, 20–23	14.1	4		B	Bedding		13	90	56	23	S	
3H-3, 4–25	13.94	12		Ft	Fault		83	270	174	83	W	Normal fault
3H-4	15.3	NIL										
3H-5, 20–22	17	5		B	Bedding		15	90	65	32	S	
3H-5, 143–146	18.23	6		B	Bedding		10	90	334	11	E	
3H-6, 5–8	18.35	7		B	Bedding		13	90	53	21	S	
3H-6, 35–38	18.65	8		B	Bedding		14	90	40	18	E	
3H-7, 32–33	20.12	9		B	Bedding		4	90	51	6	S	
3H-7, 2–5	19.82	10		B	Bedding		12	90	18	13	E	
3H-7, 0–25	19.8	11		Ft	Fault		76	90	7	76	E	Normal fault
3H-CC	20.4	NIL										
4H-1, 3–6	20.43	1		B	Bedding		23	90	48	32	S	
4H-1, 115–116	21.55	2		B	Bedding		2	270	95	23	S	
4H-1, 134–136	21.74	3		B	Bedding		5	270	103	21	S	
4H-2, 42–44	22.32	4		B	Bedding		2	270	94	28	S	
4H-2, 140–143	23.3	5		B	Bedding		5	90	79	25	S	
4H-3, 7–9	23.47	6		B	Bedding		7	90	62	15	S	
4H-3, 68–69	24.08	7		B	Bedding		2	270	104	8	S	
4H-3, 32–33	23.72	11		B	Bedding		35	90	7	35	E	
4H-4, 11–12	24.91	8		B	Bedding		8	270	62	17	S	
4H-4, 33–34	25.03	9		B	Bedding		4	270	106	15	S	
4H-4, 39–40	25.09	10		B	Bedding		0	90	90	8	S	
4H-5	26.2	NIL										
4H-6	27.7	NIL										
4H-7	29.2	NIL										
4H-CC	29.9	NIL										
5H-1, 146–148	31.36	1		B	Bedding		4	270	225	6	W	
5H-2, 7–10	31.07	2		B	Bedding		1	270	96	10	S	
5H-2, 28–30	31.28	3		B	Bedding		4	270	104	16	S	
5H-2, 91–92	31.91	4		B	Bedding		14	90	317	19	E	
5H-3	32.5	NIL										
5H-4	33.9	NIL										
5H-5	35.4	NIL										
5H-6	36.4	NIL										
5H-7	37	NIL										
5H-CC, 47–49	38.37	5		B	K-Bedding		9	90	331	10	E	

Table 11 (continued).

Core, section, interval (cm)	Depth (mbsf)	X-ref hand sheets	Photo?	ID	Identifier	Thickness (cm)	Core face orientation App. dip	Core face orientation Direction	Corrected Core ref frame Strike	Corrected Core ref frame Dip	Corrected Core ref frame Dir	Comments
141-860B- (Cont.)												
6H-1	39.4	NIL										
6H-2	40.9	NIL										
6H-3	42.4	NIL										
6H-4	43.9	NIL										
6H-5	45.4	NIL										
6H-6	46.9	NIL										
6H-CC	48.4	NIL										
7H-1, 19–19.5	49.09	1		B	Bedding		5	270	106	18	S	
7H-1, 21–22	49.11	2		B	Bedding		0	90	90	22	S	
7H-1, 41–43	49.31	3		B	Bedding		11	270	124	19	S	
7H-1, 49–49	49.39	4		B	Bedding		6	270	153	7	N	
7H-2, 24–39	50.24	5		Ft	Fault	15	62	270	115	77	S	Probable normal fault
7H-3, 63–63	52.33	6		B	Bedding		1	90	87	18	S	
7H-3, 74–74	52.44	7		B	Bedding		1	270	95	11	S	
7H-3, 108–108	52.78	8		B	Bedding		0	90	90	6	S	
7H-4	53.2	NIL										
7H-5	54.6	NIL										
7H-6	56.1	NIL										
7H-7	57.5	NIL										
7H-8	58	NIL										
7H-CC	58.4	NIL										
9X-CC	59.9	NIL										
10X-CC, 3.5–4	68.735	1		B	Bedding		6	90	0	6	E	
CC, 18–19	68.88	2		B	Bedding		4	90	333	4	E	
CC, 22–24	68.92	3		B	Bedding		21	270	0	21	W	
12X-1	87.7	NIL										
12X-2	89.2	NIL										
12X-3, 94–96	91.64	1		DS	Dark seams		14	90	345	15	E	Minor faults, welded
12X-4, 66–68	92.86	2		DS	Dark seams		84	270	25	84	W	Minor fault, welded
12X-CC	93.7	NIL										
13P-1	97.6	NIL										
14X-1, 39–43	99.49	1		DS	Dark seams		62	270	146	63	W	
14X-2, 53–54.5	101.13	2		DS	Dark seams		6	90	58	10	E	Cross-laminated
14X-2, 60–60	101.2	3		DS	Dark seams		15	90	37	18	E	
14X-2, 71–72	101.31	4		DS	Dark seams		5	90	74	15	E	
14X-3	102.1	NIL										
14X-CC	103.6	NIL										
15X-1, 28–50	107.48	1		DS	Dark seams		20	270	132	29	S	
15X-1, 28–50	107.48	1		DS	Dark seams		70	90	32	73	E	
15X-2, 55–85	109.25	2		DS	Dark seams		20	270	206	22	W	
15X-2, 55–85	109.25	2		DS	Dark seams		2	90	68	55		
15X-3, 2–9	110.22	3		DS	Dark seams		55	90	29	58	E	
15X-3, 55–65	110.75	4		DS	Dark seams		38	270	188	38	W	
15X-3, 83–88	111.03	5		DS	Dark seams		27	90	350	27	E	
15X-3, 83–88	111.03	5		DS	Dark seams		18	270	152	20	W	
15X-3, 36–38	110.56	8		DS	Dark seams		40	90	45	50	E	
15X-4, 20–26	111.9	6		DS	Dark seams		50	90	337	52	W	
15X-4, 20–26	111.9	6		DS	Dark seams		40	270	157	42	W	
15X-4, 55–65	112.25	7		DS	Dark seams		84	270	193	84	E	
15X-4, 55–65	112.25	7		DS	Dark seams		38	270	155	41	W	
15X-5	113.2	NIL										
15X-CC	114.7	NIL										
16X-1	116.8	NIL										
16X-2, 9–10	118.39	1		B	Bedding		14	270	133	20	S	
16X-2, 129–130	119.59	2		B	Bedding		9	90	318	12	E	
16X-3	119.8	NIL										
16X-CC	121.3	NIL										
17X-1, 135–135	127.85	1		DS	Dark seams		82	270	190	82	W	
17X-1, 135–135	127.85	1		DS	Dark seams		4	270	100	22	S	
17X-2, 30–40	128.3	2		DS	Dark seams		85	90	47	87	S	
17X-2, 30–40	128.3	2		DS	Dark seams		2	90	86	26	S	
17X-3, 110–140	130.6	3		DS	Dark seams		77	270	100	88	S	
17X-4, 132–137	132.32	4		DS	Dark seams		2	270	269	60	N	
17X-4, 132–137	132.32	4		DS	Dark seams		68	270	185	68	W	
17X-5	132.5	NIL										
17X-CC	134	NIL										
19X-1, 24–25	137.34	1		B	Bedding		2	90	304	4	W	
19X-1, 138–145	138.48	2		DS	Dark seams		58	270	132	67	S	
19X-2	138.6	NIL										
19X-3	140.1	NIL										
19X-4, 10–20	141.7	3		DS	Dark seams		80	270	184	80	W	
19X-4, 10–20	141.7	3		DS	Dark seams		2	90	272	45	N	
19X-4, 70–86	142.3	4		Ft	Fault		70	270	183	70	W	Normal fault
19X-5, 75–110	143.85	5		DS	Dark seams		6	270	247	15	N	
19X-5, 75–110	143.85	5		DS	Dark seams		5	270	98	33	S	
19X-5, 75–110	143.85	5		DS	Dark seams		77	90	318	80	E	
19X-6	144.6	NIL										
19X-CC	146.1	NIL										
20X-1	145.8	NIL										
20X-2	147.3	NIL										
20X-CC	148.8	NIL										
21X-1	155.5	NIL										
21X-CC	157	NIL										
22X-1	165.1	NIL										
22X-2, 142–142	168.02	1		B	Bedding		4	90	315	6	E	?
22X-2, 145–145	168.05	1		B	Bedding		12	270	202	13	W	?
22X-3, 34–36	168.44	2		B	Bedding		16	270	166	16	W	Foreset laminae
22X-3, 34–36	168.44	2		B	Bedding		6	270	121	12	S	True bedding

Table 11 (continued).

Core, section, interval (cm)	Depth (mbsf)	X-ref hand sheets	Photo?	ID	Identifier	Thickness (cm)	Core face orientation App. dip	Direction	Corrected Core ref frame Strike	Dip	Dir	Comments
141-860B- (Cont.)												
22X-CC	169.6	3		B	Bedding		17	270	190	17	W	?
23X-CC	174.8	NIL										
24X-1	184.4	NIL										
24X-2, 19–21	186.09	1		B	Bedding		12	90	305	20	N	?
24X-CC, 12–12	187.52	2		B	Bedding		4	90	74	15	S	?
24X-CC, 14–14	187.56	3		B	Bedding		4	90	74	15	S	?
25X-1	194.1	NIL										
25X-2	195.6	NIL										
25X-CC, 5–6	197.1	1		Ft	Fault		37	90	313	48	W	?
28X-1	223.1	NIL										
28X-CC	224.6	NIL										
29X-1	232.8	NIL										
29X-2	234.3	NIL										
29X-CC	235.8	NIL										
30X-1	242.5	NIL										
30X-2	244	NIL										
30X-3	245.5	NIL										
30X-CC	247	NIL										
31X-1, 11–11	252.01	1		B	Bedding?		2	90	86	27	S	
31X-1, 90–90	252.8	2		B	Bedding?		10	90	307	16	N	
31X-2, 19–23	253.59	3		B	Bedding		10	90	62	20	S	
31X-3	254.9	NIL										
31X-CC, 24–24	256.64	4		B	Bedding?		12	90	47	17	S	
32X-1	261.6	NIL										
32X-2	263.1	NIL										
33X-1	271.2	NIL										
33X-2	272.7	NIL										
33X-CC	274.2	NIL										
34X-1, 129–131	282.09	1		PS	Polished surface		50	270	215	56	W	53/331, slick line
34X-2	282.3	NIL										
34X-3	283.8	NIL										
34X-4, 5–10	285.35	3		PS	Polished surface		20	270	223	31	N	8/023, slick line
34X-4, 25–30	285.55	3		PS	Polished surface		19	270	238	33	N	30/359, slick line
34X-CC	286.8	NIL										
35X-1, 77–80	291.17	1		DS	Dark seams		88	270	332	88	W	
35X-1, 77–80	291.17	2		DS	Dark seams		12	270	81	53	S	
35X-CC	291.9	NIL										
36X-1	301.06	1		DS	Dark seams		10	90	58	19	E	
36X-1	301.06	1		DS	Dark seams		14	270	327	16	W	
36X-2	302.06	2		B	Bedding		19	270	62	35	W	
36X-2	302.11	2		DS	Dark seams		6	270	259	28	N	
36X-2	302.17	2		B	Bedding		38	90	39	45	E	
36X-2	302.41	3		DS	Dark seams		19	270	41	25	W	
36X-2	302.41	3		DS	Dark seams		35	90	60	55	E	
36X-2	302.44	3		DS	Dark seams		1	90	86	19	S	
36X-2	302.44	3		DS	Dark seams		11	90	69	31	E	
36X-3	303.1	NIL										
36X-4	304.6	NIL										
36X-CC	306.1	NIL										
37X-1	309.8	NIL										Gravel
37X-2	311.3	NIL										Gravel
37X-3	312.8	NIL										Gravel
37X-4	314.3	NIL										Gravel
37X-CC	315.8	NIL										Gravel
38X-1, 21–24	319.61	1		DS	Dark seams		65	90	350	66	E	
38X-2	320.9	NIL										
38X-3	322.4	NIL										
39X-1, 90–95	329.6	1		PS	Polished surface		23	90	45	73	E	73/136, slick line
39X-2	330.2	NIL										
39X-CC	331.7	NIL										
40X-CC	338.4	NIL										
41X-1, 76–80	348.76	1		B	Bedding		34	270	228	45	E	
41X-2, 25–35	349.75	2		Fr	Fracture		28	90	37	34	E	
41X-3	351	NIL										
41X-4, 55–55	353.05	3		B	Bedding		27	270	211	31	W	
41X-5, 88–92	354.88	4		Fr	Fracture		30	90	17	31	E	
41X-6	355.5	NIL										
42P-1	357.7	NIL										
43X-1	359.2	NIL										
43X-2	360.7	NIL										
43X-CC	362.2	NIL										
45X-CC	376.9	1		B	Bedding		6	90	49	9	S	
46X-1	386.6	NIL										
46X-2, 47–52	388.57	1		PS	Polished surface		40	270	225	50	W	65/336, slick line
46X-CC	389.6	NIL										
47X-CC	396.3	NIL										
48X-1, 20–22	406.2	1		DS	Dark seams		32	270	4	32	W	
48X-1, 23–24	406.23	2		B	Bedding		20	270	122	34	S	
48X-2	407.5	NIL										
48X-3	409	NIL										
48X-4	410.5	NIL										
48X-5, 8–11	412.08	3			Dark seams		87	270	8	33	W	
48X-5, 8–11	412.08	3			Dark seams		53	270	13	54	W	
48X-5, 42–47	412.42	4			Dark seams		86	90	350	84	E	
48X-CC	413.5	NIL										
49X-1	415.7	NIL										
49X-CC	417.2	NIL										
50X-1, 70–90	426	1		Fr	Fracture		12	270	118	25	S	

Table 11 (continued).

Core, section, interval (cm)	Depth (mbsf)	X-ref hand sheets	Photo?	ID	Identifier	Thickness (cm)	Core face orientation App. dip	Direction	Corrected Core ref frame Strike	Dip	Dir	Comments
141-860B- (Cont.)												
50X-1, 116–119	426.46	2		DS	Dark Seam	<0.1	30	90	348	31	E	
50X-1, 133–138	426.63	3		DS	Dark Seam		44	270	211	48	W	
50X-1, 136–138	426.66	4		DS	Dark Seam		12	90	66	28	W	
50X-2, 140–142	428.2	5		DS	Dark Seam	<1	12	270	227	17	N	
50X-3, 0–5	428.3	6		DS	Dark Seam		8	270	104	31	S	These two a set
50X-3, 0–5	428.3	6		DS	Dark Seam		13	90	295	28	N	These two a set
50X-4, 2–5	429.82	7		DS	Dark Seam		50	90	340	52	E	
50X-4, 12–18	429.92	8		DS	Dark Seam		44	90	33	49	E	
50X-5, 53–54	431.83	9		B	Beddimg		10	270	127	16	S	
50X-CC	432.8	NIL										
51X-1	434.8	NIL										
51X-2, 15–30	436.45	1		DS	Dark Seam		38	90	330	42	E	
51X-2, 66–69	436.96	2		DS	Dark Seam		17	270	225	23	W	Bounds lithological package (bed)
51X-3, 30–36	438.1	3		DS	Dark Seam		55	270	162	56	W	
51X-CC	439.3	NIL										
52X-CC	444.4	NIL										
53X-1, 19–21	449.1	1		DS	Dark Seam	0.5	69	90	352	69	E	
53X-2, 49–52	451.09	1		DS	Dark Seam	0.5			32	61	E	
53X-2, 49–50	451.09	2		DS	Dark Seam	0.5			295	44	N	
53X-2, 46–47	451.06	3		DS	Dark Seam	0.5			270	77	N	
53X-2, 53–53	451.13	4		DS	Dark Seam	0.5			28	31	E	
53X-2, 56–48	451.16	5		DS	Dark Seam	0.5			285	61	N	
53X-2, 110–111	451.7	1		DS	Dark Seam	0.5–2			111	23	S	
53X-2, 110–111	451.7	1		DS	Dark Seam	0.5–1			214	35	W	
53X-2, 104–111	451.64	2		DS	Dark Seam	0.5			27	63	E	
53X-2, 105–110	451.65	3		DS	Dark Seam	0.5			265	78	N	
53X-2, 103–111	451.63	4		DS	Dark Seam	0.5			259	78	N	
53X-2, 103–111	451.63	5		DS	Dark Seam	0.5			255	85	N	
53X-2, 103–104	451.63	6		DS	Dark Seam	0.5			220	57	W	
53X-2, 110–113	451.7	7		DS	Dark Seam				26	51	E	42/73, slick line
53X-2, 107–107	451.67	8		DS	Dark Seam	0.5			248	47	N	
54X-CC	453.7	NIL										
55X-CC	463.8	NIL										
56X-CC	473.4	NIL										
57X-CC	483.1	NIL										
58X-1, 9–10	492.89	1		DS	Dark Seam		9	90	331	10	E	
58X-1, 9.5–12	492.895	2		DS	Dark Seam		36	90	326	41	E	
58X-1, 21–21	493.01	3		DS	Dark Seam		7	90	81	37	S	
58X-1, 20–28	493	4		DS	Dark Seam		69	270	151	71	W	
58X-1, 24–28	493.04	5		DS	Dark Seam		82	270	140	84	W	
58X-1, 25–28	493.05	6		DS	Dark Seam		4	90	305	6	N	
58X-1, 36–36	493.16	7		DS	Dark Seam		7	90	286	24	N	
58X-1, 52–53	493.32	8		DS	Dark Seam		1	270	93	17	S	
58X-1, 52–53	493.32	9		DS	Dark Seam		1	270	96	10	S	
58X-1, 80–82	493.6	10		DS	Dark Seam		16	270	263	66	N	
58X-1, 80–82	493.6	11		B	Bedding		16	270	116	34	S	Cross lamina
58X-1, 82–84	493.62	12		DS	Dark Seam		2	90	273	33	N	
58X-1, 86–89	493.66	13		DS	Dark Seam		36	270	112	63	S	
58X-1, 90–93	493.7	14		DS	Dark Seam		35	270	107	67	S	
58X-1, 94–94	493.74	15		B	Bedding		4	90	309	6	N	
58X-1, 97–102	493.77	16		DS	Dark Seam		64	270	128	73	S	
58X-1, 122–125	494.02	17		DS	Dark Seam		42	90	332	46	E	
58X-1, 131–132	494.11	18		DS	Dark Seam		7	270	164	7	W	Parallel to bedding
58X-1, 130–136	494.1	19		DS	Dark Seam		62	90	322	67	E	
58X-2, 123–132	495.53	1		DS	Dark Seam				133	67	S	
58X-2, 127–127	495.57	2		DS	Dark Seam				112	11	S	
58X-2, 128–129	495.58	3		DS	Dark Seam				320	15	E	
58X-2, 127–128	495.57	4		DS	Dark Seam				174	10	W	
58X-2, 124–126	495.54	5		DS	Dark Seam				5	61	E	
58X-2, 128–128	495.58	6		DS	Dark Seam				188	21	W	
58X-2, 126–131	495.56	7		DS	Dark Seam				25	78	E	
58X-2, 103–106	495.33	20		DS	Dark Seam		48	270	146	53	W	
58X-2, 112–113	495.42	21		DS	Dark Seam		12	270	262	55	N	
58X-2, 113–114	495.43	22		DS	Dark Seam		27	90	60	45	S	
58X-2, 117–119	495.47	23		DS	Dark Seam		26	90	50	37	S	
58X-2, 121–122	495.51	24		DS	Dark Seam		46	90	354	46	E	
58X-2, 121–129	495.51	25		DS	Dark Seam		60	270	121	74	S	
58X-2, 126–128	495.56	26		DS	Dark Seam		11	270	200	12	W	
58X-3, 9–12	495.89	27		DS	Dark Seam		47	270	105	75	S	
58X-3, 67–68	496.47	28		DS	Dark Seam		10	270	242	20	N	
58X-3, 68–70	496.48	29		B	Bedding		36	270	166	37	W	
58X-CC, 3–5	497.33	30		DS	Dark Seam		56	90	319	63	E	
59X-CC	502.4	NIL										
60X-1, 13–18	512.13	1		DS	Dark Seam		63	90	341	64	E	
60X-1, 13–18	512.13	1		DS	Dark Seam		78	270	230	82	N	
60X-1, 13–18	512.13	1		DS	Dark Seam		5	270	256	21	N	
60X-2, 68–72	514.18	2		DS	Dark Seam		34	270	176	34	W	
60X-2, 68–72	514.18	2		DS	Dark Seam		8	90	296	18	N	
60X-3, 86–86	515.86	3		DS	Dark Seam		3	90	285	11	N	
60X-4	516.5	NIL										
60X-CC	518	NIL										
61X-1, 21–23	521.91	1		DS	Dark Seam		37	270	240	56	N	Third
61X-1, 21–22	521.91	2		DS	Dark Seam		82	90	62	86	S	First
61X-1, 23–24	521.93	3		DS	Dark Seam		20	270	258	61	N	Third
61X-1, 24–25	521.94	4		DS	Dark Seam		73	270	240	81	N	First
61X-1, 27–33	521.97	5		DS	Dark Seam		42	270	173	42	W	Third
61X-1, 31–32	522.01	6		DS	Dark Seam		8	90	277	48	N	First
61X-1, 33–36	522.03	7		DS	Dark Seam		58	270	190	58	W	Second

Table 11 (continued).

Core, section, interval (cm)	Depth (mbsf)	X-ref hand sheets	Photo?	ID	Identifier	Thickness (cm)	Core face orientation App. dip	Direction	Corrected Core ref frame Strike	Dip	Dir	Comments
141-860B- (Cont.)												
61X-1, 36–37	522.06	8		DS	Dark Seam		6	270	162	6	W	First
61X-1, 39–43	522.09	9		DS	Dark Seam		10	270	249	26	N	Third
61X-1, 23–25	521.93	10		DS	Dark Seam		72	90	11	72	E	First
61X-1, 64–66	522.34	11		DS	Dark Seam		40	270	152	44	W	Third
61X-1, 70–72	522.4	12		DS	Dark Seam		17	270	127	27	S	Third
61X-1, 80–90	522.5	13		DS	Dark Seam		78	270	160	79	W	Second
61X-1, 114–115	522.84	14		DS	Dark Seam		28	270	171	28	W	Third
61X-1, 85–95	522.55	15		DS	Dark Seam		11	270	138	15	W	First
61X-2, 70–72	523.6	16		DS	Dark Seam		2	90	81	12	S	
61X-2, 106–112	523.96	17		DS	Dark Seam		10	270	110	27	S	
61X-2, 106–112	523.96	18		DS	Dark Seam		34	270	195	35	W	
61X-3	524.4	NIL										
61X-4	525.9	NIL										
61X-5	527.4	NIL										
61X-6	528.9	NIL										
61X-7	530.4	NIL										
61X-CC	530.8	NIL										
62X-1, 119–121	532.09	1		DS	Dark Seam	0.1	42	270	189	42	W	Third
62X-2	532.4	NIL										
62X-3	533.9	NIL										
62X-4, 113–116	536.54	2		B	Bedding	0.2–0.5	10	270	197	31	W	
62X-4, 21–27	535.61	3		DS	Dark Seam		12	270	227	17	W	Third
62X-4, 23–29	535.63	4		DS	Dark Seam		45	90	8	45	E	First or second
62X-4, 40–43	535.8	5		DS	Dark Seam		42	90	351	42	E	Third
62X-CC	536.9	NIL										
63X-CC	540.5	NIL										
64X-1, 40–55	550.6	1		DS	Dark Seam		80	270	190	80	W	First
64X-1, 40–55	550.6	2		DS	Dark Seam		62	90	349	62	E	Second
64X-1, 40–55	550.6	3		DS	Dark Seam		31	90	344	32	E	Third
64X-2	551.7	NIL										
64X-3, 91–94	554.11	4		DS	Dark Seam		20	90	304	33	N	
64X-4, 3–7	554.73	5		DS	Dark Seam		35	90	328	40	E	
64X-4, 3–7	554.73	5		DS	Dark Seam		13	90	276	67	N	
64X-4, 43–57	555.13	6		DS	Dark Seam		87	270	210	87	W	First
64X-4, 43–57	555.13	6		DS	Dark Seam		50	270	115	71	S	Second
64X-4, 43–57	555.13	6		DS	Dark Seam		72	270	175	72	W	Third
64X-4, 51–56	555.17	a1		DS	Dark Seam	<1 mm	32	270	150	36	W	
64X-4, 53–57	555.17	A2		DS	Dark Seam	<1 mm	79	270	152	80	W	
64X-4, 53–56	555.17	A3		DS	Dark Seam	<1 mm	48	270	160	50	W	
64X-4, 51–53	555.17	A4		DS	Dark Seam	<1 mm	52	270	153	53	W	
64X-4, 51–53	555.17	A5		DS	Dark Seam	<1 mm	70	270	147	73	W	
64X-4, 51–53	555.17	A6		DS	Dark Seam	<1 mm	87	270	148	87	W	
64X-4, 83–93	555.53	7		DS	Dark Seam	2 mm	57	270	168	58	W	
64X-4, 83–93	555.53	7		DS	Dark Seam		71	270	206	73	W	Second
64X-4, 83–93	555.53	B1		DS	Dark Seam	2 mm	58	270	172	58	W	Second
64X-4, 83–93	555.53	B2		DS	Dark Seam		75	270	174	75	W	Second
64X-4, 83–90	555.53	B3		DS	Dark Seam		74	270	163	75	W	Second
64X-4, 90–93	555.53	B4		DS	Dark Seam		72	270	186	72	W	Second
64X-CC, 6–7	556.26	8		DS	Dark Seam		33	90	316	42	E	
65X-CC	559.9	NIL										
66X-1, 22–32	569.72	1		DS	Dark Seam		46	270	133	57	S	
66X-2, 0–11	571	2		DS	Dark Seam		65	270	154	67	W	
66X-CC	572.5	NIL										
67X-1, 10–15	579.3	1		B	Bedding?		41	90	25	43	E	
67X-1, 54–60	579.74	2		DS	Dark Seam		18	270	117	38	S	
67X-1, 52–54	579.72	A1		DS	Dark Seam		22	270	152	25	W	
67X-1, 54–54	579.74	A2		DS	Dark Seam		4	270	258	18	N	
67X-1, 54–56	579.74	A3		DS	Dark Seam		32	270	153	35	W	
67X-1, 55–55	579.75	A4		DS	Dark Seam		2	270	236	4	N	
67X-1, 56–56	579.76	A5		DS	Dark Seam		26	270	174	26	W	
67X-1, 56–56	579.76	A6		DS	Dark Seam		22	270	138	29	W	
67X-1, 55–56	579.75	A7		DS	Dark Seam		30	270	148	34	W	
67X-1, 70–72	579.9	3		DS	Dark Seam		1	90	284	4	N	
67X-2, 52–52	581.22	4		DS	Dark Seam		41	90	9	41	E	
67X-2, 57–57	581.27	4		DS	Dark Seam		7	90	344	7	E	
67X-2, 53–58	581.23	4		DS	Dark Seam		69	270	148	72	W	
67X-2, 75–77	581.45	5		DS	Dark Seam		13	270	163	13	W	
67X-2, 72–75	591.42	5		DS	Dark Seam		67	90	339	68	E	
67X-2, 70–75	581.4	5		DS	Dark Seam		65	270	181	65	W	
67X-3, 10–20	582.3	6		DS	Dark Seam		66	270	163	67	W	
67X-3, 11–14	582.31	6		DS	Dark Seam		54	90	23	56	E	
67X-3, 15–18	582.35	B1		B	Bedding		46	90	320	54	E	
67X-3, 22–28	582.42	B2		DS	Dark Seam		60	270	128	70	S	
67X-3, 27–28	582.47	B3		DS	Dark Seam		42	90	328	47	E	
67X-3, 21–25	582.41	7		DS	Dark Seam		61	270	154	63	W	
67X-3, 26–26	582.46	7		DS	Dark Seam		30	90	85	82	S	
67X-3, 51–52	582.71	8		DS	Dark Seam	0.5-2	18	270	245	38	N	
67X-3, 64–67	582.84	9		DS	Dark Seam		58	270	130	68	S	
67X-3, 60–65	582.8	9		DS	Dark Seam		30	270	109	60	S	
67X-3, 73–74	582.93	10		DS	Dark Seam		10	270	257	39	N	
67X-3, 78–80	582.98	11		DS	Dark Seam		28	90	53	41	S	
67X-3, 80–84	583	11		DS	Dark Seam		60	270	187	60	W	
67X-3, 83–84	583.03	11		DS	Dark Seam		45	270	147	50	N	
67X-4, 11–14	583.81	12		DS	Dark Seam		50	270	187	50	W	
67X-4, 14–19	583.84	13		Ft	Fault		48	90	8	48	E	
67X-CC	585.2	NIL										
69X-CC	598.4	NIL										
70X-CC	608.2	NIL										

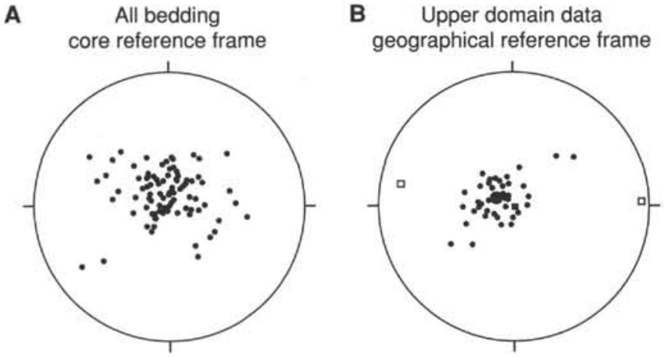

Figure 22. Stereographic projection of poles to bedding at Site 860. (**A**) Uncorrected bedding data in the core reference frame. (**B**) Stereographic projection of poles to bedding (small circles) and normal faults (squares) in the geographic reference frame, for piston cores from the upper domain, where multishot data are available. Large circle shows the vector mean of the poles to bedding.

Table 12. Rotations used to reorient structural data from the core reference frame into the geographic reference frame.

Core	Rotation	Method
141-860B-2H	319°	Tensor
141-860B-3H	004°	Tensor
141-860B-4H	272°	Tensor
141-860B-7H	311°	Tensor

All rotations are around vertical axes and are quoted as clockwise rotations looking down-axis.

141-860B-36X and -37X. Thrusts are required within the intervals where stratigraphic ages are reversed because normal faults alone cannot explain the observed repetitions.

Biostratigraphy constrains the shallower thrust to between 195 and 300 mbsf. This thrust is further constrained between Cores 141-860B-29X and -30X (235.1–242.5 mbsf) by a change in lithostratigraphy (see Lithostratigraphy section, this chapter). A lithostratigraphic repetition, on the scale of several meters, occurs between Cores 141-860B-25X and -28X (196.7–223.1 mbsf), suggesting that a second, less-significant thrust may occur in this interval. Because neither of these postulated thrust surfaces were observed in the cores, it is likely that they lie within the intervals of no recovery.

Biostratigraphic data constrain the deeper thrust to between 305 and 309.8 mbsf (see Biostratigraphy section, this chapter). This location corresponds to a lithostratigraphic repetition (see Lithostratigraphy section, this chapter). Again the thrust is not observed in the recovered cores, either because it is in the 4.8 m of unrecovered core or because the thrust, at its intersection with the borehole, rides on unconsolidated gravels (Core 141-860B-37X, Fig. 10). These gravels could accommodate significant displacement without signs of internal deformation, especially if pore-fluid pressures were high.

The boundary of the thrust stack domain with the broken formation domain corresponds to both an increase in lithification and a lithostratigraphic repetition (see Lithostratigraphy section, this chapter); thus we suggest that this boundary is another thrust surface. The lithostratigraphic repetition is pinned between Cores 141-860B-48X and 141-860B-50X (412 mbsf to 425 mbsf), corresponding exactly to the interval in which discrete, insignificant

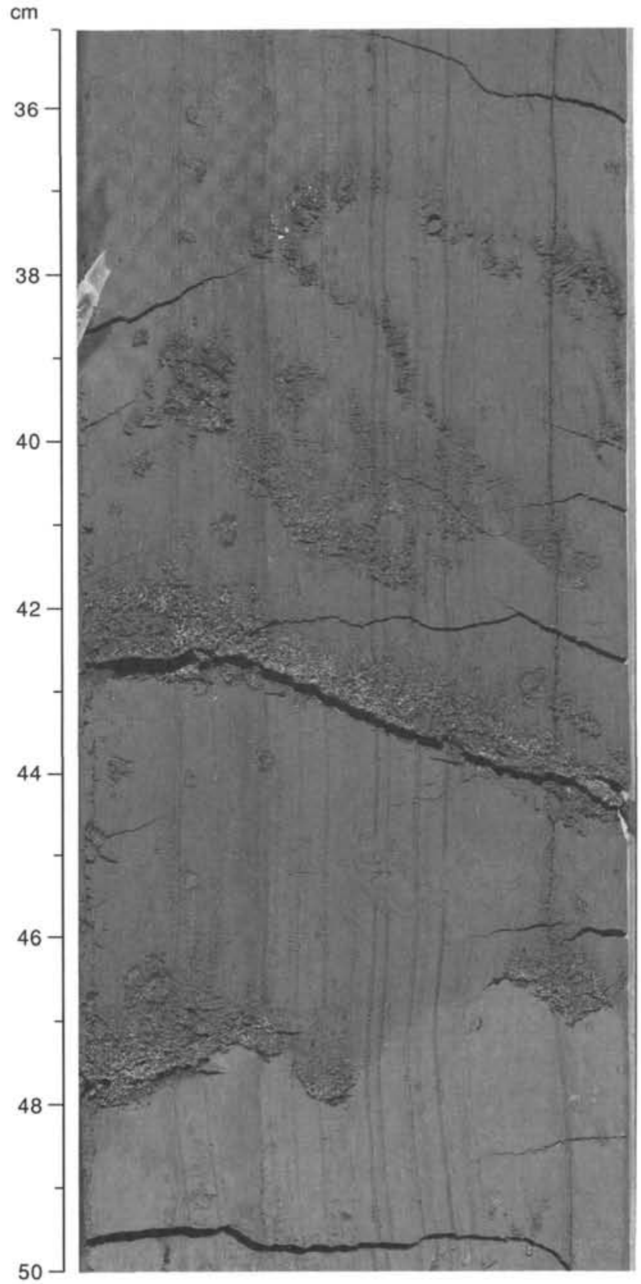

Figure 23. Core photograph, slump fold defined by sand bed in silty claystone. The two graded sand layers under the fold closure may also be part of the lower limb of the slump fold. Interval 141-860A-1H-7, 35–50 cm.

deformation bands give way to intense networks of deformation bands.

Bedding Orientations and Thrust Geometry, Significance and Age

Bedding throughout the upper 420 m of Hole 860B is horizontal to gently inclined (Fig. 22). The lack of steep bedding in the first 420 m of Hole 860B and more specifically, above and below the inferred thrust contacts, indicates that Hole 860B intersected a region of hanging-wall flat on footwall flat (Boyer and Elliot, 1982), or that ramp angles are low (nominally less than 10°).

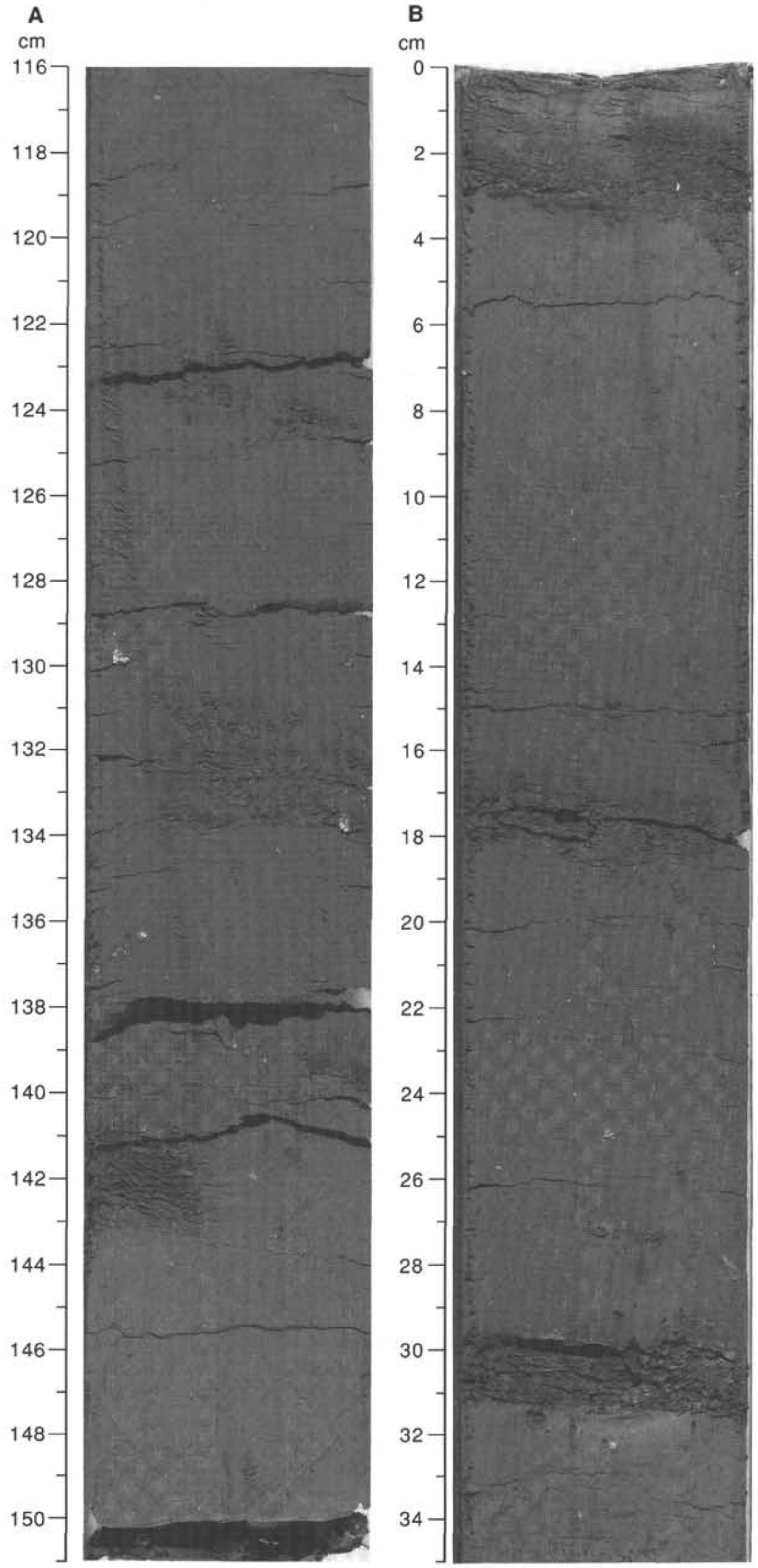

Figure 24. Core photographs, normal fault that offsets silt and sand beds with a separation of at least 12 cm. The fault plane is marked by a zone of dark-gray silt that varies in width on the core face from 2 to 4 mm. Cracks perpendicular to core walls are gas expansion cracks. **A.** Interval 141-860B-3H-6, 116–151 cm. **B.** Interval 141-860B-3H-7, 0–35 cm.

These observations are borne out by comparisons with depth-migrated seismic section 745 (Bangs et al., this volume). The postulated thrust at approximately 240 mbsf corresponds approximately with a flat-lying reflector and the postulated thrust at approximately 420 mbsf corresponds to a very bright flat-lying reflector. No discrete reflector corresponds to the postulated thrust at approximately 310 mbsf. In the vicinity of Site 860, numerous weak reflectors dip shallowly landward, suggesting that the thrust stack is part of a landward-dipping thrust system typical of an accretionary prism (Moore, 1989). The material involved in the thrusting comprises mainly forearc basin sediments that have never been at the toe of the accretionary complex. For this reason it is likely that the thrust system represents an out-of-sequence structure.

The observed stratigraphic repetitions together with shallow ramp angles or flat-on-flat thrust geometry require several hundred meters of thrust displacement. None of the postulated thrusts correspond to significant perturbations in physical properties (see Physical Properties section, this chapter), thus stacking of the inferred thrusts must have been postdated by a period of compaction. The thrusts must represent relatively old, perhaps late Pliocene, deformation. The thrusts correspond to freshwater signatures in pore waters (see Inorganic Geochemistry section, this chapter).

Small-Scale Faults

Steep normal faults occur in intervals 141-860B-14X-1, 39–43 cm, and -15X-3, 3–10 cm, in Core 141-860B-31X, and in Section 141-860B-34X-3. Discrete polished surfaces (less than a millimeter in thickness and spaced 1–20 cm apart) with slickenlines are observed in intervals 141-860B-34X-1, 129 cm, to -34X-4, 30 cm, and -46X-1, 47–52 cm. These surfaces typically have true dips of about 35°, although some are as steep as 55° (Fig. 25). Slickenlines indicate that movement on these surfaces is generally close to dip slip with some surfaces showing oblique slip. No consistent stepping of slickenlines to indicate normal or reverse motion was observed. It is likely that these surfaces are small-scale manifestations of thrusting.

Deformation Bands

Deformation bands (see Site 859 chapter, this volume) are observed in almost every core from Core 141-860B-12X to the base of Hole 860B. In the thrust domain only one or two isolated deformation bands are observed per core, extending for no more than 5–10 cm in length. Deformation bands are manifested on the cut core surface as dark seams, generally of submillimeter thickness with some individual bands up to 2 mm in thickness (Fig. 26). Deformation bands can be extremely complex in geometry: on close examination with a binocular microscope, dark seams that appear to the eye as individual traces can be seen to comprise an anastomosing network of extremely fine seams (Fig. 27).

Thin-section observations reveal variation in the microstructure of deformation bands. Figure 28 shows the microstructure of a steep (true dip 84°) deformation band comprising a 4-mm-wide anastomosing network of dark seams from Interval 141-860B-48X-5, 47-49 cm (this is the same deformation band shown in Figs. 26 and 27). The narrower seams are typical of narrow deformation bands throughout the thrust domain: the grain structure of the host rock is not modified within the band, whereas the matrixes in the deformation band and in the host rock have subtle color differences, indicative of slight differences in mineralogy. Opaque grains are entrained in a few of the narrow seams. In one wide seam (1 to 1.5 mm), the grain fabric of the host rock and the deformation band are quite different (Fig. 28A). The host rock has a weak, bedding-parallel grain alignment that is absent in the deformation band (Fig. 28B). The deformation band contains considerably fewer grains, and those grains present within the band are aligned in subvertical trains although they define no shape fabric. Some of the matrix within the deformation band is aligned: an elongate area of 100 by 10 µm close to and parallel to the margin of the deformation band contains similarly aligned fine phyllosilicates. Color banding parallel to the margins suggests

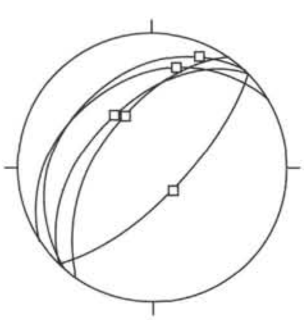

Figure 25. Great-circle projections of polished surfaces with slickenline orientations marked by open squares. All data in the core reference frame.

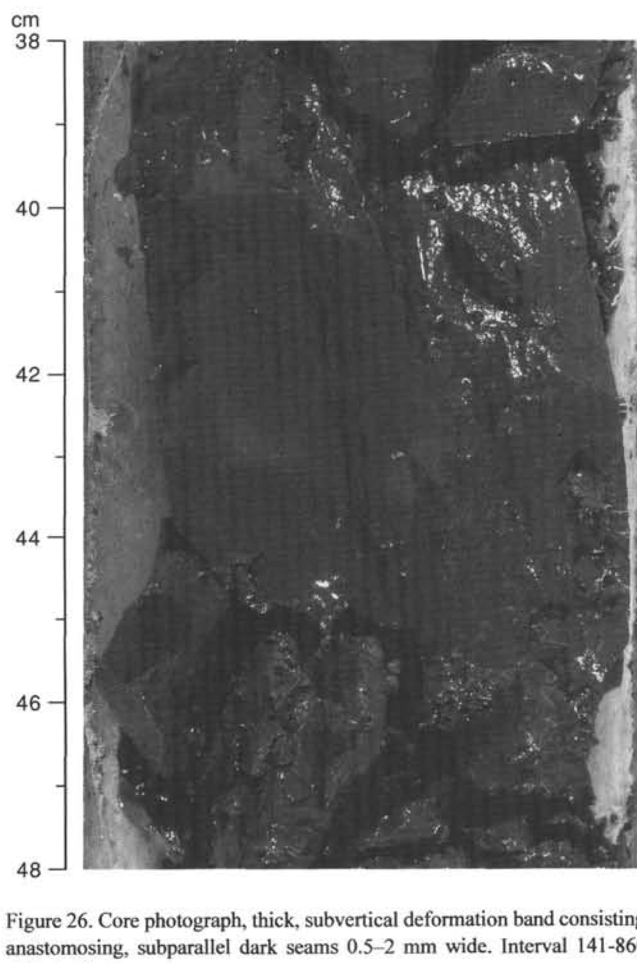

Figure 26. Core photograph, thick, subvertical deformation band consisting of anastomosing, subparallel dark seams 0.5–2 mm wide. Interval 141-860B-48X-5, 38–48 cm.

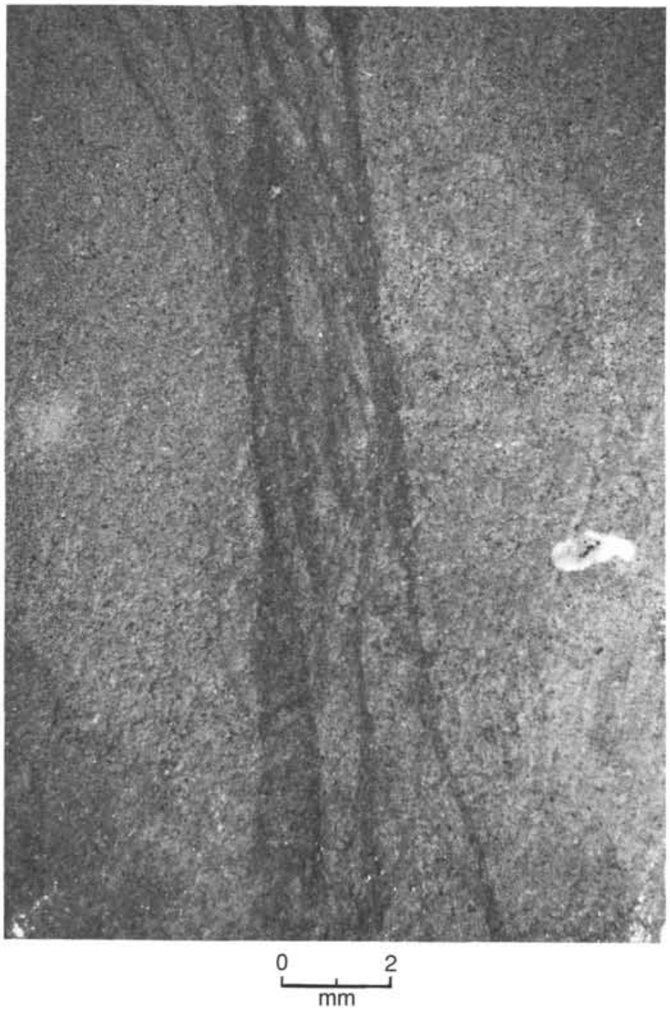

Figure 27. Photomicrograph (binocular microscope) of deformation band in Figure 26, showing the fine-scale anastomosing pattern of individual dark seams. Interval 141-860B-48X-5, 42–44 cm.

internal mineralogical differences in the matrix. One margin of the thick seam of this deformation band is sharp. The other margin is mostly sharp but is gradational over 20 to 50 µm for 100- to 200-µm segments. Sharp boundaries are marked by finer dark seams. The faces of many of the predominantly angular grains in the host siltstone abut these seams (Fig. 28C).

Deformation band orientations measured throughout the thrust domain are plotted in Figure 29. The data are plotted in the core reference frame; although individual measurements are randomly rotated around a vertical axis with respect to each other, the range of dips suggests that no pattern to deformation-band geometry exists within the thrust domain.

Broken Formation

Cores below 420 mbsf exhibit a variety of features suggesting broken formation (Raymond, 1984). These structures consist predominantly of networks of deformation bands that exhibit mesoscopic and microscopic characteristics similar to those in the thrust domain, although typically developed very intensely. Many deformation bands show both normal and reverse offsets that have dismembered original strata into discontinuous phacoids of different lithologies. Primary bedding contacts are not preserved: all lithological boundaries, recognizable as changes in texture and composition, are bounded by deformation bands.

Morphology of Deformation Bands

Deformation bands like those observed in the thrust domain are characteristic of the broken formation. Deformation bands in the broken formation differ from those in the thrust domain in three major characteristics:

1. Deformation bands are found in large numbers in every core in which structures are preserved.
2. Deformation bands generally form complex arrays in which more than one generation of deformation band can be observed (Fig. 30).
3. Individual specimens exhibit more variety in deformation-band morphology, geometry, and size than those in the thrust domain.

Some deformation bands are relatively planar and form conjugate sets (Fig. 30), others develop irregular anastomosing networks. On a small scale, the anastomosing deformation bands are extremely complex, showing self-similarity on the mesoscopic and microscopic scales (Fig. 31). Deformation bands show considerable variation in thickness. Under a binocular microscope an individual seam that can be seen to lie within a given deformation band may vary from 0.1 to 0.5 mm, with a few thicker seams up to 2 mm; the resultant deformation bands vary from 0.1 mm (a single seam) to several millimeters in thickness (Fig. 32).

Many deformation bands show displacements. Reverse and normal separations are observed on the core face (Fig. 32). One deformation band with normal separation in the core face (interval 141-860B-53X-2, 106–112 cm) has slickenlines indicating oblique slip. In no other case is the slip vector constrained, even within the core reference frame. Observed separations are generally a few millimeters or less. A lithologic layer in interval 141-860B-53X-2, 106–112 cm, is displaced at least 60 mm by a deformation band with normal separation. In one example (interval 141-860B-53X-2, 103–112 cm) where a steep deformation band, with reverse separation, bifurcates upward, the sum of separations of the two higher strands matches the total separation across the lower single strand. Where a fossil or small pebble is truncated by a deformation band (Fig. 33), it is found only on one side of the deformation band. In other cases deformation bands anastomose around small pebbles (Fig. 31).

Some deformation bands serve as boundaries to areas of different texture, composition, and color (Figs. 33, 34, and 35). These surfaces are not bedding, but are tectonic surfaces that slice off or terminate lithologies to produce phacoids.

Some relatively thick (ca. 2 mm) deformation bands lack anastomosing patterns on the mesoscopic or microscopic scale. These tend to have true dips between 10° and 60° and typically form structural breaks in the core. In isolation these structures would be regarded as faults. Here they have many mesoscopic and microscopic characteristics in common with deformation bands and are included in this family of structures. A thick planar deformation band in Figure 35 (interval 141-860B-64X-4, 85–93 cm) shows contrasts between the footwall and hanging-wall deformation. In the hanging wall, at least three ages of deformation bands form a complex interlocking network with a millimeter-to-submillimeter spacing of individual bands. In contrast, the footwall is dominated by a single set of deformation bands at a shallow angle to the main deformation band, with a centimeter-scale spacing. The footwall is also characterized by a shape fabric subparallel to the footwall deformation band set.

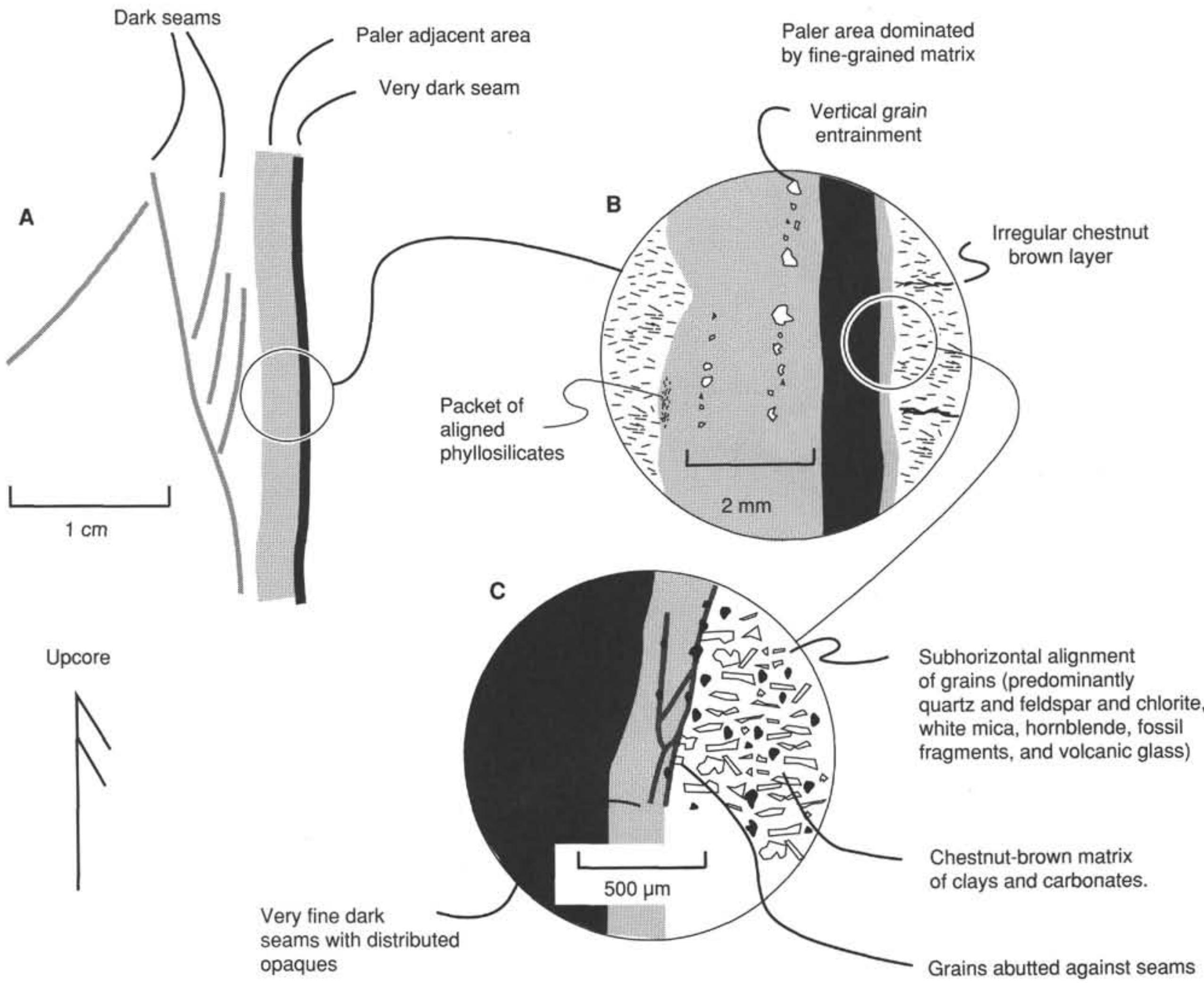

Figure 28. Sketches from a thin-section of a deformation band from interval 141-860B-48X-5, 42–44 cm. **A.** Geometry of seams that comprise deformation bands within the thin section. The thinner seams on the left are characterized by a change in matrix color. There is no grain or matrix alignment in these, except in one case where elongate ore grains fill the seam. **B.** The larger seam truncates a subhorizontal bedding fabric. The seam is characterized by fewer grains than the host rock and contains one very dark seam where the matrix is much darker. The few grains in the wide seam are entrained parallel to the seam walls. **C.** At the right-hand margin, fine anastomosing dark seams contain irregular ore grains. Some of the host grains abut these seams.

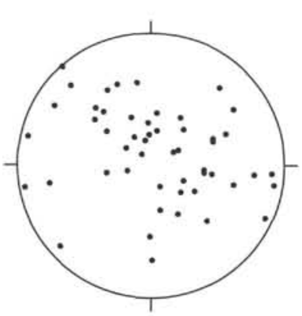

Figure 29. Stereographic projection of poles to deformation bands within the thrust domain at Site 860. Core reference frame.

Microstructure of Deformation Bands and their Relationship to Cementation and Mineralization

The number of deformation bands successfully thin sectioned so far is small, and the data set incomplete. Some deformation bands observed in thin section have the same characteristics as the majority of those observed in the thrust domain: a change in matrix color is the only contrast with the host rock. In many cases, however, deformational fabrics are observed in deformation bands.

The thick deformation band shown in Figure 35 (interval 141-860B-64X-4, 85–93 cm) is characterized microscopically by a zone of matrix that contrasts in color with the surrounding material and contains grains aligned to the walls of the deformation band (Figs. 36B and 36D). Fine phyllosilicates of the matrix are also aligned parallel to the deformation band walls. Very fine bands of matrix phyllosilicate alignment are developed at about 40° to the deformation band boundaries, dipping the same direction and more shallowly than the band itself (Fig. 36B). These are

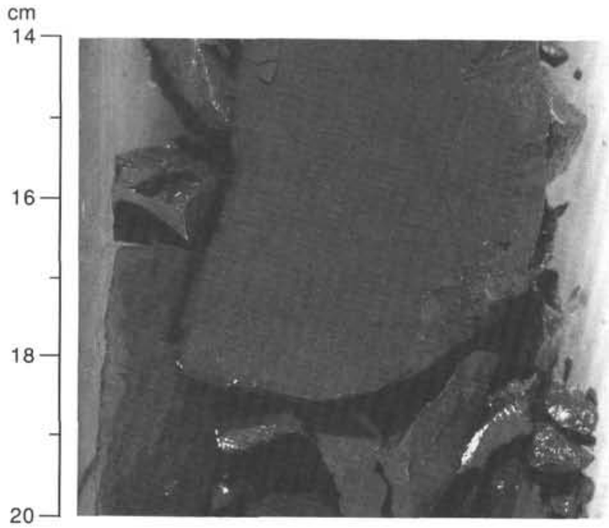

Figure 30. Core photograph, network of at least three generations of deformation bands. The earliest generation is subhorizontal and defines lithologic boundaries; the middle generation consists of a steeply inclined conjugate set of bands; and the youngest generation consists of a steeply inclined conjugate set of bands that offsets both the middle and older generations. Interval 141-860B-60X-1, 14–20 cm.

spaced 0.5 to 1 mm and in one case, phyllosilicates aligned to the deformation band walls are bent into alignment with the shallower, spaced structure indicating a reverse separation (Fig. 36D) that is extensional with respect to the phyllosilicate allignment. The spaced structures have the geometrical characteristics of Riedel I shears (Logan, et al., 1979), indicating that this deformation band accommodates reverse motion.

The anastomosing set of deformation bands in the hanging wall to the thick deformation band comprises 100- to 200-µm-wide zones of grain and matrix phyllosilicate alignment separating phacoidal domains of varying fabric intensity, style, and orientation (Figs. 36B, 36C).

In the binocular microscope, the fabric in the footwall of this deformation band can be seen to comprise a weak grain-shape component coupled to sub-0.1-mm zones in which the fabric is more intense; many of these deformation bands contain stringers of fine pyrite. One zone in which fabric is more intense cuts a millimeter-size pebble and gives rise to a 0.5-mm reverse separation (Fig. 37). A thin section from interval 141-860B-64X-4, 90–92 cm, shows that the fabric is defined by the alignment of angular grains, very similar to those observed in similar lithologies without a fabric. Zones of more intense deformation are characterized by alignment of phyllosilicates in the matrix, and by inequant grains (Figs. 36E, 36F). Grains are concentrated in the zones of more intense deformation fabric. Grain-grain contacts are observed, including quartz-quartz, calcite-calcite, and quartz-calcite. Neither indentation nor suturing are observed at these contacts.

Locally, zones of color changes in host rock are developed adjacent to the deformation bands. Cross-cutting the deformation bands, and possibly localized along their intersections, are sparsely distributed pyrite vugs. Parts of the surrounding sediment are also characterized by widely disseminated pyrite that cements the host rock grains, and pyrite-filled fractures within large clasts. Clusters of fine framboids up to 15 mm in size also occur, and may be rimmed up to 3-mm-thick by intergrown quartz and chlorite with a sub-0.1-mm grain size. Rarely, pyrite and quartz

Figure 31. Detail of anastomosing deformation bands from a steep set with reverse separations in interval 141-860B-53X-2, 103–112 cm. These are the latest deformation bands in this interval.

are localized along the deformation bands; for example, Sections 141-860B-50X-3, -53X-2, and -62X-3.

Orientation of Deformation Bands

Indiscriminant analysis of deformation-band orientations suggests that overall they are randomly oriented (Fig. 38). However, our observations suggest that in individual specimens or discrete intervals a chronology of deformation bands can be established and each phase within this chronology has a characteristic orientation and sense of displacement. Deformation-band orientations were recorded wherever possible during initial core description. The problem in correlating structures between cores, sections, and even intervals within sections is that in the XCB coring used in this part of Hole 860B, rotation of different intervals around the vertical axis is likely. However, most recovered intervals contain a suite of deformation bands with two or more distinct orientations and a characteristic deformation history. Thus we can correlate deformation bands between neighboring intervals that have undergone rotations relative to each other and can rotate the deformation bands of one interval into close alignment with those of an adjoining interval. To do this we pick the phase of deformation bands that varies least in orientation and rotate these bands to the best fit with correlative bands in the second interval. The

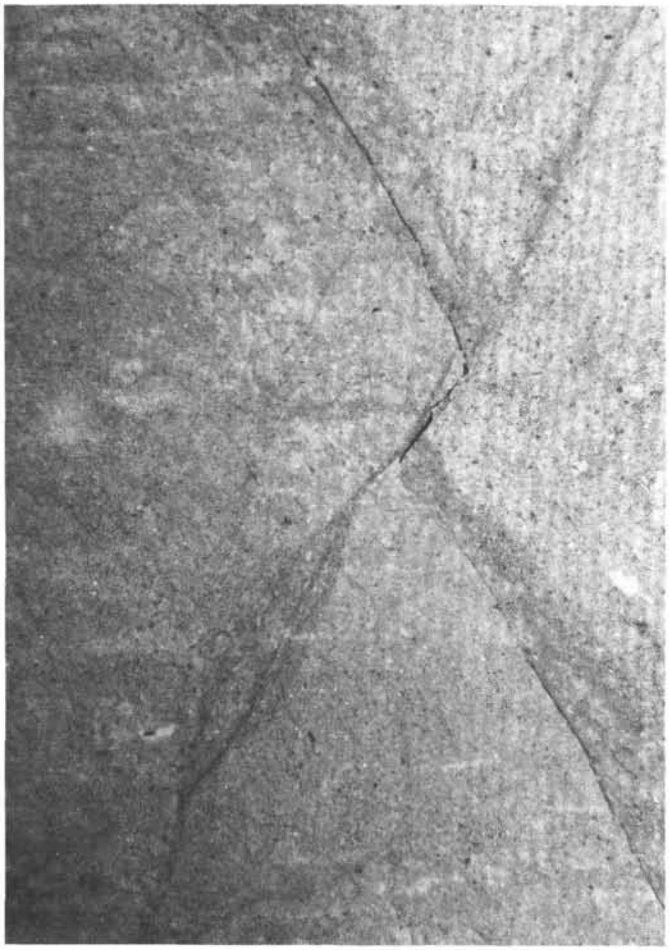

Figure 32. Detail of reverse separation on a steep deformation band (top right to bottom left) from interval 141-860B-53X-2, 103–112 cm. This is part of the latest set of deformation bands in this interval and links upward to the more obviously anastomosing bands shown in Figure 31. The offset deformation band (top middle to bottom right) has a normal separation in excess of 60 mm and is of the middle generation of deformation bands in this specimen.

Figure 33. Detail of steep deformation bands in interval 141-860B-64X-4, 83–93 cm. These are the dominant set of deformation bands in the hanging wall of the thick planar deformation band shown in Figure 35. A fossil (*Quinqueloculina*(?) sp.) is truncated against one seam of the deformation band array.

other phases of deformation bands in both intervals are subjected to the same rotation. All rotations are made around a vertical axis.

Careful analysis of stereonet data coupled with observations of deformation-band chronology and style allows six domains of relatively coherent structural chronology and geometry to be defined in the broken formation between 420 mbsf and the base of Hole 860B at 617.8 mbsf.

Domain A (420–520 mbsf) is defined on the basis of coherent intervals 141-860B-53X-2, 49–55 cm, and 103–112 cm, -58X-1, 1–42 cm, and 58–95 cm, and -58X-2, 111–137 cm. The orientations in the core reference frame for each interval are shown in Figure 39. The earliest deformation bands have shallow true dips (Fig. 40). They are only slightly anastomosing but significant variation in orientation of individual deformation bands occurs on either side of a later cross-cutting deformation band. The early flat-lying deformation bands are postdated by steep deformation bands with normal separations. One slickenline measurement (Fig. 39B) indicates oblique slip. A small number of the second-phase deformation bands have an apparently conjugate orientation relative to the majority (Fig. 40). The intersection of the two apparently conjugate sets is close to the orientation of the slickenline. The second-phase deformation bands form discrete planes up to 1.5 mm thick. Dark seams anastomose within these planes, but the deformation bands do not form an anastomosing network. The latest deformation bands form a steep anastomosing (Fig. 31) network with reverse separations (Fig. 32). The latest phase occurs only in the upper part of the domain. All data have been rotated into the reference frame of interval 141-860B-53X-2, 49–55 cm, using the second phase of deformation bands. The relative rotations for each interval are given in Table 13. The rotated data are shown in Figure 41. The data for each deformation phase fall into well-constrained orientations, whereas the combined data give an overall random distribution. Isolated measurements that could not be related to a local chronology in Cores 141-860B-50X, -51X, -60X, and the remaining parts of Core 141-860B-58X (Fig. 42) are compatible with inclusion in Domain A.

Domain B (520–530 mbsf) is defined on the basis of coherent intervals 141-860B-61X-1, 20–50 cm and 64–95 cm. The orientations in the core reference frame for each interval are shown in Figure 43. The earliest deformation bands have shallow true dips. They are only slightly anastomosing, but their orientation varies significantly for individual deformation bands on either side of a later cross-cutting deformation band. The flat-lying deformation

Figure 34. Detail of a complex anastomosing set of deformation bands separating phacoids of different lithologies in interval 141-860B-64X-4, 47–57 cm.

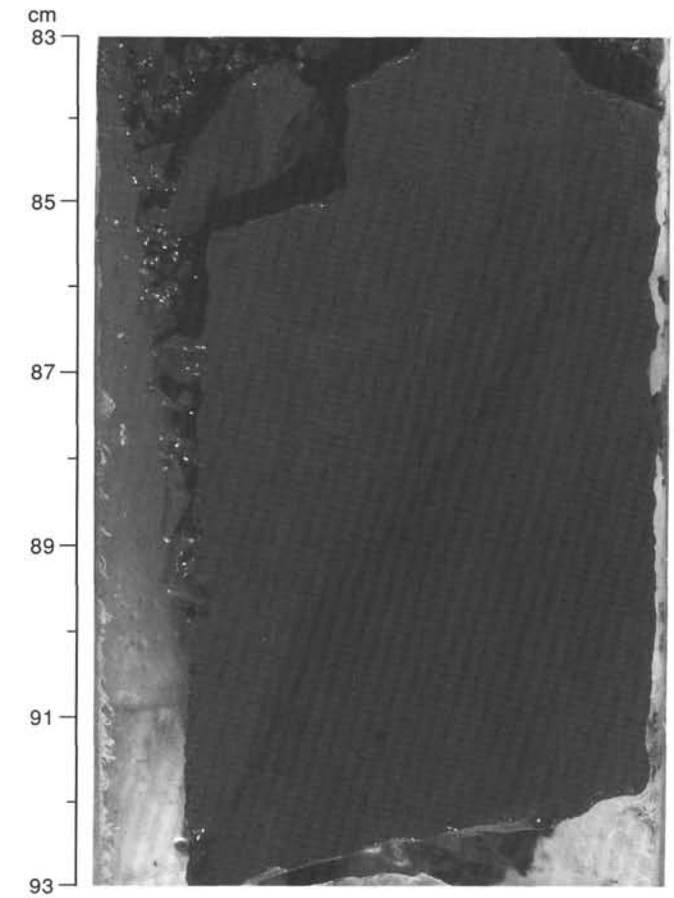

Figure 35. Core photograph, a major deformation band/fault (top right to bottom left) that separates contrasting structural styles in the footwall and hanging wall of interval 141-860B-64X-4, 83–93 cm. Deformation bands juxtapose different lithologies (light above dark) along a contact slightly steeper than the main deformation band. The contact is truncated by the deformation band at 91 cm. The hanging wall is characterized by a strongly anastomosing set of deformation bands subparallel to the major band. Earlier steep deformation bands form a 2- to 3-mm-thick array 15 mm to the right and subparallel to the lithologic boundary. Deformation bands are steep and widely spaced in the footwall, becoming a little more intense further from the main deformation band.

bands are postdated by steep, irregular deformation bands with reverse separations. The latest deformation bands form a shallow anastomosing network that dominates the structure of this domain (Fig. 44). Matching displaced features across the latest set of deformation bands is problematic. Some tenuous links suggest that separations are in the reverse sense. The data from interval 141-860B-61X-1, 64–95 cm, have been rotated into the reference frame of interval 141-860B-61X-1, 20–50 cm, using the latest phase of deformation bands. The relative rotation is given in Table 13. The rotated data are shown in Figure 45. These data give a relatively simple picture, dominated by the latest, flat-lying phase of two deformation bands. Isolated measurements which could not be related to a local chronology in interval 141-860B-61X-1, 70 cm, through -62X-1, 121 cm (Fig. 46), are compatible with inclusion in Domain B.

Domain C (530–550 mbsf) is defined on the basis of coherent intervals 141-860B-62X-4, 21–116 cm, and -64X-1, 40–55 cm. The orientations in the core reference frame for each interval are shown in Figure 47. The earliest deformation bands form steep anastomosing planes 2–10 mm thick that can be traced for up to 15 cm in the core (Fig. 48). The discrete deformation bands that make up these planes have rather shallower true dips but the bands are too small to measure. The second phase-deformation bands are steep with mixed normal and reverse separations. Rare conjugate sets are observed. The latest deformation bands form a shallow anastomosing network (Fig. 48) with mixed normal and reverse separations. The data from interval 141-860B-64X-1, 40–55 cm, have been rotated into the reference frame of interval 141-860B-62X-4, 21–116 cm, using the latest phase of deformation bands. The relative rotation is given in Table 13. The rotated data are shown in Figure 49.

Domain D (550–579 mbsf) is defined on the basis of coherent intervals 141-860B-64X-4, 47-57 cm and 83–93 cm. The orientations in the core reference frame for each interval are shown in Figure 50. Two phases of steep deformation bands are cut by a moderately to steeply dipping anastomosing network with reverse separations, which dominates the structure of this domain. The earliest deformation bands form steep anastomosing planes 2–10 mm thick that can be traced for up to 10 cm in the core. There are two distinct morphologies of the latest set of deformation bands: intense anastomosing networks (Figs. 34, 35) and thick (up to 2 mm) planar surfaces (Fig. 34). The planar deformation band in interval 141-860B-64X-4, 85-93 cm, has been described in detail in the morphology and microstructure sections. Thick, planar

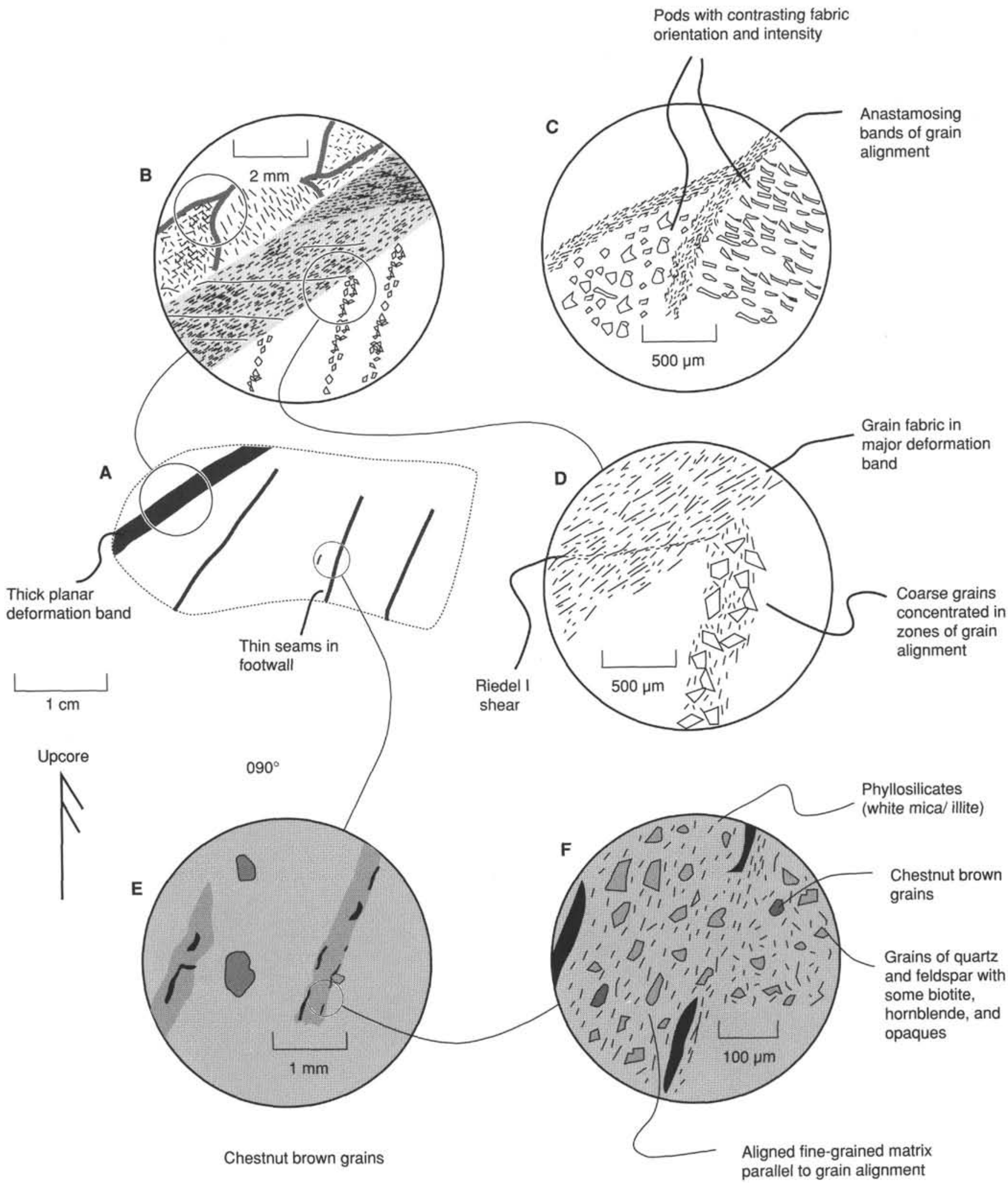

Figure 36. Sketches from a thin section of the thick deformation band from interval 141-860B-64X-4, 83–93 cm (see Figs. 33, 35 and 37). **A.** General view to show main deformation band and discrete deformation band in the footwall. **B.** Main fabric and Riedel I shears in the main deformation band. The hanging wall is characterized by anastomosing deformation bands separating phacoids of different lithology and fabric. Zones of fabric intensification, often associated with planes where grains are larger, are shown in the footwall. **C.** Fabric in hanging wall deformation bands. **D.** Riedel I shear in main deformation band and zone of fabric intensification in the footwall. **E.** Relationship of footwall deformation bands to elongate ore phases and large clasts of chestnut brown cement. **F.** Close-up view of footwall deformation band showing strong fabric within an area of weaker fabric.

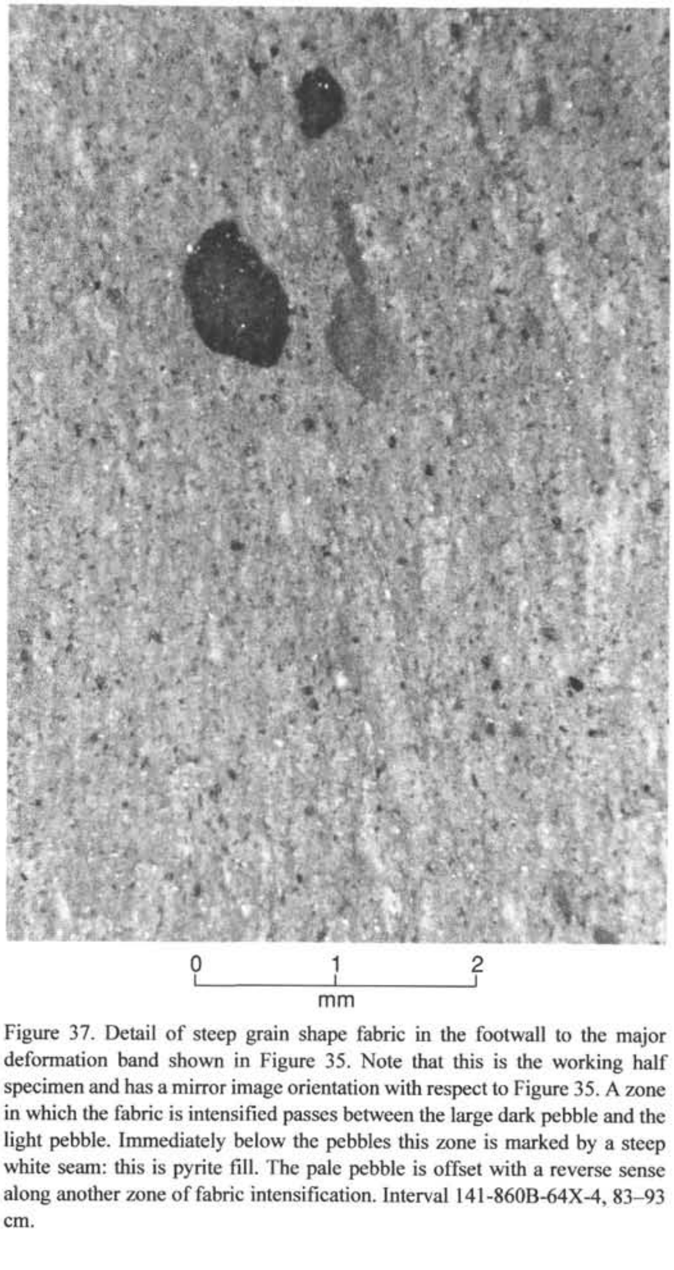

Figure 37. Detail of steep grain shape fabric in the footwall to the major deformation band shown in Figure 35. Note that this is the working half specimen and has a mirror image orientation with respect to Figure 35. A zone in which the fabric is intensified passes between the large dark pebble and the light pebble. Immediately below the pebbles this zone is marked by a steep white seam: this is pyrite fill. The pale pebble is offset with a reverse sense along another zone of fabric intensification. Interval 141-860B-64X-4, 83–93 cm.

deformation bands often separate zones in which the anastomosing deformation bands are developed with different intensity. The data from interval 141-860B-64X-4, 83–93 cm, have been rotated into the reference frame of interval 141-860B-64X-4, 47–57 cm, using the latest phase of deformation bands. The relative rotation is given in Table 13, and the rotated data are shown in Figure 51. These data give a relatively simple picture, dominated by the latest phase of deformation bands. Isolated measurements that could not be related to a local chronology in Section 141-860B-64X-3, the remainder of Section 141-860B-64X-4, and Core 141-860B-66X (Fig. 52), are compatible with inclusion in Domain D.

Domain E (579.7 mbsf) is defined on the basis of coherent interval 141-860B-67X-1, 54–60 cm. All the deformation bands in this interval are shallow (Fig. 53) and form a very intense anastomosing network. No coherent age relationships can be established. No clear separations are observed to define reverse or normal movement sense.

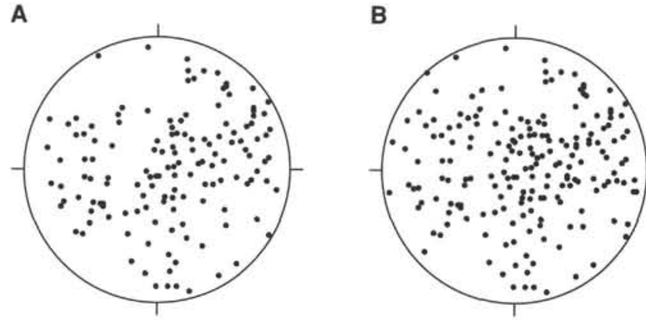

Figure 38. Stereographic projection of poles to deformation bands, in the core reference frame, at Site 860. **A**. Data from the broken formation only. **B**. All data.

Domain F (580–618+ mbsf) is defined on the basis of coherent intervals 141-860B-67X-2, 52–75 cm, and -67X-3, 10–26 cm. The orientations in the core reference frame for each interval are shown in Figure 54. The earliest deformation bands have shallow and steep true dips and are cut by a moderately dipping set with mixed normal and reverse separations. The third phase of deformation bands is flat-lying with reverse separations. The latest phase is an apparently conjugate set with mostly reverse separations and a few normal separations. The data from interval 141-860B-67X-3, 10–26 cm, have been rotated into the reference frame of interval 141-860B-67X-2, 52–75 cm, using the second phase of deformation bands. The relative rotation is given in Table 13. The rotated data are shown in Figure 55. The data for each deformation phase fall into well constrained orientations. These combined data show a strike common to most of the deformation bands. Isolated measurements that could not be related to a local chronology in interval 141-860B-67X-3, 10–26 cm (Fig. 56), are compatible with inclusion in Domain F.

Significance of Deformation Bands: Forearc Basin Shear Zones

The domains defined by analysis of deformation band geometry and chronology are summarized in Figure 57. They fall into two broad categories:

1. The structure is dominated by deformation bands with a common strike, so that deformation associated with deformation bands must approximate to plane strain if there is no volume loss. Domains B, C, D and E all show plane-strain characteristics. Most of these domains have a distinct asymmetry suggesting a significant component of simple shear, the most extreme cases being domains B and E, which are dominated by a single set of shallow deformation bands.
2. A more complex structure involving deformation bands in all orientations is observed in domains A and F and must represent a more generalized non-plane-strain deformation. The complex meshwork of deformation bands seen in domains A and F provides enough potential surfaces to satisfy the Von Mises criterion for general volumetric deformation.

Although individual deformation bands accommodate little strain, large strains and displacements can be accommodated by the cummulative effect of a large number of deformation bands, particularly where the deformation bands accomodate overall simple shear. An interpretation of the geometric domains inferred from deformation bands, is that domains B, C, D, and E represent a broad simple-shear zone in which large displacements are localized on domains B and E. Domains A and F represent blocks of material undergoing the more complex volume deformations necessary to allow large displacements on the zones of simple shear.

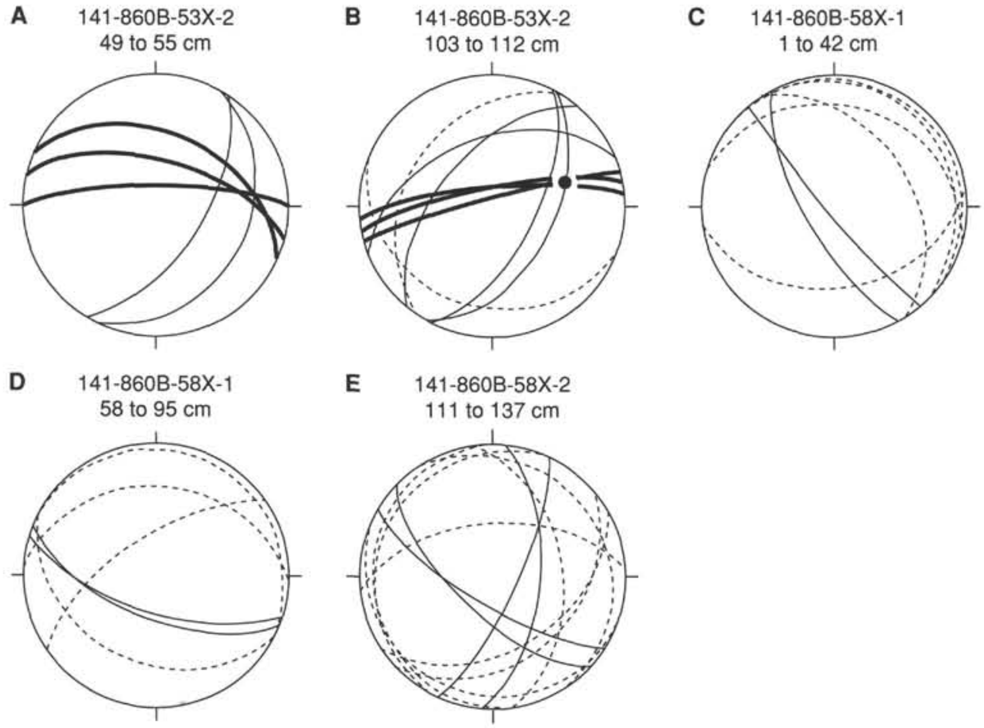

Figure 39. Stereographic projections of deformation bands in all coherent intervals within Domain A, plotted in the reference frame for each individual interval. Deformation bands are represented as great circles. Earliest deformation bands are shown as dashed lines, middle bands as solid lines, and latest deformation bands as bold lines. In (**B**) the black dot represents the slickenline orientation on one of the middle generation of deformation bands.

The structural data suggest major shear zones at 520–530 mbsf and at 580 mbsf, with a zone of broad simple-shear between them. Presence of the upper shear zone is supported independently by a possible lithological repetition between Cores 141-860B-58X and -64X (see Lithostratigraphy section, this chapter). Evidence from discrete separations on the dominant set of deformation bands in domains B, C, and D suggests that shearing is in a thrust sense.

Domains within the broken formation are mechanically detached from each other by shear zones, and hence have different deformation histories and geometries. Contrasts in hanging wall and footwall structures across some individual deformation bands provide small-scale examples of mechanical detachment.

Domains C and D show some continuity of structure. The differences in discrete chronology probably reflect heterogeneities within the broad simple shear zone. It is notable that most of the thick planar deformation bands interpreted as accommodating larger displacements are observed in domains C and D. These may be high strain-rate zones that accommodate the linkage between the two high-strain (and presumably, high strain rate) bounding shear zones. As such, the thick deformation bands approximate to various forms of Riedel shear (Logan et al., 1979).

Volume deformation in broken formation on a meshwork of planes satisfying the Von Mises criterion has been suggested by Agar (1989), in an example where the movement surfaces required are progressively developed during back rotation in an accretionary complex and then reactivated. Site 860 penetrates a forearc basin where a complex accretionary history is not possible and the patterns of deformation bands observed must have been developed in situ.

The intimate relationship of deformation bands with matrix modification and mineralization suggests that deformation and fluid flow are linked processes. Deformation bands described from Site 860 have a variety of morphologies and geometries. Irregular and planar deformation bands with differences in matrix composition but not fabric are similar to "vein structures" described by Lundberg and Moore (1986) from accretionary complexes, Pickering et al. (1990) from a forearc basin, and Lindsley-Griffin et al. (1990) from a number of forearc environments. Deformation bands with entrained grains are similar to those described by Knipe (1986) and Kemp (1990). Deformation bands with varying degrees and orientations of grain alignment have been described by a number of authors using the terms shear bands (Taira, Hill, Firth, et al., 1991; Byrne et al., in press; Maltman et al., in press), kinks (Lundberg and Moore, 1986) and deformation bands (Karig and Lundberg, 1990). A full microstructural study is required to assess the mechanism paths and conditions associated with the development of the various types of deformation bands observed at Site 860 and to determine how these structures relate to the flow of fluid.

Folds and Faults Caused by Drilling Disturbance

Some striking features that could be interpreted as natural structures are believed to be due to drilling disturbance or to the processes of pulling and saving the core. Examples are the apparent diapir, bulls-eye folds, and transposed bedding in the interval 141-860B-4H-4, 60 cm, to -CC, 45 cm, and the clastic "dike" in Section 141-860B-5H-4. Many of the features can be identified as drilling-related because in a cross section of the core, the banding or contacts defining these structures are curved subparallel to the core liner.

Faults and fractures that offset drilling biscuit boundaries are interpreted as the product of deformation within the core barrel. These features can be recognized only if they crosscut demonstrable drilling disturbance, as in the examples shown in Figure 58. Because these unquestioned examples of post-drilling structures have orientations similar to many of the fractures in other cores,

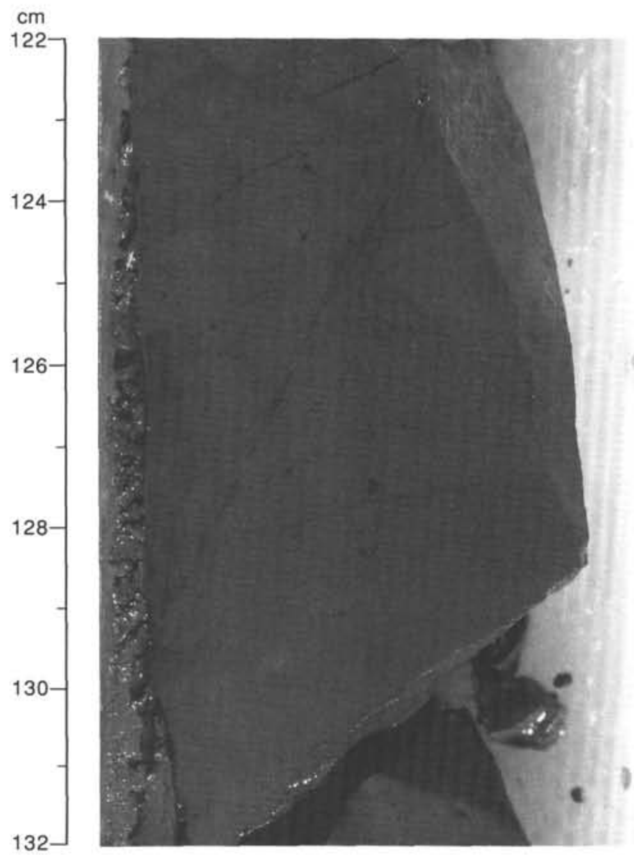

Figure 40. Typical geometry and morphology of deformation bands in the lower part of structural Domain A. Nearly flat-lying set of earliest deformation bands is crosscut by conjugate steep bands with normal separations. Interval 141-860B-58X-2, 122–132 cm.

Table 13. Rotations used to reorient structural data into single coherent orientations for Domains A to F of the broken formation.

Domain	Interval rotated 141-860B-	Reference frame interval 141-860B-	Magnitude of clockwise rotation
A	53X-2, 49–55 cm	53X-2, 103–112 cm	6°
A	58X-1, 1–42 cm	53X-2, 103–112 cm	−125°
A	58X-1, 54–95 cm	53X-2, 103–112 cm	34°
A	58X-2, 111–137 cm	53X-2, 103–112 cm	−22°
B	61X-1, 64–95 cm	61X-1, 20–50 cm	57°
C	64X-1, 40–55 cm	62X	172°
D	64X-4, 47–57 cm	64X-4, 83–93 cm	−21°
F	67X-3, 10–26 cm	67X-2, 52–75 cm	11°

all orientation data on open faults and fractures should be evaluated with caution. Faults and fractures that are lithified or are themselves cut by drilling biscuit boundaries are probably pre-drilling structures. It is not clear whether polished surfaces with slickenlines can be formed by drilling disturbance, but such features should also be interpreted with caution.

ORGANIC GEOCHEMISTRY

Shipboard organic geochemical analyses of sediments from Holes 860A and 860B included chromatography of volatile hydrocarbon and nonhydrocarbon gases, organic matter fluorescence estimation, total hexane soluble lipid/bitumen analysis, and

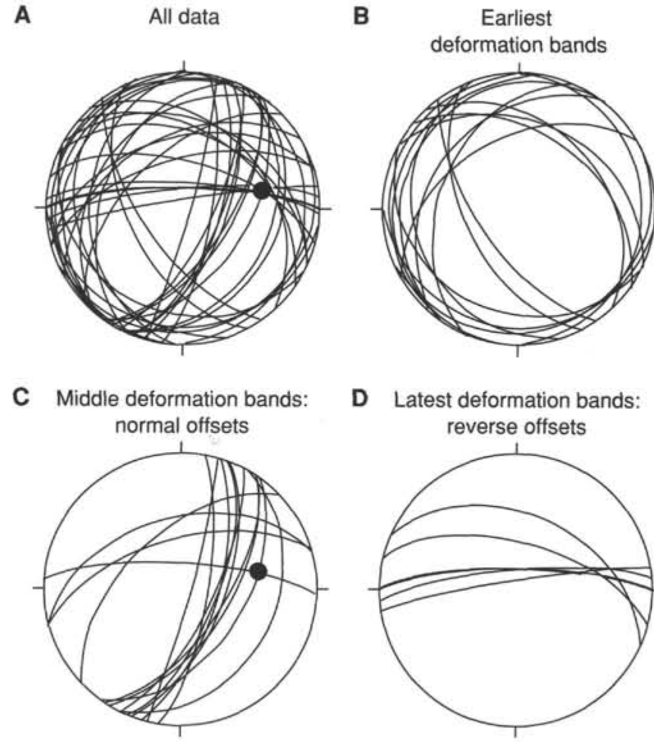

Figure 41. Stereographic projections of deformation bands in all coherent intervals within Domain A rotated into the reference frame of interval 141-860B-53X-2, 49–55 cm. Deformation bands are represented as great circles. In **C**. the black dot represents the slickenline orientation on one of the middle generation of deformation bands.

Rock-Eval analysis. The instrumentation, operating conditions, and procedures are summarized in the Explanatory Notes chapter (this volume).

Volatile Gases from Sediments

Volatile gases (hydrocarbons, CO_2, H_2S, N_2, O_2) released by the sediments recovered at Site 860 were continuously measured by gas chromatography as part of the shipboard safety and pollution monitoring program. We used the headspace technique, in which a sediment plug is heated in a sealed vial to drive off gases (Emeis and Kvenvolden, 1986). The results are listed in Table 14 and illustrated in Figure 59. The methane concentrations in the headspace volumes range between 1 and 67,863 ppm (v/v). In the uppermost part, methane increased steeply from 1 ppm at 1.1 mbsf to 12236 ppm at 15.3 mbsf. Ethane and higher hydrocarbons up to C_7 (heptane) were also detected. The downhole profiles for headspace ethane and propane are also shown in Figure 59. Both compounds were absent at sub-bottom depths shallower than 160 mbsf, below which ethane appeared and increased with sub-bottom depth to above 100 ppm at 250 mbsf. Below 250 mbsf propane was detected; it increased slightly with sub-bottom depth whereas ethane concentrations remained roughly constant. The overall gas contents of these sediments as determined by headspace analysis were found to range from 0.001 to 0.452 cm^3 of methane per cm^3 of sediment, with the predominant gas being methane. No H_2S was detected in the samples collected at this site.

Two zones with different volatile gas characteristics were observed: an upper zone (5.8 to about 220 mbsf) where the gases consist predominantly of methane with small amounts of ethane and a general composition consistent with a biogenic origin; and,

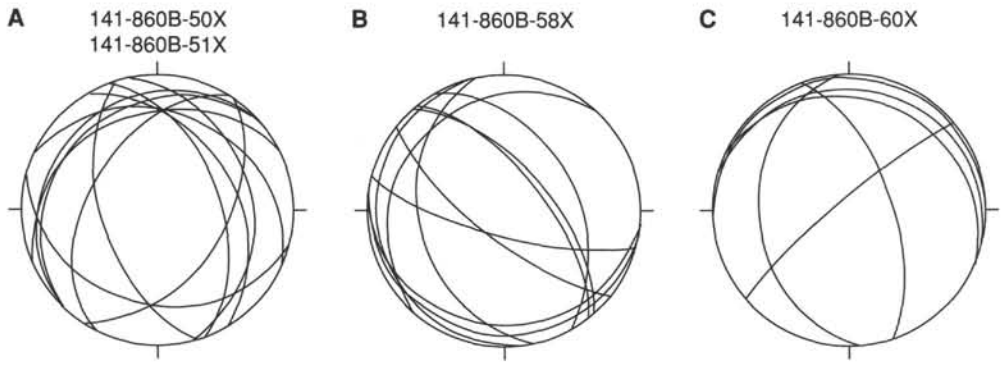

Figure 42. Stereographic projections of unconstrained deformation bands assigned to Domain A. These are isolated measurements where the timing of the deformation bands within the local chronology cannot be established. Deformation bands are represented as great circles.

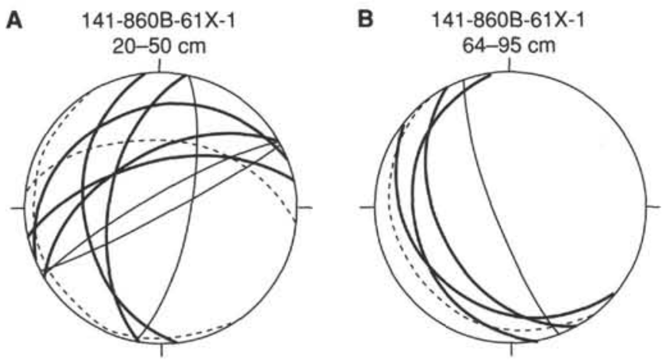

Figure 43. Stereographic projections of deformation bands in all coherent intervals within Domain B, plotted in the reference frame for each individual interval. Deformation bands are represented as great circles. Earliest deformation bands are shown as dashed lines, middle bands as solid lines, and latest deformation bands as bold lines.

a lower zone (about 220 to 608.3 mbsf) where, in addition to methane and ethane, small amounts of heavier hydrocarbons (C_3 to C_7) were observed, which suggests a contribution of thermogenic hydrocarbons.

Methanogenic bacteria are generally active after complete sulfate depletion by sulfate-reducing bacteria (Claypool and Kaplan, 1974). The sulfate content in interstitial waters is relatively low throughout Hole 860B with almost complete sulfate depletion observed around the 15–55 mbsf interval (see Inorganic Geochemistry section, this chapter). Therefore, environmental conditions for methanogenesis via CO_2 reduction, the major process by which microbial methane is produced in deep-sea sediments, were probably favorable for biogenic methane generation in the sedimentary column.

Organic matter maturation in the lower zone indicates that local thermal maturity would be too low to generate heavier and thermogenic hydrocarbons, and so thermogenic hydrocarbons are most likely of migrational origin from deeper sources in the accretionary prism (see below).

Carbon dioxide was present at concentrations up to 2395 ppm in gases desorbed from the sediments by the headspace method (Table 14). Even higher amounts of free CO_2 could have been present in the sediments and pore waters prior to the depressurization that occurs during core retrieval. Large fluctuations in CO_2 concentration were observed throughout the sequence of recovered sediments, suggesting possible alterations due to drilling fluid contamination (sea water) degassing during depressurization and core sectioning and air contamination at sample introduction in headspace containers.

Fluorescence

The extract colors progressed from intense yellow, to pale yellow, and finally to faint yellow with increasing sub-bottom depth. The fluorescence of the extracts was orange-red for the upper 10 mbsf of the hole, and was yellow to light yellow down to about 200 mbsf, where it turned blue-white. The concentrations of extractable organic matter are low, based on their color, fluorescence intensities, and the relative intensities of chromatograms of extractable organic matter (see below). Yellow fluorescence is interpreted to indicate incipient thermal maturation of bitumen to the mature stage, and white (or blue-white fluorescence) has been associated with mature and overmature bitumen enriched in polynuclear aromatic hydrocarbons (PAH) (Shipboard Scientific Party, 1982).

Gas in Core Expansion Voids

After retrieval on deck, gas expansion voids were observed in the core-liner contained core. The gas was sampled directly from the gas voids by piercing the core liner with a sampling needle and collecting the gases in pre-evacuated vacutainers. Upon chromatographic analysis the expansion void gases (EVG) were found to contain hydrocarbons in the C_1 to C_7 range with a composition somewhat different from the gases isolated by headspace analysis (Table 15 and Fig. 60).

EVG hydrocarbon contents were found to be significantly higher (up to 970,142 ppm v/v; 97.0 % vol.) than headspace gas and presented different gas ratios for equivalent depths. Due to higher gas concentrations, EVG gas allows a better detection of heavier hydrocarbons (C_3 plus), but headspace analysis gives lower C_1/C_2 ratios. Thus Site 860 gas analyses for an equivalent depth range (160 to 560 mbsf) gave C_1/C_2 ratios from 13510 to 321 for the EVG gas, whereas C_1/C_2 levels of only 5744 to 49 were obtained for the same interval by the headspace analyses. This difference is most likely due to different gas fugacities and degassing processes occurring during core retrieval, and the inevitable air exposure of headspace samples, which results in a preferential loss of methane and so a decrease of the C_1/C_2 ratio in the headspace gases. Simultaneously, the gas released in the core is enriched in methane and will give consistently higher C_1/C_2 ratios. These differences have importance for the drilling safety criteria as C_1/C_2 or C_1/C_3 ratios as analyzed on board are method-dependent. Therefore, different safety limits should be established for data based on headspace and core-liner gas analysis.

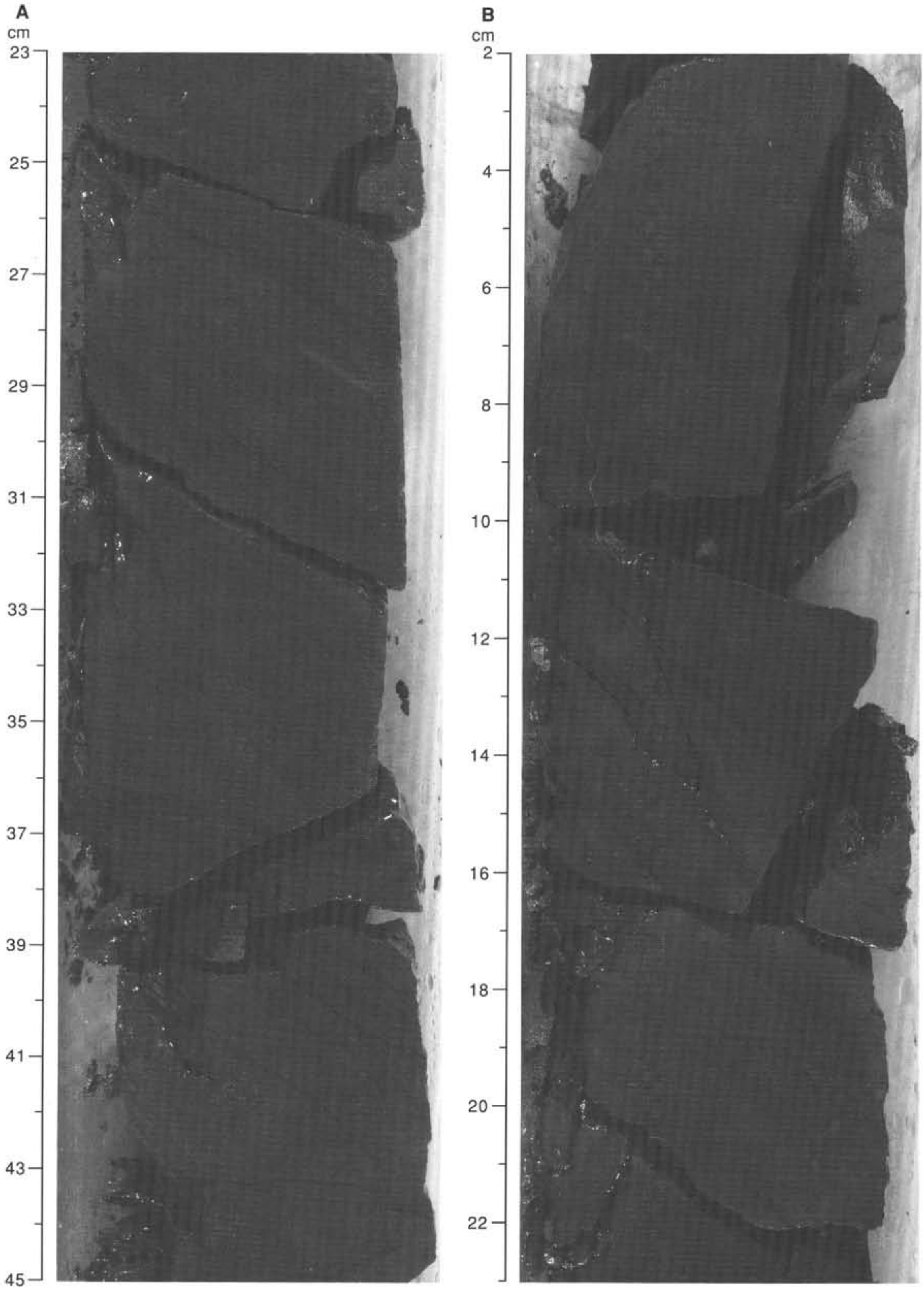

Figure 44. Core photographs, typical geometry and morphology of deformation bands in structural Domain B. The oldest, nearly flat-lying deformation bands are crosscut by a steeper set of bands with reverse separations. These are cut by a third set of shallow anastomosing deformation bands, with individual bands commonly attaining 2 to 3 mm thickness. This latest set of deformation bands dominates the structure of Domain B. **A.** Interval 141-860B-61X-1, 23–45 cm. **B.** Interval 141-860B-61X-2, 2–23 cm. Note that these are photographs of the working half.

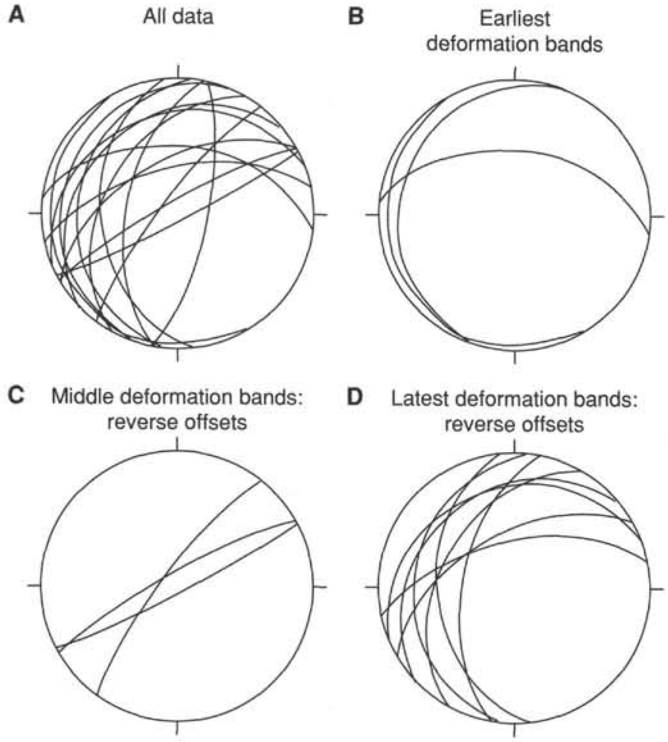

Figure 45. Stereographic projections of deformation bands in all coherent intervals within Domain B, rotated into the reference frame of interval 141-860B-61X-1, 20–50 cm. Deformation bands are represented as great circles.

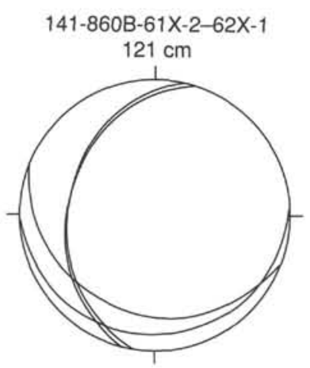

Figure 46. Stereographic projections of unconstrained deformation bands assigned to Domain B. These are generally isolated measurements where the timing of the deformation bands within the local chronology cannot be established. Deformation bands are represented as great circles.

Consistently, and in spite of these compositional differences, two distinct EVG zones can also be observed: an upper layer down to about 195 mbsf of predominantly biogenic gas composed almost exclusively of methane with high C_1/C_2 ratios (2021 to 131,271), and a deeper layer from about 280 mbsf downward containing a gas with somewhat higher ethane content and small but significant amounts of C_3-plus compounds (up to 217 ppm v/v at 529.2 mbsf). Several samples in the deeper layer contain heavier hydrocarbons extending up to C_7 (heptane) well within the natural gasoline range. Exceptionally high *n*-butane and C_6+ concentrations compared to other compounds were detected at 89.5, 101, 282.9, and 330.9 mbsf and high *i*-pentane concentrations were detected in the interval from 108 to 167.3 mbsf. The origin of those compounds is currently unknown. In both head-

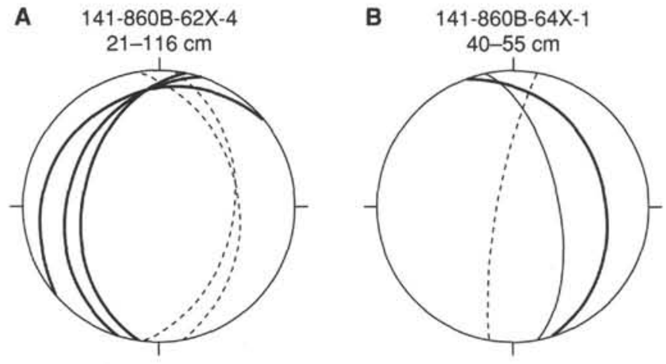

Figure 47. Stereographic projections of deformation bands in all coherent intervals within Domain C, plotted in the reference frame for each individual interval. Deformation bands are represented as great circles. Earliest deformation bands are shown as dashed lines, middle bands as solid lines and latest deformation bands as bold lines.

space and expansion void gas analysis the carbon range cutoff is at C_7, and is determined by the chromatographic conditions and the volatility of the heavier hydrocarbons under sampling and handling conditions. The presence of heavier hydrocarbons was confirmed by organic extraction analysis (see below).

Bitumen Analyses and Organic Matter Characterization

The hexane extracts (500 µL) of the samples from the fluorescence assessment were concentrated under a stream of helium to about 10–40 µL. These concentrates were analyzed by high-resolution gas chromatography and examples of traces are shown in Figure 61. The dominant compound series in the total extracts are hydrocarbons ranging from *n*-C_{15} to *n*-C_{36} with pristane ($C_{19}H_{40}$) and phytane ($C_{20}H_{42}$) as the major isoprenoid alkanes. The extractable organic matter from the sediments of Site 860 has in general a bimodal distribution with two relative maxima. The first group of hydrocarbons, which ranges up to C_{24}, has a maximum at about C_{20} with an unresolved complex mixture (UCM) of branched and cyclic compounds typical of autochthonous marine bitumen derived from alteration of microbial lipids (Simoneit, 1977, 1978). The second group, composed of hydrocarbons >C_{24} maximizing at about C_{33}, corresponds to hydrocarbons derived from terrestrial plant wax influx and represents the contribution of land-derived organic matter.

On the basis of the characteristics of the organic matter, the sedimentary sequence can be divided in two sections: an upper unit (0 to about 220 mbsf) where relatively comparable amounts of marine and terrigenous organic inputs were observed, and a lower unit where the terrigenous organic input is predominant in the range 220–550 mbsf, with a slight increase of the marine input toward the bottom of the hole at 550–600 mbsf.

In general, the *n*-alkanes >C_{26} have a significant predominance of homologues with odd carbon numbers (carbon preference index, CPI>1.0; Table 16), typical of immature organic matter (Simoneit, 1977, 1978). The value of the carbon preference index decreases with geothermal maturation, approaching values of CPI≈1 for crude oils and mature organic matter. For the samples of Site 860 the CPI had to be calculated for the range C_{26}-C_{35} because in some samples *n*-C_{25} coelutes with a contaminant that was found to be more abundant in samples taken from split cores and is most likely associated with core-liner plasticizer and plastic-derived contaminants derived from the core liner. Even if care was taken to collect sediment samples as close as possible to the center of the core, liner-derived plastic contaminants can be incorporated during drilling and core splitting.

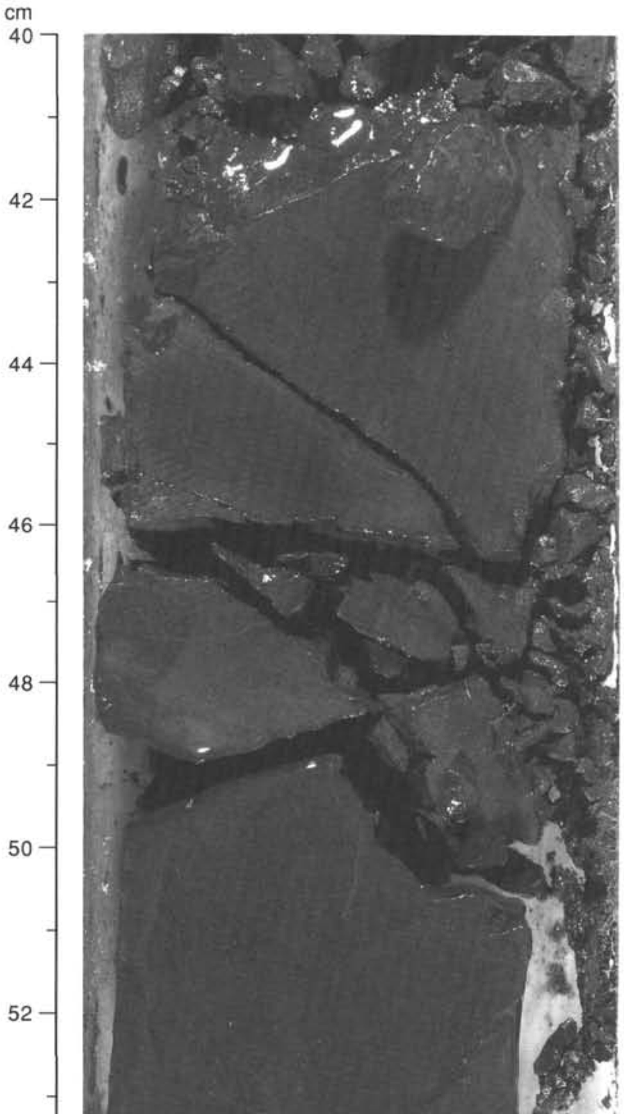

Figure 48. Core photograph, typical geometry and morphology of deformation bands in structural Domain C. The oldest deformation bands form a 2- to 3-mm thick array running from the center of the core at 42 cm to the left hand side at 57 cm. The individual bands that make up the array are shallower than the array as a whole. The steep array is crosscut by steep deformation bands, oriented top left to bottom right, with mixed reverse and normal separations. These are cut by shallower deformation bands oriented from top right to bottom left. Interval 141-860B-64X-1, 40–58 cm.

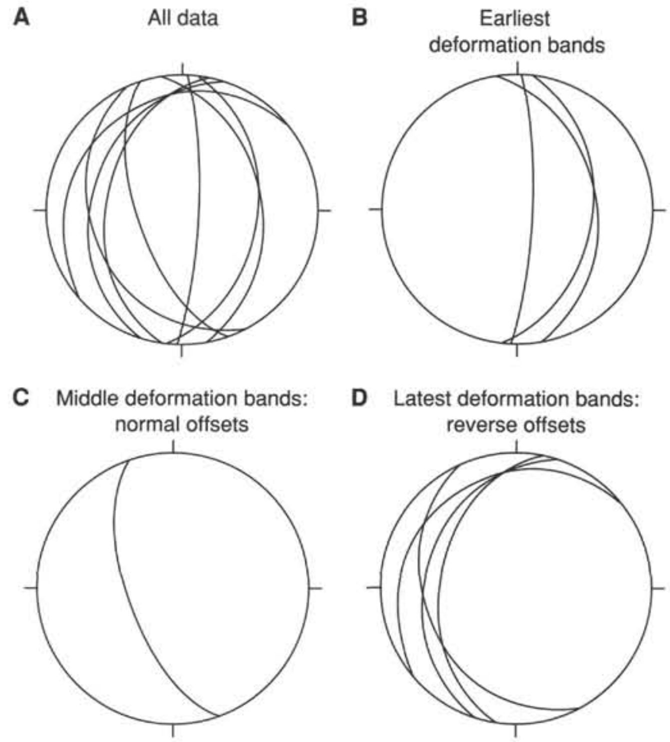

Figure 49. Stereographic projections of deformation bands in all coherent intervals within Domain C, rotated into the reference frame of interval 141-860B-62X-4, 21–116 cm. Deformation bands are represented as great circles.

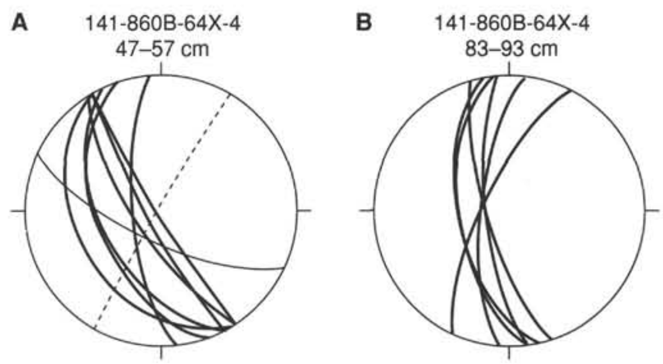

Figure 50. Stereographic projections of deformation bands in all coherent intervals within Domain D; plotted in the reference frame for each individual interval. Deformation bands are represented as great circles. Earliest deformation bands are shown as dashed lines, middle bands as solid lines, and latest deformation bands as bold lines.

The organic matter for Site 860 has an overall CPI trend that shows a low degree of geothermal maturity with higher CPI values in the upper portion of the drilled section and a moderate decrease with sub-bottom depth consistent with a gradual increase in maturation (Table 16). Superimposed on this low maturational background, some significant anomalies were detected at 90.5, 290.6, and 598.5 mbsf, which show the presence of significantly more mature hydrocarbons (with CPI about 1) emplaced in sediments of a lower degree of maturation (CPI>2) as illustrated by the paired Samples 141-860B-12X-2, 132–135 cm (CPI =1.0), and 141-860B-10X-CC, 0–3 cm (CPI = 4.79); and 141-860B-

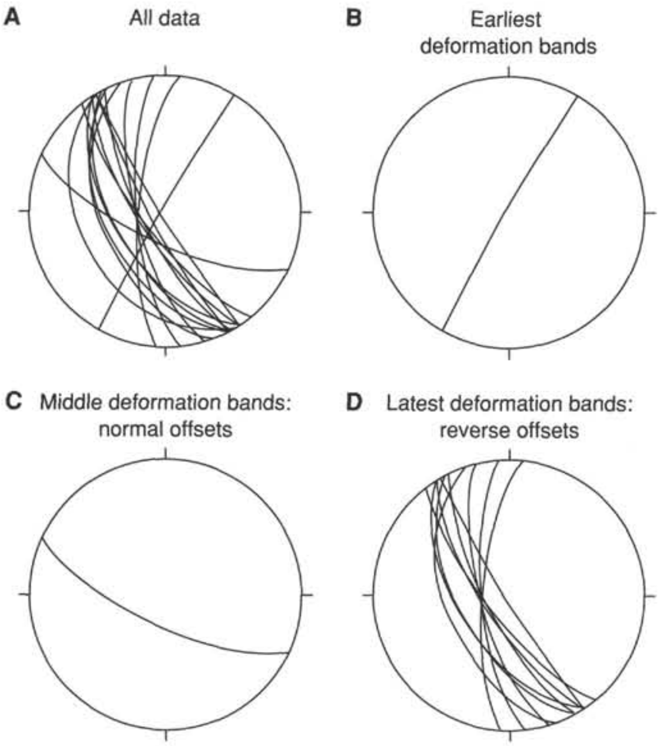

Figure 51. Stereographic projections of deformation bands in all coherent intervals within Domain D, rotated into the reference frame of interval 141-860B-64X-4, 47–57 cm. Deformation bands are represented as great circles.

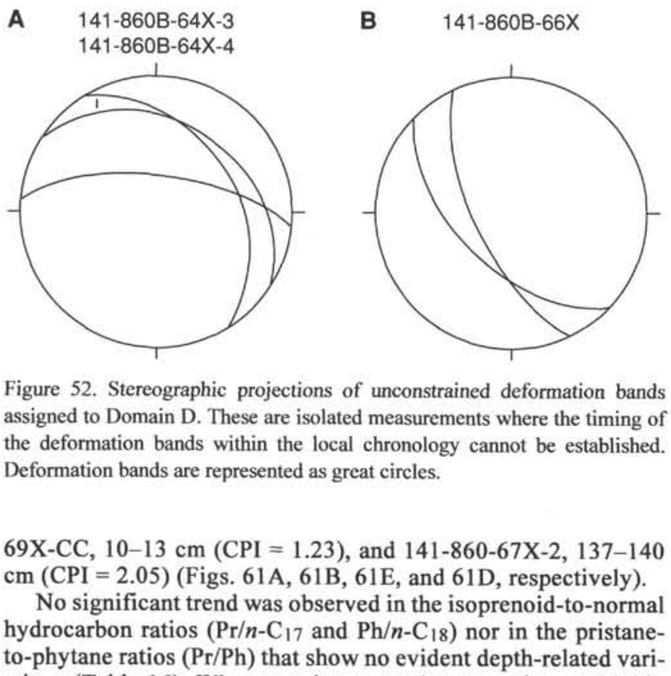

Figure 52. Stereographic projections of unconstrained deformation bands assigned to Domain D. These are isolated measurements where the timing of the deformation bands within the local chronology cannot be established. Deformation bands are represented as great circles.

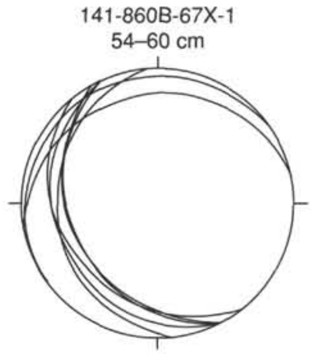

Figure 53. Stereographic projections of deformation bands in all coherent intervals within Domain E, plotted in the core reference frame. Deformation bands are represented as great circles.

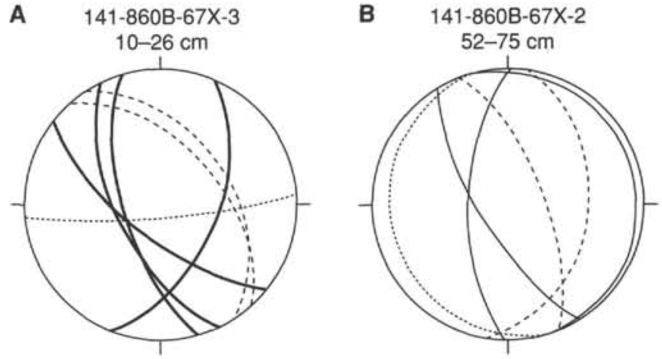

Figure 54. Stereographic projections of deformation bands in all coherent intervals within Domain F, plotted in the reference frame for each individual interval. Deformation bands are represented as great circles. Earliest deformation bands are shown as dotted lines, second generation as dashed lines, third generation as solid lines, and latest deformation bands as bold lines.

69X-CC, 10–13 cm (CPI = 1.23), and 141-860-67X-2, 137–140 cm (CPI = 2.05) (Figs. 61A, 61B, 61E, and 61D, respectively).

No significant trend was observed in the isoprenoid-to-normal hydrocarbon ratios ($Pr/n\text{-}C_{17}$ and $Ph/n\text{-}C_{18}$) nor in the pristane-to-phytane ratios (Pr/Ph) that show no evident depth-related variations (Table 16). Whereas pristane to phytane ratios are highly formation-dependent (Farrington et al., 1988), they have been reported to be an indicator responding to maturation (Simoneit et al., 1981), as well as an indicator of anoxic conditions of sedimentation (Didyk et al. 1978).

Analysis of gases released in the core liner as well as gases released from sediments by headspace analysis indicated the presence of gasoline-range hydrocarbons up to C_7, the upper limit of detection of the chromatographic conditions and calibration of the natural gas analyzer. The presence of gasoline-range hydrocarbons was also corroborated by the extraction analyses which show that hydrocarbons up to C_{12}, well in the natural gasoline carbon atom range, can be observed on the solvent elution peak when contrasted with the solvent extraction blank. The relative amount of gasoline-range hydrocarbons is lower in the upper sedimentary units, increasing with sub-bottom depth, and is indicative of an increased thermal stress and/or the existence of a deeper-located source of thermogenic hydrocarbons.

The actual nature of this deeper source of thermogenic hydrocarbons could be related to a conventional slowly matured hydrocarbon source or, alternatively, the thermogenic hydrocarbons could be generated by a high-temperature energy source (Simoneit et al., 1981) and/or by petroleum hydrocarbon generation by the action of hydrothermal fluids upon immature sedimentary organic matter (Didyk and Simoneit, 1989).

Organic Content and Type of Organic Matter

Because the NCS analyzer was inoperable during Site 860 operations, the content of total organic carbon (TOC) in the sediments was measured by means of the Rock-Eval pyrolysis technique (Espitalié et al., 1977). TOC values were found to be relatively low except for the uppermost sediments (0.2–1 mbsf) that have higher values (1.59%–1.74%). TOC contents of most samples range from 0.2% to 0.5% and show no trend related to depth (Table 17 and Fig. 62). Sediments at 51.3, 109.7, 253.7, and

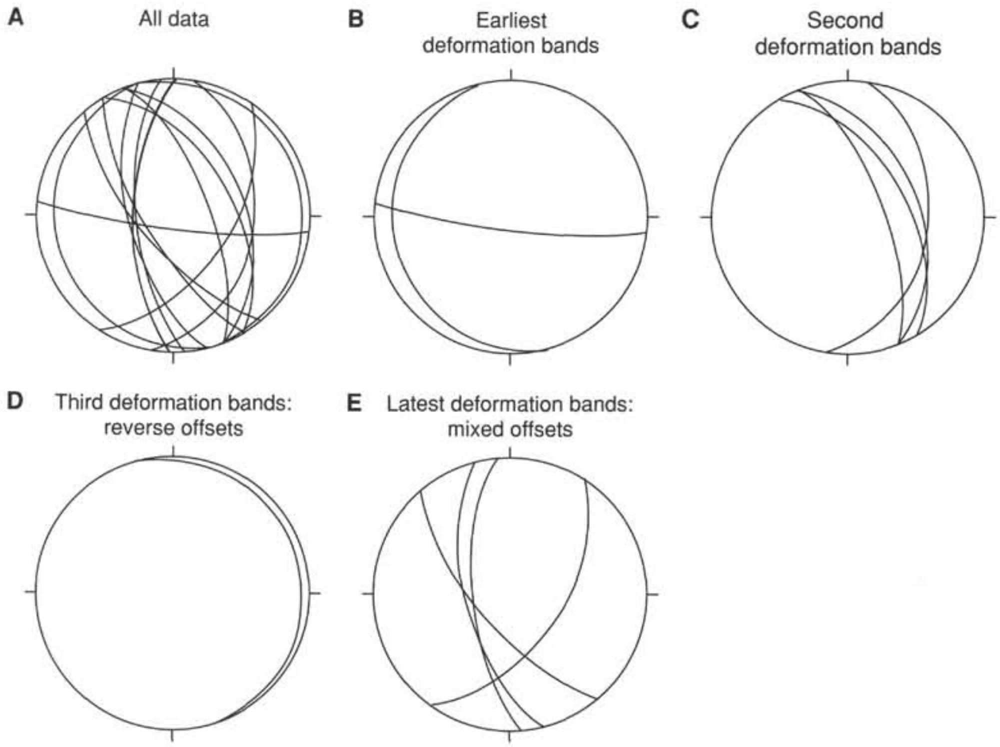

Figure 55. Stereographic projections of deformation bands in all coherent intervals within Domain F, rotated into the reference frame of interval 141-860B-64X-4, 47–57 cm. Deformation bands are represented as great circles.

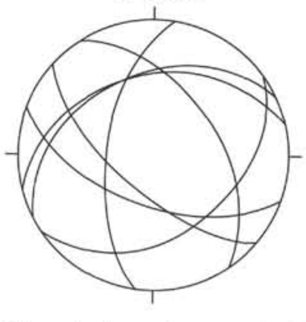

Figure 56. Stereographic projections of unconstrained deformation bands assigned to Domain F. These are isolated measurements where the timing of the deformation bands within the local chronology cannot be established. Deformation bands are represented as great circles.

533.4 mbsf have slightly higher TOC values (>0.5%), suggesting the possible existence of narrow zones of slightly higher organic contents. The samples at 109.7 and 253.7 mbsf were sampled from core sections where specks or lenses of organic matter (plant fragments?) were observed (see Core Description Forms "Barrel Sheets" section, this volume). The decrease in TOC within the uppermost sediments suggests decomposition of organic matter occurring in the sediments near the surface by microbial metabolism.

The T_{max} value of Rock-Eval pyrolysis indicates organic maturity. However, T_{max} values for samples with low S_2 contents are often inaccurate and should be rejected (Peters, 1986). Based on the pyrogram of S_2 peaks, samples with S_2 contents less than 0.5 mg HC/g rock were rejected for Site 860. Rock-Eval pyrolysis of the samples with S_2 contents more than 0.5 mg HC/g rock indicated the presence of immature kerogen with T_{max} ranging from 392° to 417°C, which can be tentatively associated with vitrinite reflectance levels not higher than about 0.5%.

The kerogen from Site 860 is relatively homogeneous and shows no trends related to depth, and has low hydrogen indexes (HI<200 mg HC/g TOC) together with high oxygen indexes (OI>100 mg CO_2/g TOC) characteristic of Type III, gas-prone kerogen of terrigenous origin (Fig. 63). However, for clay-rich sediments containing less than 0.5% of TOC, the measured hydrogen indexes are likely to be too low due to adsorption of pyrolytic organic compounds onto the mineral matrix (Peters, 1986), which suggests that the actual HI values can be higher but well within the Type III, gas-prone kerogen zone (Fig. 63). Significantly high levels of the OI are suggestive of oxidative alteration of the organic matter during sedimentation and early diagenesis and/or long-range transport processes that contributed to the oxidation of the organic matter.

Conclusions

Biogenic gas composed mainly of methane and ethane was detected in the upper zone of the sedimentary sequence of Site 860. Thermogenic hydrocarbons extending into the gasoline range are present in the lower part of the sequence. The organic matter of the sediments corresponds to a Type III, gas-prone, kerogen with a low degree of maturation. Localized maturational and organic anomalies suggest the occurrence of migrational processes and a deeper source of thermogenic hydrocarbons.

INORGANIC GEOCHEMISTRY

The purposes of the pore-water program at Site 860 were to test whether methane hydrates are present above a bottom-simulating seismic reflector (BSR) at ~150 mbsf, and to determine pore-fluid compositions to evaluate fluid migration pathways and

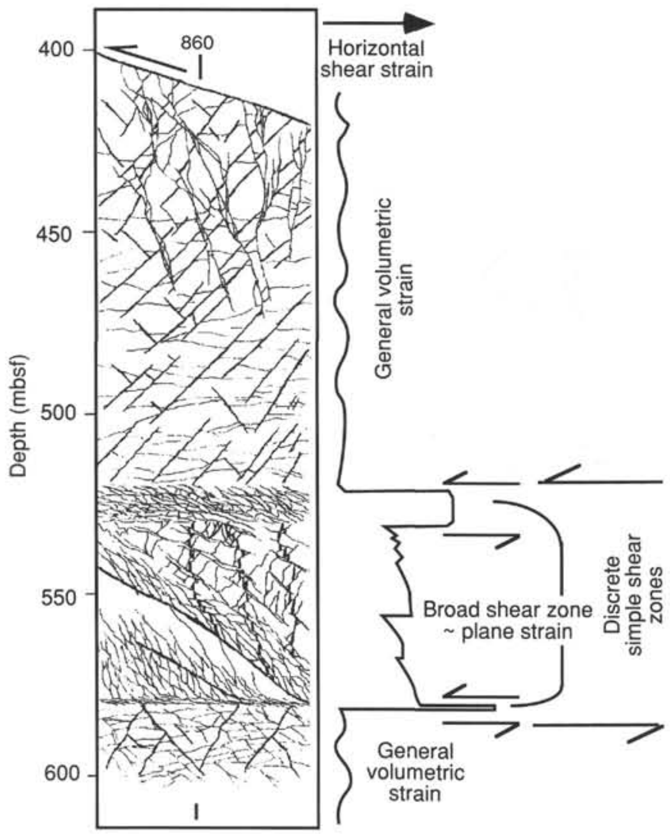

Figure 57. A summary of structural domains within the broken formation. The column is a two-dimensional diagrammatic representation of the deformation band geometry and chronology in domains A to F. The central dividing line of the column represents the structure at the borehole site. The graph on the right-hand side gives a qualitative estimate of the horizontal shear strain associated with the various deformation-band geometries and intensities.

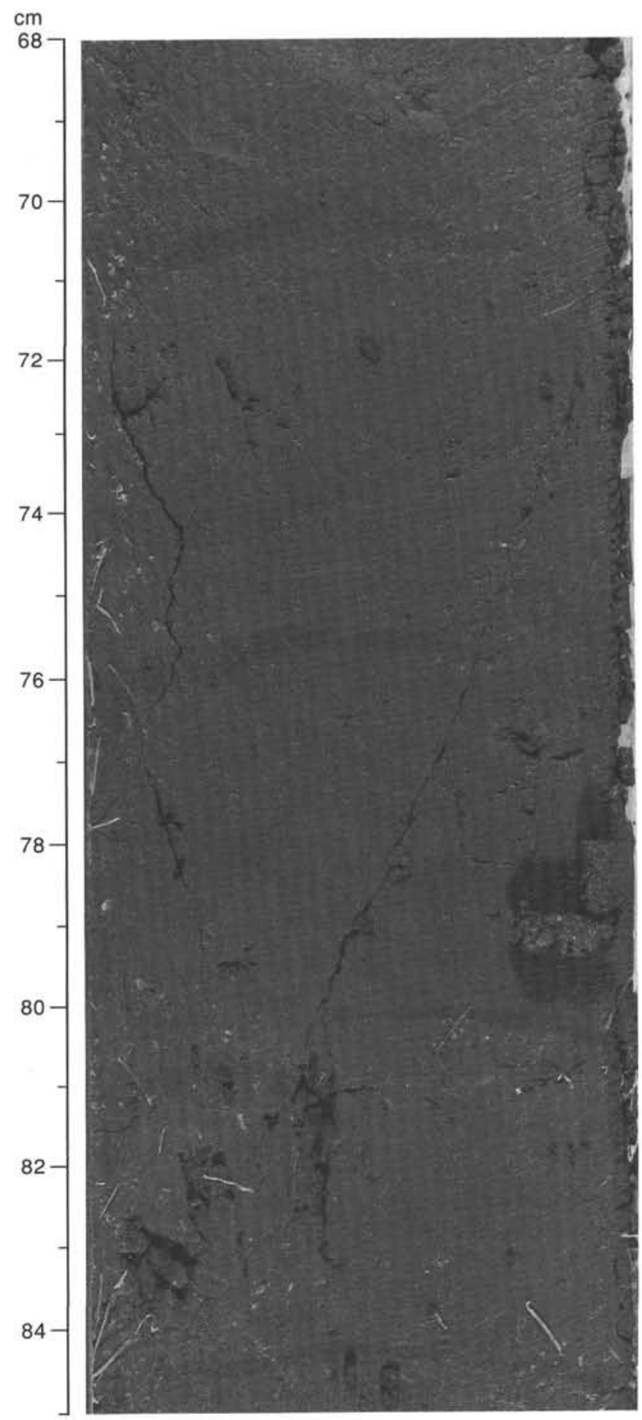

Figure 58. Core photograph of post-drilling fault that offsets boundaries of drilling biscuits, defined by subhorizontal dark zones spaced 4–5 cm apart. The open fracture along the fault also helps to identify it as a late feature (interval 141-860B-19X-4, 68–85 cm).

sources. No hydrates were recovered during coring, and there was no major anion or cation evidence for hydrate presence in the upper section as at Site 859. The sediment sequence and pore-fluid composition are consistent with a complex system of multiple thrust zones and intense tectonic deformation.

The fluid geochemistry program included analyses of fluids from core whole-rounds, in-situ samples from the water sampler temperature probe (WSTP), and deployments of the pressure coring system (PCS). Fluids were analyzed for salinity, chloride, calcium, magnesium, pH, alkalinity, sulfate, ammonia, potassium, sodium, silica, strontium, lithium, fluoride, and boron. These data are presented in Table 18 and Figure 64.

In-situ fluids were collected with the WSTP in four deployments. In all cases we collected samples in both the titanium coil and the overflow chamber. These samples were analyzed for chloride, calcium, magnesium, and sulfate. These data are presented in Table 19 and Figure 65. In all cases, deployment of the tool in a fractured formation resulted in contamination of the samples with drilling fluid. This is reflected in large deviations in the composition of the in-situ samples from fluids obtained by squeezing.

The PCS was run four times in Hole 860B. Core 141-860B-8P (PCS #5: 58.4–59.9 mbsf) retained a pressure on deck of 3790 psi, higher than hydrostatic. It was transferred to a water bath at 4°C, equilibrated for 1 hr, and the pressure released by expansion through a gas manifold. No gases or fluids could be recovered. The core barrel contained only water, recovering no sediment or gas. Core 141-860B-13P (PCS #6: 97.6–99.1 mbsf) retained 3014 psi on deck, slightly below hydrostatic. Upon equilibration in the water bath at 9°C, the pressure stabilized at 2772 psi. After expansion through the gas manifold, all pressure was lost, and no pressure increase was observed after depressurization, indicating

Table 14. Composition of headspace gases for sediments from Holes 860A and 860B.

Core, section, interval (cm)	Depth (mbsf)	Hydrocarbon concentration (ppm) C_1	C_2	C_3	i-C_4	n-C_4	i-C_5	n-C_5	C_{6+}	CO_2	C_1 (cm^3/cm^3)	C_1/C_2
860A-												
1H-5, 135–140	7.4	98	0	0	0	0	0	0	0	496	0.001	
860B-												
1H-1, 111–114	1.1	1	0	0	0	0	0	0	0	763	0.000	
2H-3, 135–140	5.8	5,925	0	0	0	0	0	0	0	845	0.040	
3H-3, 140–145	15.3	12,236	0	0	0	0	0	0	0	361	0.082	
4H-3, 137–140	24.8	6,170	0	0	0	0	0	0	0	120	0.041	
5H-2, 137–140	32.8	3,358	0	0	0	0	0	0	0	632	0.022	
6H-5, 132–135	46.7	10,090	0	0	0	0	0	0	0	1092	0.067	
7H-4, 137–140	54.8	2,987	0	0	0	0	0	0	0	850	0.020	
9X-CC, 0–3	59.9	5,927	0	0	0	0	0	0	0	511	0.040	
10X-CC, 0–3	68.8	1,425	0	0	0	0	0	0	0	2395	0.010	
12X-2, 132–135	90.5	2,769	0	0	0	0	0	1	0	2147	0.018	
14X-1, 132–135	100.4	11,052	0	0	0	0	0	0	5	613	0.074	
15X-2, 137–140	110.1	5,619	0	0	0	0	0	0	3	791	0.037	
16X-2, 132–135	119.6	4,376	0	0	0	0	2	0	3	953	0.029	
17X-3, 137–140	130.4	2,821	0	0	0	0	2	0	2	228	0.019	
19X-4, 132–135	142.8	4,233	0	0	0	0	0	0	0	338	0.028	
20X-1, 147–150	147.2	4,779	0	0	0	0	4	0	4	578	0.032	
21X-1, 121–124	156.7	3,084	0	0	0	0	3	0	tr	1258	0.021	
22X-1, 130–135	160.4	17,232	3	0	0	0	7	0	2	967	0.115	5744
24X-1, 132–135	185.7	12,380	6	0	0	0	0	0	0	790	0.083	2063
25X-1, 137–140	195.5	6,113	4	0	0	0	0	0	0	746	0.041	1528
28X-CC, 0–3	223.1	2,578	12	0	0	0	0	0	3	504	0.017	215
29X-1, 132–135	233.1	16,886	48	0	0	0	0	0	0	194	0.113	352
30X-1, 44–47	243.0	9,707	35	0	0	0	0	0	40	135	0.065	277
31X-2, 132–135	254.7	19,151	138	5	1	0	0	0	4	79	0.128	139
32X-1, 59–62	262.2	10,454	62	tr	0	0	0	0	8	105	0.070	169
33X-1, 127–130	272.5	21,687	105	4	tr	tr	0	0	27	313	0.145	207
34X-3, 15–18	284.0	12,282	67	3	0	0	0	0	16	745	0.082	183
35X-1, 20–23	290.6	9,760	66	3	0	0	0	0	3	183	0.065	148
36X-2, 132–135	302.9	17,270	100	4	1	0	0	0	0	768	0.115	173
37X-2, 147–150	312.8	9,141	37	tr	tr	0	0	0	0	33	0.061	247
38X-1, 123–126	320.6	10,872	59	3	tr	0	1	0	0	371	0.072	184
39X-1, 132–135	330.0	8,397	57	3	1	2	2	0	0	508	0.056	147
40X-CC, 10–13	338.5	4,117	27	3	tr	0	0	0	0	318	0.027	152
41X-5, 127–130	355.3	8,378	40	tr	tr	0	0	0	5	34	0.056	209
43X-1, 82–85	360.0	6,467	44	5	2	tr	3	0	1	105	0.043	147
44X-CC, 0–3	367.3	2,462	20	5	6	1	6	0	0	482	0.016	123
45X-CC, 0–5	379.9	4,113	30	2	2	tr	2	0	0	449	0.027	137
46X-1, 96–99	387.6	13,655	80	7	4	0	0	0	3	486	0.091	171
47X-CC, 10–13	396.4	945	9	2	3	0	2	0	0	641	0.006	105
48X-2, 31–34	407.8	37,391	160	8	3	0	0	0	0	628	0.249	234
49X-CC, 0–3	416.2	739	6	0	0	0	0	0	4	51	0.005	123
50X-3, 47–50	428.8	15,656	91	5	3	0	2	0	0	359	0.104	172
51X-1, 147–150	435.3	15,865	58	7	4	0	3	0	0	467	0.106	274
52X-CC, 10–13	444.5	2,296	24	12	4	2	5	0	0	880	0.015	96
53X-1, 127–130	450.4	67,863	239	26	10	2	6	0	0	1228	0.452	284
54X-CC, 5–10	453.8	4,184	34	8	4	2	8	0	0	2340	0.028	123
56X-CC, 10–13	473.5	1,673	34	11	7	1	8	0	0	1036	0.011	49
57X-CC, 10–13	483.2	3,550	26	8	4	0	5	0	0	664	0.024	137
58X-2, 132–135	495.5	19,867	102	9	3	0	2	0	0	95	0.132	195
59X-CC, 10–13	502.5	36,430	149	15	5	0	5	0	0	144	0.243	244
60X-2, 72–75	514.2	19,055	87	11	3	0	3	0	0	188	0.127	219
61X-4, 147–150	527.7	13,681	77	12	4	0	4	0	0	372	0.091	178
62X-3, 132–135	535.2	47,478	360	52	16	2	14	0	0	904	0.317	132
64X-2, 37–40	551.1	16,138	129	40	17	3	12	0	0	1119	0.108	125
66X-1, 132–135	570.8	13,503	92	20	9	0	4	0	0	86	0.090	147
67X-2, 137–140	582.1	31,737	224	40	14	2	7	0	0	34	0.212	142
69X-CC, 10–13	598.5	18,381	157	23	6	0	3	0	0	80	0.123	117
70X-CC, 10–13	608.3	17,994	172	29	10	0	6	0	1	524	0.120	105

absence of hydrates. No gases were recovered, but 90 mL of fluid were recovered from the manifold water trap. This fluid represents that trapped inside the core barrel above the core (Fig. 65). Core recovery was 61 cm. Core 141-860B-18P (PCS #7: 136.1–137.1 mbsf) did not latch and thus did not seal. It recovered no pressure and no core material. Core 141-860B-42P (PCS #8: 357.7–359.2 mbsf) was an attempt to capture deep in-situ gases to confirm thermogenic gas compositions obtained by head space and Vacutainer analyses. This PCS failed to retain pressure and recovered 30 cm of sediment.

The ammonia, sulfate, and alkalinity profiles in the upper 90 m of the sequence show the typical distributions associated with sulfate consumption by oxidation of organic matter in highly reducing environments. The sediment sequence in this interval reflects hemipelagic deposition with minor deformation and no indication of stratal disruption. The sequence below ~190 mbsf, on the other hand, is characterized by a series of thrusts in which there are both lithological and biostratigraphic repetitions (see Lithostratigraphy and Structural Geology sections, this chapter). Two major thrusts have been defined between 195 and 250 mbsf and at 310 mbsf based on biostratigraphic constraints (see Biostratigraphy section, this chapter). The porosity of the sediments is elevated, centered at ~100 mbsf (see Physical Properties section, this chapter), which might provide a migration pathway for

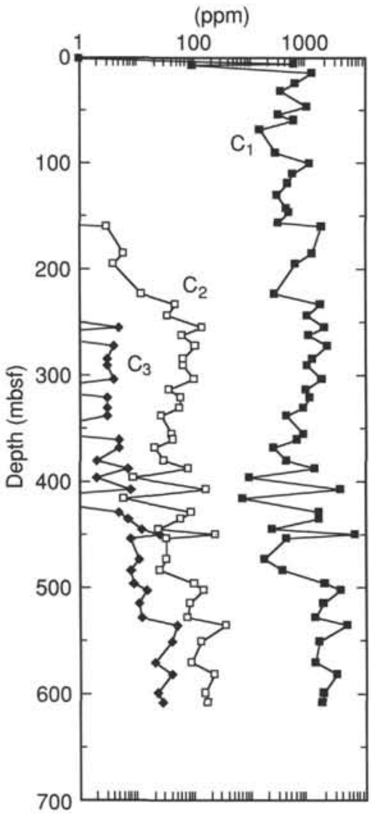

Figure 59. Composition of headspace gases vs. depth (mbsf) for sediments from Holes 860A and 860B.

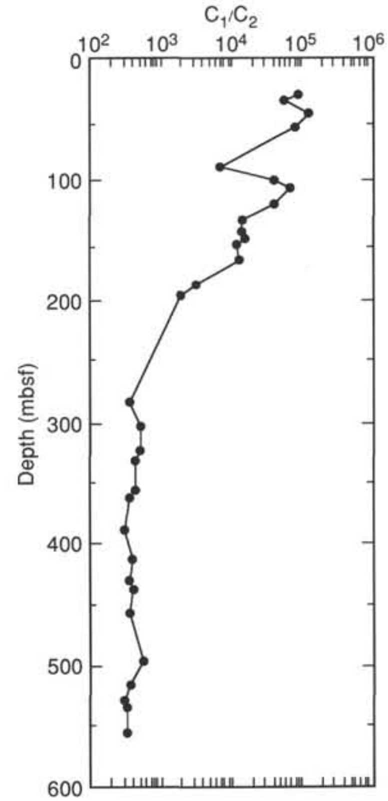

Figure 60. C_1/C_2 ratio of gases from core expansion voids of sediments from Hole 860B.

lateral fluid flow. This interval is barren of biostratigraphic indicators, and therefore any time-sequence reversal associated with thrusting in this horizon could not be documented.

The distribution of the dissolved components below ~190 mbsf is characterized by geochemical disruptions that may be associated with fluid flow along thrust planes. All samples below ~190 mbsf are depleted in chloride with concentration minima centered at about 200 and 360 mbsf. These depths correspond to minima in salinity and sodium. The low chloride contents may represent relict dissociation of gas hydrates and subsequent release of water to the pore fluids. In this scenario, one can postulate the consecutive formation and decomposition of hydrates as the methane-rich sediments undergo tectonic and/or stratal disruption, passing through time-transgressive temperature, pressure, and methane "windows." Several other mechanisms have been suggested to explain low-chloride contents of fluids in other ODP sites. For example, membrane filtration through clays can separate ions from the interstitial water and produce fresh water dilution, and release of interlayer water from clay dehydration reactions can also result in low chloride anomalies.

Calcium, magnesium, and strontium concentrations are also lower than seawater. The calcium profile has maxima in two of the intervals characterized by depleted chloride, a feature that might indicate an association with fluid flow or imbrication processes. The decrease in alkalinity, calcium, and magnesium below 90 mbsf is likely associated with in-situ carbonate formation.

The thermal structure of the uppermost 50 m at this site suggests that conduction dominates heat transport. The base of the hydrate stability zone is estimated to occur at ~150 mbsf, so the salinity anomalies at ~200 mbsf and ~360 mbsf are not due to in-situ hydrate decomposition on drilling and recovery.

In addition, the depths of apparent pore-water anomalies and gradient changes do not correspond with depths of structural domain and biolithostratigraphic boundaries, inferred to be shallow thrust faults. Thus although lateral fluid flow may be occurring at this site, it is not sourced from deeper horizons, consistent with both the shallow thrusts and with the weak vertical pore-fluid gradients.

Below about 420 mbsf, the formation is pervasively broken. The chemistry of pore fluids in this deeper interval suggests that the base of the section in permeated by fluids that have been altered by mixtures with a common diagenetic history, perhaps involving continental basement.

PHYSICAL PROPERTIES

Core recovery from 0–60 mbsf was usually complete and gas expansion and general drilling disturbance caused by the hydraulic piston corer (APC) did not interfere with the collection of good-quality index property values. From 60–90 mbsf, the change from APC to extended core-barrel (XCB) coring resulted in poor core quality and recovery. Below approximately 100 mbsf, the quantity and quality of core recovery improved overall but remained variable down to the base of the hole. Below 200 mbsf, as at Site 859, we selected coherent pieces from fragmented core material for use in index property determinations. As a result of this procedure, there may be a slight bias toward data reflecting more coherent lithologies.

Index Properties

On the basis of the significant changes in the trends of porosity, water content, and bulk density at 90 and 130 mbsf, we divided the section at Site 860 into three physical properties units. The

Table 15. Composition of gases from core expansion voids of sediments from Hole 860B.

Core, section, interval (cm)	Depth (mbsf)	Hydrocarbon concentration (ppm) C_1	C_2	C_3	i–C_4	n–C_4	i–C_5	n–C_5	C_{6+}	CO_2	C_1/C_2	C_1/C_3	C_1/n–C_4	Pressure (psi)
141-860B-														
4H-7	30.0	738,541	8	3	0	3	0	0	0	665	92,318	246,180	246,180	–
5H-5	36.0	893,901	15	2	0	2	0	0	0	581	59,593	446,951	446,951	11
6H-5	46.0	918,900	7	3	0	3	0	0	0	370	131,271	306,300	306,300	0
7H-5	56.0	915,282	11	4	0	3	0	0	0	306	83,207	228,821	305,094	5
12X-2	89.5	13,992	2	4	2	53	tr	1	5	993	6,996	3,498	264	0
14X-2	101.0	578,722	14	3	3	60	1	2	23	821	41,337	192,907	9,645	0
15X-1	108.0	889,700	13	3	2	tr	6	0	0	813	68,438	444,850	148,283	1
16X-3	119.8	826,041	21	2	1	tr	21	2	0	675	39,335	413,021	–	0
17X-5	133.0	790,414	56	0	0	0	7	0	0	966	14,115	–	–	0
19X-5	143.0	970,672	69	3	2	0	13	0	0	832	14,068	323,557	–	6
20X-2	147.7	705,429	43	2	1	0	11	0	0	910	16,405	352,715	–	0
21X-1	153.3	782,189	66	tr	tr	tr	5	0	1	951	11,851	–	–	0
22X-2	167.3	837,649	62	tr	2	tr	9	0	3	889	13,510	–	–	0
24X-1	184.4	809,063	245	0	0	0	1	0	0	933	3,302	–	–	0
25X-2	195.5	749,855	371	0	0	1	0	0	3	846	2,021	–	749,855	0
34X-2	282.9	11,976	34	2	4	121	5	4	46	994	352	5,988	99	0
36X-3	303.4	10,361	21	0	0	2	0	0	2	891	493	–	5,181	0
38X-2	321.5	889,497	1800	26	5	3	3	0	4	819	494	34,211	296,499	0
39X-2	330.9	789,447	1707	34	6	61	5	3	24	707	462	23,219	12,942	0
41X-5	355.1	960,281	2126	35	8	0	0	0	4	918	452	27,437	–	16
43X-2	361.1	863,584	2308	62	13	3	2	0	5	108	374	13,929	287,861	0
46X-2	388.2	34,533	107	5	0	3	0	0	3	993	323	6,907	11,511	0
48X-4	411.7	856,949	2239	53	14	2	7	0	3	863	383	16,169	428,475	0
50X-3	429.0	943,376	2486	73	19	2	7	0	0	849	379	12,923	471,688	0
51X-2	436.3	685,249	1636	54	12	1	4	0	0	862	419	12,690	685,249	0
53X-2	456.2	620,622	1714	76	17	2	10	0	3	877	362	8,166	310,311	0
58X-2	494.6	90,145	166	9	2	3	2	0	2	963	543	10,016	30,048	0
60X-2	514.3	818,272	2198	126	27	3	11	0	0	nd	372	6,494	272,757	0
61X-5	529.2	859,564	2675	164	34	3	16	0	0	nd	321	5,241	286,521	0
62X-2	533.1	970,142	2917	166	31	3	11	0	0	nd	333	5,844	323,381	0
64X-4	554.5	474,112	1437	115	27	2	11	0	5	nd	330	4,123	237,056	0

index properties are listed by depth and core in Table 20 and plotted against depth in Figure 66. Physical properties Unit A extends between 0 and 90 mbsf, Unit B extends between 90 and 130 mbsf, and Unit C extends from 130 mbsf to the base of the hole.

The sediment in Unit A ranges in composition from silty clay to clay-rich silt, with a thick, graded, and poorly cemented sand unit between 39 and 48 mbsf (see Lithostratigraphy section, this chapter). The porosity and water content decrease and the bulk density increases very rapidly down section to 39 mbsf (Fig. 66). For example, the porosity decreases from over 76% near the surface to 45%–50% by 39 mbsf. In the region between 48 and 100 mbsf, the data are sparse due to poor recovery but the porosity and bulk density both appear to remain fairly constant.

In Figure 67 we plot the GRAPE bulk density data (0–60 mbsf) from the APC cores together with discrete bulk density data. The two types of bulk density data agree quite closely from 0–20 mbsf. Below 20 mbsf, only the highest GRAPE bulk density values appear to correspond to the discrete sample data. The discrepency probably relates to the increasing disruption of the core by gas expansion. The thick sand unit between 39 and 48 mbsf causes a large dispersion in the GRAPE data, as it was highly disturbed during coring. Owing to disturbance of the sand unit, and because the pore fluids had largely drained from the core, only grain density data was collected as discrete samples from this unit.

Overall, the grain density (Fig. 66) remains consistently between 2.6 and 2.85 g/cm^3 down though Unit A. In detail, however, several cycles in which grain density increases downward are apparent (Fig. 68). In the large sand unit, between 38 and 49 mbsf, the grain-density increase is associated with the coarser base of the sand. A greater abundance of heavy magnetic minerals also gives the base of this sand unit a high magnetic susceptibility (see Paleomagnetism section, this chapter). It is possible that the other cycles in the grain density data relate to broad fining up sequences (see Lithostratigaphy section, this chapter).

Unit B corresponds to a claystone lithology (Fig. 66) that appears to be somewhat more indurated than the surrounding sandy and silty lithologies (this claystone forms the top of Lithostratigraphic Unit II, see Lithostratigraphy section, this chapter). Physical properties Unit B lies occupies the interval between 90 and 130 mbsf and is associated with a sharp increase in porosity and water content, and a corresponding decrease in bulk density (Fig. 66).

Unit B exhibits none of the repeated cyclic downward increases in grain density characteristic of Unit A (Fig. 66). The claystone is associated with both an organic hydrocarbon anomaly and an anomaly in chloride (see Organic Geochemistry and Inorganic Geochemistry sections, this chapter), and thus appears to be a hydrogeologically significant feature.

Unit C (120–618 mbsf) predominantly comprises claystone, silty clay, and siltstone, with local gravel beds. Beneath 120 mbsf, water content and porosity decrease and the bulk density gradually increases down section (Fig. 66), consistent with increasing consolidation under rising overburden loads. The grain density stays relatively constant between approximately 2.65 and 2.85 g/cm^3 (Fig. 66). Significantly, the porosity and bulk density profiles are relatively unaffected by the three significant thrusts situated at approximately 240 mbsf, 310 mbsf, and a postulated thrust at 420 mbsf (see Biostratigraphy and Structural Geology sections, this chapter).

Thermal Conductivity

Thermal conductivity (TC) measurements were routinely carried out on portions of the cores that exhibited little obvious

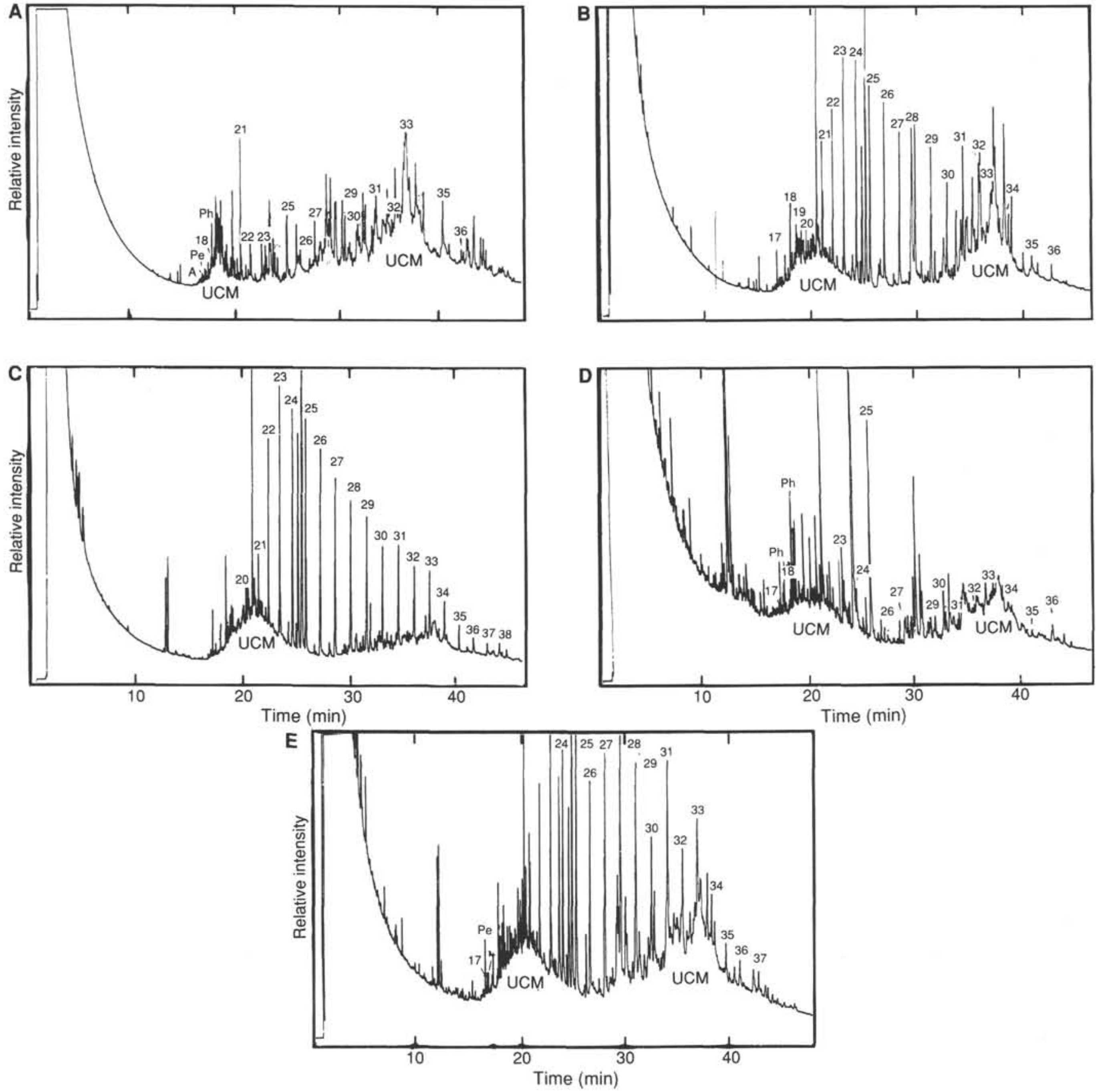

Figure 61. Gas chromatographic traces of the bitumen (hexane-soluble matter) of sediments from Hole 860B: (**A**) Sample 141-860B-10X-CC, 0–3 cm, (**B**) Sample 141-860B-12X-2, 132–135 cm, (**C**) Sample 141-860B-39X-1, 132–135 cm, (**D**) Sample 141-860B-67X-2, 137–140 cm, and (**E**) Sample 141-860B-69X-CC, 10–13 cm (numbers refer to carbon chain length of *n*-alkanes, Pr = pristane, Ph = phytane, UCM = unresolved complex mixture of branched and cyclic compounds).

drilling disturbance. The data are listed in Table 21 and plotted against depth in Figure 66. Thermal conductivity (uncorrected for pressure and temperature effects) appears to generally increase down section from 1–1.4 W/m·K near the surface to 1.3–1.9 W/m·K near the base of the hole at 600 mbsf. Through much of the upper part of the hole the sediment was soft enough to push a probe into and use the full space (FS, in Table 21) determination technique. Toward the base of the hole the scatter in the data increases. In part, this reflects problems with getting good coupling between the probe and the increasingly indurated sediment, and we eventually switched to the half space (HS, Table 21) technique for core fragments.

Sonic (V_P) Velocity

Except for the interval between 2 mbsf and 10 mbsf in Holes 860A and 860B, sonic velocity (V_P) measurements could not be carried out by either the *P*-wave logger (PWL) or the digital

Table 16. Extractable bitumen of sediments from Hole 860B.

Core, section, interval (cm)	Depth (mbsf)	C_{max}	C_{range} C_i–C_f	Pr/Ph	Pr/n-C_{17}	Ph/n-C_{18}	CPI	Organic matter type
141-860B-								
10X, CC	68.8	21	16–38	0.23	2.50	3.67	4.79	Mar = Terr
12X-2	90.5	24	10–36	0.33	0.25	0.25	1.00	Mar = Terr
20X-1	147.3	21	15–36	0.57	2.00	2.33	2.17	Mar = Terr
24X-1	185.7	21	15–36	0.50	3.00	3.00	2.00	Mar = Terr
28X-CC	223.1	21	15–36	0.70	3.50	3.33	4.39	Mar = Terr
32X-1	262.2	21	10–36	0.42	2.50	2.40	3.83	Mar << Terr
35X-1	290.6	33	17–37	0.03	0.67	1.80	5.27	Mar << Terr
39X-1	330	23	10–38	2.00	3.00	0.37	0.92	Mar << Terr
41X-5	355.2	33	10–37	1.19	4.17	3.00	2.28	Mar << Terr
49X-CC	415.7	31	10–38	0.66	1.91	5.93	2.62	Mar << Terr
58X-2	495.6	21	10–37	0.67	1.50	1.50	2.09	Mar << Terr
62X-3	535.2	21	10–37	0.75	6.00	1.60	2.48	Mar << Terr
67X-2	582.1	25	9–37	0.49	4.17	3.90	2.05	Mar = Terr
69X-CC	598.5	25	10–37	0.50	1.22	5.20	1.23	Mar = Terr

Mar = Marine; Terr = Terrigenous; CPI = carbon preference Index; Pr = pristane; Ph = phytane.

Table 17. Rock-Eval and total organic carbon (TOC) of sediments from Hole 860B.

Core, section, interval (cm)	Depth (mbsf)	T_{max} (°C)	S_1 (mg/g)	S_2 (mg/g)	S_3 (mg/g)	TOC (%)	HI	OI	PI	S_2/S_3
141-860B-										
1H-1, 22–24	0.2	415	0.78	3.18	3.53	1.74	183	203	0.20	0.90
1H-1, 98–100	1.0	417	0.61	2.88	3.75	1.59	181	236	0.17	0.77
3H-1, 100–102	11.9	518	0.09	0.45	0.63	0.33	136	191	0.17	0.71
3H-3, 114–116	15.1	390	0.13	0.45	0.96	0.48	94	200	0.22	0.47
3H-5, 100–102	17.9	393	0.12	0.45	0.98	0.53	85	185	0.21	0.46
3H-7, 50–52	20.4	381	0.05	0.15	0.95	0.25	60	380	0.25	0.16
4H-5, 105–107	27.5	415	0.07	0.22	1.43	0.34	65	421	0.24	0.15
5H-2, 104–106	32.4	466	0.03	0.19	1.23	0.27	70	456	0.14	0.15
7H-4, 88–90	51.3	406	0.13	0.57	1.81	0.58	98	312	0.19	0.31
12X-3, 48–49	91.2	461	0.07	0.36	1.40	0.33	109	424	0.16	0.26
14X-1, 52–54	99.6	395	0.08	0.43	3.33	0.42	102	793	0.16	0.13
15X-2, 100–102	109.7	404	0.14	0.65	1.92	0.71	92	270	0.18	0.34
16X-3, 27–30	120.1	390	0.09	0.36	1.65	0.41	88	402	0.20	0.22
17X-5, 29–31	132.8	549	0.06	0.34	0.71	0.35	97	203	0.15	0.48
19X-1, 133–135	138.4	410	0.06	0.26	0.83	0.31	84	268	0.19	0.31
20X-CC, 10–12	145.9	403	0.07	0.27	1.09	0.35	77	311	0.21	0.25
21X-1, 90–91	156.4	399	0.03	0.14	1.00	0.19	74	526	0.18	0.14
22X-2, 70–72	167.2	396	0.05	0.25	1.04	0.28	89	371	0.17	0.24
25X-1, 75–77	194.9	463	0.05	0.32	0.63	0.30	107	210	0.14	0.51
28X-1, 114–116	224.2	404	0.07	0.41	1.62	0.35	117	463	0.15	0.25
31X-2, 26–28	253.7	417	0.18	1.35	1.58	0.89	152	178	0.12	0.85
32X-2, 82–84	263.9	405	0.08	0.35	1.13	0.36	97	314	0.19	0.31
34X-1, 31–33	281.1	392	0.14	0.54	0.96	0.46	117	209	0.21	0.56
35X-1, 73–75	291.1	401	0.07	0.42	0.48	0.36	117	133	0.14	0.88
36X-2, 74–77	302.3	387	0.06	0.29	1.21	0.37	78	327	0.17	0.24
37X-2, 92–94	312.2	404	0.07	0.37	1.32	0.35	106	377	0.16	0.28
38X-2, 42–44	321.3	399	0.06	0.34	0.44	0.30	113	147	0.15	0.77
39X-1, 108–110	329.8	409	0.08	0.46	0.46	0.49	94	94	0.15	1.00
40X-CC, 20–22	338.6	402	0.11	0.59	0.55	0.47	126	117	0.16	1.07
41X-1, 42–44	348.4	397	0.06	0.31	0.43	0.32	97	134	0.16	0.72
43X-1, 28–30	359.5	394	0.08	0.42	0.64	0.42	100	152	0.16	0.66
46X-CC, 21–23	389.0	390	0.08	0.36	0.96	0.40	90	240	0.18	0.38
47X-CC, 46–48	396.8	420	0.04	0.19	0.64	0.31	61	206	0.17	0.30
48X-1, 28–23	406.3	407	0.07	0.35	0.42	0.41	85	102	0.17	0.83
52X-CC, 25–27	444.7	394	0.09	0.30	0.68	0.28	107	243	0.23	0.44
53X-2, 80–82	451.4	403	0.04	0.22	0.63	0.31	71	203	0.15	0.35
56X-CC, 16–18	473.6	400	0.11	0.45	1.22	0.43	105	284	0.20	0.37
57X-CC, 43–44	483.5	397	0.14	0.56	1.01	0.43	130	235	0.20	0.55
60X-3, 54–56	515.5	401	0.03	0.14	0.29	0.22	64	132	0.18	0.48
61X-3, 22–25	524.9	440	0.05	0.31	0.62	0.30	103	207	0.14	0.50
62X-2, 99–102	533.4	404	0.18	1.06	0.99	0.65	130	235	0.15	0.55
64X-4, 45–47	555.2	408	0.10	0.60	0.89	0.50	120	178	0.14	0.67
67X-2, 100–102	581.7	399	0.13	0.53	1.26	0.43	123	293	0.20	0.42
70X-CC, 22–24	608.4	394	0.09	0.38	1.23	0.35	109	351	0.19	0.31

Note: T_{max} values for samples with S_2 contents less than 0.5 mg HC/g sediment are inaccurate and should be rejected.

sediment velocimeter (DSV) owing to signal dampening by gas expansion cavities below 10 mbsf. In the interval between 2 and 10 mbsf, however, the two methods do agree well and a lot of detailed data are available (Fig. 69 and Table 22). For the general purposes of constraining seismic data, however, the discrete measurements made with the Hamilton Frame velocimeter are probably more relevant. Because of the generally poor quality of recovered core, we were only able to find large enough coherent pieces to make good measurements at a few intervals (although we tried many times). The data (Table 23 and Fig. 66), although

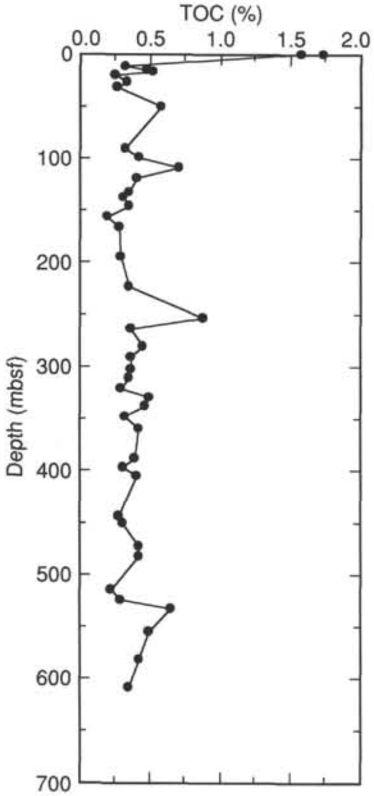

Figure 62. Total organic carbon content (Rock-Eval) vs. depth of sediments from Hole 860B.

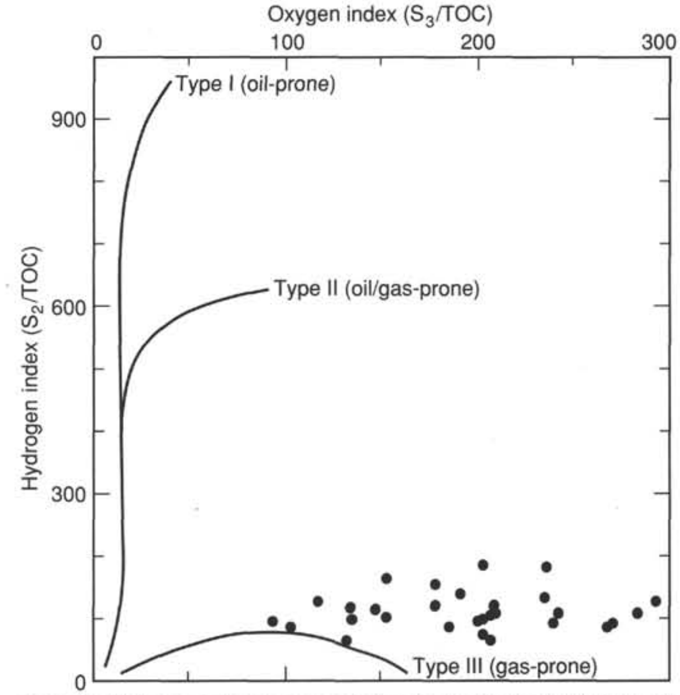

Figure 63. Hydrogen index vs. oxygen index diagram (Rock-Eval) of organic matter of sediments from Hole 860B.

not numerous, show a consistent trend in *P*-wave velocity with depth, with the velocity increasing from 1512 m/s at the surface to as much as 2101 m/s at 525 mbsf. Some particularly good measurements (with little scatter) were made below 480 mbsf, where the sediment is indurated and locally coherent with few fractures.

Discussion and Overview

If one plots porosity vs. a general Athy-type (Athy, 1930) exponential fit (Fig. 70), two main features of the index data are apparent that have significance for the general physical processes affecting the sediment at Site 860. First, in the near surface (physical properties Units A and B), the Athy fit is very poor with the porosities varying rapidly over short intervals. Second, at deeper levels below 130 mbsf, the fit becomes very good and the sediment appears to follow a fairly uniform consolidation trend.

We propose that the poor fit in the upper two physical property units relates to significant changes in lithology in this part of the sequence. The sand body at 38–49 mbsf appears to have formed a fluid pathway that has effectively allowed the top 39 m of section to drain from below as well as above, increasing the rate of consolidation of the unit above. In contrast, the claystone between 90 and 130 mbsf (physical properties Unit B) appears to have retained fluid, presumably because it has a lower permeability. Significantly, this clay unit is also associated with several geochemical anomalies (see Organic Geochemistry and Inorganic Geochemistry sections, this chapter). Exotic fluids appear to be either migrating though the clay unit, or immediately below the clay unit (so that the signal has diffused up into the aquitard formed by the clay horizon). Why the permeable sand unit (38–49 mbsf) does not form a conduit for these geochemically distinct fluids is curious; perhaps the clay prevents connection between the source of the fluids and this permeable body.

At deeper levels the negligible effect of the major thrusts on the porosity, water content, and bulk density profiles constrains the timing and/or the rate of emplacement of the thrusts. The thrusts will have originally emplaced older dense material over younger and presumably less consolidated material. In general, the section is dominated by clayey silt and silty clay that should have relatively low permeabilities. We would expect to see inversions in porosity and bulk density if the thrusts are very young features (as we do see at the toe of the accretionary wedge at Site 859). We have upper Pliocene material tectonically buried beneath lower Pliocene material. This constrains the timing of the thrust event to the Pleistocene or later. For the porosity and bulk density to have effectively come close to some equilibrium around the thrusts suggests that either the movement has continued from the early Pleistocene at a rate sufficiently slow that porosity loss (and, thus, the slow movement of fluid out of the system) can keep pace, or that the thrusting was very rapid and stopped relatively early in the Pleistocene, giving any porosity "anomalies" time to decay as the section consolidated.

WSTP AND ADARA TEMPERATURE MEASUREMENTS

Site 860 is situated in a mid-slope position in a tectonized slope basin (see Structural Geology section, this chapter). Due to its greater distance from the oceanic spreading center, generally lower geothermal gradients were expected here in comparison with Site 859. A local prominent BSR (bottom simulating reflector) at approximately 200 mbsf suggested that gas hydrate was present at this site. In brief, the principal objectives of the temperature measurement program at Site 860 were: (1) to establish the geothermal gradient, (2) to determine the principal mechanism

Table 18. Interstitial water data obtained from titanium squeezers for Site 860.

Core, section, interval (cm)	Depth (mbsf)	IW vol. (mL)	pH	Alk (mM) (Gran)	Sal (Refr)	Cl (mM) (Tit'n)	SO_4 (mM) ($BaSO_4$)	NH_4 (μM) (Spec)	Si (μM) (Spec)	Mg (mM) (Tit'n)	Ca (mM) (Tit'n)	K (mM) (AES)	Sr (μM) (AAS)	F (μM) (ISE)	B (mM) (Spec)	Na (mM) (AES)	Li (μM) (AES)
141-860A-																	
1H-5, 145–150	7.5	37	8.28	20.89	34.0	548	0.6	1170	568	41.13	1.65	12.0	59	49	0.54	486	22
141-860B-																	
2H-3, 145–150	5.9	36	8.27	16.70	34.0	556	6.1	1190	591	42.27	2.63	12.2	67	47	0.59	489	22
3H-3, 145–150	15.4	28	8.07	25.28	34.0	559	0.4	2420	633	39.87	0.81	11.9	52	45	0.64	493	21
4H-3, 145–150	24.9	16	8.16	37.42	35.0	563	0.6	3820	568	43.39	2.28	12.4	55	54	0.61	490	26
5H-2, 140–150	32.8	34	8.04	46.37	34.5	559	0.7	5480	585	44.59	3.20	11.7	59	57	0.61	495	27
6H-5, 140–150	46.8	22	8.05	46.98	36.0	559	0.9	7170	502	46.53	3.83	11.6	67	60	0.63	503	25
7H-4, 140–150	54.8	42	8.15		35.5	562	0.5		778	44.59	3.50	12.6	63	63	0.59	507	37
12X-2, 140–150	90.6	36	7.84	44.63	36.0	561	1.2		616	38.44	3.11	11.4	55	54	0.64	516	26
14X-1, 140–150	100.5	26	7.87	34.74	34.0	535	5.6		551	36.58	2.95	11.1	55	52	0.64	496	27
15X-2, 140–150	110.1	28	7.97	37.36	33.5	534	2.2		626	33.48	2.67	10.9	55	52	0.63	500	31
16X-2, 140–150	119.7	34	7.94	36.12	34.0	559	0.5		760	27.43	1.89	11.5	55	50	0.70	513	36
17X-3, 140–150	130.9	28	7.98	27.29	32.5	541	5.8	23170	612	28.87	2.12	11.8	59	52	0.72	519	35
19X-4, 140–150	143.0	28	8.08	30.68	33.5	548	2.2		704	26.92	1.67	12.8	52	57	0.64	529	48
20X-2, 0–10	147.3	23	8.04	23.77	33.0	540	8.6	23700	688	29.80	2.48	11.4	59	52	0.66	514	36
21X-1, 124–134	156.7	25	8.11	25.93	33.0	528	6.6		647	26.74	2.20	11.1	52	56	0.59	509	37
22X-2, 140–150	166.5	20	8.09		32.0	525	5.6		672	26.88	2.65	10.4	55	43	0.67	499	33
24X-1, 140–150	185.8	26	7.98	25.82	29.5	496	4.1		678	25.02	2.79	9.1	52	40	0.50	458	38
25X-1, 140–150	195.5	14	8.14	25.32	30.5	510	5.6		532	25.63	3.40	9.6	55	40	0.57	468	29
29X-1, 140–150	234.2	8.5			33.5	539	8.6	21500	502	27.89	3.68	10.2	63	43	0.60	503	28
30X-1, 47–57	243.4	1.5			33.0	545	5.3		616		3.12	10.4			0.59	502	
31X-2, 140–150	254.8	2			33.5	543	7.4		691	21.30	3.12	11.1		45	0.54	499	
32X-1, 62–76	262.2	5.5			33.0	540	6.0		688	25.67	2.34	11.0	59	42	0.63	499	40
33X-1, 130–145	272.5	8			33.0	542	5.3		642	24.00	2.61	10.7	63	35	0.58	503	40
34X-3, 0–15	283.8	15	8.21		33.0	538	4.2		520	23.27	3.05	11.4	63	36	0.58	505	41
35X-1, 0–15	290.4	4			32.0	537	7.2		538	26.31	4.03	11.0	66	38	0.53	493	45
36X-2, 140–150	303.0	5			33.0	541	5.0	21200	601	23.01	3.07	10.7	66	35	0.54	496	48
38X-1, 131–141	320.7	2.5			32.0	537	7.0		654		3.34	10.7	70	34	0.55	494	51
39X-1, 135–150	330.0	3.5			32.0	542	4.7		724	20.71	3.34	11.1	70	35	0.55	508	53
41X-5, 135–150	355.3	2			29.0	475	4.5	17800				10.8	66	34	0.46	458	47
43X-1, 85–100	360.0	5			33.0	533	8.0		572	20.27	4.50	11.3		35	0.56	516	59
46X-1, 114–129	387.7	3			33.0	521	5.9		626	19.10	3.89	11.1	70	35	0.48	513	54
53X-1, 135–150	450.4	2			33.0	543	2.2		676	12.93		10.7		35	0.42	524	
58X-2, 140–150	495.7	5			32.0	547	2.7			13.72	3.56	10.9	78	34	0.39	527	66
60X-2, 80–90	514.3	3.5			33.0	537	3.6		636	13.41	4.50	10.9	81	33	0.36	521	76
62X-2, 140–150	535.3	2.5			32.0	544	3.5	5580			4.15	11.2		34	0.34	539	
64X-2, 40–50	552.1	15	8.39	12.47	31.0	542	3.0	6310	733	12.66	5.52	10.8	81	32	0.41	529	101
66X 01, 140–150	570.9	6.6			33.0	550	1.6	5880	695	11.38	5.42	11.0	89	32	0.40	550	108
67X 02, 140–150	582.1	6.5			32.0	546	4.9	5910		13.92	6.39	10.8	92	32	0.37	532	96

Note: Gran = gran titration, Refr = refractometer, Tit'n = titration, AES = atomic absorption spectrometry, ISE = ion specific electrode, and Spec = spectrophotometer. All methods are described in the Explanatory Notes (this volume).

of heat transport, and (3) to determine the temperature at the depth of the BSR observed on seismic reflection sections.

Temperature Measurements

At Hole 860B the ADARA tool was deployed four times, the newer WSTP tool twice, and the old WSTP temperature probe four times. Both the new and old WSTP temperature probes failed repeatedly to penetrate the formation without either cracking the formation or being disturbed by movement of the drill pipe. Thus we are unable to report any useful data from these runs, with the exception of one run at 126 mbsf. In this deployment (Fig. 71), the formation either cracked 4 min after penetration or the tool was pulled out of the formation and the beginning of the thermal equilibration curve is all that is available to fit in 1/t space. When we make this fit, we find that the three points immediately before the tool was disturbed fall on a straight line that trends toward approximately 11.45°C. We mention this point (with some significant reservations) as it is the only temperature measurement we have below 60 mbsf.

The ADARA tool was deployed four times and gave useful results on three occasions. Bottom-water temperatures are around 2.2°C. We used the APCTFIT shipboard program to analyze the data (see Explanatory Notes, this volume). Initially, we encountered problems because the data were collected at a three-second interval and the program was only set up to use 5- or 10-s intervals. We interpolated the data to provide a 10-s interval for extrapolation purposes. The thermal conductivity data generally varied between 1.1 W/m·K and 1.3 W/m·K in the upper 60 m of the hole. We used a thermal conductivity of 1.2 W/m·K to fit the ADARA data. The results are shown in Table 24. The deployment at 29.9 mbsf has a moderately disturbed temperature decay profile, but we were able to obtain a fairly good fit to the less-disturbed tail of the data (in the portion marked x on Fig. 72) that extrapolates to 5.4°C. The ADARA deployment at 48.9 mbsf again has a moderately disturbed decay profile and the less-disturbed tail of the data (in the region marked x on Fig. 73) extrapolates to 7.2°C. The deployment at 58.4 mbsf has the best profile of the three ADARA measurements (Fig. 74). The initial disturbance in the profile arises from the pumps initially being left on to drive the partially inserted core barrel into the formation. As the probe was steadily driven into the formation there was a large, fairly long-lived spike in the temperature data. Once full penetration was achieved, the pumps were switched off and the temperature then decayed. The fit to the long-undisturbed tail of the data gives a temperature of 8.97°C.

In the ADARA runs at 29.9 and 48.9 mbsf, disturbance of the tool causes problems in fitting the data. Subjective evaluation of the data introduced a variability of about ±0.3°C around the chosen value. The variability in the fitting of the data from the good deployment at 58.4 mbsf is much less (±0.08°C).

Results and Discussion

The results of the ADARA deployments are plotted against sub-bottom depth in Figure 75. The sea-floor water temperature and the ADARA deployment at 58.4 mbsf are the most constrained data points and we favor these two points in our straight-line fit. With some minor fluctuations the temperature gradient in the top 60 m of the section is approximately linear, with a gradient

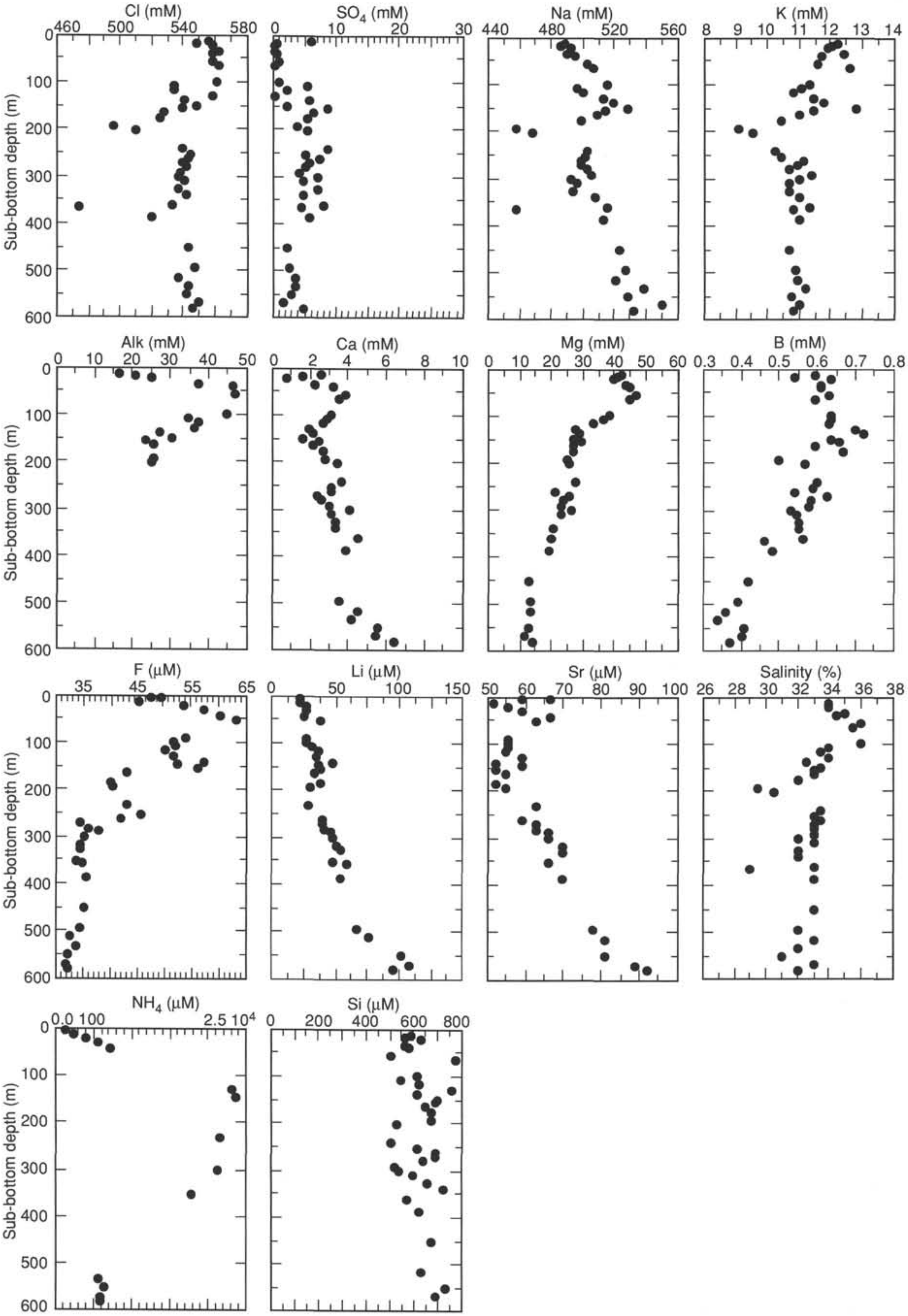

Figure 64. Interstitial water compositions vs. depth for Site 860. All data are from squeezed whole rounds.

Table 19. Interstitial water data obtained from WSTP runs for Site 860.

Core, section, interval (cm)	Depth (mbsf)	Designation	Vol (mL)	Sal (Refr)	Cl (mM)	SO_4 (mM)	Mg (mM)	Ca (mM)	F (μM)
141-860B-									
5H	29.9	WT	6	32.0	519	26.7	50.74	9.73	32.0
5H		WO	1200	30	495	25.6	47.86	8.98	38
10X	68.7	WT	6	31	522	26.9	50.89	9.22	60
10X		WO	235	25	404	20.2	38.84	6.64	36
14X	99.1	WT	6	33	517	25.2	45.02	8.37	70
14X		WO	90	14	216	9.7	20.53	3.54	42
17X	126.5	WT	6	35	519	25.5	50.05	9.24	59
17X		WO	310	26	414	21.5	39.92	7.53	41

WT = titanium coil; WO = overflow chamber.

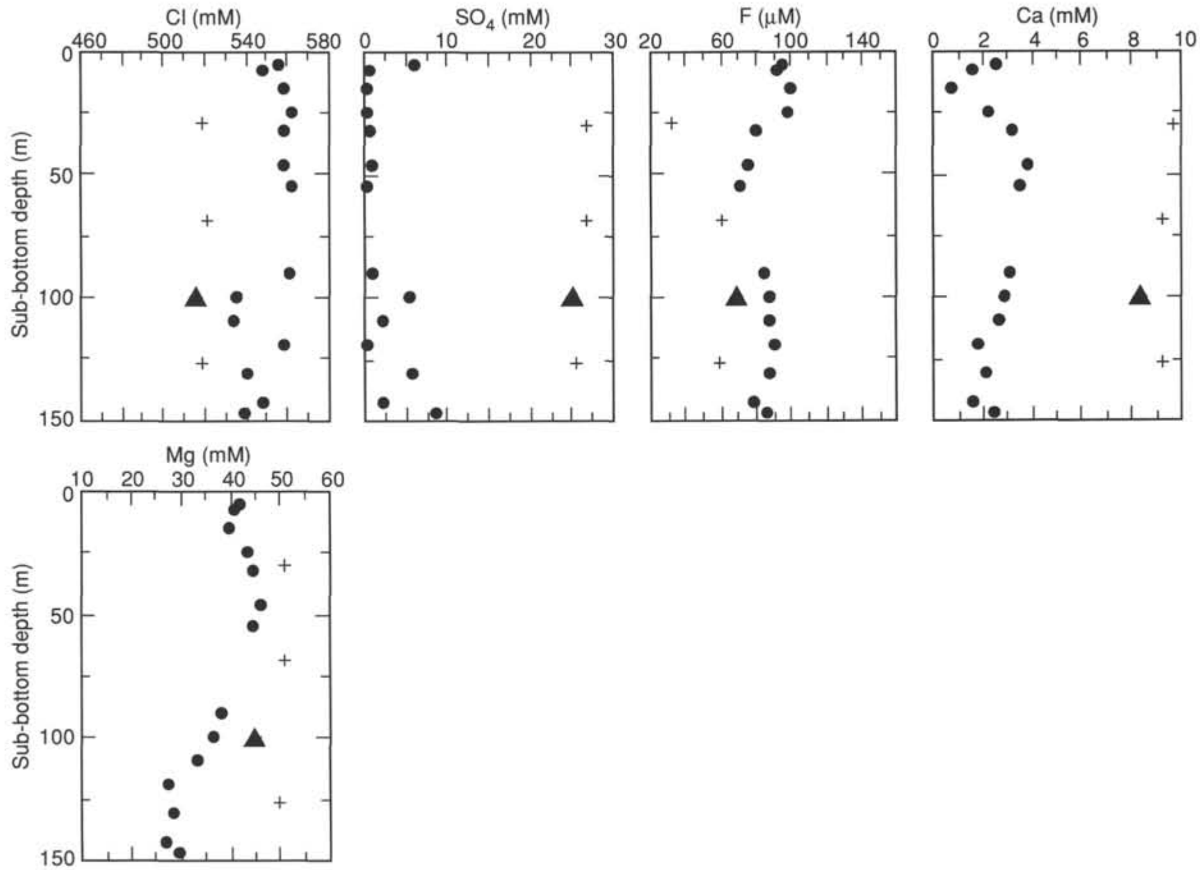

Figure 65. Comparison of interstitial water (IW) data from squeezed whole rounds (dots), from the WSTP (crosses) and from the PCS (triangles).

of 100°C/km. We have not extended it down to intersect the upper temperature limit of the gas hydrate stability field because we do not know if this temperature gradient remains constant below 60 mbsf (with a linear extrapolation it would intersect the stability field in the region of 160 mbsf). At Site 859, for example, the temperature gradient is 320°C/km in the top 40–50 mbsf but rapidly drops below this level. The rather poor constraint of the WSTP measurement at 126 mbsf (of 11.45°C) suggests that, indeed, the temperature gradient at Site 860 may similarly decrease with depth. The main conclusion that can be drawn from the temperature profile at Site 860 (which is in a mid accretionary-slope position) is that, over an equivalent depth range, the temperature gradient in the top 60 mbsf is approximately one third of that at Site 859 (at the wedge toe).

WIRELINE MEASUREMENTS

Introduction

The primary objective of downhole measurements at this site was the measurement of in-situ properties of rocks comprising the middle portion of the accretionary wedge. Of additional interest were the physical properties of a gas hydrate zone presumed to overlie a bottom-simulating reflector (BSR) observed on the site survey seismic profile. The lack of hydrate in the recovered cores, presumably due to drilling disturbance, allowed no direct characterization of its properties. Downhole measurements at this site had the potential to complement core observations for both characterization of the hydrate properties and distinction of the lith-

Table 20. Physical property index values for Site 860.

Core, section, interval (cm)	Depth (mbsf)	Wet bulk density (g/cm^3)	Grain density (g/cm^3)	Wet-sediment porosity (%)	Wet-sediment water-content (%)	Wet-sediment void ratio	Dry-sediment void ratio
141-860A-							
1H-1, 30–32	0.3	1.53	2.61	71.8	48.2	2.55	2.37
1H-2, 30–32	1.8	1.67	2.77	68.7	42.2	2.20	1.97
1H-2, 110–112	2.6	1.75	2.78	62.8	36.8	1.69	1.58
1H-4, 110–112	5.6	1.80	2.79	58.2	33.2	1.39	1.35
1H-3, 110–112	4.1	1.81	2.68	56.3	31.8	1.29	1.22
1H-6, 110–112	8.60	1.91	2.81	52.6	28.2	1.11	1.08
1H-7, 29–31	9.29	1.81	2.82	57.5	32.6	1.35	1.33
141-860B-							
1H-1, 100–102	1.0	1.58	2.71	71.6	46.5	2.53	2.3
1H-1, 30–32	0.3	1.46	2.66	76.5	53.6	3.26	2.99
2H-2, 115–117	4.05	1.89	2.76	53.5	29.0	1.15	1.10
2H-3, 111–113	5.51	1.79	2.76	58.8	33.7	1.43	1.37
2H-4, 59–61	6.49	1.83	2.84	58.9	33.1	1.43	1.37
2H-5, 96–98	8.36	1.94	2.84	53.9	28.5	1.17	1.10
2H-6, 98–100	9.88	1.89	2.69	53.7	29.1	1.16	1.08
3H-2, 100–102	13.4	1.88	2.76	55.2	30.0	1.23	1.15
3H-4, 100–102	16.4	1.91	2.79	52.6	28.1	1.11	1.07
3H-6, 100–102	19.4	1.89	2.77	54.0	29.2	1.18	1.11
3H-6, 70–72	19.1	2.06	2.81	47.9	23.8	0.92	0.86
4H-1, 100–102	21.4	2.04	2.86	46.4	23.4	0.87	0.85
4H-4, 100–102	25.9	1.92	2.73	51.8	27.6	1.08	1.02
4H-6, 100–102	28.9	2.02	2.72	45.5	23.0	0.83	0.79
5H-2, 100–102	32.4	2.03	2.75	49.0	24.7	0.96	0.88
5H-5, 90–92	36.8	2.02	2.77	47.2	23.9	0.89	0.85
5H-6, 71–73	38.11	1.99	2.75	48.7	25.1	0.95	0.90
6H-3, 19–21	42.59	2.77		0.80	0.78		
6H-3, 100–102	43.40	2.77		0.77	0.75		
6H-6, 24–26	47.14	2.93		0.49	0.55		
7H-1, 27–29	49.17	1.95	2.76	49.5	26.0	0.98	0.95
7H-1, 94–96	49.84	1.90	2.79	52.1	28.0	1.09	1.06
7H-2, 82–84	51.22	1.92	2.76	50.8	27.1	1.03	1.00
7H-3, 110–112	53.0	1.91	2.75	51.9	27.8	1.08	1.03
10X-0, 22–24	68.92	1.97	2.75	49.9	25.9	1.00	0.94
12X-1, 62–64	88.32	1.99	2.74	51.8	26.7	1.07	0.97
12X-2, 65–67	89.85	1.97	2.81	52.4	27.3	1.10	1.03
12X-3, 43–45	91.13	1.96	2.83	53.4	27.9	1.15	1.07
12X-4, 61–63	92.81	1.98	2.73	52.2	27.0	1.09	0.98
14X-1, 47–49	99.57	1.82	2.73	57.7	32.5	1.36	1.28
14X-2, 37–39	100.97	1.88	2.74	57.3	31.3	1.34	1.22
14X-0, 15–17	102.33	1.87	2.81	58.5	32.0	1.41	1.29
15X-1, 10–12	107.30	1.80	2.72	58.2	33.1	1.40	1.32
15X-3, 90–92	111.10	1.78	2.78	59.5	34.1	1.47	1.41
15X-4, 50–52	112.20	1.89	2.63	53.3	28.9	1.14	1.04
16X-1, 30–32	117.10	1.93	2.84	51.5	27.4	1.06	1.05
16X-0, 3–5	120.44	1.96	49.5	25.9	0.98	1.04	
17X-2, 34–36	128.34	2.11	2.82	43.1	20.9	0.76	0.73
17X-0, 2–3	133.72	1.96	2.75	51.9	27.1	1.08	1.00
19X-1, 130–132	138.40	2.05	2.68	49.7	24.9	0.99	0.87
19X-2, 130–132	139.90	1.94	2.70	55.9	29.5	1.27	1.10
19X-5, 40–42	143.50	2.04	2.76	46.0	23.1	0.85	0.81
20X-1, 50–52	146.30	1.99	2.91	47.6	24.5	0.91	0.92
20X-0, 10–12	148.03	2.11	2.81	42.9	20.9	0.75	0.72
21X-1, 87–89	156.37	2.09	2.80	41.8	20.4	0.72	0.70
21X-0, 8–10	156.92	2.00	2.72	45.3	23.2	0.83	0.80
22X-1, 120–122	166.30	2.09	2.73	43.9	21.4	0.78	0.73
22X-2, 70–72	167.30	2.09	2.80	41.7	20.5	0.72	0.70
22X-3, 35–37	168.45	2.09	2.83	43.2	21.2	0.76	0.74
22X-0, 24–26	169.15	2.13	2.76	44.5	21.4	0.80	0.74
24X-0, 9–11	186.46	2.10	2.76	44.9	21.9	0.81	0.75
25X-1, 100–102	195.10	2.10	2.80	42.3	20.6	0.73	0.71
25X-0, 12–14	196.41	2.14	2.81	39.3	18.8	0.65	0.63
28X-1, 20–22	223.30	2.14	2.78	41.2	19.7	0.70	0.66
28X-0, 16–18	224.47	2.23	2.75	34.7	15.9	0.53	0.51
29X-2, 14–16	234.44	2.10	2.80	41.9	20.4	0.72	0.70
29X-1, 55–57	233.35	2.17	2.82	40.0	18.9	0.67	0.64
30X-1, 20–24	242.70	2.26	2.82	34.9	15.8	0.54	0.52

ologic units. That potential was not realized in Hole 860B due to operational difficulties (see Operations section, this chapter). Two attempts were made to log with the gamma-ray, sonic, and resistivity tools, but only 100 m of the upper part of the open hole were logged. The Lamont temperature tool (TLT) was run both times, obtaining temperature data in drill pipe from the surface to the total depth of the hole.

Log Quality

The large size of the washed-out borehole was the primary factor in degrading the logs from Hole 860B. The caliper and gamma-ray logs were particularly affected. The sonic and resistivity tools, which are affected less than other tools by the size and rugosity of the borehole, recorded good-quality data. The

Table 20 (continued).

Core, section, interval (cm)	Depth (mbsf)	Wet bulk density (g/cm^3)	Grain density (g/cm^3)	Wet-sediment porosity (%)	Wet-sediment water-content (%)	Wet-sediment void ratio	Dry-sediment void ratio
141-860B- (Cont.)							
30X-3, 20–22	244.77	2.21	2.87	39.9	18.5	0.66	0.64
31X-2, 25–26	253.65	2.05	2.66	41.5	20.7	0.71	0.68
32X-1, 20–21	261.80	2.13	2.80	36.4	17.5	0.57	0.58
32X-2, 80–81	263.16	2.17	2.80	38.7	18.3	0.63	0.61
33X-1, 120–122	272.40	2.12	2.76	40.5	19.6	0.68	0.65
33X-2, 20–22	272.90	2.18	2.85	40.3	19.0	0.67	0.65
34X-1, 26–28	281.06	2.18	2.81	39.5	18.6	0.65	0.63
34X-2, 28–30	282.58	2.15	2.81	40.2	19.1	0.67	0.65
34X-3, 28–30	284.08	2.14	2.80	44.1	21.1	0.79	0.73
34X-4, 24–26	285.04	2.15	2.79	40.7	19.4	0.69	0.66
34X-0, 11–13	285.53	2.18	2.81	42.2	19.8	0.73	0.68
35X-1, 76–78	291.16	2.23	2.79	35.8	16.5	0.56	0.54
35X-0, 10–12	291.95	2.22	2.75	35.1	16.2	0.54	0.52
36X-1, 16–18	300.26	2.16	2.89	39.8	18.9	0.66	0.66
36X-3, 36–38	303.46	2.20	2.80	40.3	18.8	0.68	0.63
36X-4, 24–26	304.34	2.26	2.76	36.1	16.4	0.56	0.53
38X-1, 58–60	319.98	2.22	2.78	36.8	17.0	0.58	0.56
38X-2, 21–23	321.02	2.13	2.72	38.8	18.7	0.63	0.61
39X-1, 110–112	329.80	2.21	2.74	35.6	16.5	0.55	0.53
40X-0, 14–16	338.54	2.09	2.80	41.2	20.2	0.70	0.69
41X-1, 144–146	349.44	2.29	2.75	32.3	14.4	0.48	0.45
41X-4, 100–102	353.50	2.25	2.75	36.2	16.5	0.57	0.53
43X-1, 26–28	359.46	2.19	2.80	36.4	17.0	0.57	0.56
46X-1, 60–62	387.20	2.18	2.66	39.5	18.5	0.65	0.59
46X-2, 32–34	388.21	2.23	2.80	36.7	16.9	0.58	0.55
46X-0, 25–27	389.18	2.33	2.83	31.5	13.8	0.46	0.44
47X-0, 23–25	396.53	2.12	2.82	40.4	19.5	0.68	0.67
47X-0, 49–50	396.79	2.23	2.78	37.1	17.1	0.59	0.56
48X-1, 25–27	406.25	2.23	2.72	33.0	15.2	0.49	0.47
48X-2, 3–5	407.53	2.30	2.77	34.4	15.4	0.53	0.49
48X-3, 30–32	408.34	2.28	2.78	33.3	14.9	0.50	0.48
48X-4, 55–57	410.09	2.26	2.81	34.3	15.5	0.52	0.50
48X-5, 37–40	411.41	2.29	2.78	33.9	15.2	0.51	0.48
49X-1, 18–20	415.88	2.21	2.72	36.0	16.7	0.56	0.53
49X-0, 31–33	416.75	2.17	2.76	38.7	18.3	0.63	0.61
50X-1, 80–82	426.10	2.21	2.81	35.8	16.6	0.56	0.55
50X-4, 62–64	429.57	2.21	2.84	38.3	17.7	0.62	0.60
50X-0, 32–34	430.83	2.14	2.76	40.9	19.6	0.69	0.66
51X-1, 38–40	435.18	2.19	2.70	38.1	17.8	0.61	0.57
51X-2, 100–102	437.30	2.26	2.69	32.6	14.8	0.48	0.45
52X-0, 19–21	444.59	2.19	2.76	37.8	17.6	0.61	0.58
53X-1, 85–87	449.95	2.23	2.85	34.7	16.0	0.53	0.53
53X-2, 82–84	451.42	2.36	2.79	31.2	13.5	0.45	0.43
58X-1, 4–7	492.84	2.21	2.67	33.8	15.7	0.51	0.48
58X-1, 71–73	493.51	2.37	2.74	28.2	12.2	0.39	0.37
58X-2, 51–53	494.81	2.25	2.63	34.7	15.8	0.53	0.48
60X-1, 66–68	512.66	2.27	2.78	35.0	15.8	0.54	0.51
60X-2, 62–64	514.12	2.19	2.70	34.6	16.2	0.53	0.51
60X-3, 50–52	514.90	2.41	2.73	35.0	14.9	0.54	0.47
60X-4, 48–50	516.38	2.18	2.77	32.6	15.3	0.48	0.49
61X-3, 65–67	525.35	2.34	2.78	30.8	13.5	0.44	0.42
61X-5, 95–97	528.65	2.29	2.79	31.6	14.1	0.46	0.45
61X-0, 15–17	531.30	2.25	2.78	34.8	15.8	0.53	0.51
62X-1, 70–72	531.60	2.20	2.81	34.8	16.2	0.53	0.53
62X-3, 96–98	534.86	2.33	2.78	29.7	13.1	0.42	0.41
64X-1, 78–100	550.98	2.26	2.74	32.7	14.8	0.48	0.47
64X-2, 32–34	552.02	2.25	2.77	33.6	15.3	0.51	0.49
64X-3, 65–67	552.85	2.41	2.87	32.6	13.9	0.48	0.45
66X-1, 71–73	570.21	2.20	2.79	36.6	17.1	0.58	0.56
66X-2, 91–93	571.91	2.33	2.73	31.8	14.0	0.47	0.43
66X-0, 9–11	572.09	2.48	2.86	31.0	12.8	0.45	0.41
67X-1, 122–124	580.42	2.23	2.74	39.1	18.0	0.64	0.59
67X-2, 91–93	581.61	2.21	2.70	35.6	16.5	0.55	0.52
67X-3, 91–93	583.11	2.24	2.77	35.9	16.4	0.56	0.53
67X-4, 38–40	584.08	2.29	2.72	34.4	15.4	0.52	0.49
70X-0, 24–25	608.44	2.32	2.80	37.0	16.3	0.59	0.53

sonic tool is capable of providing accurate measurements in large boreholes. As long as the tool is no less than 76 cm from the formation, the first arrival at the receiver will travel through the formation rather than through the borehole fluid, and provide good results. The deep-penetration resistivity tool probes up to 2 m into the formation. The borehole at Hole 860B was washed out to nearly 35 cm between 72 and 120 mbsf, and to greater than 40.7 cm, the maximum range of the caliper, between 120 mbsf and the deepest penetration of the tool at 185 mbsf.

The depth calibration of the logs is somewhat uncertain due to difficulties encountered in conducting logging operations (see Operations section, this chapter). The difficulty encountered in re-entering the drill pipe at the end of the logging run led to uncertainty in the depth estimate of the gamma-ray, sonic, and resistivity logs. The absolute depth is usually determined by correlating the drillers' figures of pipe length with the entry of the tool string into the pipe. The uncertainty in the depth estimate on these logs stems largely from the difficulty in determining where

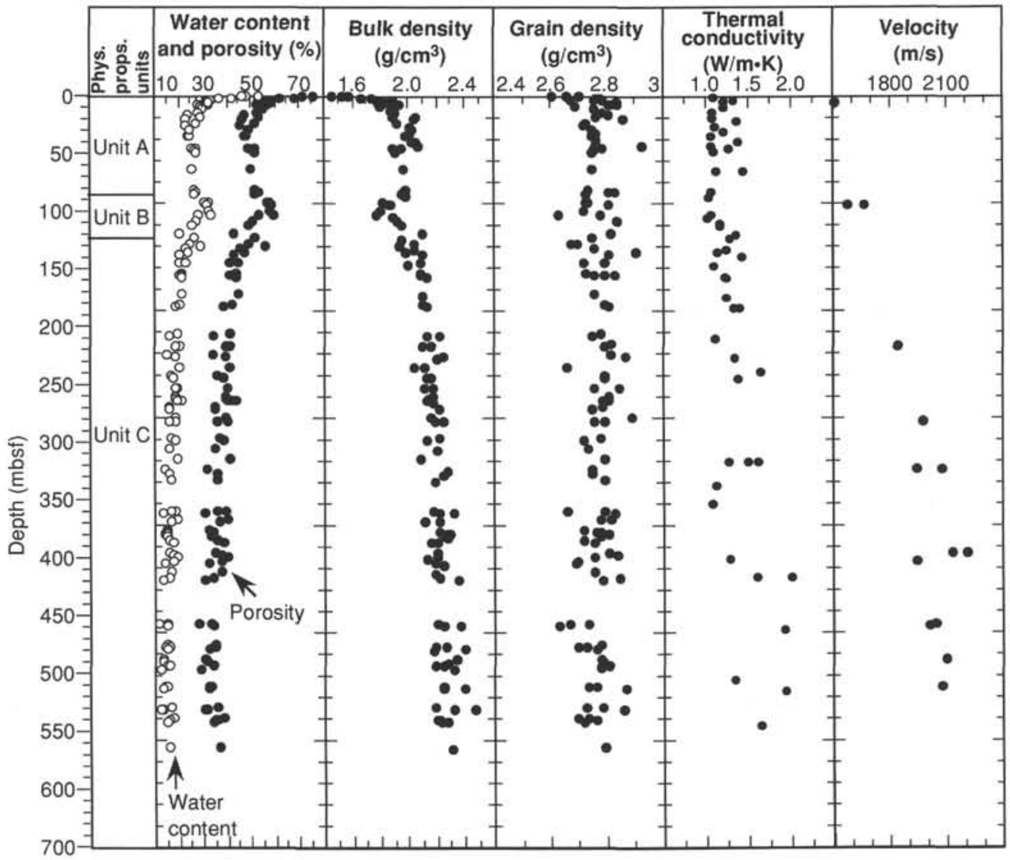

Figure 66. Index properties, thermal conductivity, and Hamilton-Frame velocity, V_p, at Site 860.

on the logs the tool string entered the pipe, because the top of the tool string did not enter the pipe normally, but became snagged on the bottom of the drill string. The logs were positioned in depth assuming that the cable tension log indicates where the top of the tool became snagged at the bottom of the pipe. The possible scenarios of how the tool could have snagged shift the position of the log by no more than 1 m. With the heave compensator off during the reentry of the tool into the pipe, the ship's motion may also have contributed an additional ± 2 m of depth uncertainty. The data that appear on the logs above 72 m were recorded as the cable was stretched and are not recorded on the logs at the proper depth. These data are disregarded.

The depth calibration of the temperature logs recorded during the first run are also subject to error due to the uncertainty in determining the position of the tool string. Depth was determined using the pressure recorded in the TLT, and a depth vs. pressure table was derived from pressure readings at depths noted during logging.

During the second log run, temperatures were recorded from the surface to the bottom of the borehole. All of these values were recorded while the tool was inside the drill pipe and may not accurately reflect the temperature of the borehole because of the isolation of the TLT in the pipe and the thermal influence of the pipe. The depth calibration of these data was difficult because of the uncertainty of the effect on the apparent pressure when the tool is moving inside the drill pipe. Large oscillations of pressure are observed that are believed to be caused by the restricted flow of borehole fluid through the narrow passage between the tool and the pipe. Individual pressure readings are not believed to be an accurate indicator of depth. A 30-point running average was used to smooth the pressure values before converting them to depth with the depth vs. pressure table. Comparison of the temperatures from the two runs (Fig. 76) shows reasonable agreement between the first run and the return trip of the TLT during the second run. We believe the higher temperatures recorded during the upward trip are more accurate than those recorded during the descent of the tool.

Logging Results

We use the log data to define three separate log units (Fig. 77) within the uppermost 180 m of Hole 860B. These units are defined mainly using the sonic and resistivity logs directly, and to some extent the porosity logs derived from them. Pronounced changes on the logs at similar depths formed the distinctive boundaries between the logging units.

Log Unit 1—72 (shallowest data point) to 120 mbsf

This unit is characterized by a reasonably uniform seismic velocity between 1.7 and 1.8 km/s, as shown in both the near and far receiver sonic logs. A small decrease in velocity within the middle of the unit, at approximately 100 mbsf, indicates an increase in porosity as seen in both the sonic porosity and the resistivity porosity logs and, as observed in the core porosity measurements (see Physical Properties section, this chapter). The resistivity of this unit lies between 1 and 1.5 ohm·m with the lowest values near the bottom of the interval. All three resistivity logs are similar, suggesting low formation penetration of borehole fluid.

Log Unit 2—120 to 158 mbsf

Unit 2 is characterized by a pronounced increase in both the seismic velocity and the resistivity relative to the values above

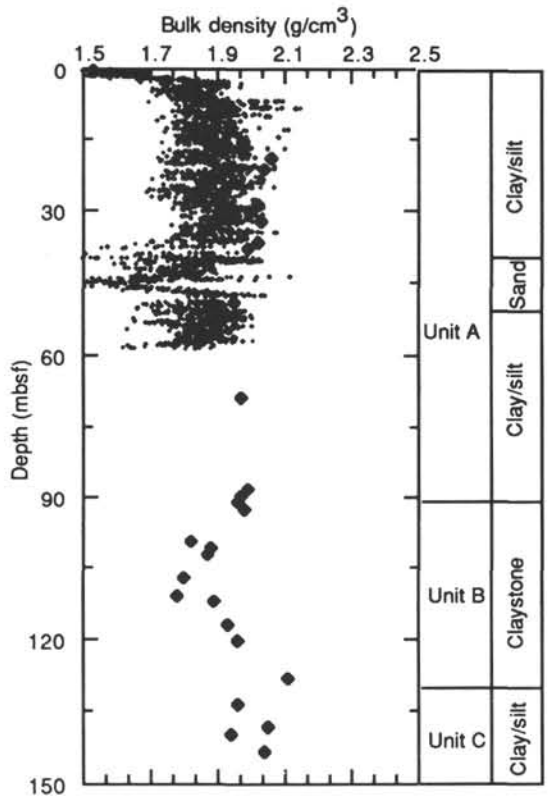

Figure 67. Grape and discrete sample bulk density, Site 860. Discrete samples shown by diamonds, GRAPE bulk-density data are the small dots. General lithologies and physical properties unit boundaries are marked.

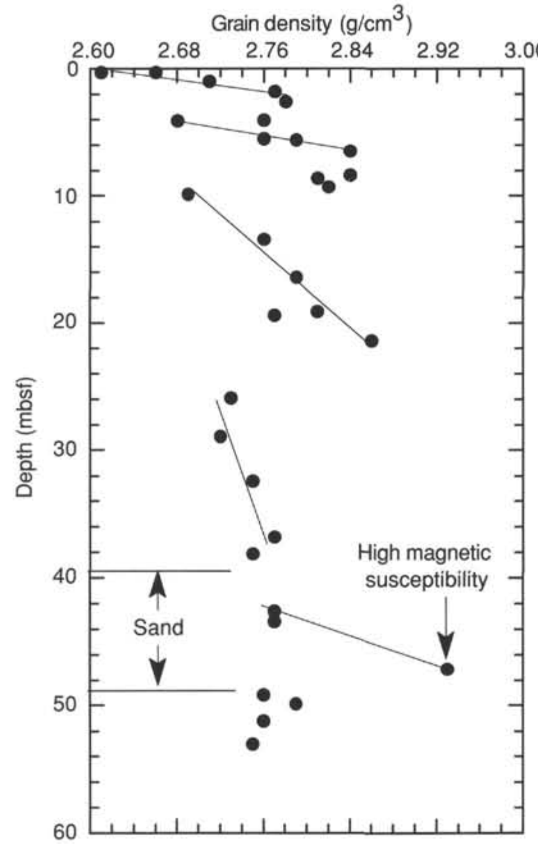

Figure 68. Grain density data, 0–60 mbsf, at Site 860.

and below this interval. Seismic velocities are generally between 1.85 and 1.9 km/s and show considerably more variability than in the overlying unit. The increase in velocity is believed to reflect the greater lithification of the siltstone and claystone observed in the recovered cores (see Physical Properties section, this chapter). Resistivity is also higher within this unit, and there is a difference between deep and shallow resistivity values. This presumably reflects the greater penetration of the less-resistive borehole fluid into the formation.

Log Unit 3–158 to 180 mbsf (the deepest penetration of the logging toolstring)

Resistivities and sonic velocities within the unit are extremely low (1 ohm·m and 1.6 km/s, respectively). The velocities recorded are sufficiently low that we suspect that these values may reflect properties of the borehole fluid rather than those of the formation. Values at the top and bottom of the unit are more reasonable for these depths. If the interval is washed out more than 1.5 m, then arrivals traveling through the borehole are received earlier than those traveling through the formation, and velocities of this interval will reflect those of the borehole fluid. Arrivals traveling through the formation may also be attenuated and scattered and not produce a clear signal at the receiver due to excessive washout and hole rugosity. In that case, the first arrivals detected at the receiver may be arrivals that travel through the borehole fluid. The sand content was observed to increase within this interval, making it more prone to washout; however, much of the interval was a zone of poor recovery and the lithology is not well constrained (see Lithostratigraphy section, this chapter).

Downhole Temperature Measurements

Two runs of the TLT downhole temperature tool produced results from a shallow run (to 185 mbsf) and a deep run to the bottom of the hole at 607 mbsf (Fig. 76). The best agreement between the overlapping sections of these runs occurs on the upward trips of the tool rather than the downward trips. The thermal gradient is 70°C/km in the top 100 m of the borehole and 35°C/km below 100 mbsf. The break in the thermal gradient implies either a decrease in the thermal conductivity of the upper section or advective flow of warm fluids into the uppermost strata. The geochemical anomalies indicate little possibility of vertical fluid flow (see Inorganic Chemistry section, this chapter). Lateral flow of warm fluids is a possible model that satisfies both the thermal and geochemical constraints.

SUMMARY AND CONCLUSIONS

Site 860 is the central site of a set of three sites across the trench slope near the Chile margin triple junction. Site 860 is located on the seaward flank of a small forearc basin underlain by deformed and accreted forearc material and by the continental basement of South America (Fig. 1; location in Fig. 78). The objectives at Site 860 were to determine the lithologies and depositional environment(s) of the sediment sequences of the forearc basin, to determine the vertical-motion history at this mid-slope position in the forearc, and to determine the lithology and age of the basement underlying the forearc basin.

The most prominent, relatively continuous seismic reflector that can be resolved beneath the mid- and upper- slope region of

Table 21. Thermal conductivity data from Site 860.

Core, section, interval (cm)	Depth (mbsf)	Probe type	Thermal conductivity (W/m·K)
141-860B-			
1H-1, 35	0.35	FS	1.0813
2H-3, 100	5.40	FS	1.2008
2H-6, 100	9.90	FS	1.1976
2H-2, 100	3.90	FS	1.3135
3H-3, 100	14.90	FS	1.0636
3H-6, 100	19.40	FS	1.0705
4H-2, 100	22.90	FS	1.3660
4H-6, 64	28.54	FS	1.0943
5H-2, 92	32.32	FS	1.2014
5H-5, 88	36.78	FS	1.0559
6H-2, 99	41.89	FS	1.3739
6H-5, 100	46.40	FS	1.0584
6H-6, 90	47.80	FS	1.2542
7H-2, 95	51.35	FS	1.0826
10X-0, 28	68.98	FS	1.1072
10X-0, 37	69.07	FS	1.4359
12X-1, 41	88.11	FS	1.0499
12X-4, 100	93.20	FS	1.0181
15X-2, 100	109.70	FS	1.0490
15X-4, 100	112.70	FS	1.0154
16X-1, 100	117.80	FS	1.1595
16X-3, 26	120.06	FS	1.1498
17X-2, 100	129.0	FS	1.3526
17X-4, 100	132.00	FS	1.2716
19X-4, 100	142.60	FS	1.2344
19X-5, 100	144.10	FS	1.1229
20X-0, 10	148.03	FS	1.4279
21X-0, 10	156.94	FS	1.0891
22X-2, 100	167.60	FS	1.2192
22X-0, 6	168.97	FS	1.2360
24X-0, 23	186.60	FS	1.2232
25X-2, 50	196.10	FS	1.3219
25X-0, 25	196.54	FS	1.3919
28X-0, 16	224.47	FS	1.0924
30X-1, 24	242.74	FS	1.3314
31X-3, 75	255.65	FS	1.6349
32X-1, 14	261.74	FS	1.3712
40X-0, 14	338.54	FS	1.6082
40X-0, 14	338.54	FS	1.5002
42X-1, 10	357.80	FS	1.2407
40X-0, 14	338.54	FS	1.2583
43X-0, 15	361.03	FS	1.1152
45X-0, 34	377.24	FS	1.0660
50X-3, 15	428.45	FS	1.2726
52X-0, 25	444.65	FS	2.0114
52X-0, 25	444.65	FS	1.5987
58X-1, 83	493.63	HS	1.9156
63X-0, 7	540.57	FS	1.3304
64X-1, 82	551.02	FS	1.9287
67X-3, 43	582.63	HS	1.6369

Note: FS = full-space, HS = half-space determination.

Table 22. P-wave velocity data, Site 860.

Core, section, interval (cm)	Depth (mbsf)	Velocity (m/s)
141-860B-		
2H-4, 70	6.60	1512.0
14X-2, 56	101.16	1583.0
14X-2, 62	101.22	1675.0
29X-2, 14	234.44	1853.0
36X-0, 4	304.66	1978.0
41X-1, 132	349.32	1946.0
41X-2, 60	350.10	2085.0
50X-1, 138	426.68	2213.0
50X-2, 10	426.90	2140.0
51X-1, 38	435.18	1953.0
58X-1, 88	493.68	2051.0
58X-2, 125	495.55	2011.0
61X-3, 65	525.35	2101.0
64X-1, 52	550.72	2078.0

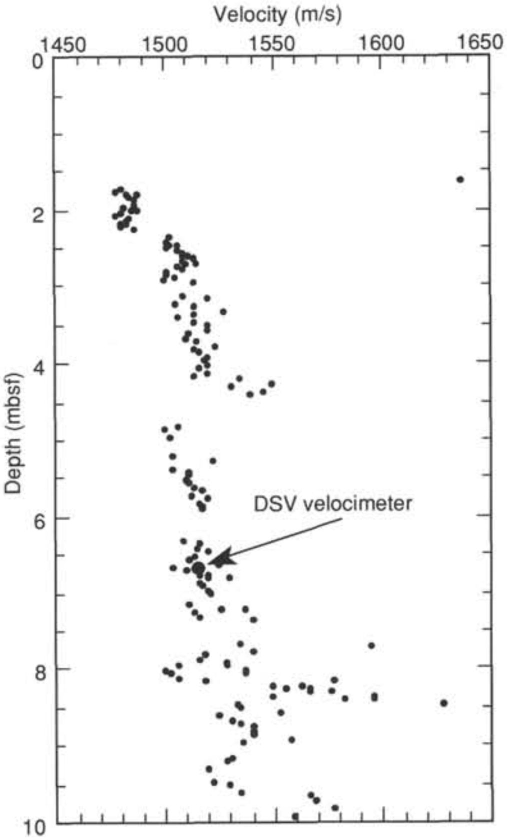

Figure 69. *P*-wave logger and DSV velocimeter data, 0–10 mbsf, Site 860.

the forearc occurs at approximately 0.7 s sub-bottom at the landward end of Line 745 (Fig. 1). It can be traced seaward to within about 6 km of the base of the trench slope. This reflector, offset by a series of normal faults landward of Site 860 near CDP 1800, was interpreted prior to drilling to be continental basement in this region. Although the basement reflector was not penetrated at Site 860, other downhole observations indicate that this reflector most likely represents continental basement.

The normal faults in the mid-slope region strongly suggest that this portion of the margin is subsiding, presumably through the removal of forearc material as the ridge-trench collision progresses. If so, then the record of that subsidence should be preserved in the sedimentary record of the forearc basin at Site 860. The combination of lithofacies analysis in terms of depositional environment and paleontological age dating and paleowater depth determinations should provide the observations necessary to constrain the vertical-motion history of this segment of the forearc during the time up to and including ridge subduction.

Drilling at Site 860 (Fig. 79) sampled the seaward flank of a forearc basin and the accretionary wedge upon which the forearc basin sediments were deposited. The ages of both the forearc basin strata and the fault wedges drilled in the underlying accretionary wedge range from late Pliocene to early Pliocene, with about 70 m of Quaternary slope hemipelagic material overlying the older units (Fig. 80). The Pliocene age of this portion of the accretionary wedge is identical, within the biostratigraphic age resolution, to that drilled at Site 859, at the base of the trench slope. The age of formation of the accretionary wedge at both Sites 859 and 860 corresponds to a period of rapid uplift and shallowing of paleowater depths on the shelf in this region.

Lithologic Unit I, 0–87.7 mbsf, is of late Pliocene to Quaternary age. This unit is composed of clayey silt to silty clay with

Table 23. Velocity measurements on discrete samples.

Core, section, interval (cm)	Depth (mbsf)	Velocity (m/s)	Core, section, interval (cm)	Depth (mbsf)	Velocity (m/s)
141-860A-			141-860A- (Cont.)		
1H-2, 12	1.62	1636.0	1H-4, 112	5.62	1514.0
1H-2, 22	1.72	1479.9	1H-4, 117	5.67	1517.4
1H-2, 24	1.75	1479.9	1H-4, 122	5.72	1512.3
1H-2, 27	1.77	1478.2	1H-4, 127	5.77	1519.2
1H-2, 29	1.79	1487.3	1H-4, 132	5.82	1516.5
1H-2, 32	1.82	1483.1	1H-4, 137	5.87	1517.4
1H-2, 34	1.85	1484.0	1H-4, 142	5.92	1517.4
1H-2, 37	1.87	1486.5	1H-5, 32	6.32	1508.0
1H-2, 44	1.95	1486.5	1H-5, 37	6.37	1515.7
1H-2, 47	1.97	1481.6	1H-5, 42	6.42	1514.8
1H-2, 49	2.0	1487.4	1H-5, 47	6.47	1519.1
1H-2, 52	2.02	1484.9	1H-5, 52	6.52	1513.1
1H-2, 54	2.05	1480.0	1H-5, 57	6.57	1510.6
1H-2, 57	2.07	1478.4	1H-5, 62	6.62	1513.1
1H-2, 59	2.10	1478.4	1H-5, 67	6.67	1503.8
1H-2, 62	2.12	1484.1	1H-5, 72	6.72	1509.8
1H-2, 64	2.14	1483.2	1H-5, 77	6.77	1520.0
1H-2, 67	2.17	1480.7	1H-5, 82	6.82	1520.0
1H-2, 69	2.19	1482.4	1H-5, 87	6.87	1515.7
1H-2, 72	2.22	1480.7	1H-5, 92	6.92	1516.6
1H-2, 74	2.25	1486.4	1H-5, 97	6.97	1519.2
1H-2, 84	2.35	1502.9	1H-5, 102	7.02	1520.9
1H-2, 92	2.42	1501.3	1H-5, 117	7.17	1510.7
1H-2, 94	2.45	1505.5	1H-5, 122	7.22	1526.0
1H-2, 97	2.47	1503.0	1H-5, 127	7.27	1514.0
1H-2, 99	2.50	1500.6	1H-5, 132	7.32	1515.7
1H-2, 102	2.52	1505.6	1H-6, 17	7.67	1533.8
1H-2, 107	2.57	1508.3	1H-6, 22	7.72	1594.4
1H-2, 109	2.60	1509.1	1H-6, 27	7.77	1539.9
1H-2, 112	2.62	1510.7	1H-6, 32	7.82	1518.3
1H-2, 114	2.64	1513.2	1H-6, 37	7.87	1516.5
1H-2, 117	2.67	1509.1	1H-6, 42	7.92	1527.7
1H-2, 119	2.70	1514.1	1H-6, 47	7.97	1527.7
1H-2, 122	2.72	1509.9	1H-6, 52	8.02	1536.4
1H-2, 124	2.75	1506.5	1H-6, 57	8.07	1536.4
1H-2, 127	2.77	1508.2	1H-6, 67	8.17	1576.8
1H-2, 129	2.80	1501.5	1H-6, 72	8.22	1562.2
1H-2, 132	2.82	1500.6	1H-6, 77	8.27	1555.8
1H-2, 134	2.85	1501.4	1H-6, 82	8.32	1566.7
1H-2, 137	2.87	1504.7	1H-6, 87	8.37	1595.4
1H-2, 139	2.89	1504.7	1H-6, 92	8.42	1596.3
1H-2, 142	2.92	1500.5	1H-6, 97	8.47	1532.9
1H-2, 144	2.95	1513.2	1H-6, 102	8.52	1534.6
1H-3, 12	3.12	1508.8	1H-6, 107	8.57	1553.2
1H-3, 17	3.17	1519.0	1H-6, 112	8.62	1525.1
1H-3, 22	3.22	1504.5	1H-6, 117	8.67	1531.1
1H-3, 27	3.27	1513.9	1H-6, 122	8.72	1533.8
1H-3, 32	3.32	1526.8	1H-6, 127	8.77	1539.9
1H-3, 37	3.37	1513.1	1H-6, 132	8.82	1540.0
1H-3, 42	3.42	1505.5	1H-6, 137	8.87	1540.0
1H-3, 47	3.47	1513.2	1H-6, 142	8.92	1557.7
1H-3, 52	3.52	1519.2	1H-6, 147	8.97	1535.6
1H-3, 57	3.57	1519.2	1H-7, 17	9.17	1531.1
1H-3, 62	3.62	1511.5	1H-7, 22	9.22	1527.6
1H-3, 67	3.67	1509.7	1H-7, 32	9.32	1519.1
1H-3, 72	3.72	1514.8			
1H-3, 77	3.77	1523.3	141-860B-		
1H-3, 82	3.82	1513.1	2H-4, 72	6.62	1524.5
1H-3, 87	3.87	1515.7	2H-4, 87	6.77	1515.9
1H-3, 92	3.92	1519.9	2H-4, 92	6.82	1529.6
1H-3, 97	3.97	1518.2	2H-4, 132	7.22	1537.4
1H-3, 102	4.02	1519.9	2H-4, 147	7.37	1540.9
1H-3, 107	4.07	1515.7	2H-5, 57	7.97	1505.9
1H-3, 112	4.12	1519.9	2H-5, 62	8.02	1500.0
1H-3, 117	4.17	1513.1	2H-5, 67	8.07	1502.4
1H-3, 122	4.22	1533.8	2H-5, 72	8.12	1505.8
1H-3, 127	4.27	1549.6	2H-5, 77	8.17	1518.4
1H-3, 132	4.32	1531.2	2H-5, 82	8.22	1549.7
1H-3, 137	4.37	1545.2	2H-5, 87	8.27	1566.6
1H-3, 142	4.42	1539.1	2H-5, 92	8.32	1576.7
1H-4, 32	4.82	1505.5	2H-5, 97	8.37	1549.7
1H-4, 37	4.87	1500.5	2H-5, 102	8.42	1582.2
1H-4, 47	4.97	1502.2	2H-5, 107	8.47	1627.7
1H-4, 72	5.22	1503.7	2H-6, 57	9.47	1521.9
1H-4, 77	5.27	1521.6	2H-6, 62	9.52	1529.6
1H-4, 87	5.37	1503.8	2H-6, 72	9.62	1533.9
1H-4, 92	5.42	1511.5	2H-6, 77	9.67	1566.6
1H-4, 97	5.47	1511.5	2H-6, 82	9.72	1568.5
1H-4, 102	5.52	1509.8	2H-6, 92	9.82	1577.6
1H-4, 107	5.57	1510.7	2H-6, 102	9.92	1558.5

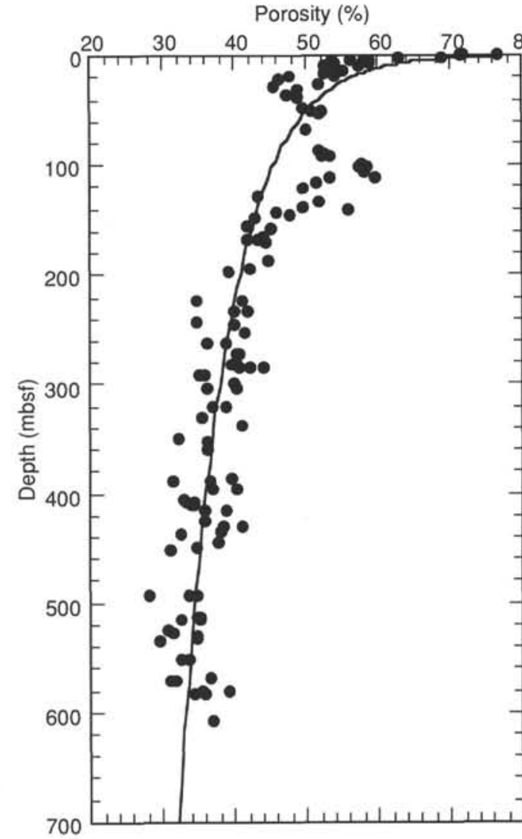

$Y = M0 * e^{M1 * X}$	
M0	78810.4824
M1	-0.14661401412
R	0.82587710385

Figure 70. Porosity plotted against a general best-fit Athy-type exponential relationship.

nannofossils, and contains graded silt and sand interbeds. One 10-m-thick massive sand unit occurs at the base of the unit. Unit II, defined between 87.7 and 242.5 mbsf, is of early Pliocene to late Pliocene age with lithologies that include claystone to silty claystone as well as sandstone and thin conglomerate beds. Subunit IIIA, between 242.5 and 309.8 mbsf, is of early Pliocene to late Pliocene age. Lithologies include clayey siltstone, silty claystone with nannofossils, and sandy silty claystone with thin conglomerate beds. Subunit IIIB occurs between 309.8 mbsf and the bottom of the hole at 617.8 mbsf. The age of Subunit IIIB is early Pliocene to late Pliocene, with lithologies that include gravel, clayey siltstone, silty claystone, and sandy silty claystone in three intervals. Three thin conglomerate beds also occur in this unit.

The upper section of lithologic Unit I is interpreted to be the result of hemipelagic sedimentary processes, with high- and low-density distal (fine-grained) turbidites dominating the lower section. The massive sand unit that defines the base of Unit I is the result of a single grain-flow depositional event.

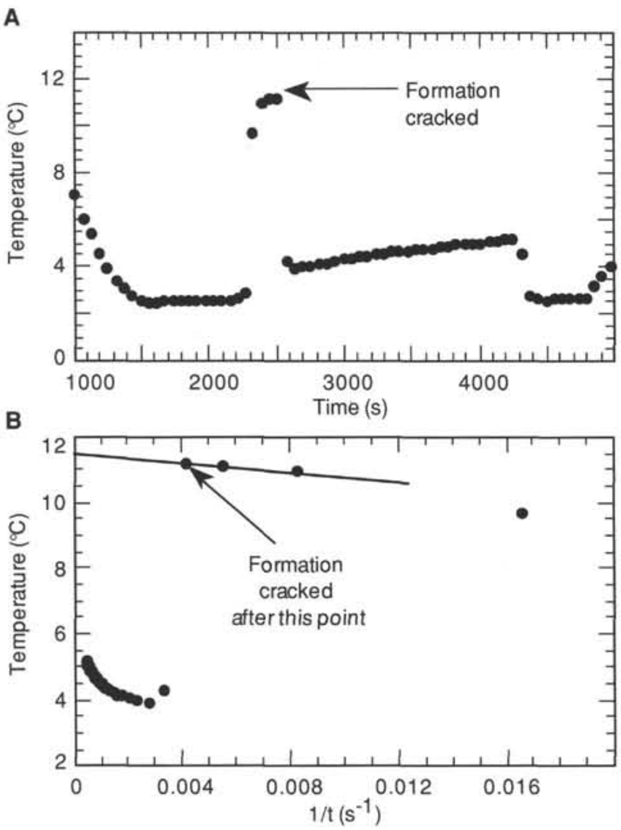

Figure 71. WSTP temperature measurement at 126.5 mbsf, Site 860B. The formation cracked or the temperature probe was pulled out of the formation 4 min after penetration. **A.** Deployment temperature record. **B.** 1/t fit.

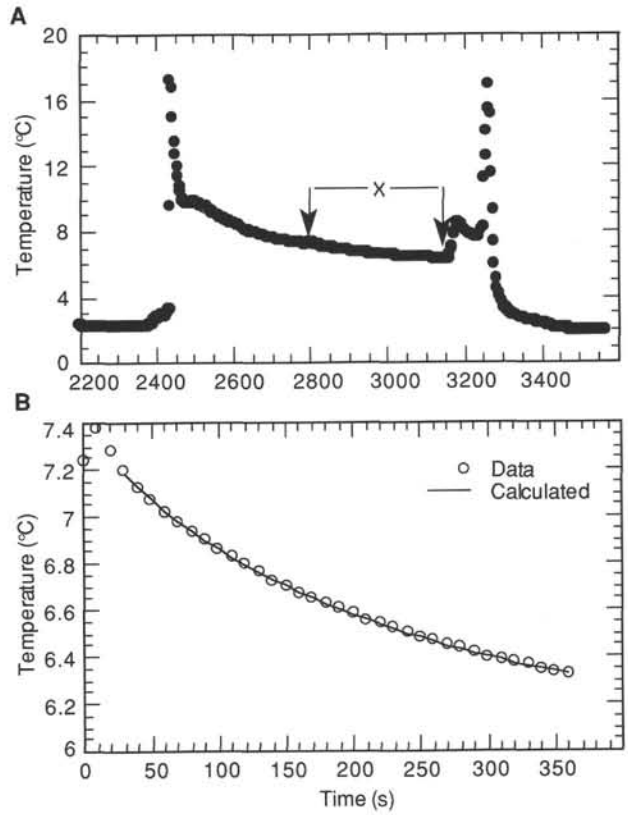

Figure 72. ADARA deployment record at 29.9 mbsf, Site 860B. The fitted portion (**B**) is marked (x) on (**A**), the deployment record.

Table 24. Temperature data for Site 860.

Depth (mbsf)	Temperature (°C)	Error (± °C)
0.0	2.2	
29.9	5.4	0.3
48.9	7.4	0.3
58.4	8.97	0.08

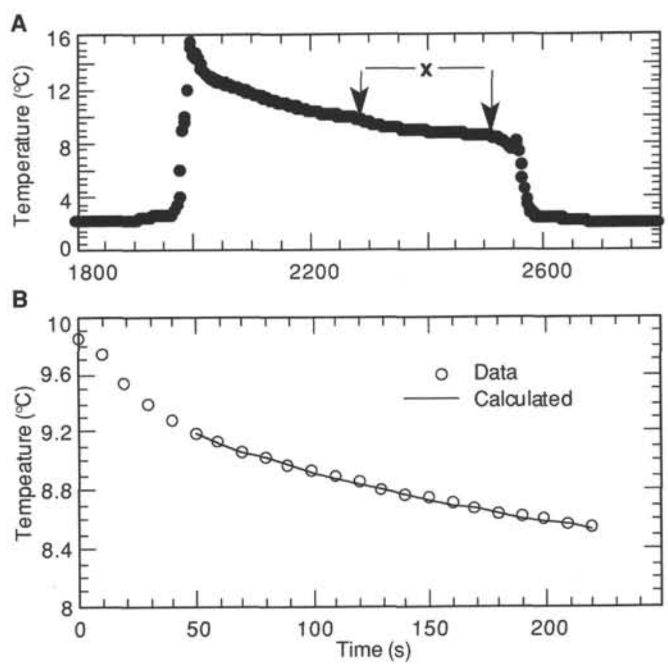

Figure 73. ADARA deployment record at 48.9 mbsf, Site 860B. The fitted portion (**B**) is marked (x) on (**A**), the deployment record.

Lithologic Unit II is characterized in its upper section by hemipelagic sedimentation mixed with mud turbidite deposition. Unit II also exhibits evidence of traction transport and reworking by bottom current flow.

The upper part of Subunit IIIA is characterized by hemipelagic and fine-grained turbidite depositional units, with the lower part of the subunit composed of high-density fine-grained turbidites with signs of reworking. Subunit IIIB exhibits a grain-flow event accompanied by background hemipelagic deposition in its upper section, with successions of high-density fine-grained turbidites in its lower section. Subunit IIIB also shows signs of bottom-current reworking. Lithologic Unit III contains at least five repetitions of sedimentary sequences. This is likely the result of imbrication by thrust faults.

The Pliocene/Pleistocene boundary occurs at about 70 mbsf, with the depth interval 70 mbsf to the bottom of Hole 860B at 617.8 mbsf of Pliocene age. Two biostratigraphically constrained age reversals are observed at 240 mbsf and at 310 mbsf. Another

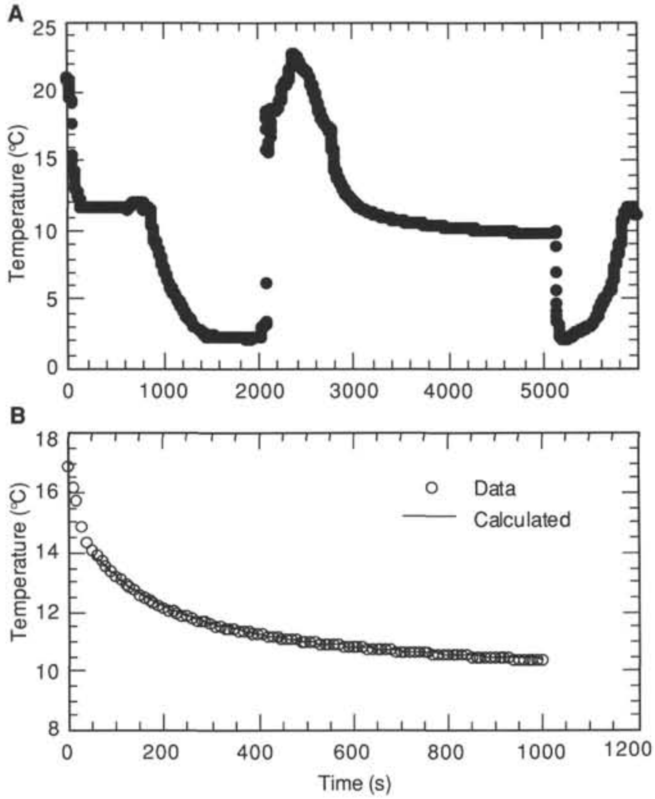

Figure 74. **A.** ADARA deployment record at 48.9 mbsf, Site 860B. **B.** APCTFIT program fit to these data.

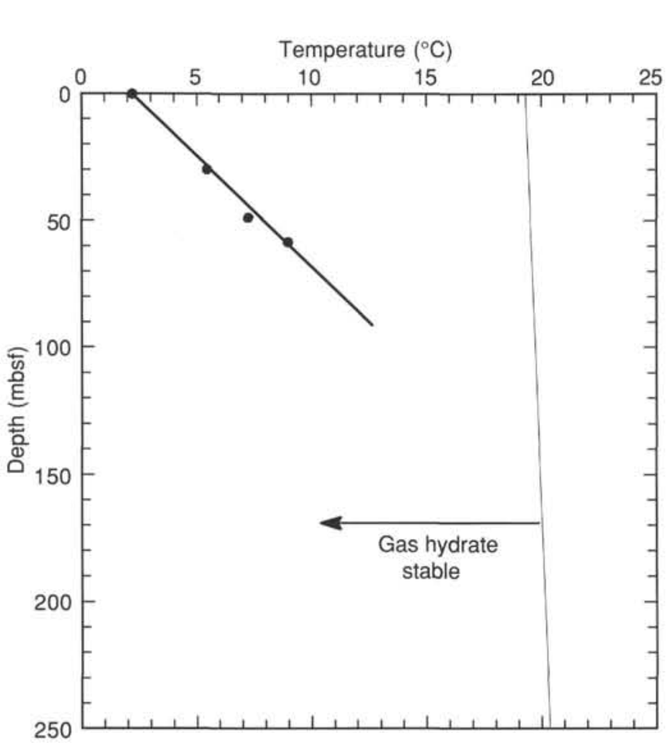

Figure 75. Temperature vs. sub-bottom temperature depth at Site 860. The upper temperature bound for the gas hydrate stability field is shown. Bottom-water temperature and data at 58.4 mbsf are favored in the linear fit.

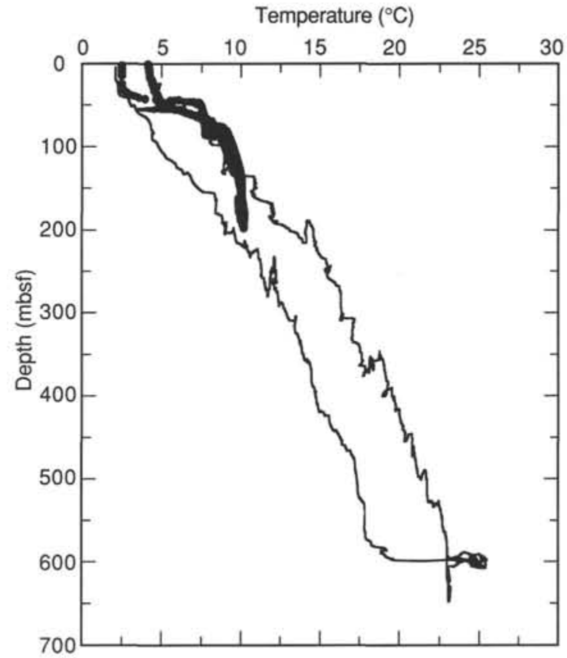

Figure 76. Compilation of borehole temperature measurements from two runs of the Lamont temperature tool in Hole 860B. Clustered dots show the first run, which terminated at 187 mbsf. The thin, continuous line is the temperature curve from the second run, which reached the bottom of the hole. Data from the second run were recorded while the tool was in the drill pipe.

possible age reversal may occur at 360 mbsf. All age reversals are characterized by upper Pliocene strata appearing beneath a section of lower Pliocene. Lower Pliocene foraminifers were recovered from Core 141-860B-65X, at 560 mbsf, to the bottom of Hole 860B.

Paleowater depth determinations from benthic foraminifer analysis indicates that Site 860 has experienced uplift during the Pliocene. Down to approximately 370 mbsf paleowater depths were middle bathyal. Below about 370 mbsf paleowater depths were lower bathyal to abyssal.

The structural domains recognized at Site 860 are a near-surface domain from the seafloor to 100 mbsf characterized by slump deformation, a unit from 100 mbsf to 420 mbsf that contains a sequence of thrust faults, and a domain from 420 mbsf to the bottom of the hole composed of broken formation and stratal disruption. Based on biostratigraphic and lithostratigraphic repetitions faults are inferred at depths of 240 mbsf(?), 310 mbsf, 420 mbsf (?), 520 mbsf, and 580 mbsf. All observed bedding laminations below 420 mbsf are deformed or sheared. Bedding above 420 mbsf is shallowly dipping 10°SE in oriented APC cores. Thrust faults must be flats or shallow ramps at this location and have large (hundreds of meters) offsets to produce the observed stratal repetitions and simultaneously maintain the shallow bedding dips encountered.

Several short sections of coherent core yield a sequence of deformation events. The earliest deformation is characterized by flat-lying deformation bands. The second deformation is manifested by shear surfaces with moderate dips and normal offsets. The last observed deformation event is expressed by high-angle deformation bands showing reverse offsets. This sequence applies to at least 90 m of core.

Deformation bands within the broken formation occur in two styles, deformation bands with random orientations and deforma-

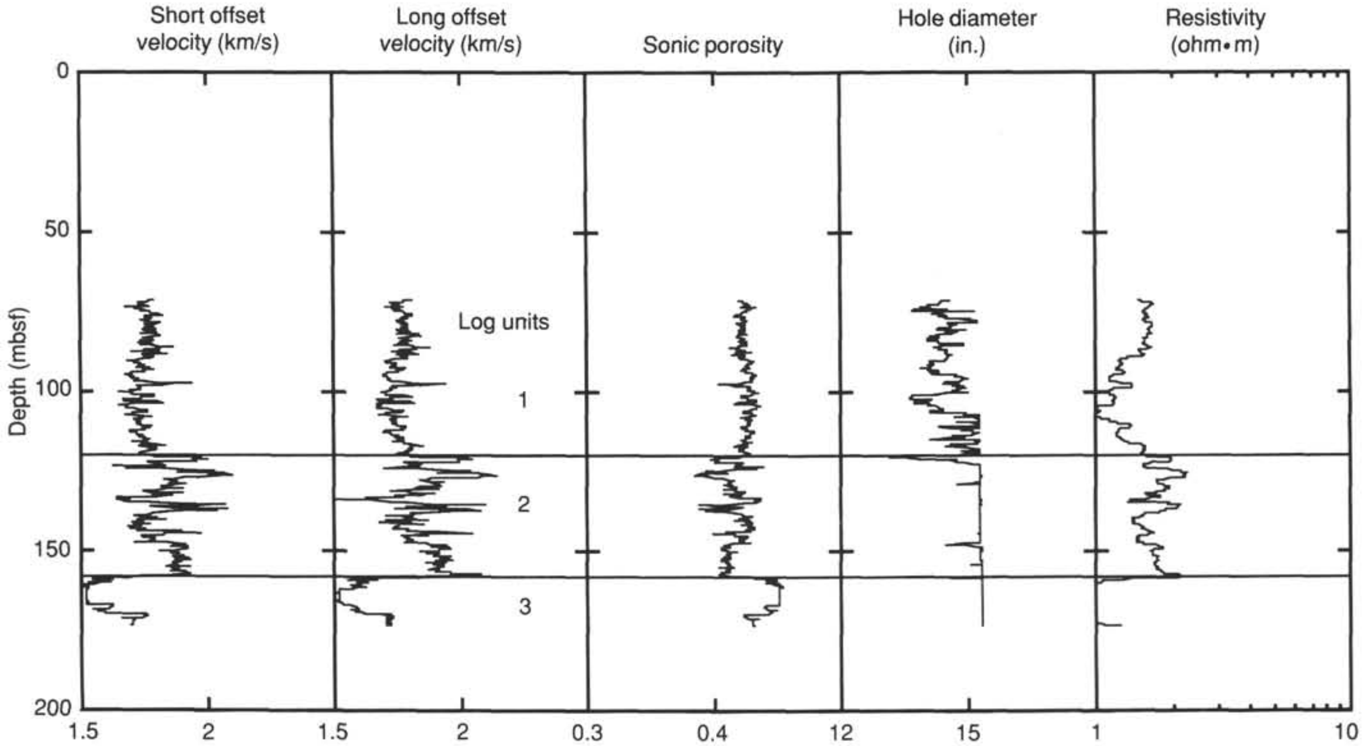

Figure 77. Log units in Hole 860B and the logs used to define the units. The short- and long-offset velocities are derived from the near and far sonic logs. The sonic porosity is derived from the sonic log. The hole diameter is from the mechanical caliper device. The induction log shown is the deep resistivity.

tion bands with flat-lying orientations and consistent reverse offset. Simple shear is the deformation mechanism in the zones of reverse offset, and occurs within the shear zones themselves. Zones with random orientations characterize the regions between shear zones, and reflect bulk deformation between shear zones that allows fault-bounded rock units to change shape during slip on non-planar faults. The cementation in deformation bands is different from that in the host rock, and varies with depth. Perhaps this reflects fluid flow along the deformation bands. The timing of these deformation events suggests that the sediments sampled at the base of Site 860 have been deformed by out-of-sequence thrust faulting associated with ongoing deformation of the accretionary wedge.

The upper 200 m of Site 860 contains biogenic hydrocarbon gas dominated by methane, while below 200 mbsf the gas has a clear thermogenic component. There was no detectable methane in the top core, but subsequent headspace gas analyses indicate that the methane level is relatively constant at approximately 10,000 ppm to total depth (TD). The first appearance of ethane occurs at 60 mbsf, and propane first appears at 250 mbsf. The solid organic matter recovered is thermally immature throughout the cored section. This observation, together with the presence of ethane and propane gas at depth at Site 860, indicates that those higher hydrocarbon gases have migrated to the stratigraphic level drilled at Site 860 from deeper structural/ stratigraphic levels within the forearc, and have not formed at the shallow levels drilled.

Inorganic geochemical trends of interstitial fluids do not display typical equilibrium profiles at Site 860. Sulfate quickly drops from typical seawater values to near 0 above 60 mbsf, but then maintains a level of about 5–10 mM to TD. Chloride decreases below 100 mbsf, and has local minima at 140 mbsf, 200 mbsf, and 360 mbsf. The chloride profile might reflect relict hydrate dissociation that would decrease the salinity of pore water. Other explanations include fresh water transport from land along subsurface aquifers, or release of interlayer water from clay dehydration reactions at depth with fluid migration along thrust faults.

Bulk density measurements on discrete samples shows a local minimum at 100 mbsf. Thrust faults identified by biostratigraphic or structural criteria have no apparent signature in bulk density data, perhaps suggesting that there is little recent movement on the faults. Grain density shows a local increase at 40-50 mbsf, the same interval that contains a peak in magnetic susceptibility, suggesting that high-density and strongly magnetic minerals may be concentrated at this depth interval.

A combination of ADARA piston core shoe and WSTP/Uyeda temperature measurements establishes a geothermal gradient of about 140°C/km in the upper 70 m of Hole 860B, but one apparently reliable measurement at about 130 mbsf suggests that the gradient decreases to about 30°C/km at depth. This relatively low geothermal gradient is consistent with the low level of thermal maturity of the organic component of the sediment sampled at Site 860.

Recovery of broken formation at the bottom of Site 860 of the same age and lithology as that drilled at Site 859 at the base of the trench slope indicates that at least the most seaward 12 kilometers of the forearc at the latitude of CDP Line 745 is composed of offscraped and accreted material of Pleistocene and Pliocene age. If the continental basement further landward, as interpreted on the seismic reflection data, is actually subsiding in response to the removal of material from deep levels of the subduction zone, then simultaneous frontal accretion, thrust faulting and imbrication, and structural uplift are occurring at shallower structural levels further seaward. This observation suggests that very complex patterns of mass movement and deformation result from the processes of subduction erosion and accretion in the context of spreading ridge subduction. The transitional nature of the structural involvement of the forearc basin strata in the thrust faulting

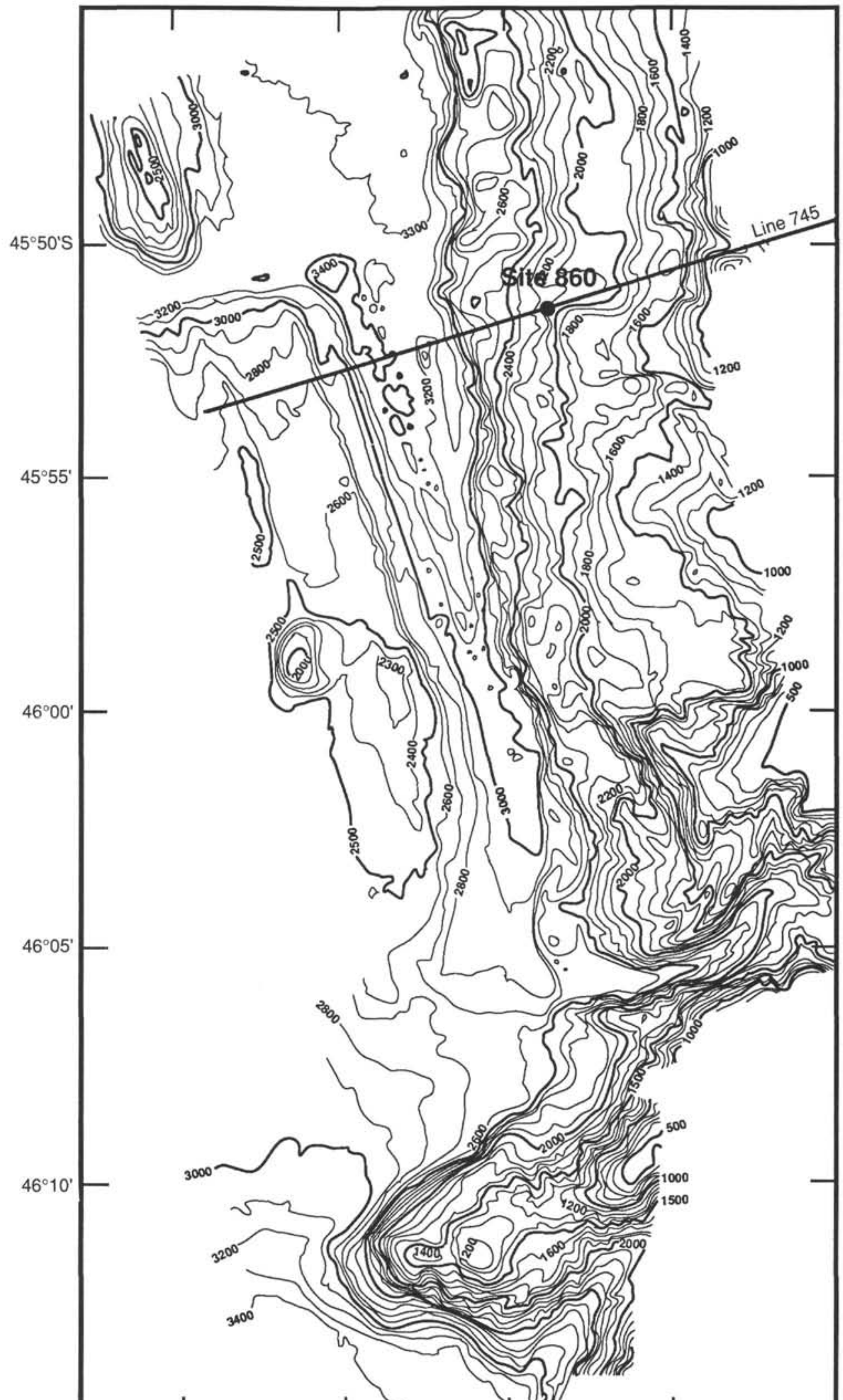

Figure 78. Bathymetric map of the Chile margin triple junction region, showing the location of Site 860.

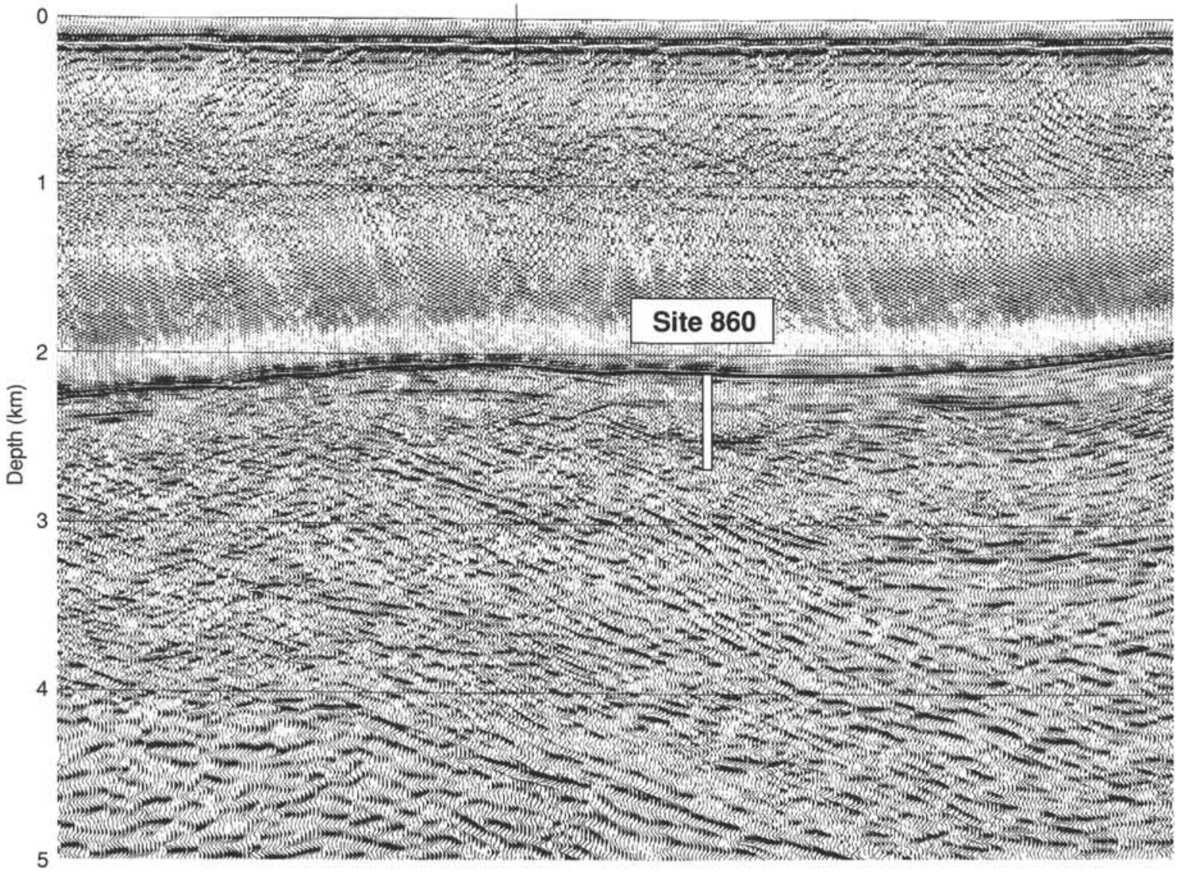

Figure 79. Depth-migrated seismic section of Site 860 (processed at GEOMAR by N. Bangs).

associated with frontal accretion indicates that deformation of the accretionary wedge has continued as far landward as the seaward side of the forearc basin, and that out-of-sequence thrusting is an important mechanism of deformation here.

Paleowater depth estimates at Site 860 suggest a shallowing trend in this mid-slope region during the Pliocene. The Darwin #1 well, drilled on the continental shelf approximately 75 km north of Site 860, also shows a strong pattern of uplift and shallowing paleowater depth since the middle Miocene. The middle Miocene-Holocene uplift at the Darwin #1 well on the shelf and the likely Pliocene-Holocene uplift at Site 860 on the slope may indicate a period of subduction accretion and uplift of regional extent along the margin at that time. The late Miocene was a period of very rapid plate convergence at this location along the Peru-Chile Trench, with subduction rates as high as 130 mm/yr (Chase, 1978; Cande et al., 1982). Rapid frontal accretion is implied by the lack of detectable age gradients between the broken formation at Site 859 and Site 860. This rapid accretion and regional tectonic uplift of the forearc may be a consequence of rapid late Miocene-Pliocene subduction. Drilling at Site 860, together with the results from Site 859, suggest that if subduction erosion is an important result of ridge subduction, such subduction erosion is not yet taking place at the latitude of Sites 860 and 859, only about 35 km north of the triple junction.

REFERENCES

Agar, S.M., 1989. Shearing of partially consolidated sediments in a lower trench slope setting. *J. Struct. Geol.,* 10:21–32.

Arason, P., and Levi, S., 1990. Models of inclination shallowing during sediment compaction. *J. Geophys. Res.,* 95:4481–4500.

Athy, L.F., 1930. Density, porosity and compaction of sedimentary rocks. *AAPG Bull.,* 14:24.

Bandy, O.L., 1961. Distribution of foraminifera, radiolaria and diatoms in sediments of the Gulf of California. *Micropaleontology,* 7:1–21.

Barron, J.A., 1985. Miocene to Holocene planktic diatoms. *In* Bolli, H.M., Saunders, J.B., and Perch-Nielsen, K. (Eds.), *Plankton Stratigraphy:* Cambridge (Cambridge Univ. Press), 763–809.

Bolli, H.M., and Saunders, J.B., 1985. Oligocene to Holocene low latitude planktic foraminifera. *In* Bolli, H.M., Saunders, J.B., and Perch-Nielsen, K. (Eds.), *Plankton Stratigraphy:* Cambridge (Cambridge Univ. Press), 155–262.

Boltovskoy, E., and Theyer, F., 1970. Foraminiferos Recientes de Chile Central. *Rev. Mus. Argent. Cienc. Natur. "Bernardino Rivadavia," Hidrobiol.,* 2:279–379.

Boyer, S.E., and Elliot, D., 1982. Thrust systems. *AAPG Bull.,* 66:1196–1230.

Burckle, L.H., 1977. Pliocene and Pleistocene diatom datum levels from the equatorial Pacific. *Quat. Res.,* 7:330–340.

Byrne, T., Maltman, A.J., Lallement, S., Karig, D.E., Soh, W., and Stephenson, E., in press. Deformation and fluid flow in the Nankai Accretionary Prism, Japan. *In* Hill, I., Taira, A., et al., *Proc. ODP. Sci. Results,* 131: College Station, TX (Ocean Drilling Program).

Cande, S.C., Herron, E.M., and Hall, B.R., 1982. The early Cenozoic tectonic history of the southeast Pacific. *Earth. Planet. Sci. Lett.,* 57:63–74.

Chase, C.G., 1978. Plate kinematics: the Americas, East Africa, and the rest of the world. *Earth Planet. Sci. Lett.,* 37:355–368.

Claypool, G.E., and Kaplan, I.R., 1974. The origin and distribution of methane in marine sediments. *In* Kaplan, I.R. (Ed.), *Natural Gases in Marine Sediments:* New York (Plenum), 99–139.

Deamer, G.A., and Kodama, K.P., 1990. Compaction-induced inclination shallowing in synthetic and natural clay-rich sediments. *J. Geophys. Res.,* 95:4511–4530.

Didyk, B.M., and Simoneit, B.R.T., 1989. Hydrothermal oil of Guaymas Basin and implications for petroleum formation mechanisms. *Nature,* 342:65–68.

Didyk, B.M., Simoneit, B.R.T., Brassell, S.C., and Eglinton, G., 1978. Organic geochemical indicators of palaeoenvironmental conditions of sedimentation. *Nature,* 272:216–222.

Emeis, K.-C., and Kvenvolden, K.A., 1986. Shipboard organic geochemistry on JOIDES Resolution. *ODP Tech. Note,* 7.

Espitalié, J., Madec, M., Tissot, B., Menning, J.J., and Leplat, P., 1977. Source rock characterization method for petroleum exploration. *Proc. 9th Ann. Offshore Technol. Conf.,* 3:439–448.

Farrington, J.W., Davis, A.C., Tarafa, M.E., McCaffery, M.A., Whelan, J.K., and Hunt, J.M., 1988. Bitumen molecular maturity parameters in the Ikpikpuk well, Alaskan North Slope. *Org. Geochem.,* 13:303–310.

Ingle, J.C., Keller, G., and Kolpack, R.L., 1980. Benthic foraminiferal biofacies, sediments and water masses of the southern Peru-Chile Trench area, southeastern Pacific Ocean. *Micropaleontology,* 26:113–150.

Karig, D.E., and Lundberg, N., 1990. Deformation bands from the toe of the Nankai Accretionary Prism. *J. Geophys. Res.,* 95:9099–9109.

Kemp, A.E.S., 1990. Fluid flow in "vein structures" in Peru forearc basins: evidence from back-scattered electron microscopy. *In* Seuss, E., and von Heune, R. (Eds.), *Proc. ODP, Sci. Results,* 112: College Station, TX (Ocean Drilling Program), 3–16.

Kennett, J.P., and Srinivasan, M.S., 1983. *Neogene Planktonic Foraminifera:* Stroudsburg, PA (Hutchinson Ross).

Knipe, R.J., 1986. Microstructural evolution in vein arrays preserved in Deep Sea Drilling Project cores from the Japan Trench, Leg 57. *In* Moore, J.C. (Ed.), *Structural Fabrics in Deep Sea Drilling Project Cores from Forearcs.* Mem.—Geol. Soc. Am., 166:75–88.

Lazarus, D., 1990. Middle Miocene to Recent radiolarians from the Weddell Sea, Antarctica, ODP Leg 113. *In* Barker, P.F., Kennett, J.P., et al., *Proc. ODP, Sci. Results,* 113: College Station, TX (Ocean Drilling Program), 709–727.

Lindsley-Griffin, N., Kemp, A., and Swartz, J.F., 1990. Vein structures of the Peru Margin, Leg 112. In Seuss, E., von Heune, R., et al., *Proc. ODP, Sci. Results,* 112:3–16.

Logan, J.M., Friedman, M., Higgs, N., Dengo, C., and Shimamoto, T., 1979. Experimental studies of simulated fault gouge and their application to studies of natural fault zones. *Proc. Conf. VIII—Analysis of Actual Fault Zones in Bedrock.* Open File Rep.—U.S. Geol. Surv., 79-1239:305–343.

Lundberg, N., and Moore, J.C., 1986. Macroscopic structural features in Deep Sea Drilling Project cores from forearc regions. *In* Moore, J. C. (Ed.), *Structural Fabrics in Deep Sea Drilling Project Cores from Forearcs.* Mem.—Geol. Soc. Am., 166:13–44.

Maltman, A.J., Byrne, T., Karig, D.E., Lallement, S., Knipe, R.J., and Prior, D.J., in press. Deformation structures at ODP Site 808. *In* Hill, I., Taira, A., et al., *Proc. ODP. Sci. Results,* 131: College Station, TX (Ocean Drilling Program).

McCollum, D.W., 1975. Diatom stratigraphy of the southern ocean. *In* Hayes, D.E., Frakes, L.A., et al., *Init. Repts. DSDP,* 28: Washington (U.S. Govt. Printing Office), 515–571.

Moore, J.C., 1989. Structural geology and hydrogeology of accretionary prisms. *J. Struct. Geol.,* 11:95–106.

Nigrini, C., 1991. Composition and biostratigraphy of radiolarian assemblages from an area of upwelling (northwestern Arabian Sea, Leg 117). *In* Prell, W.L., Niitsuma, N., et al., *Proc. ODP, Sci. Results,* 117: College Station, TX (Ocean Drilling Program), 89–126.

Peters, K.E., 1986. Guidelines for evaluating petroleum source rock using programmed pyrolysis. *AAPG Bull.,* 70:318–329.

Pickering, K.T., Agar, S.M., and Prior, D.J., 1990. Microstructural evidence for the origin of vein structures in Miocene forearc sediments, Miura-Boso Peninsula, S. W. Japan. *In* Knipe, R.J., et al. (Eds.), *Deformation Mechanisms Rheology and Tectonics.* Geol. Soc. London Spec. Publ., 54:417–430.

Pickering, K.T., Hiscott, R.N., and Hein, F.J., 1989. *Deep Marine Environments: Clastic Sedimentation and Tectonics:* London (Unwin).

Raymond, L., 1984. *Melanges: Their Origin and Significance.* Spec. Pap.—Geol. Soc. Am., 198.

Resig, J.M., 1990. Benthic foraminiferal stratigraphy and paleoenvironments off Peru, Leg 112. *In* Suess, E., von Huene, R., et al., *Proc. ODP, Sci. Results,* 112: College Station, TX (Ocean Drilling Program), 263–296.

Sanfilippo, A., Westberg-Smith, M.J., and Riedel, W. R., 1985. Cenozoic radiolaria. *In* Bolli, H.M., Saunders, J.B., and Perch-Nielsen, K. (Eds.), *Plankton Stratigraphy:* Cambridge (Cambridge Univ. Press), 631–712.

Shanmugam, G., and Moiola, R.J., 1982. Eustatic control of turbidites and winnowed turbidites. *Geology,* 10:231–235.

Shipboard Scientific Party, 1982. Guaymas Basin: Sites 477, 478, and 481. *In* Curray, J.R., Moore, D.G., et al., *Init. Repts. DSDP,* 64, Part I: Washington (U.S. Govt. Printing Office), 210–415.

Simoneit, B.R.T., 1977. Diterpenoid compounds and other lipids in deep-sea sediments and their geochemical significance. *Geochim. Cosmochim. Acta,* 41:463–476.

_______, 1978. The organic chemistry of marine sediments. *In* Riley, J.P., and Chester, R. (Eds.), *Chemical Oceanography* (2nd ed.) (Vol. 7): New York (Academic Press), 233–311.

Simoneit, B.R.T., Brenner, S., Peters, K.E., and Kaplan, I.R., 1981. Thermal alteration of Cretaceous black shale by basaltic intrusions in the eastern Atlantic. II: Effects on bitumen and kerogen. *Geochim. Cosmochim. Acta,* 45:1581–1602.

Srinivasan, M.S., and Kennett, J.P., 1981. A review of Neogene planktonic foraminiferal biostratigraphy: applications in the equatorial and South Pacific. *Spec. Publ.—Soc. Econ. Paleontol. Mineral.,* 32:395–432.

Suess, E., von Huene, R., et al., 1988. *Proc. ODP, Init. Repts.,* 112: College Station, TX (Ocean Drilling Program)

Taira, A., Hill, I., Firth, J.V., et al., 1991. *Proc. ODP, Init. Repts.,* 131: College Station, TX (Ocean Drilling Program).

Tarduno, J.A., 1990. Absolute inclination values from deep sea sediments; a reexamination of the Cretaceous Pacific record. *Geophys. Res. Lett.,* 17:101–104.

van Morkhoven, F.P.C.M., Berggren, W.A., and Edwards, A.S., 1986. Cenozoic cosmopolitan deep-water benthic Foraminifera. *Bull. Cent. Rech. Explor.-Prod. Elf-Aquitaine,* 11:1–421.

Voloshinova, N.A., 1958. On new systematics of the Nonionidae. *In Microfauna of the U.S.S.R.* (Vol. 9): Tr. Vses. Neft. Nauchno-Issled. Geologorazved Inst., N.S. 115:117–223.

Ms 141IR-107

NOTE: For all sites drilled, core-description forms ("barrel sheets") and core photographs have been reproduced on coated paper and can be found in Section 3, beginning on page 449. Forms containing smear-slide data can be found in Section 4, beginning on page 665.

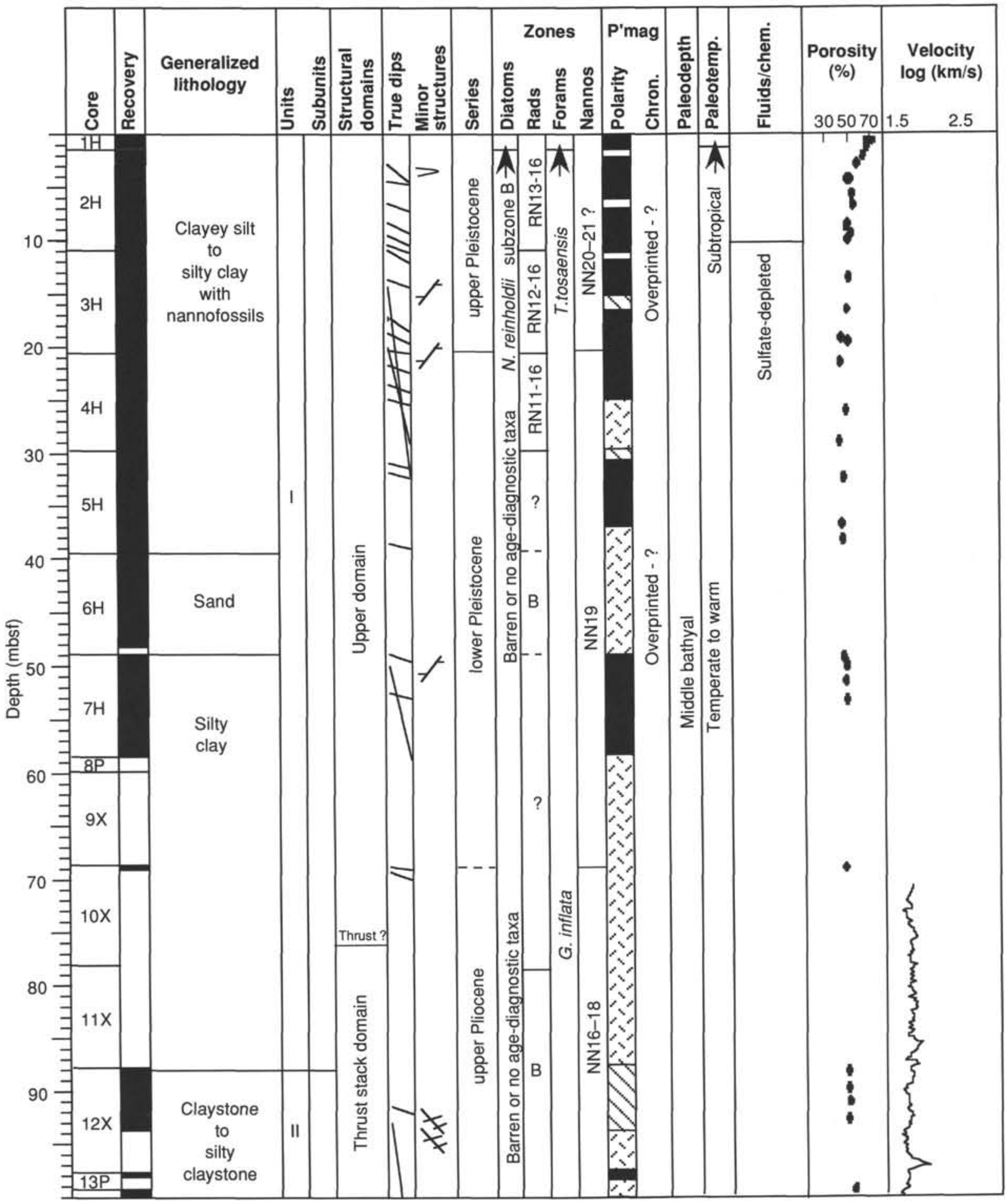

Figure 80. Master chart for Site 860.

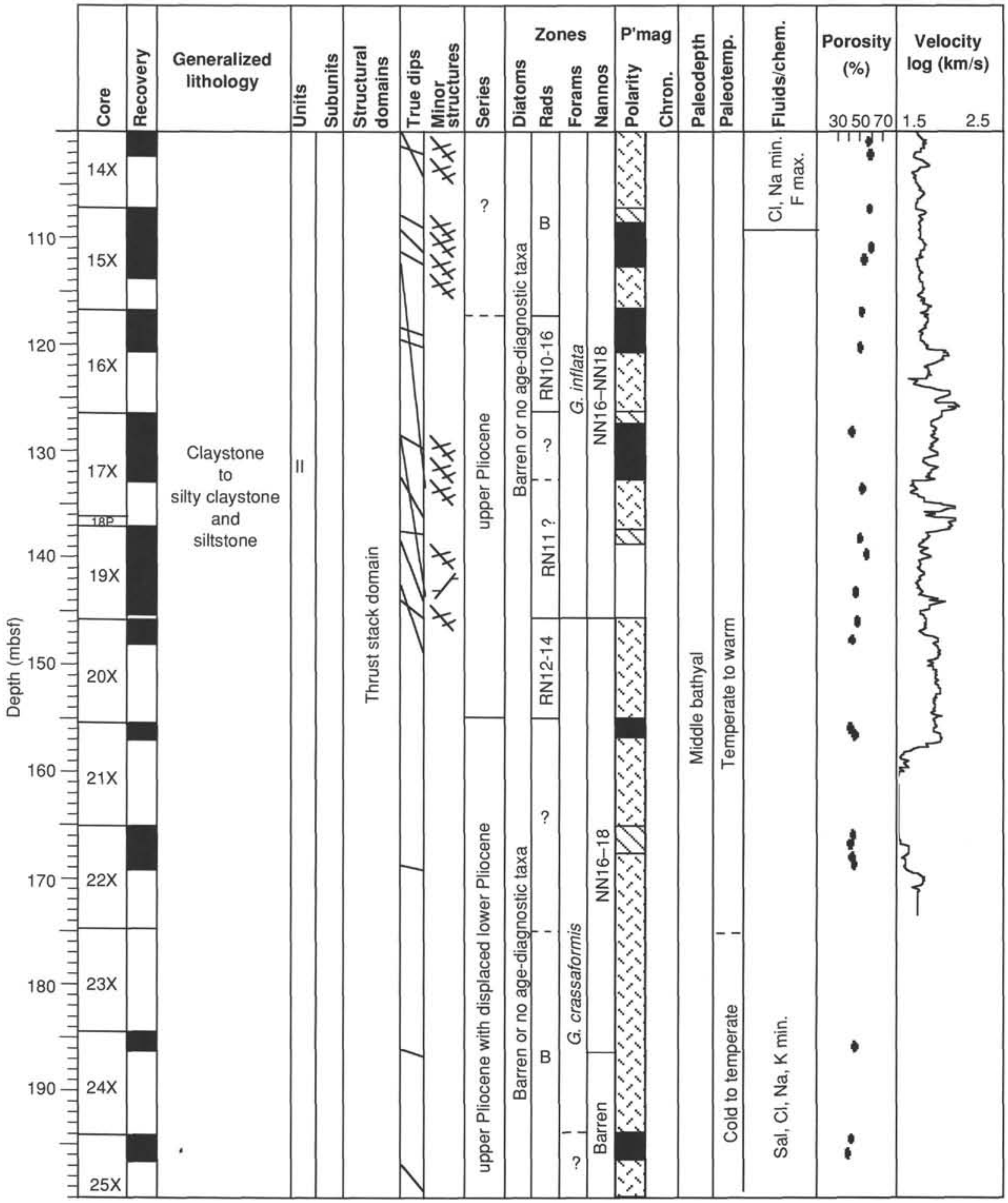

Figure 80 (continued).

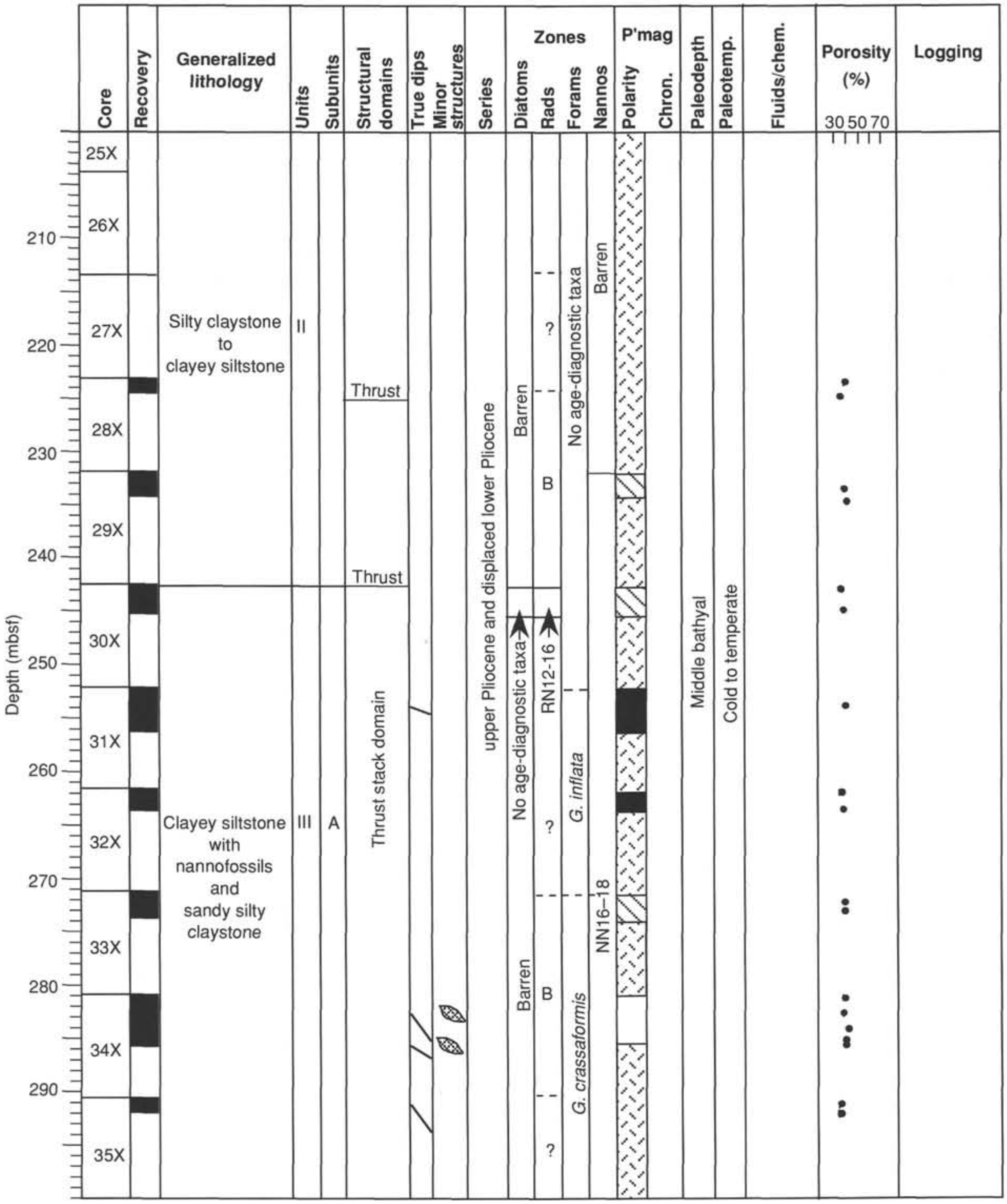

Figure 80 (continued).

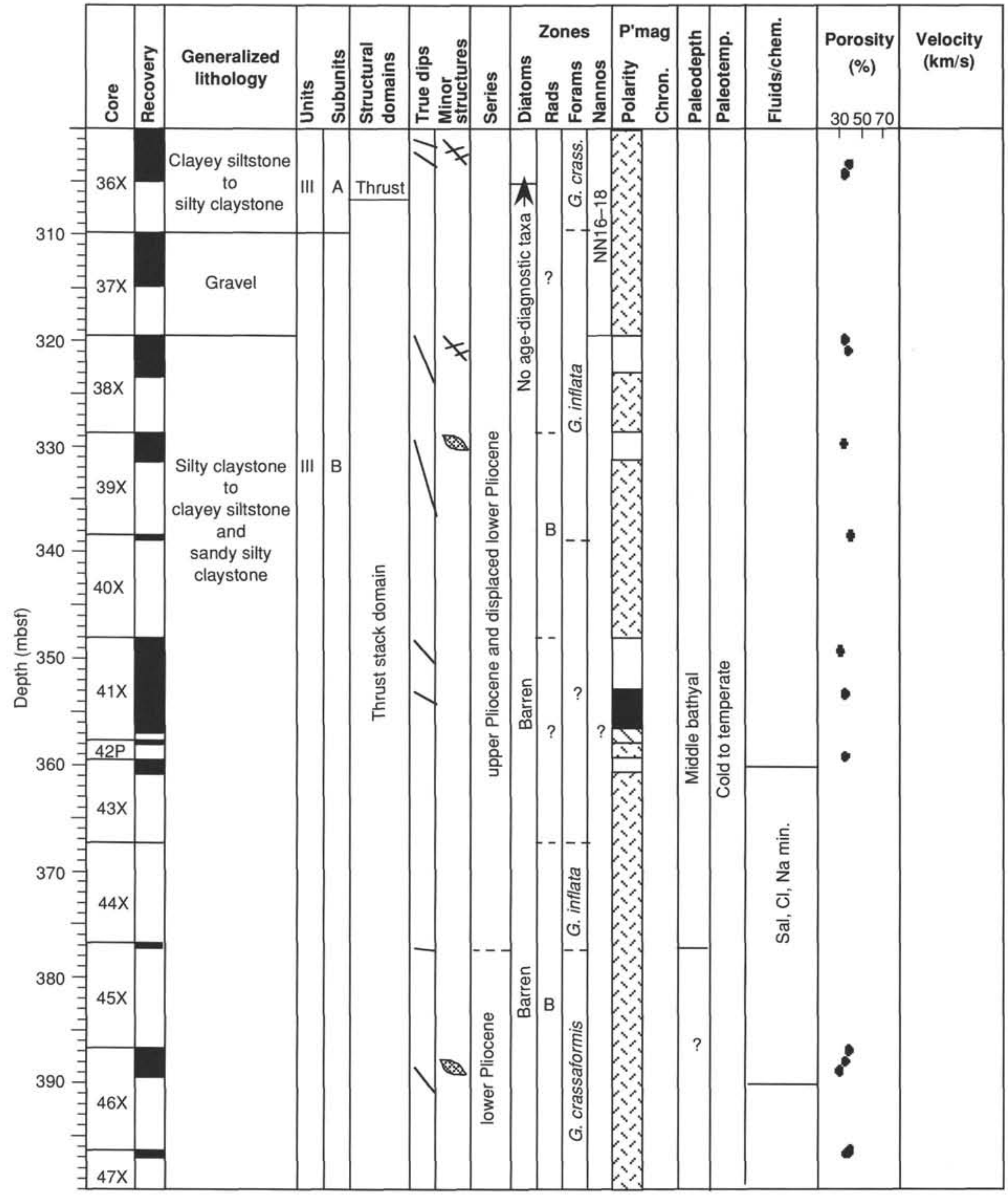

Figure 80 (continued).

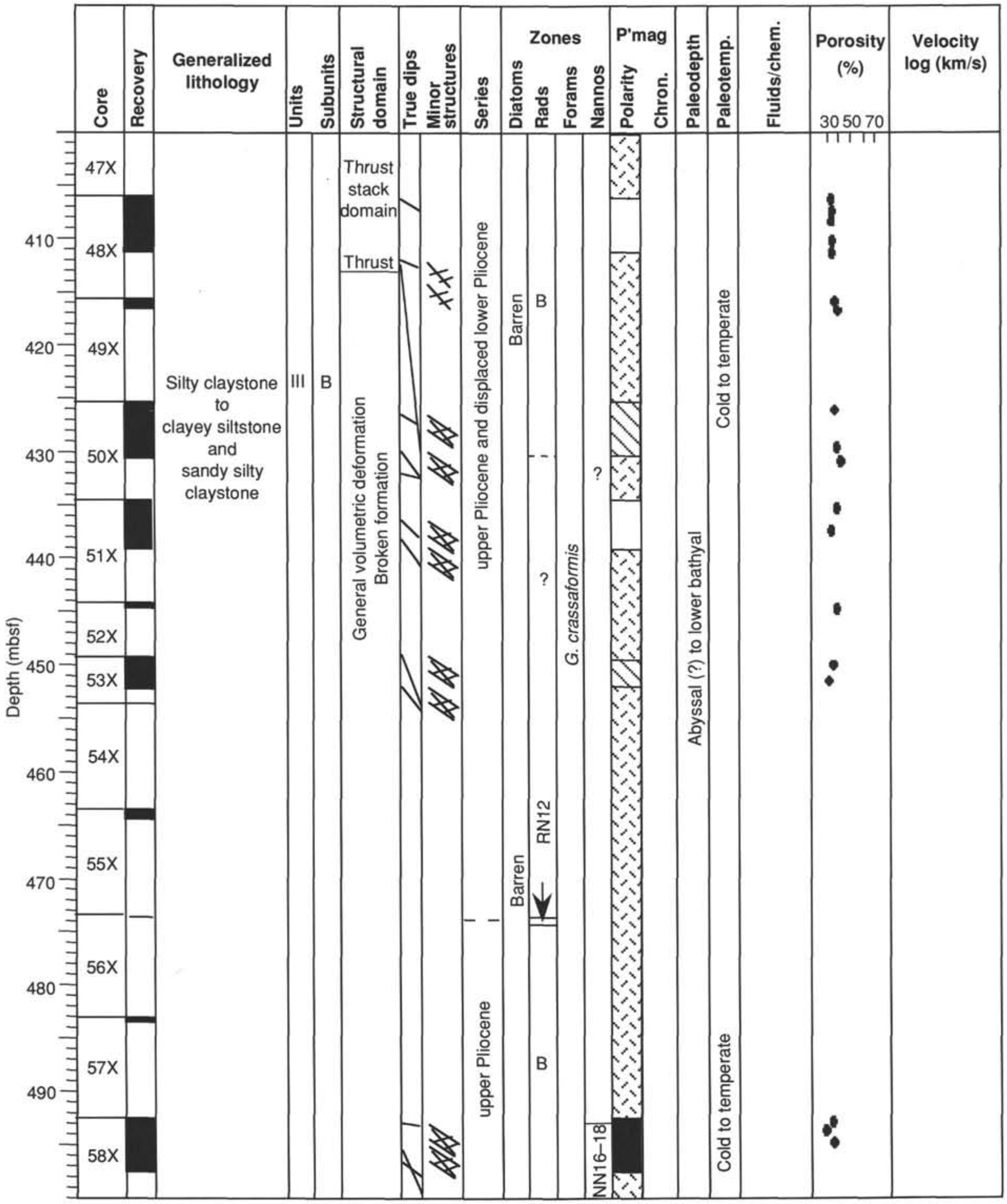

Figure 80 (continued).

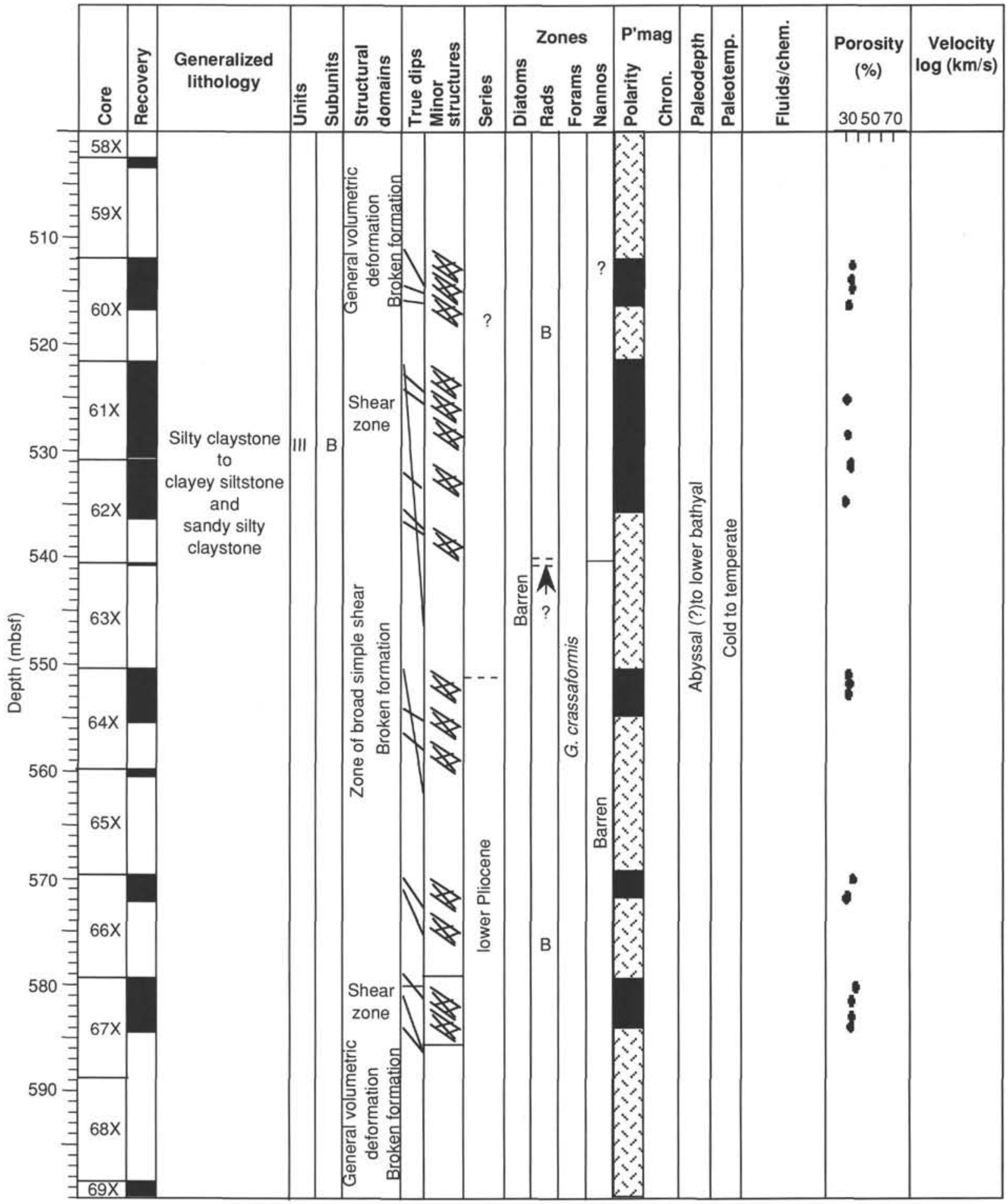

Figure 80 (continued).

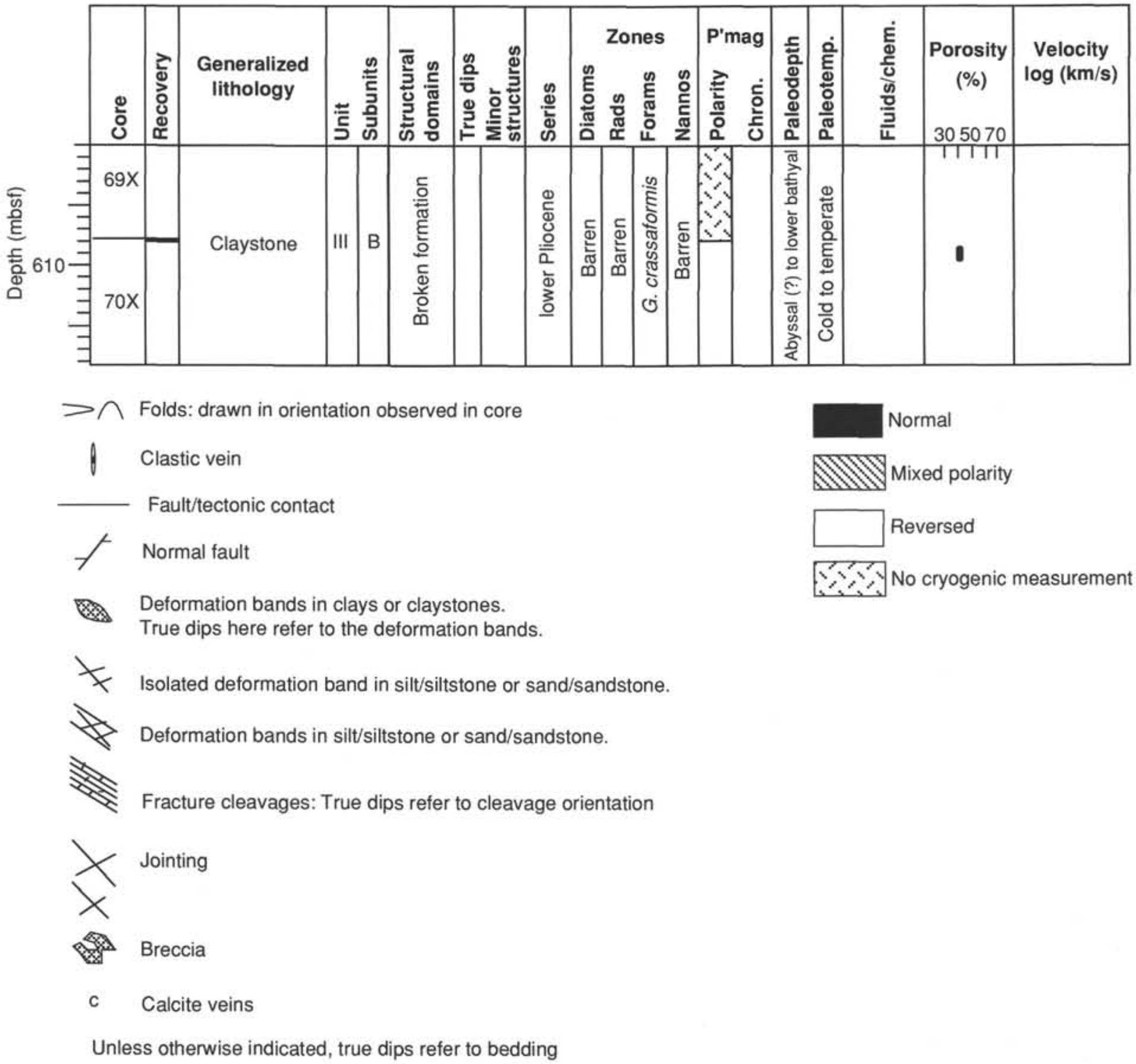

B = Barren

Tropical radiolarian zones (After Sanfilippo et al., 1985)

RN16 = *Buccinosphaera invaginata*
RN15 = *Collosphaera tuberosa*
RN14 = *Amphirhopalum ypsilon*
RN13 = *Anthocyrtidium angulare*
RN12 = *Pterocanium prismatium*
RN11 = *Spongaster pentas*
RN10 = *Stichocorys peregrina*

Figure 80 (continued).

Hole 860B: Resistivity-Velocity-Natural Gamma Ray Log Summary